UNIVERSITEIT VAN PRETORIA
UNIVERSITY OF PRETORIA
YUNIBESITHI YA PRETORIA

Investigation of a modified low-drag body for an alternative wing-body-tail configuration

by

Lelanie Smith

Submitted in partial fulfilment of the degree

Doctor of Philosophy in Engineering

Department of Mechanical and Aeronautical Engineering

University of Pretoria

Supervisors: Prof JP Meyer, Prof KJ Craig and Prof GR Spedding

August 2017

ABSTRACT

Title:	Investigation of a modified low-drag body for an alternative wing-body-tail configuration
Supervisors:	Prof JP Meyer, Prof KJ Craig and Prof GR Spedding (University of Southern California)
Department:	Mechanical and Aeronautical Engineering
Degree:	Doctors of Philosophy in Engineering

A wing-body-tail (WBT) configuration has been proposed without the conventional tailplane, allowing for new design objectives for the aerodynamic shape of the fuselage. A shorter, low-drag body (LDB) can be employed with a lower structural mass and lower drag per unit volume. There is an additional possibility that a carefully-designed deflector flap (Kutta edge or KE) can modify the flow around the body to allow for a more uniform circulation between the body and the wing. This basic idea has been tested and supported in wind tunnel tests but there have been no systematic attempts to quantify or explore the design space for these WBT geometries. All prior investigations were experimental on the full configuration at a low Reynolds number (Re) range where the aerodynamics of simple, rigid, fixed wings becomes extraordinarily sensitive to small changes in geometry and the environment. Therefore, the purpose of this study was to first investigate a simple case of the NACA0012 airfoil and wing, which becomes non-trivial when making baseline comparisons for experimentation and computation purposes. A diagnostic procedure then guides comparisons and predictions in subsequent more complex cases. In a preliminary attempt to bring specifically-designed low-drag bodies (LDB) into the design space, a numerical study was conducted to investigate the effect of adding a KE to two LDBs whose properties have been well established in the technical literature. Initial experimental tests on KE deflection were always accompanied by aftbody deflection, and the same procedure was adopted in the numerical studies, so tail deflection was achieved through deflection of the entire aftbody. It was further noted that such measures were quite sensitive to details of separation over the body and tail and that, paradoxically, a preferred arrangement would be to locate the KE entirely within the bounds of the viscous wake. Finally, the notion that the body-tail combination can be used in conjunction with the wing to improve the net downwash of the configuration was considered. The two bodies used previously with the KE were fitted with an NACA0012 wing at a fixed angle of attack of 6°. The overall purpose of this study was to provide some insight into the differences between the previous experimental and numerical studies and to investigate a potential design space of the initially tested WBT configurations. Then further exploration of the design space was conducted by using 10 discrete WBT configurations (five deflection angles with and without KE) for the original experimental WBT at chord-based, $Re_c = 10^5$ and two LDBs at their specific design length-based, Re_l (1.2×10^6 for F-57 LDB and 10^7 for Myring LDB). This work confirms that the KE can influence the WBT wake structure as initially estimated in experiment. The results here suggest that the original KE concept requires careful matching in the reality of viscous flows over bodies and wings at finite Re. In particular, if the KE is wholly or partially immersed in a wake that derives from earlier upstream separation or wing-induced wake effects, then the KE cannot operate effectively and the body termination conditions must already be judged to be sub-optimal. Adding the trailing-edge increased the total drag coefficient and the expected improvement of induced drag did not lead to a net benefit. If there is an optimal WBT configuration that leads to significant benefits in lift-to-drag, L/D, then it presumably would have to live in a domain where separation is almost completely avoided. The second modifying consideration is that if an entire system is designed for a certain lifting objective, then the option of providing that weight support through a modified geometry that includes a KE might not be well described by a single number such as L/D. When system benefits of reduced wing length, area and weight are included (and subsequently fed back into the new design set-point for the lift coefficient), the interlocked design benefits of each component might be difficult to isolate. The properties of the idealized WBT project with real bodies at finite Re are not easy to predict, this work offers useful guidelines and a helpful start, with recommendations for further numerical and experimental investigations.

JOURNAL AND CONFERENCE PAPERS

The conference papers and articles below were prepared and produced as progress was made in the preparation and completion of this PhD.

Articles

Smith, L., Craig, K.J., Meyer, J.P. and Spedding, G.R., 2017. “Modifying low-drag bodies to generate lift: a computational study,” *Journal of Aircraft*, Vol. 54, No. 3, pp. 1150–1161.

Tank, J., Smith, L. and Spedding, G.R., 2016. “On the possibility (or lack thereof) of agreement between experiment and computation of flow over wings at moderate Reynolds numbers,” *Interface Focus*, Vol. 7, Iss. 1, pp. 1–15.

Smith, L., Craig, K.J., Meyer, J.P. and Spedding, G.R., 2017. “Numerical investigation of the aerodynamic performance for an alternative wing-body-tail configuration,” *Journal of Aircraft*, Manuscript ID. 2017-05-C034595, submitted 25 May 2017.

Conference papers presented (published in proceedings)

Smith, L., Spedding, G.R. and Meyer, J.P., “Numerical and laboratory experiments on a new wing-body-tail configuration,” *54th AIAA Aerospace Sciences Meeting*, AIAA 2016-0800, San Diego, CA, 4–8 January 2016.

Smith, L., Craig, K.J., Meyer, J.P. and Spedding, G.R., “Optimisation of a wing-body-tail configuration with an alternative low drag fuselage and body trailing-edge,” *30th Congress of the International Council of Aeronautical Sciences*, ICAS 2016-0223, Daejeon, 25–30 September 2016.

Conference papers presented (not published in proceedings)

Smith, L., Craig, K.J., Meyer, J.P. and Spedding, G.R., “Investigation of a low drag body for an alternative wing-body-tail configuration,” International Aerospace Society of South Africa, Stellenbosch, South Africa, 14–16 Sept 2015.

Smith, L., “The advantages and challenges of the use of CFD to assist with experimental evaluation,” Star conference South Africa, Centurion, South Africa, 19–20 Sept 2016.

ACKNOWLEDGMENTS

I wish to express my sincere gratitude to all my supervisors, Prof JP Meyer, Prof KJ Craig and Prof GR Spedding, for their continual support, insight, guidance and commitment to me and the project. I have the greatest respect for all of them and appreciate their mentorship during this project as well as in my academic career.

I would like to thank Mr RJ Huyssen for the hours of arm-chair research and sharing his knowledge and experience with me on his novel aircraft configuration. It has been a pleasure to be a part of the gull-wing configuration team. I would also like to thank Mr C de Wet for his assistance and guidance with Star-CCM+ and for allowing me a space to work at Aerotherm during my training and during my PhD sabbatical. As a special thanks also to Dr Sean Thuling who shared some thoughts and guidance on my work.

I would also like to thank the National Aerospace Center and Airbus for their financial support as well as the Department of Research and Innovation Support at the University of Pretoria for its funding to complete parts of the research at the University of Southern California (USC).

Finally, I would like to thank my parents, Whity and Cecile Smith, and my family (especially Joggie and Ria Lubbe) for their support and encouragement; my dear friends who inspire and motivate me to greatness; my colleague Helen Inglis, for all her wise PhD survival tips; my fellow PhD students at USC for all the entertainment and support during my exchanges in Los Angeles; and Zanete Osner, Ilande Vorster and Elizabeth Stanley for their continual and unconditional support during challenging phases of my PhD. I would also like to express my sincere gratitude to my healing team, Madelief Fischli, Dr Tania Blake, Aleksandra Trend, Dr Belinda Glen, Julia Hastie and fellow teachers at Yoga Connection, for being a source of strength, inspiration and energy, and for their hours of guidance on a personal level. In addition, for carrying me through trying times in L.A., I wish to thank Irina Madder, Trystan Madison, Katia Durand, Brock Kokenge, Pierre van Breda and the Dalessandro family. A special word of thanks also goes to Prof Geoff and Liszl Spedding and little Kelvin for offering me a place to stay during the end of my exchange in Los Angeles 2016.

Truly PhD should stand for “Personal hectic Development”.

“A mystical truth is not something you “learn” but something that is revealed to you and you are transformed by the power of that truth. Such truth shatters the limitations of ordinary reason.”

- Caroline Myss

CONTENTS

LIST OF FIGURES

LIST OF TABLES

NOMENCLATURE

A_{KE} = Surface area of the Kutta edge (m^2)
A_{m} = Body cross-sectional area at maximum diameter (m^2)
AR = Aspect ratio, b^2/S
b = Wing span (m)
c = Chord length (m)
C_{d} = Sectional drag coefficient
C_{D} = Drag coefficient
C_{DA} = Drag coefficient based on frontal area
$C_{\mathrm{D,i}}$ = Induced drag coefficient
C_{DV} = Volume-based drag coefficient
C_{f} = Skin friction coefficient
C_{N} = Normal to the body force coefficient
C_{l} = Sectional lift coefficient
C_L = Lift coefficient
C_P = Pressure coefficient
D = Drag force (N)
d = Body diameter (m)
e = Oswald efficiency factor
f_{sb} = Blockage correction factor
f_{wb} = Wake blockage correction factor
F_{length} = Function of control transition length
F_{onset} = Function of control transition onset location
F_{s} = Safety factor
$F_{\theta\mathrm{t}}$, F_1 = Blending functions
G = Observed parameter for mesh convergence
I = Turbulence intensity
k = Turbulent kinetic energy (J/kg)
K = Interference factor
L = Lift force (N)
l = Body length (m)
N_{crit} = critical amplification number
p = Order of convergence
P = Static pressure (Pa)
P_{Total} = Total pressure ($P + \rho U^2$) (Pa)
q = Constant refinement ratio
r = Body radius (m)
Re_{l} = Reynolds number based on body length
Re_{c} = Reynolds number based on wing chord length
$\mathrm{Re}_{\theta\mathrm{t}}$ = Transition onset momentum thickness Reynolds number, $\rho U\theta_{\mathrm{t}}/\mu$
$\overline{\mathrm{Re}_{\theta t}}$ = Transport scalar
S = Surface area of the wing (m^2)

S_{m} = Semi-span of the KE (m)
t = Time (s)
T_{W} = KE width (m)
u^{*} = Friction velocity (m/s)
U = Freestream velocity (m/s)
$\|U\|$ = Velocity magnitude, ($\|U\| = \sqrt{U_x^2 + U_y^2 + U_z^2}$) (m/s)
U_{x} = Streamwise velocity component (m/s)
U_{z} = Vertical velocity component (m/s)
V_{b} = Body volume (m^3)
W_{D} = Wake diameter (m)
x = Streamwise direction (m)
y = Horizontal spanwise direction (m)
y^{+} = Non-dimensional wall distance
z = vertical (wall-normal) direction (m)

Greek letters

α = Angle of attack (°)
β = Turbulent viscosity ratio
γ = Intermittency
δ = Aftbody deflection angle (°)
δ^{*} = Boundary layer displacement thickness (m)
δ_{ij} = Kronecker delta
ε = Relative error (or turbulent dissipation)
θ_{t} = Transition onset momentum thickness
Λ_{0} = Angle between the body and the KE (°)
λ = Fineness ratio
μ = Dynamic viscosity (kg/(m.s))
σ = Streamline curvature correction factor
ρ = Density ($\mathrm{kg/m}^3$)
τ_{w} = Wall shear stress (Pa)
τ_{ij} = Reynold shear stress (Pa)
ν = Kinematic viscosity (m^2/s)
ω = Vorticity magnitude or specific dissipation rate (1/s)

Subscripts

B = Related to the body
B(KE) = Body influence on KE
c = Parameter based on chord
C = Combination
F = F-57 LDB
f = Friction component

i, j, k = Nodal point indexing in the *x*-, *y*- and *z*-directions, respectively
KE = Related to the KE
KE(B) = KE influence on body
L = Parameter based on bod length
L, B = Lift slope of the body
L, KE = Lift slope of the KE
L, T = Lift slope of the body and KE
L, wing = Lift slope of the wing
L, α = Lift slope at angle of attack
L, δ = Lift slope at angle of deflection
M = Myring LDB
mod = Modified parameter
p = Pressure component
t = Turbulent
θt = Transition onset momentum thickness
1, 2, 3 = Mesh refinement index number

1. INTRODUCTION

1.1 Research background

In the last two decades, major research initiatives around the world have been working on new aircraft configuration development, under the priority heading of "The Green Aircraft". The most well-known of these initiatives is the National Aeronautics and Space Administration (NASA)'s Environmentally Responsible Aviation (ERA) project, the European Commission's New Aircraft Concepts Research (NACRE) and the Clean Sky project. Spurred by the growing consensus that the current dominant aircraft configuration will have to be substituted, the search is intensifying for a superior new configuration as the pressure of the growing aviation industry on the environment demands substantially better flight efficiency.

The current dominant configuration (CDC) in commercial air transport is that of the tube-and-wing. The Douglas DC-3 entered service in 1936, having all the elements now common to all commercial transport aircraft. It is composed of a long tubular body, (hard, load-bearing external shell) supporting a single main pair of wings and a tailplane at the aft end, the purpose of which is to ensure static longitudinal stability. In the 80 years since then, very little has changed (perhaps engines may be mounted on the fuselage, perhaps on the wings). However, in times of continued scarcity and cost increases in fossil fuel, we are ever more concerned about whether potentially fundamental changes are necessary.

One of the favoured alternative configurations is the blended wing body (BWB) (Liebeck *et al.*, 1998; Liebeck, 2004). Although a review of the CDC is necessary, the general suitability of the CDC should not be lost (Huyssen *et al.*, 2016). Some of the BWB's most renowned qualities are the lift-producing centre-body, the elimination of the wing-body junction interference effects and the improvement of volumetric efficiency – all these qualities accumulate to a drag reduction of approximately 27% (Liebeck, 2004; Kuntawala, 2011). If general suitability of the configuration is to be maintained, a tube-and-wing configuration, with a similar fuel reduction, would be a meaningful avenue to explore. One such candidate already exists which could replace the CDC, known as the N+3 D8 configuration by Drela (2011).

The reasons for apparent penalties of the tube-and-wing configuration are mostly associated with the fuselage, and its existence as volume-carrying structure. Multhopp (1942), Dodbele *et al.* (1987), Wickens (1990), Zedan *et al.* (1994), Coiro and Nicolosi (1994) and Reneaux (2004) have emphasised the importance of reducing drag over the fuselage surface by noting that all turbulent airplane fuselage drag comprises 50% of the total profile drag (friction and form drag). The fuselage is not required to provide a portion of the lift, in fact, the necessary addition of the fuselage to the wing leads to a local loss of lift (Munk, 1923; Prandtl, 1932; Jones, 1980) and associated drag increase (Hoerner, 1965).

A side-by-side comparison between the fuselage of the BWB and an adjusted tube-and-wing configuration (D8) shows design principles considered in the search for an improved configuration Drela (2011):

a. Lower wetted surface area
    - D8 has the advantage of a shorter body with a reduced centre of gravity range, allowing the tail to shrink.
    - BWB will find it challenging to achieve low-drag and generate sufficient lift at a reasonable deck angle for a thick airfoil shape.

b. Fuselage or centre-body contributes to lift
    - D8 has a potential disadvantage since a substantial increase to lift over the fuselage could mean an increase in induced drag.
    - BWB has a disadvantage since the centre-body needs to maintain trim and positive static margin.

c. Airfoil-shaped fuselage
    - Both the D8 and BWB could benefit from the airfoil shape to reduce pressure drag or for the rear mounting of the engines to improve propulsion efficiency via fuselage boundary layer ingestion.

Although only some aspects of the two are similar, these points could serve as a good starting point for what the ideal fuselage body should be.

Huyssen *et al*. (2012) proposed an alternative wing-body-tail (WBT) arrangement. The key argument is that, in principle, a tailplane is unnecessary, since static longitudinal stability can be achieved with variations in the main wing geometry alone (Agenbag *et al*., 2009). Without this requirement, the long tubular body is neither necessary, nor close to an optimum, for either drag reduction or for packing efficiency (minimum wetted area per unit volume). If a different, shorter body is employed, it is possible to modify the flow around that body so that the circulation distribution between the body and the wings is much more uniform than with a tailplane. If that is so, both the induced drag and the total viscous drag can be reduced, owing to an improved body shape with a reduced wetted area. Therefore, two design objectives are proposed: a body with lower drag and a body that can provide some lift to the whole aircraft.

In terms of drag reduction, the fuselage design can consider a low-drag body (LDB) shape, which is typically shorter than traditional fuselage bodies. Various studies have found (experimentally and computationally) that the optimum drag body would have a fineness ratio, λ, (length to maximum body diameter ratio, l/d) of between 4 and 6, which is significantly different from the current dominant passenger transport configuration (the so-called "tube-and-wing") that uses $9 < \lambda < 13$. These studies include Young (1939), Gertler (1950), Stoney (1961), Boltz *et al*. (1960), Carmichael (1964; 1966), Chevray (1968), Krauss (1968), Parsons and Goodson (1972), Patel *et al*. (1974), Myring (1972; 1981), Hess and James (1976), Patel and Lee (1977), Chappell (1978), Meier and Kreplin (1981), Pinebrook and Dalton (1983), Markatos (1984), Patel and Chen (1986), Cebeci (1989), Lutz and Wagner (1998), Hammache *et al*. (2002) and Li *et al*. (2011) and mostly relate to underwater bodies and airships.

Figure 1.1 shows a schematic summary of aircraft fuselage and research bodies in terms of the relationship between λ and the Reynolds number (Re). Although the λ range is the same as in the case of practical aircraft design, the fuselage/body length-based Re ranges of practical aircraft design far exceed those of experimental work available.

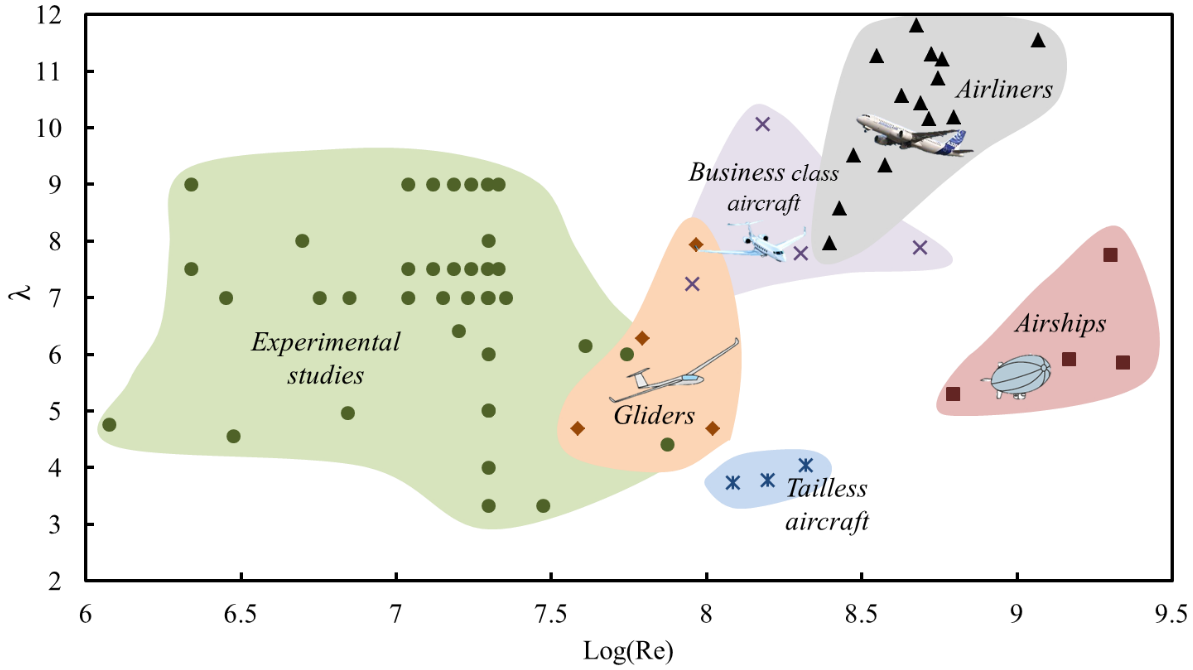

Figure 1.1: Past research on bodies of revolution including low-drag bodies.

In terms of the second design objective, the proposed WBT configuration would modify the flow around the wing-body by using a deflector plate called the Kutta edge (KE), shown in Figure 1.2. This KE would control the downwash distribution in order to maintain the highest possible span efficiency for the wing during all flight conditions. This implies that lift can be supported on an LDB simply by adding camber to the body of revolution. When combined with a trailing-edge tail/plate it could yield quite significant performance benefits by improving wing effectiveness and at some deflection positions, act as a high-lifting device. In principle, if a KE contributes to the lift of an aircraft, it allows flight at a lower lift coefficient, C_L, of the main wing, further reducing the drag of the overall system, offsetting any additional wetted surface area required for the KE.

The experimental investigations were conducted at Re = 5 x 10^4 (Huyssen *et al.*, 2012) and Re = 10^5 (Davis and Spedding, 2015). The KE appeared to modify the global flow around the body so that the circulation distribution between the body and the wings was more uniform, which, in principle, leads to a reduction in induced (inviscid) drag. However, the argument was only indirectly supported by the findings of modified downwash profiles in the near wake, and the mechanism by which the global flow-field was changed could not be directly identified, either from particle image velocimetry (PIV) in the wake (Huyssen *et al.*, 2012; Davis and Spedding, 2015) or with global force balance measurements (Davis and Spedding, 2015). It is also noted that no attempt was made to optimise the WBT, and both studies used a NACA0012 wing, a simple geometric form for the shorter body (not an LDB), and a discrete KE, which was not blended or integrated into the body shape. The KE itself was also fixed to the conical aftbody, so that KE deflection was always linked with deflection of the aftbody. The deflection was described by a single angle, δ.

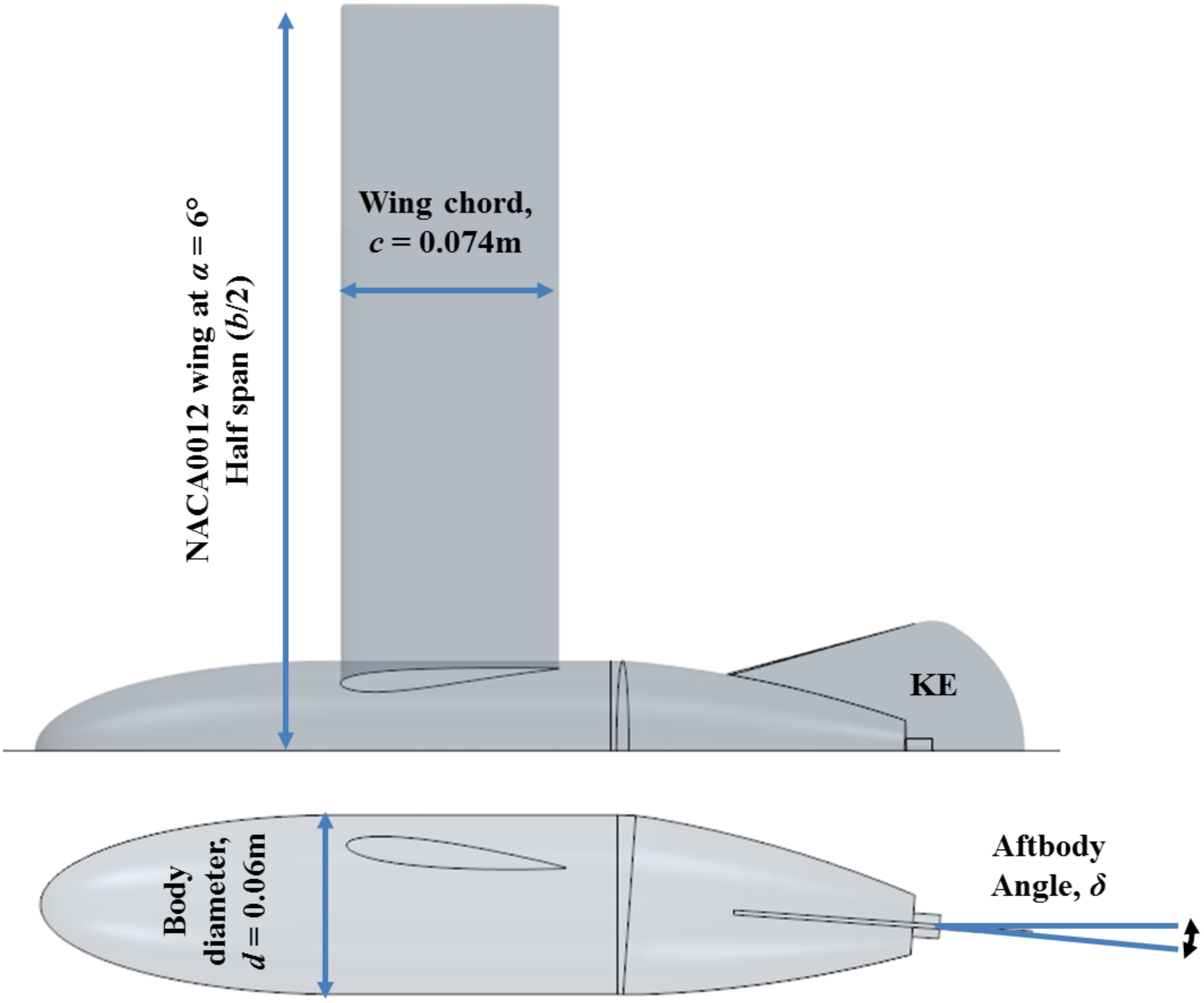

Figure 1.2: Geometry of the WBT configuration, top and side view, showing the aftbody deflection angle.

The assumption was made that global flow-field phenomena observed at these low Re, where accurate measurements are sensitive to small changes in geometry and the environment, would be similar than to those at a higher Re where these sensitivities do not play a role - a fair assumption given the deliberate use of boundary layer tripwires. Re < 10^5 is considered to be low Re and typically Re > 10^6 is the higher Re numbers. Leo1840727

The baseline comparison for experimentation and computation at a low Re is non-trivial since the lower limits of most turbulence models is 10^5 (Catalano and Tognaccini, 2010; Rumsey and Spalart, 2009). The simple NACA0012 airfoil case at a low Re has been investigated by Jones *et al*. (2008) and Rumsey and Spalart (2009) who provide some insight into the difficulty of the modelling, but do not offer a full set of results for purpose of comparison. No attempt has been made to provide experimental and numerical force coefficient data with careful comparisons of the sensitivities around obtaining results for a NACA0012 airfoil at Re = 10^5.

1.2 Importance of the proposed work

1.2.1 Low-drag bodies and the Kutta edge in the wing-body-tail configuration

Fuselage design objectives can be reconsidered if a payload-carrying fuselage is no longer required to support the tailplane. Replacing the fuselage with a LDB that is typically shorter and wider compared to the conventional fuselage, will lead to a lower drag per unit volume and lower structural mass. An overall fuselage geometry improvement (delayed transition over the nose and preventing separation over the aftbody) also leads to a reduction to the viscous drag. There is an additional possibility that a carefully-designed deflector flap at the aft margin can be used to control the location of the rear stagnation point, and hence, the circulation on the preceding body in subsonic flow. Converting the body into a lifting device is obviously advantageous, but there are also secondary effects, one of which is that the more uniform spanwise loading distribution (even over the central body) can yield a reduction in drag, as there are fewer losses in kinetic energy associated with numerous strong streamwise vortices. This basic idea has been tested and supported in wind tunnel tests (Huyssen *et al.*, 2012; Davis and Spedding, 2015) but the precise nature of the Kutta edge and body interaction were not considered, rather only the global flow-field effects. There have also not been any systematic attempts to quantify or explore the design space for these WBT geometries.

1.2.2 Agreement between experimental and computational results at a low Re

There is great uncertainty over rather basic quantities such as time-averaged lift and drag for wings and wing sections, simply because the Re is interesting and/or inconvenient. This unfortunate state is a consequence of the high sensitivity to small variations in conditions, and to the fact that most testing facilities are not well-suited to measuring such small forces with small tolerances. If a sound technical database is required, there is much work be done for low Re. Furthermore, many sensitive problems of laminar boundary layer stability, separation, transition and reattachment combine in complex ways that are intrinsically interesting.

Various authors (Abbott and Von Doenhoff, 1959; Selig *et al.*, 1995) provide comparative experimental resources for simple, rigid, fixed wings at a high Re. It has also been the focus of most commercially developed computational codes to predict flow-fields around these wings with good agreement. The same is not true for a low Re range where there is an increasing interest in the flight prediction of micro-air vehicles (Ol *et al.*, 2005; Yuan *et al.*, 2005; Rumsey and Spalart, 2009; and Catalano and Tognaccini, 2010). Quantitative experiments and plausible simulations on the peculiar behaviour of airfoils and wings at a low Re are now converging in a search for optimising tools, but the standards for agreement are vague as the usual supposedly simple problems are neither simple nor necessarily general. The agreement between experimental measurements and computational predictions will establish one or more baseline results and provide some insight into sensitivities at these low Re. The idea was that the diagnostic procedures will help guide such comparisons in subsequent more complex cases for example the proposed WBT configuration in this work.

1.3 Aim

The purpose of this study was to investigate the lift potential of low-drag bodies with Kutta edges, by numerically solving the flow-field around two low-drag bodies selected from literature. This was then extended to the full WBT to determine the important characteristics of LDBs in the WBT. Also exploring a section of the design space of the WBT to establish sensitive variables in terms of the KE geometry and deflection angle for future more detailed shape optimisation studies.

As a secondary aim, a set of experimental results for the NACA0012 at Re = 10^5 was compared to the numerical model. Reasonable comparison of the simple NACA0012 provided further confidence in the subsequent numerical evaluation of the LDB-KE and WBT configurations.

1.4 Research objectives

The primary research objectives for the study are as follows:

- Establish the characteristics of LDBs from literature and select LDBs that have experimental or numerical data from literature to model using Reynolds-averaged Navier-Stokes (RANS). Compare experimental and numerical results with literature and ensure good agreement is achieved.

- Modify the bodies selected from literature by adding short Kutta edges, for aftbody deflection angles of 2, 4, 6 and 8° at body length based Reynolds numbers of 1.2 x 10^6 and 10^7 and compare these to that of the reference body used in (Huyssen *et al.*,2012; Davis and Spedding, 2015). Determine a measure for the effective use of the LDB-KE in terms of providing lift. Describe the LDB characteristics at play when adding the KE and define the function of a KE.

- Establish a numerical baseline agreement by modelling a simple NACA0012 airfoil and wing with a low Re, similar to the wing used in the reference WBT, and compare these results to the new experimental results. Comment on reliability of both sets of data.

- Expand the series of RANS computations used previously on LDBs and reference body by fitting them with a NACA0012 wing at a fixed angle of attack of 6°. These configurations were modelled at wing chord based Reynolds numbers of 2.7 x 10^5, 2.4 x 10^6 and 10^5 respectively.

- Consider low-drag bodies within the WBT configuration to establish important characteristics of these bodies when combined with a wing and tail. Establish the sensitive variables in a design space.

1.5 Structure of the dissertation

Chapter 2 gives a detailed description of LDBs and the history of their development. A short overview is given in terms of the lift on bodies, wings and the body-tail interactions as described by existing literature. The basic principles of the proposed WBT configuration and experimental work that has been completed is summarised. A basic description is given of turbulence and transition models applicable to aerospace applications and their limitations at a low Re.

Chapter 3 shows the experimental set-up and compares the results of a NACA0012 at Re = 10^5

which are investigated in terms of modelling and experimental sensitivities.

Chapter 4 considers the numerical investigation of the LDB-KE to provide lift. It also details the fluid dynamics that enables this. Making use of two well-defined LDBs from literature, the KE is added and its effectiveness is evaluated and compared to the reference body (RB-KE combination).

Chapter 5 describes the numerical investigation of the experimental WBT configuration. Thereafter an LDB is introduced into the design space as part of the WBT. In all configurations the KE is found to be less efficient than without a KE.

Chapter 6 summarizes the research and provides a conclusion of the results. Recommendations for future work and improvements are suggested.

2. LITERATURE SURVEY

2.1 Introduction

The investigation of the proposed WBT configuration led to the consideration of three external aerodynamic applications, low-drag bodies, slender and delta wings as the tail and the wing. This chapter provides relevant knowledge in order to understand the reasoning behind the proposed WBT configuration selected. Some fundamental concepts that are key to various parts of the WBT are summarised. First, low-drag body characteristics are identified and two bodies are selected from literature to introduce to the WBT. Second, modifying bodies to provide lift are investigated. In this regard, low aspect ratio wings and delta wings as well as the slender wing-body theory are considered as it will make up the KE tail of the WBT. Third, the NACA0012 wing is considered in the context of agreement between experimental and computational results. Finally, the previous experimental measurements of the proposed WBT configuration are outlined. The computational model used is briefly discussed to provide insight into the selection of the specific models used in the study.

2.2 Non-dimensional parameters

To evaluate and compare flow regimes and aerodynamic forces, the non-dimensional Re, drag and lift coefficients are used. However since this study consists of bodies of revolution, wings and full aircraft configurations, the difference in reference area in each case becomes important.

2.2.1 Reynolds number

The Re_l for a body of revolution is defined as the ratio between viscous forces ($\mu U/l^2$) and inertial forces ($\rho U^2/l$) as:

$$\mathrm{Re}_l = \frac{\rho U l}{\mu}, \qquad (2.1)$$

where ρ is the density, U is the freestream velocity, l is the body length and μ is the dynamic viscosity. When considering an airfoil or a wing the reference length is the chord, c, and the Re is referred to as Re_c.

Re indicates the influence between the inertial and viscous forces in the fluid by defining three different regimes: laminar, transitional and turbulent. Laminar flow, for example, is where viscous forces dominate the inertial forces. In classical aerodynamics a Re_c ranging between 10^6 and 10^8 is considered a large number. In such cases the effects of viscosity are either easily ignored entirely, or are limited to a thin region close to the lifting surface, the boundary layer, where the outer potential flow adjusts to the presence of a solid body. Transition in external fluid dynamics is considered to be around $\mathrm{Re}_c = 10^5$ and is important for selecting models for the numerical simulations to understand whether transition modelling is relevant or important (White, 2009).

2.2.2 Lift coefficient

Lift generation for a body and a wing depends on different areas. The lift coefficients are therefore also defined using different reference areas. The body lift, L, depends on the displacement of streamlines over the body, so the appropriate reference area is the cross-sectional area at the maximum body diameter, $A_{m,}$ and C_L is defined as:

$$C_L = \frac{L}{0.5\rho U^2 A_m} \,. \qquad (2.2)$$

The lift coefficient for a wing or aircraft uses the planform area of the wing *S*, as reference area. For an airfoil, lift coefficient is defined as, C_l and uses *c* as the reference length.

2.2.3 Drag coefficient

When considering bodies of revolution or body-tail combinations, the volume of the specific body is used rather than the maximum diameter cross-sectional area. Specifically, LDBs might have similar diameters, but the streamwise profile of the body could be significantly different, so a volume-based drag coefficient is preferred:

$$C_{DV} = \frac{D}{0.5\rho U^2 V_b^{2/3}} \,, \qquad (2.3)$$

where V_b is the volume (used as the reference “area”) and *D* is the drag force. The drag coefficient is further defined as either pressure based (normal forces), $C_{DV,p}$, or friction based (tangential forces), $C_{DV,f}$.

For the drag coefficient for an airfoil, *c*, is the reference length and the coefficient is defined as C_d. For a wing or full configuration, the wing planform area, *S*, is used with the coefficient defined as C_D.

2.2.4 Body fineness ratio

Hoerner (1965) and Myring (1972) developed empirical correlations to describe the relationship of the body λ in terms of drag. These expressions are based on the experimental studies referred to in Section 1.1, and either the frontal area-based, C_{DA} or the volume-based drag coefficient, C_{DV} was used to determine what the ideal λ would be. Figure 2.1 shows the results of these empirical correlations, as well as for an ellipsoid in terms of C_{DA}.

Both the correlations assume fully turbulent flow and are valid for Re > 10^6. Each of these three lines has a different local minimum, according to Hoerner (1965), at a λ of approximately 2.6, and according to Myring (1972), at approximately 2. At any given λ, C_{DA} is very dependent on the body geometry, so a more appropriate way to analyse the drag coefficient of a body of volume would be C_{DV} as described in Equation 2.3.

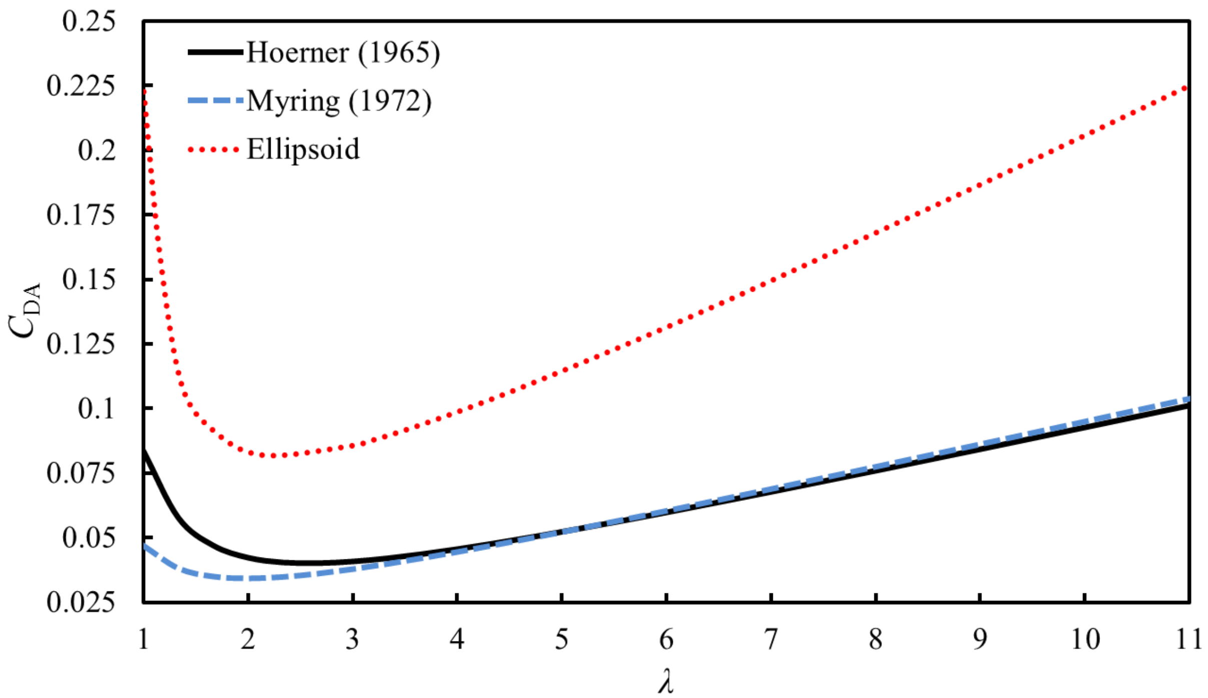

Figure 2.1: Frontal area-based drag coefficients, C_{DA}, as a function of λ.

Figure 2.2 illustrates the C_{DV} as a function of λ, where the minimum for the approximation of Hoerner as 4.6 and for that of Myring as 4.3. The suggested practical ideal based on the work of Myring (1981) on low-drag fuselages, however, shifts the λ to 5.56, to allow for realistic delay of transition over the nose and packing efficiency. Although from Figure 2.2 the increase in C_{DV} between $\lambda = 5$ and 10 seems small, it does offer a potential 11% reduction in drag which is quite significant. These correlations were found to be accurate within 2% of validated experimental results for $10^6 \leq \text{Re} \leq 10^9$, where transition could go up to 20% of the body length and Mach numbers below 1.

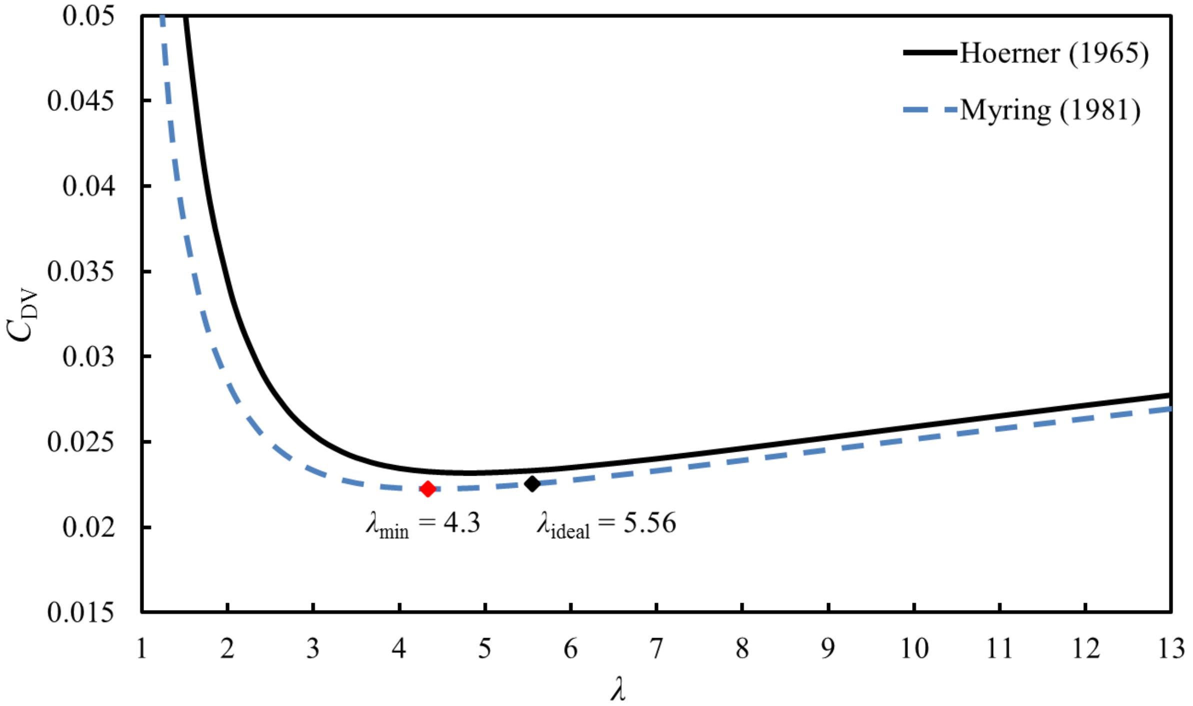

Figure 2.2: Volume-based drag coefficients, C_{DV} at Re = 10^7 as a function of λ.

2.3 Description of drag sources for external fluid dynamics

The description of drag is often somewhat ambiguous between various authors due to the interconnected nature of the force components. The description provided by Torenbeek (1982) is used in this study. as illustrated in Figure 2.3.

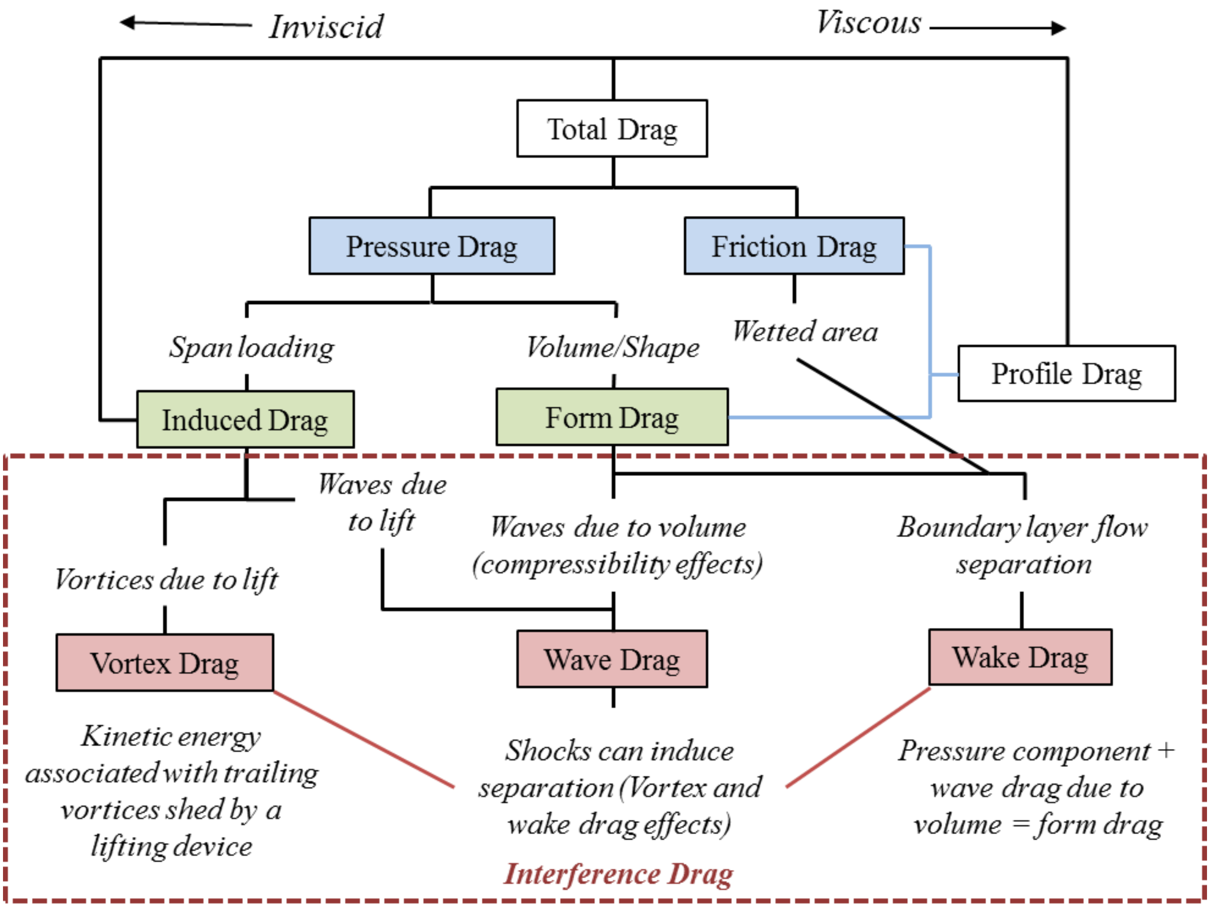

Figure 2.3: Drag breakdown of drag components (adapted from Torenbeek, 1982).

Aerodynamic drag is primarily divided into inviscid and viscous drag. Inviscid drag consists of lift-dependent drag generated by trailing vortices shed by a lifting device (vortex drag), lift-induced wave drag and also a variant of profile drag with angle of attack. Viscous drag is dependent on the surface area of the body (friction drag), volume of the body (form drag), the pressure recovery of the trailing-edge of the body and the growth of the boundary layer in unseparated flow (wake drag). Typically, when considering fuselage shapes, the viscous drag is minimised since a body is considered to be a non-lifting device, meaning that only form drag as part of the pressure component is taken into account.

2.3.1 Drag on bodies of revolution

Viscous drag involves the influence and characteristics of the velocity and pressure distribution across a body of revolution and the associated boundary layer development. In this regard, the body geometry effects (nose and tail fineness ratios) and the flow conditions (Re, Mach number and boundary layer transition position) are important variables to consider when finding an optimum λ.

The most important aspect of boundary layer development when considering a body of revolution, apart from preventing separation, is the position of transition. Along the nose section, the pressure gradient is favourable in order to delay transition. As the body starts to shrink in the aftbody, the boundary layer thickness increases due to the adverse pressure gradient, and the local shear force reduces to zero, reducing the friction drag. In the case of an adverse pressure gradient, the possibility of separated flow increases, which would affect the form and wake drag components. In low λ bodies, separation will occur and pressure drag will be high. As the λ increases, the flow would remain attached for longer, and hence friction drag ultimately dominates since the wetted surface area increases (Cebeci, 1989 and Zedan *et al*., 1994). Figure 2.4 shows the boundary layer development over a streamlined body of revolution.

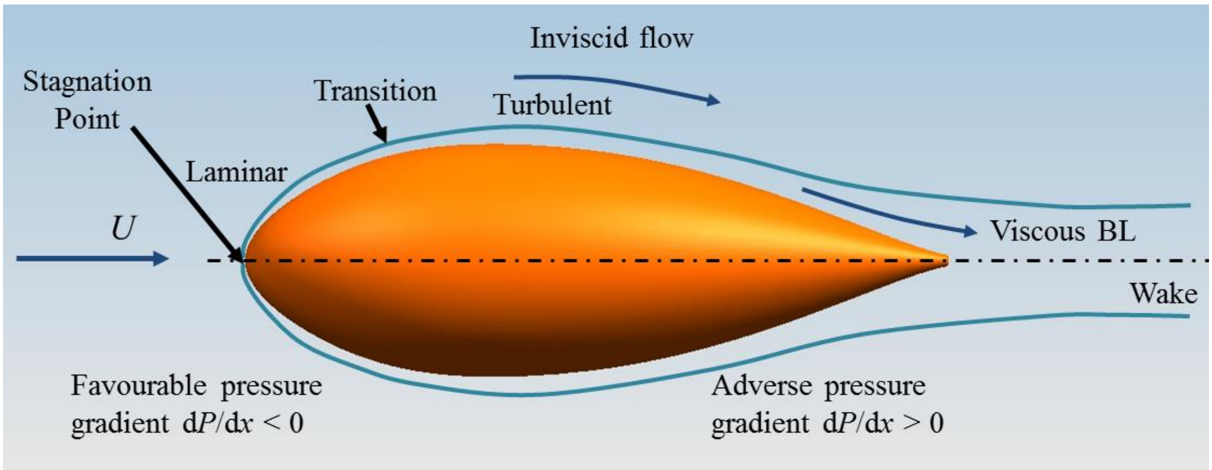

Figure 2.4: Boundary layer development over a streamlined body of revolution (Adapted from Granville, 1953).

Therefore, when considering a body of revolution, two aspects are of interest to create an LDB at a low λ: delay the transition over the nose and prevent separation over the aftbody.

2.3.2 Transition over the nose

For a low Re, the transition location is very dependent on pressure gradients where, for a higher Re, the aircraft transition location happens on the nose. At a higher Re, the aftbody recovery will also be better since pressure drag is less as the boundary layer thickness is less. The nose shape and its boundary layer characteristics have a strong influence on the final aftbody shape (Smith *et al*., 1981; Myring, 1981; Chappell, 1978). Therefore, the aftbody design is not an independent problem from the nose shape since the upstream influence of an aftbody will alter the pressure distribution on the nose in subsonic flow.

Delay of transition over a fuselage body has a practical limitation because of wing-body interference factors. Zedan *et al.* (1994) optimised an axisymmetric body for a business or commuter aircraft by using a modern low-drag aircraft, the Piaggo P.180 Avanti with a λ of 5.85, and the shape developed by Dodbele *et al*. (1987) has a λ of 6.14, x/l_{trans} = 0.36 at Re = 40.86 x 10^6. A reduced $\lambda \leq 5$ may present some limitations for the aircraft designer in terms of stability and space utilisation (Zedan *et al*., 1994).

2.3.3 Separation over the aftbody

Form drag in bodies of revolution (non-lifting bodies) happens primarily in the aftbody section due to the thickening of the turbulent boundary layer, and increases where there is separation due to body shocks or ill-shaped aftbody geometry. A streamlined body implies that the body does not have appreciable separation of flow from its surface, and therefore has little form drag resulting from the generation of separation eddies. Some form drag is still present even in perfectly streamlined bodies owing to the effect of the boundary layer in displacing the main flow outward, especially near the aftbody (Granville, 1953).

In the aftbody geometry, short sections lead to thicker boundary layer displacement than longer aftbodies; a decrease in λ increases the form drag since the boundary displacement thickness increases. In the case of $\mathrm{Re} \leq 10^5$, there is a greater possibility of separated flow as the body thickness decreases on the aftbody. The point of separation in laminar boundary layers is dependent on the body geometry, whereas for turbulent boundary layers, separation is due to strong adverse pressure gradients (Myring, 1981).

Aftbody geometry and the detailed shape of the pressure distribution are significant factors for a low-drag design. Patel and Chen (1986) commented that there is an added complexity to the flow over aftbody regions due to a rapid growth of the boundary layer, strong viscid-inviscid interaction and the effects of streamline curvature (Patel *et al*., 1974; Parsons and Goodson, 1972; Markatos, 1984).

2.3.4 Reynolds number sensitivity

Boundary layer development exhibited by axisymmetric bodies is very Re dependent, similar to that of boundary layer development over a flat plate. The optimal laminar body is a strong function of Re and very sensitive to early transition, λ and aftbody curvature. For fully turbulent flow, both the aftbody and nose becomes insensitive to geometric changes and the λ can be used here to optimise the combination of skin friction and pressure drag (Chappel, 1978; Myring 1981; Smith *et al*. 1981). Parson and Goodson (1972) optimised LDBs and showed that for each Re, a unique LDB exists in the laminar flow regime. When the shape of the body is not at the optimum λ, the body drag becomes extremely sensitive to Re.

Smith *et al*. (1981) found that aftbody shapes of axisymmetric bodies in fully turbulent flows are not appreciably affected over a wide range of Re. An optimal aftbody design for $\mathrm{Re} \leq 10^6$ will also be nearly the optimum with an increasing Re. However, this will only be true when the nose remains turbulent; if it becomes laminar or partly laminar the aftbody design is conservative and will not lead to separated flow (Cebeci, 1989). This indicates that the benefits gained from a body that reaches pressure recovery quickly (short aftbody) can be very useful for low Re ranges, but can also be more sensitive to early separation over the aftbody (ESDU, 1984). Geometry-wise, a short body, combined with a short aftbody or trailing-edge, reduces the viscous drag effects.

2.3.5 Low-drag bodies

In order to achieve a feasible LDBs the C_{DV} should, of course, decrease. However, if the pressure distribution shows a large adverse gradient, the critical Mach number is reduced and significant wave drag may appear. In addition, the first velocity peak (minimum pressure point) should occur as far downstream as possible to delay transition.

Myring (1981) found that in a body where the nose is 50% of the total length and is relatively blunt, the velocity peaks are lower and move further back in order to reduce skin-friction drag. If the nose length moves further back, the possibility of large adverse pressure gradients in the thick boundary layer in the aftbody section arises. By removing the midsection and allowing the aftbody to be longer, the second velocity peak can be removed to produce a smaller adverse pressure gradient over the aftbody. An aftbody length of 50% of the total length can be used and for a lower λ the aftbody shape can be blunter to lower velocity peaks and reduce the overall drag.

Myring (1981) compared an LDB with $\lambda = 5.56$ to a regular fuselage body with $\lambda = 10$, and noted that the LDB experiences a greater pressure drag and is therefore more sensitive to a Mach number increase. However, there is still an overall decrease of C_{DV} of 10% with this sensitivity.

2.3.5.1 F-57 low-drag body

Parson and Goodson (1972) developed a series of LDBs by means of an optimisation algorithm. Drag reduction is solely accomplished by rough manipulation of the body of revolution geometry for a fixed volume in incompressible flow at a fixed speed. A potential flow model, coupled with the drag model based on the formulation of Young (1939), assumed fully attached flow. Young (1939) made use of a modified airfoil method to predict profile drag for smooth bodies of revolution, though he found this method to have some restrictions. At a higher Re > 10^7 and low λ ($3.25 \leq \lambda \leq 5.9$), where there is early transition on the nose at $x/l \leq 0.05$, the method gave reasonable results compared to experimental cases. However, when both Re and λ are lower, the assumption of negligible pressure variation in the boundary layer on the aftbody is not correct, since the thickening boundary layer can support substantial pressure variation (Parsons and Goodson, 1972; Patel and Lee, 1977).

All the optimal designs exploited laminar boundary layers. The optimal shapes were strong functions of Re, with a high sensitivity to early transition. The Michel-e^9 correlation was used to model the transition. Parsons and Goodson (1972) compared their numerical model to two experimental bodies from literature, "the dolphin" (Carmichael, 1966) and Model 4165 of Series 58 (Gertler, 1950) and found fairly good agreement in terms of drag prediction although the transition prediction was not able to find the transition location at the point the experiments showed.

The F-57 LDB is selected here from the multiple LDBs Parsons and Goodson (1972) generated because data (pressure distribution, mean velocity distribution and Reynolds stresses) was published by Patel and Lee (1977) for the same geometry in wind tunnel experiments.

2.3.5.2 Myring's low-drag body

Myring (1972) developed a viscid-inviscid method that could predict profile drag of a body of revolution in attached subsonic axisymmetric flow conditions. The prediction method assumes early transition on the nose which leads to only a turbulent boundary layer and wake analysis being required. An integral method was preferred over a finite difference method purely because it meant a shorter computation time and had a small effect on the final drag predictions.

The computational method was compared to experimental measurements on the Akron airship (Freeman, 1932a, 1932b) with a general agreement of well within 1% of weighted mean values of external velocity. The region near the aftbody showed a fairly good prediction despite acute theoretical and experimental problems. In terms of boundary layer parameters of momentum and boundary layer thickness there was a 5% difference in results, which was contributed to uncertainties in the experimental investigation (Myring, 1972).

Within the family of shapes, Myring considered an LDB to be a shape with a continuously varying cross-sectional area, an ellipsoid nose (transition was forced at $x/l = 0.05$) and $\lambda = 5.56$. The Myring LDB is selected here since it was specifically developed as a low-drag fuselage body (unlike the hydrodynamic and airship bodies in most other studies) and the theoretical velocity distribution results were available.

2.4 Lifting bodies and low aspect ratio tails

Typically, the fuselage is not used as a lifting body, but in more recent aircraft configurations, like the BWB (Liebeck, 2004; Kuntawala, 2011) and the N+3 D8 configuration (Drela, 2011), a lift-providing centre-body is present. In this study, one of the requirements the fuselage can have in the WBT configuration is to provide a portion of lift. A fuselage body does not generate any lift when placed in-line with the flow direction in inviscid flow. However, when taking into account the viscosity (boundary layer development) and subsequent viscid-inviscid interaction over the aftbody, this scenario changes. Lift and vortex-induced drag of bodies are more sensitive to viscous effects than wings. The design objective of a body providing a portion of lift requires a means to reduce the lift-dependent drag component that arises as a result of the lift.

2.4.1 The Kutta edge

Huyssen *et al.* (2012) and Davis and Spedding (2015) showed experimentally that the trailing-edge of a fuselage can be used to control circulation in the central region of the aircraft, in support of the original notion that the primary role of the KE was to enforce a particular location of the aft stagnation point. The force balance and PIV measurements (Davis and Spedding, 2015) showed that the lift experienced by the aircraft with a KE increased with δ up to a certain maximum. The aftbody deflection makes a positive camber of the body, and thus potentially a non-zero circulation over it. The addition of the KE achieved the same effect at a lower δ and contributed to lift as δ increased. It was concluded that the most effective means of generating asymmetry and net lift on a body was through deflection of the KE.

For bodies of revolution, the boundary layer thickens over the aftbody and as a result, there is substantial variation of pressure across the boundary layer, leading into the near wake, characterised by strong viscous-inviscid interaction (Parsons and Goodson, 1972; Smith *et al.*, 1981). The added KE geometry now forms part of this aftbody, and will therefore not only be influenced by the complex flows taking place in this region, but also by the potential separation that can occur with LDBs due to the adverse streamwise pressure gradient. If separation occurs, the KE would be situated in the viscous wake of the body, and the KE shape and size would no longer greatly influence the lift, since the Kutta condition is not reached. Effective (increased L/D) LDB-KE interaction would depend on the flow remaining attached over the aftbody and the KE.

The KE in this study was modelled as a low aspect ratio or delta-like wing attached to the aftbody of the fuselage. However, since it is within the near-wake of the body of revolution, the behaviour cannot be modelled or predicted in terms of a delta-like wing, but rather by the slender-body theory, which includes the body-tail interference.

2.4.2 Low aspect ratio wings

Low aspect ratio wings are defined as wings with $AR = b^2/S < 3$, where b is the wing span. In the case where c is longer than b with a low AR wing, the trailing-edge of the wing is exposed to the flow that is deflected from the leading-edge. The downwash angle produced by this deflection is reached before the trailing-edge, which implies that when the edge is shortened, there is no loss in lift for a given span length. Therefore, C_L for slender wings is defined by span area, b^2, rather than by the wing surface, S, and leads to a lift slope, $\mathrm{d}C_L/\mathrm{d}\alpha = \pi/2\alpha$ (with α the angle of attack of the wing) since lift at such a low AR is independent of its chord. This is known as the basic circulation lift of a low AR wing (Weinig, 1947).

In addition, when considering low AR wings, the flow about the lateral edges becomes important as a secondary nonlinear lift slope component. Lift is produced by the downward deflection of the air flow or by imparting momentum on a certain cross-section of the air flow by the pair of vortex sheets curling around the lateral edges from the lower to the upper surface of the wing. In general, wings with straight sides and trailing-edges are more efficient than those that are rounded (Hoerner, 1985).

The lateral vortices do not only produce lift, but can also increase circulation over the entire portion of the wing area. As the AR reduces, there would be less surface area over which to increase circulation and the lateral vortices become the main source of lift (Hoerner, 1985). Therefore, the KE geometry should be more sensitive to spread compared to length for an improved L/D performance.

2.4.3 Delta wings

A delta wing is a triangular low AR wing, which the KE resembles. The strength of the vortex pair that develops over a delta wing is influenced by the cross-sectional shape, its angle of attack and the leading-edge angle. Typically, these vortex cores originate at the apex of the delta wing, increase in intensity over the top of the wing and continue after the trailing-edge at a downwash angle proportional to the lift. These vortices are referred to as leading-edge vortices that develop due to the downward momentum, produced by the counter-rotating vortices above the wing, result in the vortex lift component. If the angle of attack of the delta wing increases, the vortex cores move away from the surface and the strength increases as a function of an increasing pressure differential between the bottom and top surface of the wing (Hoerner, 1985). This leads to an increase in vortex lift as the angle of attack increases.

The leading-edge suction analogy (Polhamus, 1971) can predict the lift components (circulation and vortex lift) of a sharp-edged, flat plate delta wing. However, there are many limitations to the analytical model, including effects of the planform shape. The lift based on circulation can be predicted by assuming zero leading-edge suction, which translates into a Kutta-type condition being reached. This method also assumes that flow remains attached, leading to a normal force to the wing (lift) solely based on circulation over the wing, and the flow remains parallel over the trailing-edge. The leading-edge suction analogy can also predict vortex lift components with reasonable success at angles of attack lower than 20° where the vortex lift becomes the dominating component, which increases as the apex angle increases (Hoerner, 1985).

Polhamus's (1971) suction analogy was expanded by Lamar (1974) to include the estimation of the vortex lift on the side-edge along the wing. However it could be reasoned that since the KE ends in a sharp wing tip and there is no side edges to the wing, there will be no tip suction effect and therefore no need for Lamar's expansion.

Since the KE is not a delta wing alone, but has a body upstream attached to it and no distinct leading-edge, it becomes very difficult to predict the behaviour of the KE considering delta wing theory. When the KE is attached to the aftbody and later deflected, the angle as the flow approaches the portions of the KE is unpredictable and the viscous flow close to the body could interfere with the expected function of the KE. The tip shape leads to a loss in the circulation lift component too, which could imply that the aftbody shape has a strong influence on the effectiveness of the KE.

2.4.4 Lift from body-tail combinations

Lift develops over the nose of the body with fully attached flow at small angle of attack as the cross-sectional area changes. When integrating over the length of the body, positive lift over the nose and negative lift over the aftbody lead to a resultant lift force of zero. Streamlined bodies form vortices and develop normal forces (lift) similar to delta wings. The flow pattern develops in both cases as a pair of symmetrical vortex sheets from the sides of the body or the tips of the low aspect ratio wing. As the angle of attack increases, the location of the origin of these vortices moves upstream on the body, and the lateral distance between the vortex cores becomes an indication of effective lift provision. The larger this distance is, the more effective the tapering of the aftbody. A blunt cylindrical body has a lateral distance of approximately $2/3d_{\max}$ (Hoerner, 1985).

However, if the body boundary layer separates over the aftbody (which could be the case even at zero angle of attack for a badly designed aftbody) at increasing angles of attack, there will be an increase in the pressure drag component. The cause for this increase is an increase in the effective base area of the body by virtue of the boundary layer displacement (Nielsen, 1988). The boundary layer rolls up into vortices enclosing a separation region, enlarging the area the forces act on, which leads to a drag component due to lift.

When the body is combined to a delta-like tail, there would be a strong interaction between the vortex pairs of these two components. This requires an investigation into the influence of the

KE vortices on the body and on itself, as well as the body vortices on the KE and itself, further defined in Section 2.4.6. In principle, this would mean that the further forward the KE moves (or integrates into the body), the less interference there is between the vortices and the more effectively the combination provides lift.

2.4.5 Modification of the slender-body theory for the Kutta edge

Pitts *et al*. (1957) introduced a method to calculate the lift of circular-cylindrical bodies in combination with various tail shapes in subsonic flow. Certain parameters were defined to quantify the interference between the body and the tail at small angles of incidence. These parameters were defined as ratios of the lift of the components in the body-tail combination and the tail alone. These ratios were obtained by using the slender-body theory (Nielsen, 1988). Pitts *et al*. (1957) defined this method to describe large fuselage radii and to compare the tail spans of a typical missile application.

Two models were proposed to predict the lift of a body-tail combination. The first model was based on the assumption that the body and tail each provides a local lift force. Considering the body as a slender-body, the estimated lift coefficient was given as $C_{L,B} = 2\delta$, where δ is the aftbody deflection angle of the WBT as shown in Figure 1.2, and the KE as a slender wing of which the estimated lift coefficient was given (Hoerner, 1985) as:

$$C_{L,KE} = (\pi/2)AR\delta, \tag{2.4}$$

where $AR = b^2/S$ and b is the wing span. This model is quite crude and is referred to as the simple model (SM) for convenience of notation in this study. A total lift coefficient was then described as:

$$C_{L,T} = 2\delta + (\pi/2)AR\delta, \tag{2.5}$$

The second model made use of the method of Pitts *et al*. (1957) where lift was broken up into the sum of principle components of the body-tail combination, referred to as the slender-body theory (SBT). The lift from the body alone, L_B, the lift from the KE in the presence of the body, $L_{KE(B)}$, the change of the lift on the body due to the presence of the KE, $L_{B(KE)}$, and the lift of the tail alone, L_{KE} were defined. Simple closed expressions for the lift curve slopes can be obtained for the body-tail combination. However, these tend to overestimate the lift curves. This method has shown reasonably good agreement with experimental results (Pitts *et al*., 1957).

The method presented by Pitts *et al*. (1957) employs the model of Morikawa (1952) for presenting lift interference. In this method, the tail alone is defined as the exposed half-wings joined together. The lift of the combination, L_C, is then related to L_{KE} by an interference factor K_C (ESDU, 1995):

$$L_C = K_C L_{KE} \tag{2.6}$$

The interference factor K_C is decomposed into three factors:

$$K_C = K_{KE(B)} + K_{(B)KE} + K_B \tag{2.7}$$

Each decomposed component is defined as:

$$K_B = \frac{\pi r^2 \left(\partial C_N / \partial \delta\right)_B}{S_m \left(\partial C_L / \partial \delta\right)_{KE}} \ , \tag{2.8}$$

where r is the maximum body radius, S_m is the semi-span of the KE, $(\partial C_\mathrm{N}/\partial\delta)_\mathrm{B}$ is the lift curve slope of the body alone and can be approximated to 2 for all cylindrical bodies and $(\partial C_\mathrm{L}/\partial\delta)_\mathrm{KE}$ is the lift curve slope on the KE alone approximated by the slender wing theory (ESDU, 1995). The $(\partial C_\mathrm{L}/\partial\delta)_\mathrm{KE}$ relies on the aspect ratio ($AR = 2S_\mathrm{m}^2/A_\mathrm{KE}$, where A_KE is the KE surface area) and the angle between the body and the KE, Λ_0 as shown in Figure 2.5.

$$\left(\partial C_L / \partial \delta\right)_{KE(B)} = K_{KE(B)} \left(\partial C_L / \partial \delta\right)_{KE} \tag{2.9}$$

$$\left(\partial C_L / \partial \delta\right)_{B(KE)} = K_{B(KE)} \left(\partial C_L / \partial \delta\right)_{KE} \ , \tag{2.10}$$

where $K_\mathrm{KE(B)}$ and $K_\mathrm{B(KE)}$ are obtained from the SBT as a function of r/S_m. $K_\mathrm{KE(B)}$ can be considered as the interference fraction that the upwash from the body upstream has on the lift of the KE. Typically, the body upwash increases the lift provided by the KE. $K_\mathrm{B(KE)}$ is the interference fraction of lift that is carried over by the KE to the aftbody due to the close proximity of the KE to the aftbody (ESDU, 1995).

Finally, the lift coefficient curve can be approximated by:

$$C_L = \frac{\pi r^2 \left(\partial C_N / \partial \delta\right)_B}{S_m} \delta + \left(K_{KE(B)} + K_{B(KE)}\right) \left(\partial C_L / \partial \delta\right)_{KE} \tag{2.11}$$

In order to apply the two methods the geometry of the LDB-KEs has to be defined in terms of the SBT. Figure 2.5a shows the straight-forward definition of the body-KE geometric description compared to that of the prescribed SBT method. However there are two main differences in the geometric definition of the SBT compared to the LDB-KE combination. First, the cross-section of the body remains constant and has a blunt aftbody end, and for the LDB, the cross-section is continuously varying and can taper down to a very small tail edge. Second, a portion of the KE is located behind the body compared to the slender wing body definition where the tail-edges are only located on the sides of the body.

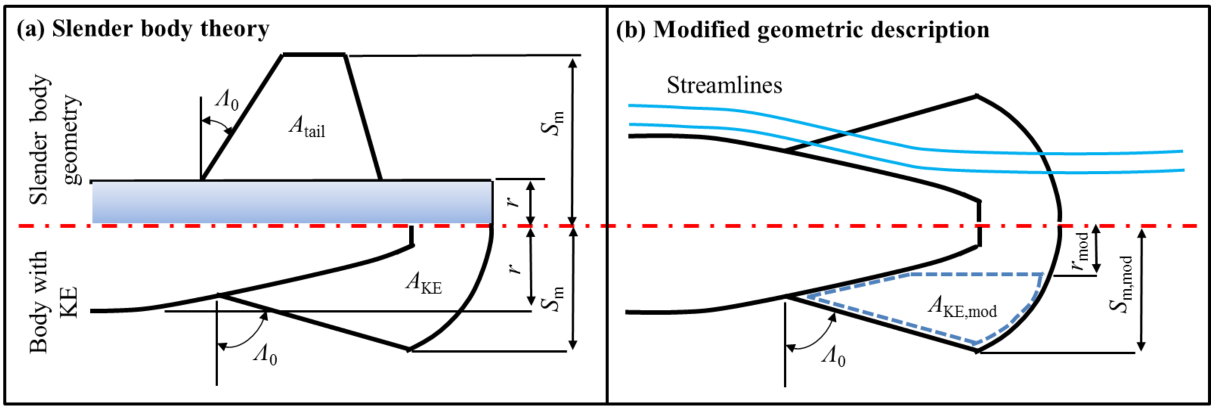

Figure 2.5: Geometric definition of the LDB-KE based on (a) slender-body theory and (b) a modified approach.

The proposed adjustment to the geometric definition is shown in Figure 2.5b. A modified body radius, r_{mod}, was defined as the wake diameter, W_{D}, for which Patel and Chen (1986) suggested that, for the majority of bodies of revolution, including LDBs $W_{\mathrm{D}} = 0.1l$. The semi-span was adjusted to only consider the portions of the KE outside the body wake, which were exposed to the freestream velocity, $S_{\mathrm{m,mod}} = S_{\mathrm{m}} - r_{\mathrm{mod}}$.

2.5 Lack of agreement of experimental and computational fluid dynamics at low Reynolds numbers for the NACA0012

There is great uncertainty (experimentally and numerically) over rather basic quantities, such as time-averaged lift and drag for wings and wing sections, simply because the Re lies in a particular range ($10^4 < \mathrm{Re}_{\mathrm{c}} < 1.5 \times 10^5$). Both previous studies (Huyssen *et al.*, 2012; Davis and Spedding, 2015) conducted experiments within this Re range and avoid these sensitivities by placing tripwires on the wings to ensure turbulent flow. The performance of wings at a low Re_{c} is dictated by the dynamics of the laminar boundary layer, specifically, whether it separates or later reattaches. In the case where the boundary layer reattaches, the resulting laminar separation bubble (LSB) dynamics can be quite influential in determining global force coefficients, both instantaneous and time-averaged (Lissaman, 1983).

The sensitivity to boundary layer separation and reattachment can make accurate and repeatable measurement, even of time-averaged C_{l} and C_{d} difficult at $\mathrm{Re}_{\mathrm{c}} < 10^5$. The extreme sensitivity can be problematic, but also can present an opportunity if it can be reliably exploited for control, and a number of publications by Yang and Spedding (2013b, c, 2014) concluded that the sensitivity to either passive or active acoustic forcing can be used to produce local sectional changes in L/D of up to 80%.

2.5.1 Experimental difficulties

McCroskey (1987) conducted a thorough review of experimental studies in more than 40 wind tunnel test facilities and found that there were quite substantial disagreements between experimental results even at $\mathrm{Re}_{\mathrm{c}} > 10^6$. This was the situation even with the suggested criteria by which to achieve reasonable agreement at a higher Re_{c} was followed. However, for a lower Re_{c}, the data were almost absent and agreement worse.

Aerodynamic force measurements at a low Re_{c} have particular sensitivities to the freestream conditions and surface geometry (Marchman, 1987; Mueller, 1999; Guglielmo and Selig, 1996; Laitone, 1996), making reliable data difficult to obtain. In addition to these sensitivities, there are compounding factors of surface finish/polish, acoustic environment (Grundy *et al.*, 2001) and the non-negligible influence of viscous corner flows on end-plate configurations (Pelletier and Mueller, 2001).

A number of experimental studies (Huang and Lee, 1999; Kim *et al.*, 2011; Tsuchiya *et al.*, 2013) on the NACA0012 near $\mathrm{Re}_{\mathrm{c}} = 5 \times 10^4$ have shown non-linearities in the curves of $C_{\mathrm{l}}(\alpha)$, even at a small α when the thin airfoil theory would predict a linear relation of $C_{\mathrm{l}} = 2\pi\alpha$. The non-linear shapes have not been the same from study to study, and no consistent explanation has been given for the phenomenon based on flow physics. An exception is (Tsuchiya *et al.*, 2013), but their results are quite different from those given here, perhaps because of the relatively higher turbulence levels. The non-linearities may sometimes be evident only in small α intervals, and many studies lack such resolution (Lee and Su, 2012; Bhat and Govardhan, 2013).

2.5.2 Computational fluid dynamics difficulties

Aeronautical flows at a low (transitional) Re are becoming accessible to computations of varying degrees of fidelity. The most rapid calculations are based on inviscid solutions with varying degrees of viscous correction. Of these, XFOIL (Drela, 1989; Drela and Youngren, 2001) is the best known and most accessible. XFOIL consists of a panel code to approximate the potential flow, coupled to a two-equation integral boundary layer formulation, which describes the boundary layer and wake. This viscid-inviscid coupling allows both transonic and low Re flows to be modelled (Drela and Giles, 1987) with some success.

Computational fluid dynamics (CFD) codes are well-packaged and readily adaptable to aeronautical flows at a transitional Re_c. Direct numerical simulation (DNS) and large-eddy simulation (LES) remain computationally expensive, with most turbulence models unable to capture the viscous boundary layers and their transition, separation and possible reattachment. Lee *et al*. (2015) compared various numerical codes for the NACA0012 at a low Re_c, including results from a two-dimensional (2D) laminar code (with no turbulence model), 2D RANS with turbulence modelling (Baldwin-Lomax) and an implicit 3D large-eddy simulation (iLES). The computations were described as satisfactory, but one may only be able to say so after the fact, when it is clear which model works best. For example, C_l at α = 4.5° varied from 0.22 (2D RANS) to 0.52 (3D iLES) for reference, $2\pi\alpha = 0.49$ for α = 4.5°.

The dangers of running a turbulence model at a lower Re_c are that the successful matching of the observed physics (laminar separation bubbles) requires a coupling to a transition model (Rumsey and Spalart, 2009). Also, in cases of relaminarisation in transitional flows, the predictions are often inconveniently sensitive to model parameter selection. Windte *et al.* (2006), Radespiel *et al.* (2007) and Yuan et al. (2005) coupled transition prediction models to RANS to simulate flow around an SD7003 airfoil at $Re_c = 6 \times 10^4$. They all used the so-called e^n-method based on local linear stability theory to predict the transition location. The drag polar results compared fairly well to experimental data, but a systematic over-prediction of the lift coefficient was observed. The final observations concluded that even though LES-based simulations lead to deeper insight into the flow physics at such low Re_c, the coupling of RANS models with transition prediction models serves as a good practical engineering tool for aerodynamic analysis and design (Yaun *et al.*, 2005). However, for simulations where a more qualitatively accurate evaluation is needed special operations, such as obtaining the transition point by the 3-D iLES or experimental results and setting the turbulence model after the derived transition point, might be needed (Lee *et al.*, 2015).

The most extensive calculations to date are the DNS of Jones *et al*. (2008), who used a fourth-order central difference scheme to compute the flow over a NACA0012 at α =5° and $Re_c = 5 \times 10^4$. The full 3D calculations were initialized by expanding initial 2D simulations, and the naturally observed process of transition was stimulated by a suitable 3D forcing, which was then relaxed after some time. The 2D C_L values fluctuated around 0.5, and then rose to 0.6

when forcing was applied in the 3D case. After a transient, C_L varied between 0.6 and 0.64. The unforced 3D flow was not steady, but transition around the periphery of the separation bubble was self-sustaining with persistent pressure fluctuation amplitudes. The separated shear layer from the bubble was identified as a possible source of absolute instability that could account for the self-sustained turbulence (Tank *et al.*, 2016). These computations were performed at a single α, with no appropriate experimental data for comparison.

Almutairi *et al*. (2010) compared the DNS results of Jones *et al*. (2008) with filtered DNS, LES and a viscous-inviscid interaction model similar to the XFOIL formulation, except for including unsteady terms. In the LES, similar to Jones *et al*. (2008), the length of the spanwise domain length was influenced by the bubble length, growth, bursting and fluctuation as well as the mean C_l. This sensitivity was attributed to the fraction of the chord that the LSB occupies. Comparison of the results from the LES and the unsteady viscous-inviscid model were promising, suggesting that considerably cheaper computations could be made at a low Re_c, over a range of α (Tank *et al*., 2016).

2.6 Proposed wing-body-tail configuration

Traditionally, the fuselage acts as a load-carrying structural member, holding the wings, landing gear and empennage. In the CDC, the empennage is placed sufficiently far rearwards from the centre of gravity to provide stability, control, trim and damping to the aircraft. This leads to the long, slender fuselage shape observed in the CDC described by the fuselage λ. The fuselage, shaped essentially like a long, streamlined tube, disrupts the wing. The fuselage itself is not usually designed to produce lift, and the adverse effects of having the fuselage interfere with the wing must be tolerated as part of the design compromise.

Assuming that longitudinal stability can be obtained by other means (Agenbag *et al*., 2009), the fuselage is not required to accommodate tail wings far behind the aircraft centre of gravity. The fuselage design objectives can be revised, and it is likely that a shorter body with a low λ, while retaining the elliptical cross-section of the current dominant arrangement becomes a feasible alternative. Another design objective could be to provide circulation control on the body itself. By modifying the fuselage aftbody one can potentially contribute to lift by improving the span efficiency and therefore reducing the induced drag (Huyssen *et al*., 2012).

2.6.1 Downwash distribution of an ideal wing

Minimum induced drag is interpreted as a constant spanwise downwash distribution, which exists as a result of an elliptical circulation distribution (Munk, 1923; Prandtl, 1932; Jones, 1980). The unique value of the local circulation on a lifting wing is determined by the Kutta condition at the trailing-edge. If a prominent body interrupts the wing trailing-edge, then the Kutta condition will not, in general, be maintained over the body itself and the local circulation will change. Figure 2.6a shows the ideal wing constant downwash and elliptical circulation distribution, with Figure 2.6b representing a more energetically wasteful solution where the fuselage is present (Huyssen *et al*., 2012).

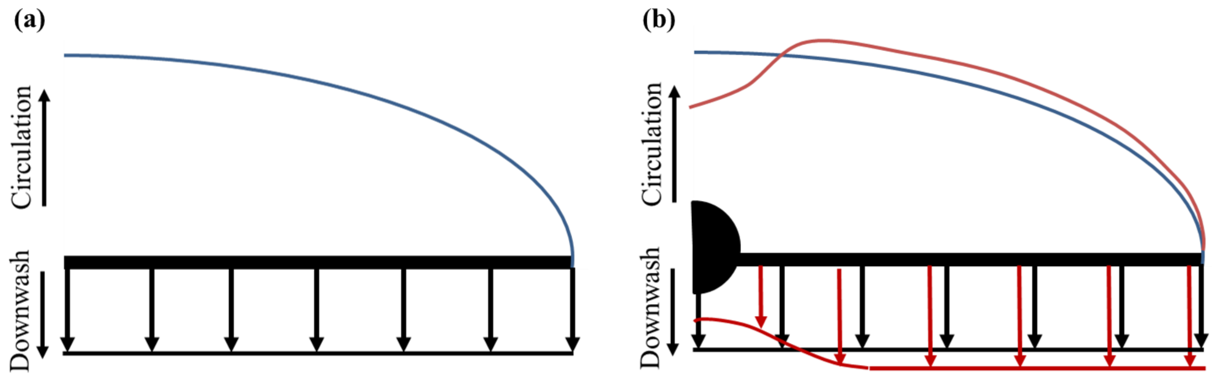

Figure 2.6: Schematic representation of (a) an elliptic spanwise distribution over a wing alone and (b) a spanwise distribution over a wing-body combination of circulation and downwash (Adapted from Prandtl, 1932).

Induced drag is described as a function of the Oswald efficiency, *e*, as a percentage deviation from the ideal elliptical distribution as:

$$C_{D,i} = \frac{C_L^2}{\pi e AR}, \tag{2.12}$$

Alternative configurations like the BWB consider the design of the fuselage to support, maintain and control a non-zero circulation profile to reduce induced drag (Porstdam *et al*., 1997; Liebeck, 2004; Qin *et al*., 2005). However, control surfaces could also provide a fixed rear stagnation line for the fuselage, to match that of the wing, allowing the fuselage to become a lifting body and a dynamic part of the wing. As a result, there would be very little variation in the spanwise downwash distribution and it would seem to the near-wake observer that there was no body present (Huyssen *et al*., 2012). In theory, *e* increases, leading to an overall decrease in the $C_{D,i}$.

Huyssen *et al*. (2012) and Davis and Spedding (2015) describe initial experiments to test the hypothesis that a suitable body circulation control device can be deployed to modify the circulation on the body and effectively erase its inviscid signature in the wake. PIV showed that the WBT can potentially approach the ideal wing-alone wake quality.

2.6.2 Initial experimental work of Huyssen *et al*. (2012) and Davis and Spedding (2015)

The KE appeared to modify the global flow around the body so that the circulation distribution between the body and the wings was more uniform, which, in principle, leads to a reduction in induced (inviscid) drag. However, the argument was only indirectly supported by the findings of modified downwash profiles in the near wake, and the mechanism by which the global flowfield was changed could not be directly identified, either from PIV in the wake (Huyssen *et al*., 2012; Davis and Spedding, 2015) or with global force balance measurements (Davis and Spedding, 2015).

The force balance and PIV measurements (Davis and Spedding, 2015) showed that the lift experienced by the aircraft with a KE increased with δ up to a certain maximum. The aftbody deflection makes a positive camber of the body and thus potentially a nonzero circulation over it. The addition of the KE achieved the same effect at a lower δ and contributed to lift as δ

increased. It was concluded that the most effective means of generating asymmetry and net lift on a body was through deflection of the KE.

The PIV seemed to suggest that the KE can control the circulation and act as a high-lift system. If this is the case, it would be conceivable to suggest that the KE can be used to provide the highest possible span efficiency during all flight conditions. This, in turn, leads to a potential reduction in wing size and angle of attack, α, for a given design objective. This may be significant for wide bodies of reduced λ and, in theory, should offset any additional wetted surface required by the KE (Huyssen *et al*., 2012). The tube-and-wing configuration can be retained to benefit from its general suitability and elaborate wing-body blending will not be required.

2.7 Numerical modelling at low Reynolds numbers

Low Re applications are becoming more common with micro-aerial vehicles, but a lot of wind tunnel experiments also take place in this $\mathrm{Re_c}$ regime. It is, therefore, important to be aware of the inherent limitations of the turbulent and transition models and how they will behave in certain cases in order to evaluate the reliability of the computed results.

The majority of CFD studies have been conducted at a higher $\mathrm{Re_c}$ ($> 10^6$) in aerospace applications. RANS is routinely used in the aerospace industry to predict flow-fields at a higher $\mathrm{Re_c}$. RANS focuses on the mean flow and the effects of turbulent fluctuations on the mean flow. With the time-averaging process, extra terms appear in the Navier-Stokes equations due to the interaction between these turbulent fluctuations. These additional terms are modelled using turbulence models to close the mean flow equations.

Although RANS can model turbulence and separation effects with reasonable accuracy at a higher $\mathrm{Re_c}$, at a low $\mathrm{Re_c}$ ($10^4 – 10^5$), the presence of separation bubbles means that the separation is laminar and transition points are very difficult to set (Windte *et al.*, 2006; Yuan *et al*., 2005; Rumsey and Spalart, 2009; Catalano and Tognaccini, 2010). Turbulence models are calibrated for separation in the turbulent flow regime and rely on modifications or couplings with transition models at $\mathrm{Re_c} \leq 10^5$ to predict transitional behaviour.

2.7.1 Shear-stress transport *k-ω* turbulence model

The most reliable turbulence model (Menter, 1992b) to deal with the difficult numerical challenges associated with separation is the shear stress transport (SST) k-ω turbulence model of Menter (1994). The SST k-ω model has seen fairly wide application in the aerospace industry, where viscous flows are typically resolved and turbulence models applied throughout the boundary layer, as well as having the ability to successfully predict the onset of flow separation (Menter *et al.*, 2006).

The SST k-ω turbulence model (Menter, 1994) effectively combines the k-ε model in the far-field and k-ω model in the near-wall regions. This combines the free-stream/inlet insensitivity of the k-ε model with the improved performance of the boundary layer and adverse gradient solutions of the k-ω model. The modelled equations for the turbulence kinetic energy, k, and the turbulence frequency, ω, are:

$$\frac{\partial \rho \overline{u_j} k}{\partial x_j} = \tau_{ij} \frac{\partial \overline{u_i}}{\partial x_j} - \beta^* \rho \omega k + \frac{\partial}{\partial x_j}\left(\left(\mu + \sigma_k \mu_t \right) \frac{\partial k}{\partial x_j} \right), \tag{2.13}$$

$$\frac{\partial \rho \overline{u_j} \omega}{\partial x_j} = \tau_{ij} \frac{\gamma}{\nu_t} \frac{\partial \overline{u_i}}{\partial x_j} - \beta \rho \omega^2 + \frac{\partial}{\partial x_j}\left(\left(\mu + \sigma_\omega \mu_t \right) \frac{\partial \omega}{\partial x_j} \right) + 2\left(1 - F_1\right) \frac{\rho \sigma_{\omega 2}}{\omega} \frac{\partial k}{\partial x_j} \frac{\partial \omega}{\partial x_j}, \tag{2.14}$$

where the Reynolds stress tensor is described as:

$$\tau_{ij} = \mu_t \left(\frac{\partial \overline{u_i}}{\partial x_j} + \frac{\partial \overline{u_j}}{\partial x_i} - \frac{2}{3} \frac{\partial \overline{u_k}}{\partial x_k} \delta_{ij} \right) - \frac{2}{3} \rho k \delta_{ij}, \tag{2.15}$$

which is the production and destruction terms of the turbulence kinetic energy equation, and F_1 is the blending function combining the two models. The modelling constants remained unchanged from the recommended settings in Star-CCM+.

2.7.2 Transition modelling

The transition model needs to be responsible for modelling the weak disturbances within the laminar boundary layer that lead to natural transition, as well as the potential reattachment of the laminar boundary layer and separation bubbles. The γ-Re_θ transition model is a correlation-based model that is coupled with the SST *k-ω* turbulence model to provide a predictive capability specifically formulated for unstructured CFD codes and also applies to low Re cases (Menter *et al.*, 2006; Langtry *et al.*, 2006). The transition model is comprised of two transport equations. First, an intermittency, γ, transport equation attempts to predict the percentage of the flow that is turbulent (triggers the transition process). The intermittency function is coupled with the SST *k-ω* turbulence model (Menter, 1994). It is used to turn on the production term of the turbulent kinetic energy downstream of the transition point in the boundary layer (Langtry, 2006).

$$\frac{\partial \left(\rho u_j \gamma \right)}{\partial x_j} = P_\gamma - E_\gamma + \frac{\partial}{\partial x_j}\left[\left(\mu + \frac{\mu_t}{\sigma_f} \right) \frac{\partial \gamma}{\partial x_j} \right] \tag{2.16}$$

$$P_{\gamma 1} = F_{length} c_{a1} \rho S \left(\gamma F_{onset} \right)^{0.5} \left(1.0 - c_{e1} \gamma \right)$$

The second transport equation is responsible for providing an empirical correlation for transition onset momentum thickness Re, Re_θ.

$$\frac{\partial \left(\rho u_j \overline{\mathrm{Re}_{\theta t}} \right)}{\partial x_j} = P_{\theta t} + \frac{\partial}{\partial x_j}\left[\sigma_{\theta t} \left(\mu + \mu_t \right) \frac{\partial \overline{\mathrm{Re}_{\theta t}}}{\partial x_j} \right] \tag{2.17}$$

$$P_{\theta t} = c_{\theta t} \frac{\rho}{t} \left(\mathrm{Re}_{\theta t} - \overline{\mathrm{Re}_{\theta t}} \right) \left(1.0 - F_{\theta t} \right) \tag{2.18}$$

These correlations are typically based on freestream values, like the turbulence intensity or the pressure gradient outside the boundary layer. Outside the boundary layer, the transport variable is forced to follow the value of $\mathrm{Re}_{\theta t}$ provided by experimental correlations. This information is then diffused into the boundary layer by a standard diffusion term. By this mechanism, strong variations of the turbulence intensity and the pressure gradient in the freestream can be taken into account (Langtry, 2006). One of the main advantages of the present approach is its suitability to predict separated flows.

Recognising, however, that the process of calibrating the needed correlations is complex and time consuming (Malan and Suluksna, 2009), the required correlations have been carefully calibrated and are provided by default within the model in Star-CCM+. The detailed formulation of both the SST *k-ω* turbulence model and the γ-Re_θ transition model in Star-CCM+ can be found in the User Manual of Star-CCM+ V8.06 (Star-CCM+, 2013) or a summary can be found in Malan and Suluksna (2009). All application cases in this study make use of the coupling of these models in Star-CCM+.

2.7.3 Modelling conditions

The numerical modelling boundary conditions are selected to determine that the appropriate physics is used, with the correct input parameters and with an adequate mesh. Within the physics modelling, two conditions relate to these tests. First, using the correct wall y^+ treatment to ensure that the mesh resolves the boundary layer, and second, by selecting the transition input parameters to ensure that the laminar to turbulent transition of the flow can be predicted.

2.7.3.1 Wall y^+ condition

The non-dimensional wall distance for wall-bounded flow is defined by:

$$y^+ = \frac{u^* y}{\nu} \qquad \text{where, } u^* = \sqrt{\tau_w/\rho} \tag{2.19}$$

where y is the distance to the nearest wall and ν is the local kinematic viscosity of the fluid. The y^+ value is used as an indication in turbulence models of whether the cell count and size at the wall is sufficient to capture the flow gradients close to the wall. The low y^+ wall treatment used in Star-CCM+ assumes that the viscous sublayer is well resolved and that the typical wall laws are not required. This wall treatment is typically used with low-Re models. In these cases, it is important to model the boundary layer flow $y^+ < 1$.

The low y^+ wall treatment is the most accurate model to resolve the viscous sublayer, but requires more cells in the boundary layer, and will therefore be computationally more expensive.

2.7.3.2 Transition model inputs

The turbulent inlet boundary conditions (turbulent intensity, *I*, and turbulent viscosity ratio, *β*) are important when using the γ-Re_θ transition model to attempt to reflect the influence of the freestream on the transition location (Langtry, 2006).

Turbulent intensity is generally defined as:

$$I = \frac{\sqrt{(2/3)k}}{U}, \tag{2.20}$$

and turbulent viscosity ratio (μ_t/μ):

$$\beta = \frac{\rho k}{\omega \mu}. \tag{2.21}$$

In the absence of measured data, the proper turbulent inflow boundary conditions become a delicate balance between an acceptable turbulent decay rate and an acceptably low turbulent viscosity ratio (μ_t/μ). In some situations, such as wind tunnels with very low background turbulence, it might be a challenge to obtain a suitable compromise between these two variables. This issue is often exacerbated when a far-field boundary is specified a large distance away from the body.

The boundary condition for $\overline{\mathrm{Re}_{\theta t}}$ in Equation 2.18 is calculated from the empirical correlation based on the inlet turbulence intensity, which is an important inlet condition to set when using this model.

The blending function, $F_{\theta t}$, is used to turn off the source term in the boundary layer and allow the transported scalar, $\overline{\mathrm{Re}_{\theta t}}$, to diffuse in from the freestream. $F_{\theta t}$ becomes 0 in the freestream and 1 in the boundary layer. The γ-Re_θ transition model relies on a definition of $\mathrm{Re}_{\theta t}$ in the freestream (Langtry, 2006). Star-CCM+ allows for a user-defined field function by which the location of the freestream edge is typically specified in terms of an iso-surface based on the distance from the cell centroid to the nearest wall (Malan and Suluksna, 2009). The transition model conditions and wall y^+ treatment are considered in Chapter 3 as part of the verification procedure.

2.8 Summary and conclusions

Investigation of the proposed WBT configuration has various avenues to explore. Not only does the configuration pose a couple of questions regarding the conventional design objectives of the fuselage, but the original experimental condition also pose some aspects to consider and investigate. As such, this study considers a variety of external aerodynamic applications of which the basic fundamentals are reported in this chapter.

The first design objective for the fuselage was to consider its replacement with an LDB and thereafter the body-tail dynamics when the KE was added. The literature reviewed here indicated two candidate LDBs: the F-57 LDB from Parsons and Goodson (1972) and the LDB from Myring (1981). The F-57 LDB is a good candidate since there are experimental results from Patel and Lee (1977) with which the numerical model can be compared. The Myring LDB, on the other hand, is selected since it is specifically designed to be a low-drag fuselage body, unlike the F-57 LDB, which was designed to be a low-drag hydrodynamic or airship body.

The secondary requirement of the fuselage to provide some lift leads to the addition of the KE. The KE attached to the aftbody of the fuselage resembles a low aspect ratio or delta-like wing. Two sources of lift were identified, which affects the spread of the KE (vortex lift component) and the length (circulation lift) of the KE. Of these two, the length would be independent of the lift, but the spread can provide greater lift at wide angles and when deflected. However, not only was the KE within the near-wake of the body (which deflects the streamlines), but the presence of the body upstream also means that the KE has no distinct tip shape similar to the delta wing. This would influence the effectiveness of the KE, but would also means that the KE does not work exactly like the delta wing. In order to predict the effectiveness of the KE in combination with a body to provide lift, the SBT was used. Interference factors between the body and the KE provide guidelines in terms of the KE geometry.

Finally, as part of the numerical validation to follow, a NACA0012 wing at a low Re_c is evaluated using CFD and compared with force measurements. Since previous studies on the WBT were conducted at these low Re_c, it was important to test the CFD models used and be aware of the limitations in both CFD and experimental results. With low Re_c studies, there are particular sensitivities when conducting experiments and CFD simulations. DNS and LES remain computationally expensive and RANS models have to be coupled with transition models to attempt to predict the boundary layer features. Some computational studies exist at a single α, with no appropriate experimental data for comparison.

Initial experimental work on the WBT by Huyssen *et al*. (2012) and Davis and Spedding (2015) indicated a potential for aerodynamic improvement when the KE was added to a short fuselage body. It was, however, unclear whether the KE truly achieved the design goals of circulation control and what the effects of its presence were to the overall performance. Therefore, the purpose of this study is to conduct a more in-depth investigation, not only in terms of the influence of the KE, but also whether the whole configuration would benefit from an LDB. These questions could not be answered by the experimental work to date, and no numerical simulations have been used to investigate the WBT.

3. EXPERIMENTAL AND NUMERICAL COMPARISON: A NACA0012 CASE STUDY

3.1 Introduction

Experimental measurements and computations of aeronautical flows in the transitional Re regime are extremely challenging, characterised by a large sensitivity to small disturbances or variations in boundary conditions. In this Re regime precisely acquiring aerodynamic forces by experiment are made difficult since the flow velocity is low and the forces consequently very small (Lee *et al*., 2015). Few have paid attention to the scarcity of reliable information until recently, as studies of natural and artificial flyers overlap this Re_c domain. Although numerical simulation is able to set ideal conditions and in some way compensate for the uncertainty of experimental measurements there is an equal amount of computational factors that cast doubt over the simulated flow features in the transitional regime. Without calibrating the turbulent and transition models it becomes impossible to predict exact flow features and without reliable wind tunnel measurements such calibration does not exist. The purpose of this chapter is to present reliable data for one specific case of the simple symmetrical airfoil NACA0012 at $Re_c = 10^5$ that is proposed as a test case for codes and experiments that aim to make predictions of aerodynamics in such a range of Re_c.

Huyssen *et al*. (2012) and Davis and Spedding (2015) both conducted experimental investigations of the proposed WBT at a low Re_c (5×10^4 and 10^5) and concluded that phenomena appearing in this low Re_c range would also appear in larger Re_c cases. Although ostensibly simple, the boundary layer and separation dynamics are quite subtle, leading to shapes of time-averaged force coefficients that would not readily have been predicted. In previous experimental work, these laminar boundary layer difficulties were circumvented by using tripwires over the body and wing.

In an attempt to show reliability of computations on a simple NACA0012 wing, RANS is used to estimate the average force coefficients before attempting the more complex LDB-KE combination in Chapter 4 and the WBT in Chapter 5. All the results in this Chapter only refer to $Re_c = 10^5$ and not the $Re_c = 5 \times 10^4$ test case. The $Re_c = 5 \times 10^4$ experimental results for the WBT in Huyssen *et al*. (2012) were merely qualitative. However the same procedure of investigation was followed for the NACA0012 at $Re_c = 5 \times 10^4$ and is documented in Appendix A.

3.2 Dryden wind tunnel set-up

The experiments were conducted in the Dryden wind tunnel at the University of Southern California. Figure 3.1 shows the closed-loop wind tunnel with a contraction ratio of 8:1, an octagonal cross-section of 1.37m and a test section with a streamwise length of approximately 6m. Twelve screens ensure a low turbulence level of 0.03% over a velocity range of $5 \leq U \leq 26$m/s with flow uniformity measurements showing less than 0.5% velocity deviation from the mean velocity for a given cross-section (Yang and Spedding, 2013). This was measured in an empty test-section for spectral frequencies between 2 and 200Hz.

3.2.1 NACA0012 wing model

The NACA0012 wing model used for $Re_c = 10^5$ was a solid model, computer numeric control (CNC) machined from aluminium, with $AR = 3.7$ (b = 28 cm and c = 7.5 cm). The model can either be mounted directly on the pedestal floor mounting with one free-end to conduct the 3D test or between end-plates to conduct the 2D tests.

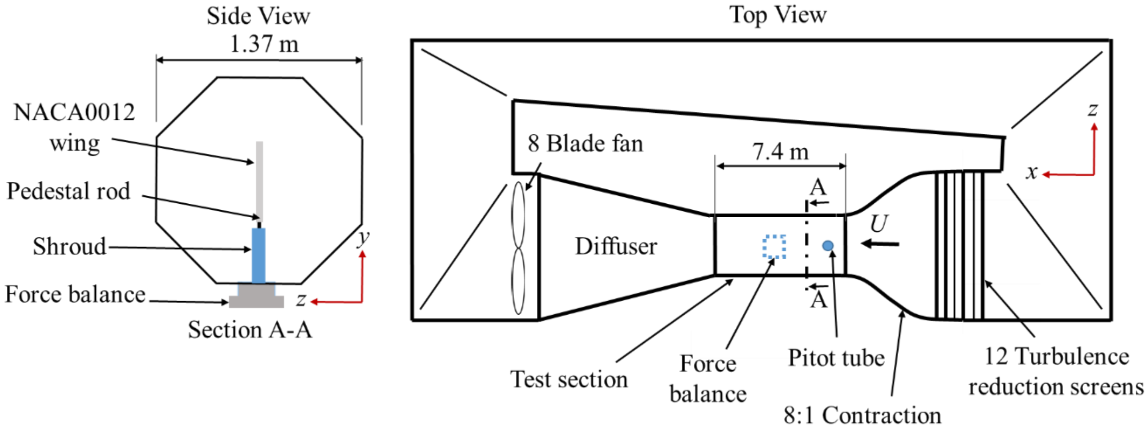

Figure 3.1: Dryden wind tunnel set-up for the force balance system and the NACA0012 wing model.

For the 2D tests, an infinite aspect ratio was approximated by placing endplates at either tip of the wing. The endplates were $9.48c$ (in x) x $4.75c$ (in z) x $0.17c$ thick, with sharp leading-edges and were aligned carefully, parallel with the flow. The ends of the model were kept within about $0.013c$ of the endplates. The actual value was 1mm, which is within the acceptable distance given by Mueller (1999) of 0.1mm to 1.4mm. This is within the separation distance of $0.005b$ (1.4 mm) recommended by Barlow *et al*. (1999) and less than the laminar boundary layer displacement thickness on the plates themselves, $\delta^* = 5.2x/Re_c^{1/2} = 2.7$ mm. The model support rod passed through a hole in the bottom endplate, $1.13c$ behind the leading-edge and equidistant from the edges in z. The bottom end of the model itself is $0.85b$ above the wind tunnel floor.

The freestream was corrected by 0.4% based on a correction suggested by Barlow *et al*. (1999) for unusually shaped objects where the model volume includes the wing, supports, endplates and shroud at a maximum α. An empirical procedure described in Selig *et al*. (1995) yields a blockage correction factor, $f_{sb} = 0.0044$. The wake blockage correction factor and the streamline curvature correction was estimated as $f_{wb} = 0.0024$ and $\sigma = 0.0007$ respectively (Tank *et al*., 2016).

3.2.2 Force balance

Force balance measurements were performed with a custom, three-component, cruciform-shaped force balance with a parallel plate structure design (Zabat *et al*. 1994). A final 3 x 4 calibration matrix that consisted of an average of the three most recent calibration sets was used during the test. During the calibration process, the sensitivities of the off-diagonal terms in the calibration matrix to estimated drag were carefully controlled. The uncertainty of lift and drag measurements was estimated to be less than 8 mN, which was 0.13% of the minimum expected drag force on a model of this size.

The force balance was located below the tunnel and was connected to the model via a pedestal floor mount that extended through the tunnel floor and was shielded by an aerodynamic shroud as shown in Figure 3.1. The model support rod was inserted into the pedestal floor mount and secured with a screw. Lift and drag measurements were zeroed with forces corresponding to the empty mount, the weight of the model, and freestream flow interaction with the mount. Because the mount was shielded by a shroud, the freestream flow interaction component was much smaller than the others, generally less than 5 mN. For 3D tests, in order to reduce the interference of the shroud with the lower wing tip vortex, the length of the shroud was reduced so that the lower end of the model was raised 1.5c above the top of the shroud, exposing the support rod to the air flow. To correct for this, the drag force on a matching rod was also measured as $C_D = 0.007$ and subtracted from the test results.

Five sweeps produced ten measurements of each α range of $-5° \leq \alpha \leq 9°$ in increments of 0.5°, which were averaged to give a single value. After each α step, the flow was allowed to settle for ten seconds before ten seconds of data were collected at 1kHz and averaged. The uncertainty of each resulting force value was taken as the standard deviation of the ten averages. The entire test procedure was repeated for the 2D and 3D configurations at each Re_c until three consecutive data sets gave the same drag coefficient values within the uncertainty limits. In the case of a symmetric model, curves were shifted by a small α to ensure zero net lift force at $\alpha = 0°$. After stall, the model begins to oscillate considerably, so measurements were not taken for post stall α (Tank *et al.* 2016).

Repeated testing showed that the drag results were extremely sensitive to the off-diagonal terms of the calibration matrix, caused by small alignment errors during calibration. Because a symmetric model was being used, non-symmetric drag results were identified as incorrect and discarded. The lift curve was relatively insensitive to these small calibration errors, and there was generally a negligible difference between lift results from test to test. Tests were generally performed on separate days, but even when two tests were performed on the same day, the entire procedure, including calibration and collection of zeroing forces, was repeated for each test.

The uncertainty for the force measurements was an accumulation of the force measurement (< 8mN), the flow speed uncertainty of 0.1m/s and the model dimension uncertainty was estimated at an conservative value of 0.5mm. The propagated uncertainty of the force coefficients was then less than 1.5%.

3.3 Computational modelling of the NACA0012

Two types of simulation techniques were used in Star-CCM+ to model the 2D solution. First, the 2D mesh option in Star-CCM+ was used, and second, a thin 3D mesh was created, referred to as pseudo two-dimensional or P2D, which was computationally less efficient than the former. The 3D model, as it is oriented in the Dryden wind tunnel, was then simulated. Both the airfoil and wing models were truncated at 0.99c for meshing convenience.

3.3.1 Two-dimensional model geometry

The NACA0012 airfoil was modelled in a circular two-dimensional plane as shown in Figure 3.2a. The total domain size consists of a 16c diameter with the inlet 8c from the airfoil leading-edge and 7c towards the outlet from the airfoil trailing-edge.

3.3.2 Pseudo two-dimensional model geometry

The P2D model consisted of the same NACA0012 airfoil with a spanwise length of 0.55*c* which falls in the suggested range by Almutairi *et al*. (2010). The rectangular domain represents an infinite span wing and was therefore regarded as P2D. The inlet was 5*c* from the leading-edge and the outlet 13*c* from the trailing-edge with a domain height of 11*c* as shown in Figure 3.2b.

3.3.3 Three-dimensional model geometry

The NACA0012 wing had $c = 0.075$m and AR = 3.7 at $Re_c = 10^5$. The full NACA0012 wing was modelled in a simplified cylindrical shape representing the octagonal Dryden wind tunnel test section (Huyssen *et al*., 2012; Davis and Spedding, 2015). The wing was positioned at 24*c* (roughly translating to 6*l*, where *l* is the length of the full WBT model) from the inlet plane of the flow domain, and the full domain size was 75*c*. The diameter of the wind tunnel was 1.37m (18*c*), as shown in Figure 3.2c.

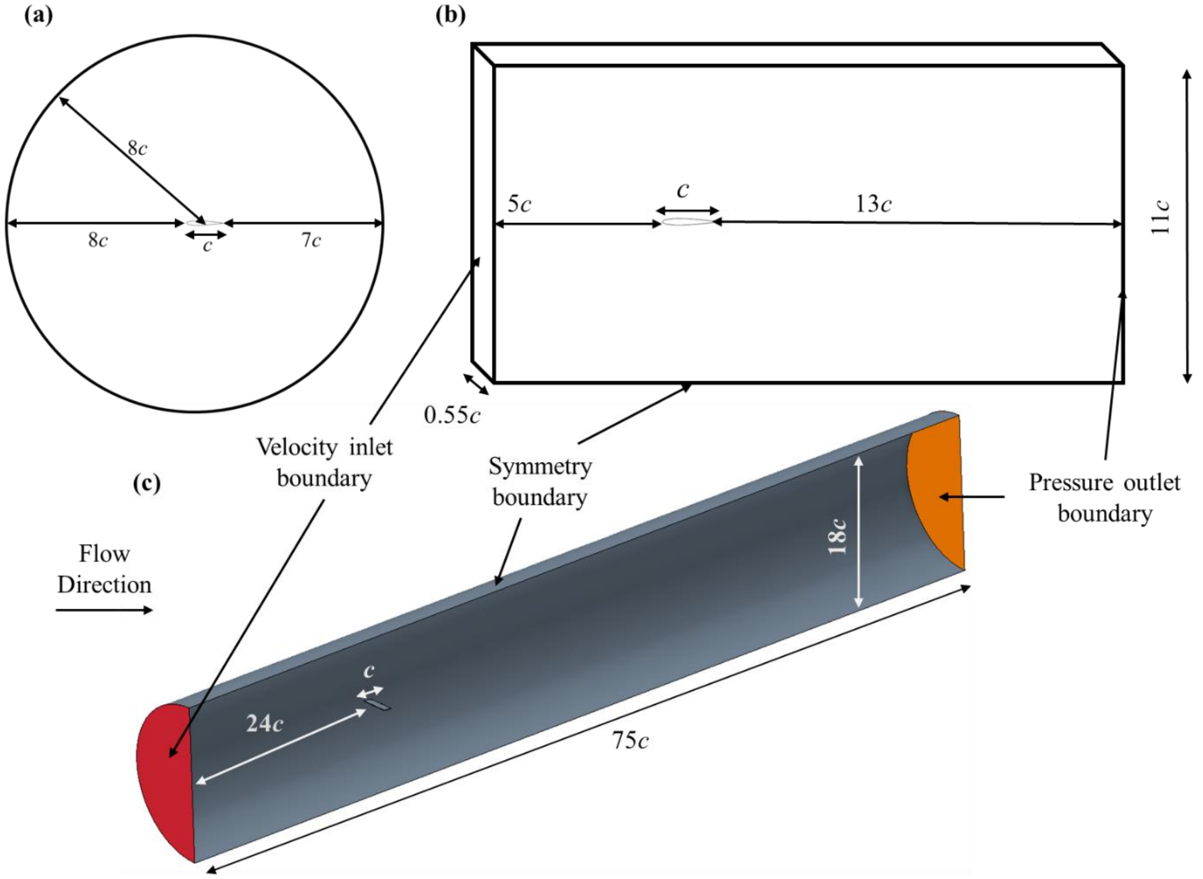

Figure 3.2: Model and domain geometries for (a) 2D; (b) P2D and (c) 3D for the NACA0012 airfoil at $Re_c = 10^5$.

3.3.4 Solution domain and mesh generation

The computational meshes that were generated for all geometries consisted of polyhedral cells and were meshed using the Advancing Layer Mesher in Star-CCM+ (Star-CCM+, 2013). This mesh function enabled the mesh to grow around sharp corners on the body without collapsing. The advancing layer mesh approach allows a homogeneous, body-conforming mesh to be generated. All models had 20 cells across the boundary layer height for accurate drag estimation, except for the 2D NACA0012 airfoil that had 22 boundary layer cells. Two boundary layer cells were sufficient for the simulated tunnel walls where these were present.

Mostly, three to four volumetric mesh refinements were used for the mesh domains. The first and second drove the cells to be finer around the bodies and to gradually increase the cell size away from the bodies, while the third drove the sections at the trailing-edge and wake regions to be finer. Primarily, these refinements increased the mesh density where viscous effects were expected to be more prevalent. Figure 3.3 shows the mesh around the 2D model. The full 3D mesh consists of 4 x 10^6 cells, the P2D of 1.5 x 10^6 cells and the 2D of 10^6 cells.

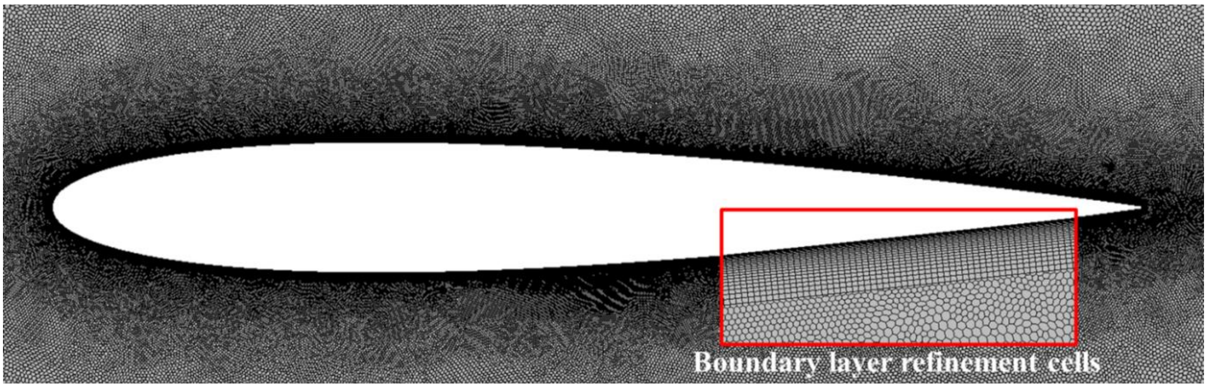

Figure 3.3: Mesh for the two-dimensional NACA0012 airfoil at $Re_c = 10^5$, boundary layer refinement cells enlarged in the red box by 7x4*c*.

The boundary conditions used for all the test cases are shown schematically in Figure 3.2. For all bodies, the flow was assumed to be steady and incompressible, with a constant velocity inlet boundary condition, with Re_c for the NACA0012 airfoil and wing. The outlet boundaries were pressure boundaries set at atmospheric conditions. The NACA0012 wing's outer surface domains were modelled as no-slip wall boundaries, where the outer boundaries for the 2D and P2D NACA0012 model had symmetry boundaries. The non-dimensional wall distance criterion, $y^+ < 1$, was satisfied for all cases (the predicted wall boundary thicknesses are less than a wall-bounding computational cell and the boundary layer could therefore be modelled on that cell).

The Star-CCM+ solver for the RANS equations with the SST *k*-ω turbulence model (Menter, 1994) was used in all cases. Although details of the turbulent fluctuations are not required to model global lift, drag is more sensitive to these details. The SST *k*-ω turbulence model was selected because it has successfully been used in predicting onset of flow separation (Menter, 1992a). The γ-Re_θ transition model (Menter *et al.*, 2006) was used to predict laminar-turbulent transition. Not only was this important for the low Re NACA0012 case where separation bubbles were expected over the aftbody, but also for the LDB simulations in Chapter 4 where there was the possibility of laminar separation over the aftbody.

3.4 Computational model verification and validation

A wide variety of results does not exist in literature (Lee *et al.*, 2015; Castiglioni and Domaradzki, 2015; Rumsey and Spalart, 2009; Jones *et al.*, 2008) of the NACA0012 airfoil at $Re_c = 10^5$. The need for reliable wind tunnel results therefore arose, and hence forms part of this work as an independent validation study. The simulation sensitivities and wind tunnel result sensitivities were investigated, and provided some insight into the difficulties and discrepancies in both cases.

The verification process refers to the numerical accuracy of the code for a specific problem and was conducted by means of a mesh convergence study. Other than the mesh convergence study, the level of uncertainty for the simulation was considered to some degree in terms of modelling assumptions and approximations and the uncertainty due to the input parameters.

3.4.1 Uncertainty related to modelling assumptions and approximations

Some modelling assumptions were made to reduce the set-up time, meshing complexity and simulation time. First, the influence of the wind tunnel's cross-sectional shape as a cylinder instead of the Dryden wind tunnel's octagonal shape was investigated by comparing the lift, L, and drag, D, forces from the simulations. Second, the simulation domain was halved with a symmetry plane at the centre of the domain with a mesh of 4.5 x 10^6 cells for the half domain and 8 x 10^6 cells for the full domain. The L and D were again compared to see what the influence of the symmetry boundary condition would be. The final results are shown in Table 3.1.

Table 3.1: Simulation domain (geometry and symmetry) set-up verification tests results for *L* and *D*.

Assumption	***D* [N]**		***L* [N]**		**Percentage difference**	
Wind tunnel cross-sectional shape	Octagon	Cylinder	Octagon	Cylinder	D	L
	0.377	0.376	4.74	4.62	0.3%	2.6%
Full to half domain	Half	Full	Half	Full	D	L
	0.376	0.368	4.62	4.52	2.2%	2.2%

Both the domain shape and symmetry plane assumption showed a larger percentage difference when computing the lift force component. The symmetry plane assumption also showed a sensitivity for the computed drag force. For the purpose of this study, these were acceptable variations in the force components to benefit from the reduced computational time.

Besides the symmetry boundary conditions, no explicit simulations with comparisons were conducted to investigate the inlet and outlet boundary conditions and positions. The conventional velocity inlet boundary and pressure outlet boundary condition were used. The outlet boundary was modelled at least 8 to 10 body or chord lengths downstream of the geometry.

3.4.2 Uncertainty due to input parameters

RANS models without transition models are unable to resolve LSBs present at a lower Re_c (Lee *et al.*, 2015; Rumsey and Spalart, 2009). A comparison of RANS with and without the γ-Re_θ transition model is shown in Figure 3.4, making use of a greyscale vorticity 0 to 150 on a NACA0012 airfoil at $\alpha = 5^\circ$ with $Re_c = 10^5$. It is clear that, without the transition model, RANS does not predict separation bubbles. However, whether the amount and location of the predicted separation bubbles were accurate when the transition model was added was unclear without any experimental verification.

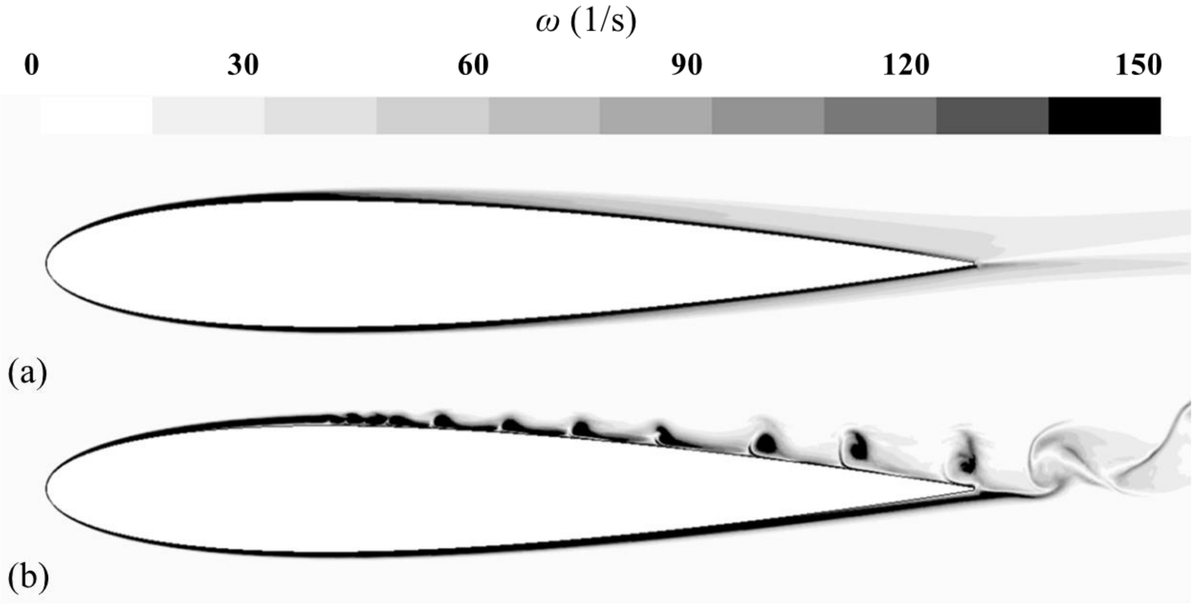

Figure 3.4: Vorticity contours for the NACA0012 airfoil at α = 5º with $\text{Re}_c = 10^5$, a) without and b) with transition modeling.

The addition of the transition model to predict the onset of turbulence provides a significant improvement in drag predictions when compared to simulations that assume fully turbulent flow in RANS. An analysis of the sensitivity to input parameters for the transition model was conducted making use of the NACA0012 airfoil at α = 5º with $\text{Re}_c = 10^5$. The turbulent intensity, I (Equation. 2.20) and turbulence viscosity ratio, β (Equation 2.21), were tested by considering the global force coefficients (C_D and C_L).

The turbulence level of the Dryden wind tunnel is 0.03% which means $I = 3 \times 10^{-4}$. For $10^{-4} \leq I \leq 3 \times 10^{-4}$, there was less than 0.2% influence on the global forces, where the difference can go up to 5% if $I = 3 \times 10^{-2}$. Therefore, the specified input values based on the Dryden wind tunnel values were seen to be a good choice for the assumption that only a minor potential uncertainty of turbulent intensity of 0.01% might exist.

The value for β acts as an indication of whether the flow was turbulent or laminar and is a strong function of Re. The flow is considered to be turbulent in the boundary layer if the value is greater than 1. The default setting ($\beta = 10$) implies that the flow domain is all turbulent. A tested sensitivity of less than 0.5% was present for $10 \leq \beta \leq 80$, with a 5% sensitivity for $0.015 \leq \beta \leq 10$. Catalano and Tognaccini (2010) propose $\beta = 0.1$ as an adjustment to low Re airfoil cases, but a difference of less than 0.5% was observed for the NACA0012 wing at $\text{Re}_c = 10^5$ when using the default setting of $\beta = 10$.

3.4.3 Mesh convergence study

A consistent numerical analysis provides a solution that approaches the actual results as the mesh resolution gets closer to zero. A mesh convergence study refers to the process of discretisation convergence tests where the discretisation error is then monitored as the mesh is systematically refined. This assessment procedure of the mesh can indicate whether it is adequate to capture the flow variables of interest (ASME V&V 20, 2009).

Roache (1997) suggested a method called the Grid Convergence Index (GCI), which results in supplying an error band on the computational solution that indicates the possible difference between the discrete and continuum values. The GCI relates the results from any mesh refinement study to the expected results from a grid doubling using a second-order method, with the objective of identifying the measure of uncertainty in grid convergence. The GCI indicates how much the solution would change with a further refinement of the grid and gives an estimate of the solution at a zero-grid size (Roache, 1997).

Roache (1997) outlines the GCI method by defining a constant refinement ratio, q, between all the tested grids. The observed order of convergence, p, can be obtained directly from three grid solutions as follows:

$$p = \frac{\ln\left(\frac{G_3 - G_2}{G_2 - G_1}\right)}{\ln(q)}, \qquad (3.1)$$

where G_1, G_2, and G_3 are the sequential approximate solutions for the selected parameter (G_1 being the most refined), in this case C_D. A minimum of three mesh solutions are performed to calculate two GCI values. The GCI for a fine grid is expressed as:

$$GCI_{fine} = F_S \frac{|\varepsilon|}{q^p - 1}, \qquad (3.2)$$

where F_s is the safety factor 1.25 for a three grid case and the relative error, ε, is defined as:

$$\varepsilon_{12} = \frac{G_2 - G_1}{G_1}. \qquad (3.3)$$

The relationship between the fine and intermediate grid (GCI_{12}) and the intermediate and coarse grid (GCI_{23}) indicates whether the mesh level yields solutions that are close to the asymptotic range of convergence for the computed solution. This relationship is expressed as:

$$GCI_{23} = q^p GCI_{12} \qquad (3.4)$$

In the case where this relationship holds, the mesh count is deemed adequate to capture the flow variables of interest, and mesh independence is assumed.

3.4.3.1 Quantitative study: drag coefficients

A mesh independence study on the 2D and 3D NACA0012 models confirmed that the mesh count was adequate to capture the flow variables of interest. Using the GCI method described, all the mesh cases were deemed independent of the mesh sizes and the mesh conditions were simulated for the rest of the cases where the models were similar. Table 3.2 describes the mesh domains in terms of refinement of the boundary layer mesh, the body and the wake regions. Figure 3.5 show a generic illustration of the position and sizes of the wake and on-body mesh domains for the airfoil. The number of cell layers normal to the airfoil surface refers to the flat polyhedral mesh layers that grow from the airfoil surface to the boundary layer edge shown in Figure 3.3. The first cell is 0.0001 from the airfoil surface and has a growth rate of 10%.

Table 3.2: Refinement domains for mesh independent models for the NACA0012 airfoil and wing at $\alpha = 5°$ at $Re_c = 10^5$.

Test case	Mesh sizes	Wake mesh dimensions	On-body mesh dimensions	Number of cell layers normal to the airfoil surface
2D	$G_1 = 2.2x10^6$ $G_2 = 1.1x10^6$ $G_3 = 0.5x10^6$	$G_1 = 0.0015c$ cell growth rate = 1.01 $G_2 = 0.003c$ cell growth rate = 1.05 $G_3 = 0.0035c$ cell growth rate = 1.1	$0.00005c < G_1 < 0.00075c$ $0.0001c < G_2 < 0.0005c$ $0.001c < G_3 < 0.002c$	G_1 = 25 layers G_2 = 25 layers G_3 = 20 layers
3D	$G_1 = 7.8x10^6$ $G_2 = 4.1x10^6$ $G_3 = 2x10^6$	$G_1 = 0.034c$ $G_2 = 0.047c$ $G_3 = 0.034c$	$0.007c < G_1 < 0.034c$ $0.02c < G_2 < 0.041c$ $0.007c < G_3 < 0.034c$	G_1 = 20 layers G_2 = 17 layers G_3 = 15 layers

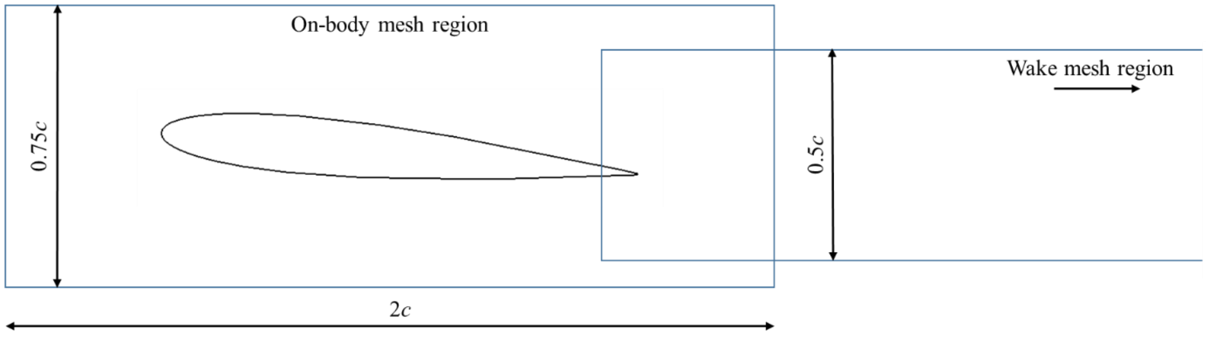

Figure 3.5: The wake and on-body mesh domain layout and sizes.

Figure 3.6 indicates the observed quantity, C_D, for the two benchmark cases specified in Table 3.2. The 2D RANS mesh models all had a variance in C_D indicated by the error bars, however the average C_D for the 2D NACA0012 airfoil showed the meshes fall within the asymptotic range of convergence. The 3D RANS models converged to solutions well within the asymptotic range of convergence.

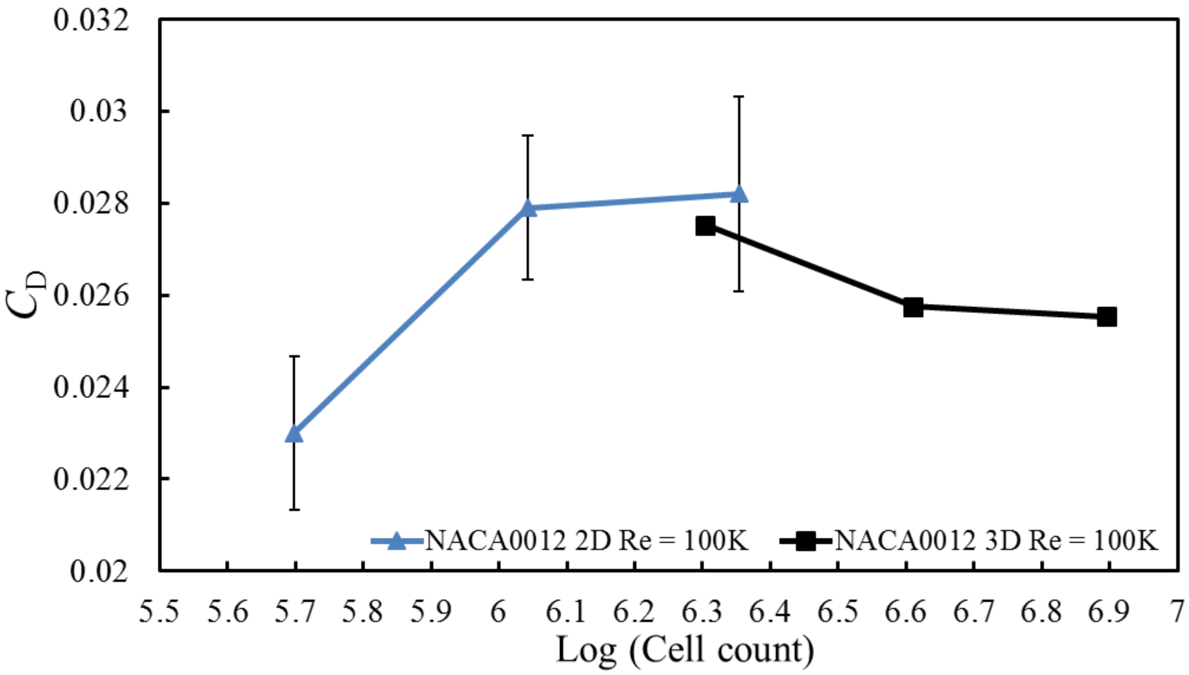

Figure 3.6: Drag coefficient of a NACA0012 at α = 5° as the observed mesh refinement quantity for each model and subsequent mesh cases.

3.4.3.2 Qualitative study: wake structures

In Section 3.4.3.1, a quantitative study was performed to determine the best suited mesh for force coefficient values in terms of computing solution accuracy. In this section, the mesh refinement study is considered from a qualitative point of view, visualizing wake structures resolution and separation bubbles. In order to compare averaged flow-field with the PIV results, the mesh resolution should be significantly refined to capture small-scale fluid features. These refinements show no sensitivity in terms of the global force coefficient results, therefore when simulations are not required to compare flow-fields, the mesh refinement in the wake and on the body does not need to be that well defined.

Figure 3.7 shows the wake of the airfoil by means of normalized streamwise velocity U_x/U contour plots. The difference in wake structures modelled for the three different meshes of the NACA0012 airfoil at α = 5º and $Re_c = 10^5$ are shown. The finer mesh, G_1, shows a more fluctuating wake structure in the near wake, with a more defined downstream wake than the less-refined wake meshes G_2 and G_3.

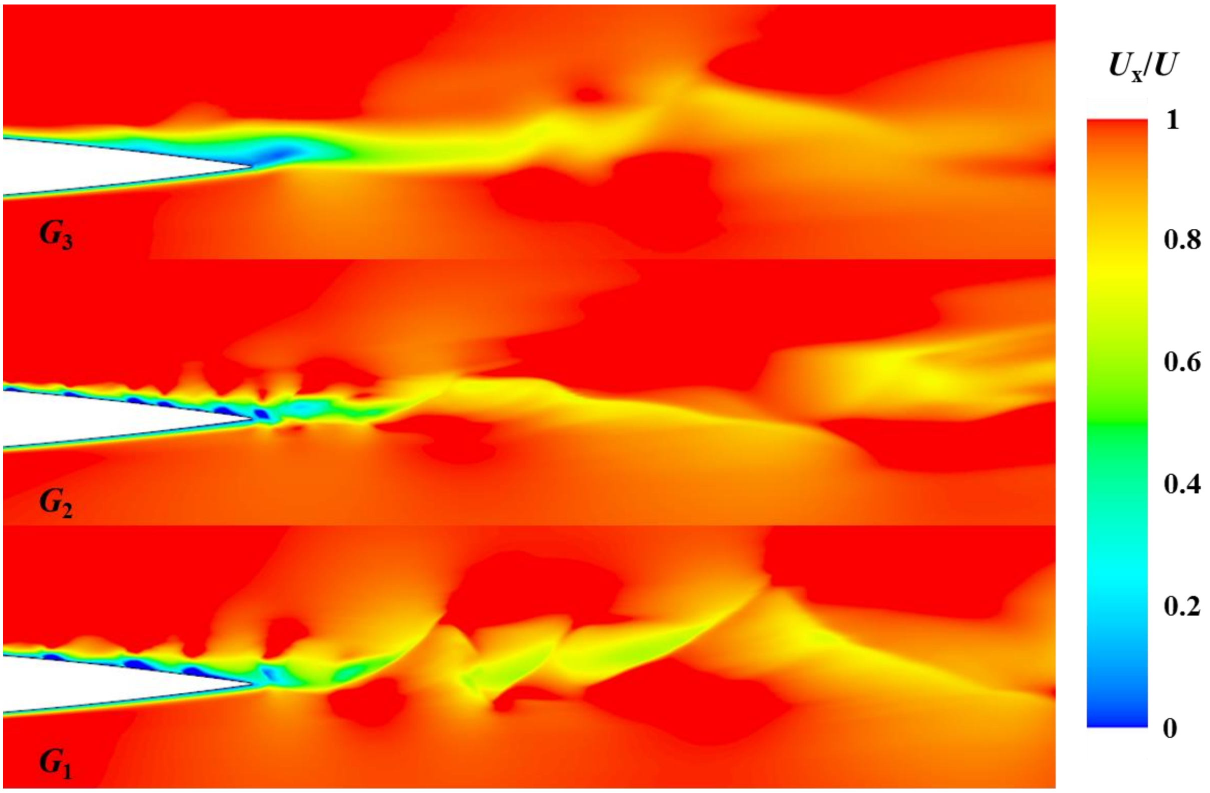

Figure 3.7: Velocity flow-fields in the wake of the three mesh cases for the 2D NACA0012 at $Re_c = 10^5$ and $\alpha = 5^o$.

Figure 3.8 shows the differences due to body mesh refinements for three different refinement cases of a 2D NACA0012 at $Re_c = 10^5$ and $\alpha = 5^o$ by plotting the vorticity contours. Jones *et al.* (2008) describe separation near the leading-edge of the airfoil at $Re_c = 5 \text{ x } 10^4$ and $\alpha = 5^o$. At $Re_c = 10^5$ the separation point is fairly close to the leading-edge ($x/c = 0.12$), but there was an early reattachment point at $x/c = 0.24$ for the coarse mesh, G_3. After refinements on the surface and in the boundary layer, as described in Table 3.2, the separation point and reattachment point moved to approximately $x/c = 0.2$ and $x/c = 0.3$, respectively.

The separated shear-layer roll-up and periodic vortex shedding shown in Figure 3.7 and Figure 3.8 give rise to the oscillating flow patterns on the body and into the wake. Ideally, these cases should be solved using unsteady RANS, but for average global force estimations, comparisons using the steady RANS simulations are assumed to be sufficient.

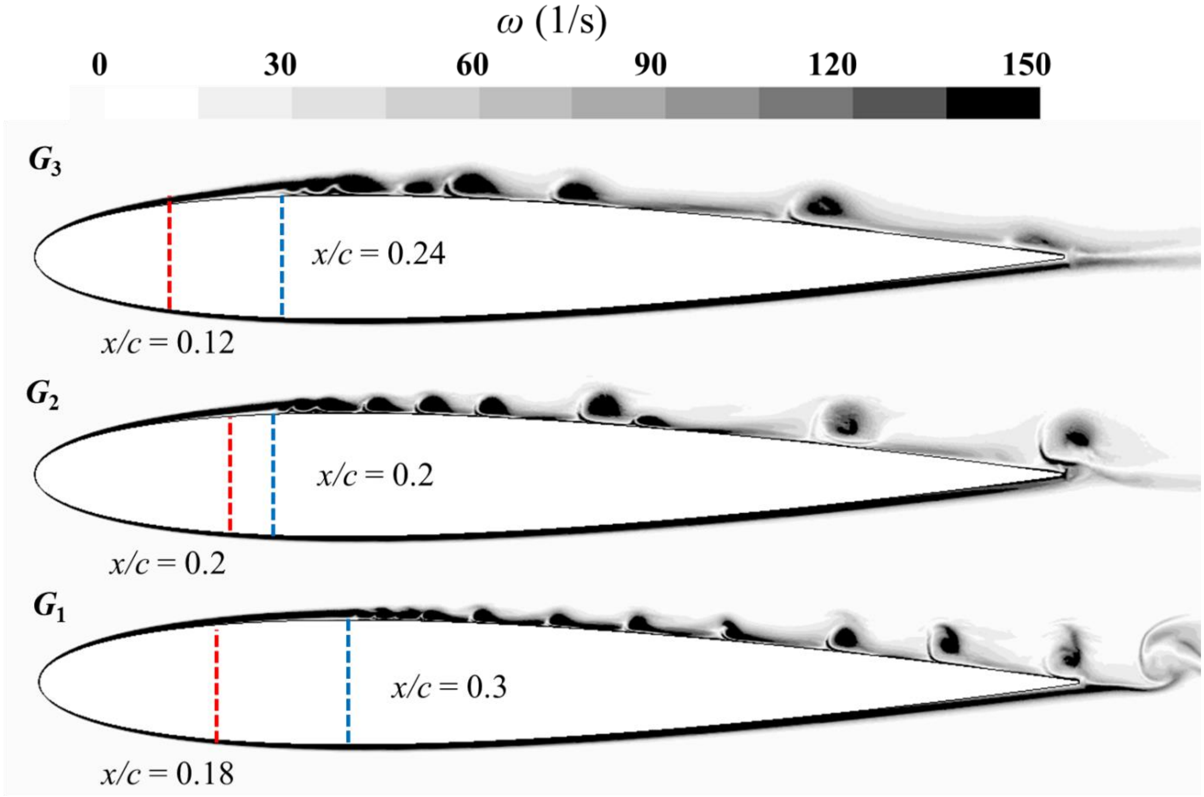

Figure 3.8: Vorticity flow-fields for the three meshes of the 2D NACA0012 at $Re_c = 10^5$ and $\alpha = 5^o$. The red line indicates the predicted initial point of laminar separation and the blue line the point of reattachment on the upper surface.

3.5 NACA0012 experimental and numerical comparison

Results obtained from Star-CCM+ on the NACA0012 airfoil using two different domain set-up techniques are compared with simulations of the same airfoil at $Re_c = 10^5$ from XFOIL 6.9 (Drela and Youngren, 2001). The critical amplification number, N_{crit} was set at 9 which is common for low turbulence wind tunnel comparisons. XFLR5 (2013) is used to model a finite NACA0012 wing by using the vortex-lattice model (with viscosity excluded) with 3D panels to estimate the aerodynamic properties at $Re_c = 10^5$. A full set of experimental data using force balance measurements was collected, as described in Section 3.2, for comparison to the $Re_c = 10^5$ simulations.

3.5.1 Two-dimensional results

The NACA0012 airfoil at $Re_c = 10^5$ was simulated for $-5^o \leq \alpha \leq 9^o$ and compared to the XFOIL numerical prediction and force balance measurements. Figure 3.9a shows the sectional lift coefficient, C_l, as a function of α for the airfoil comparisons, as well as the expected $C_l = 2\pi\alpha$ line. The 2D RANS C_l show averaged values with a variance of approximately 0.022. For $-2^o \leq \alpha \leq 2^o$, the lift slope $dC_l/d\alpha$ has a larger positive angle than the expected 2π for the experiments, as well as XFOIL and P2D simulated results. The difference in lift slope was 3.4π for XFOIL, 3π for the P2D and 2.3π for the experimental results. The 2D model does not show any non-linearity, but also has the largest variation in C_l values per iteration (Figure 3.10a).

Normally, $C_l(\alpha)$ is considered a simple calculation, determined by the pressure field, which at a higher Re is well-approximated by potential flow. Here, the lack of agreement shows that the

RANS performance is largely determined by boundary layer and model coefficients, and not by the outer potential flow.

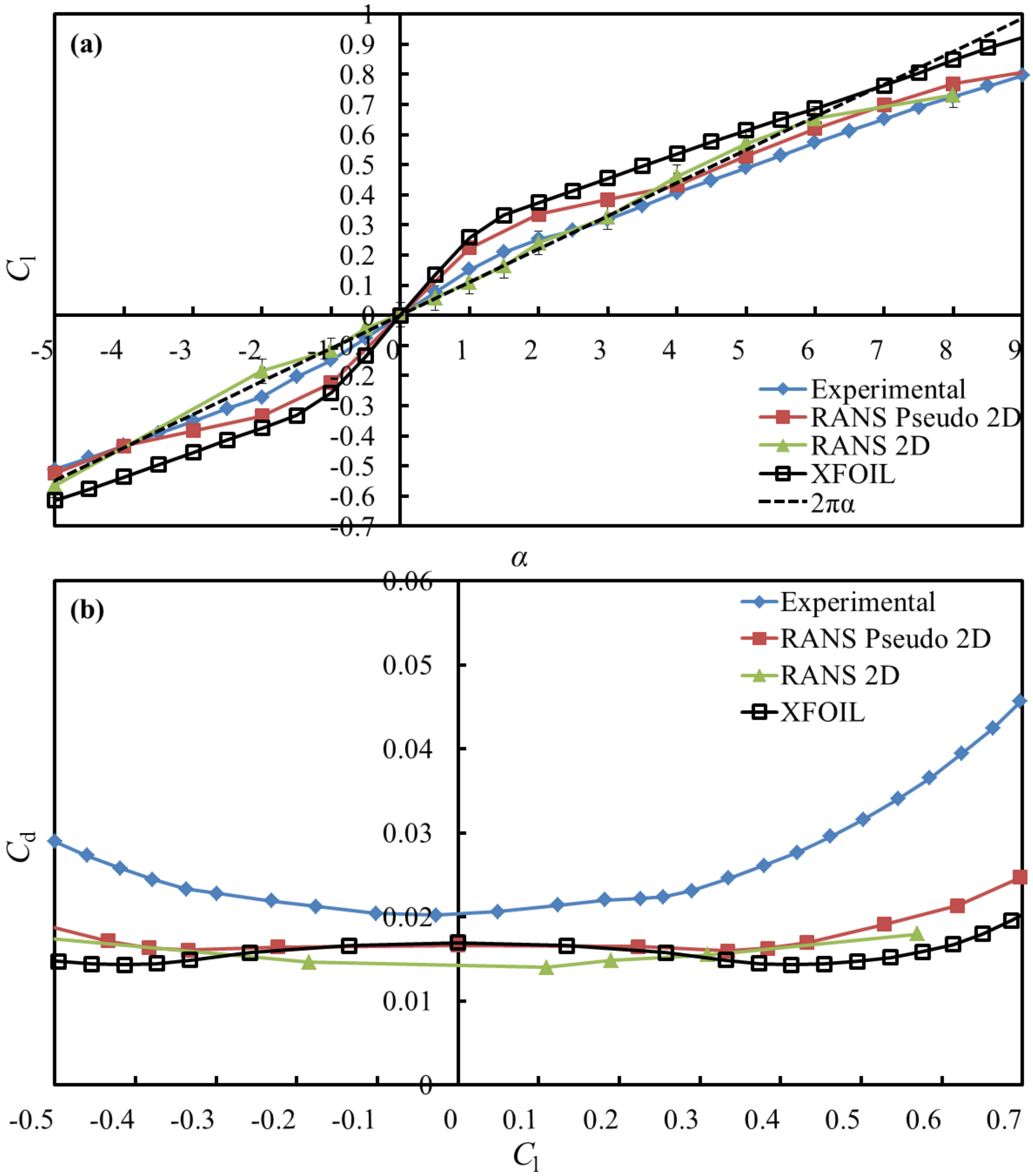

Figure 3.9: (a) Lift coefficients and (b) polar curves for a NACA0012 wing modelled at $Re_c = 10^5$ compared to results from XFOIL.

At $\alpha > 4°$, the P2D model only differs by 6.6% on average from the experimental C_l. Since this phenomenon was related to viscous separation and reattachment the agreement between two different modelling strategies suggests that physically realistic, or at least similar, viscous boundary layers were realised which was not the case when a 2D model was used. The sensitivity in both CFD models relates to the fact that the separation bubble formation and shedding was not a steady-state condition, therefore the model was unable to settle on a single value for C_l by using a steady-state CFD model as mentioned in Section 2.6.

The polar curves in Figure 3.9b show the sectional drag coeffcients, C_d, for 2D, P2D and XFOIL. Again, the 2D mesh shows a different trend to the XFOIL and P2D meshes. The γ-Re_θ transition model is 3D and the physics does not seem to correspond with the pure 2D meshes, rather a thin slice domain would be required to resolve forces for these low Re airfoil models.

The difficulty here to estimate the flow-field, even at small α, is that the true flow-field is not steady, and therefore an unsteady RANS would give a better prediction or indication of the oscillating nature of the flow-fields. Figure 3.10a shows the variation in C_l with an increasing iteration number for the steady-state solution, first for the 2D model and then for the P2D model. The last 250 iterations of a converged 2D solution is shown from 0 to 250 and from 250 to 600 the last 350 iterations of a converged P2D solution. The variations increase as the α increases, with the higher α showing a tendency to develop a low frequency oscillation pattern due to the unsteady nature of the bubble formation. The P2D model stabilises the solution and fluctuations in amplitude are reduced. However, the flow remains unsteady since although the residuals all achieve numerical convergence to a stable solution they still have large fluctuations.

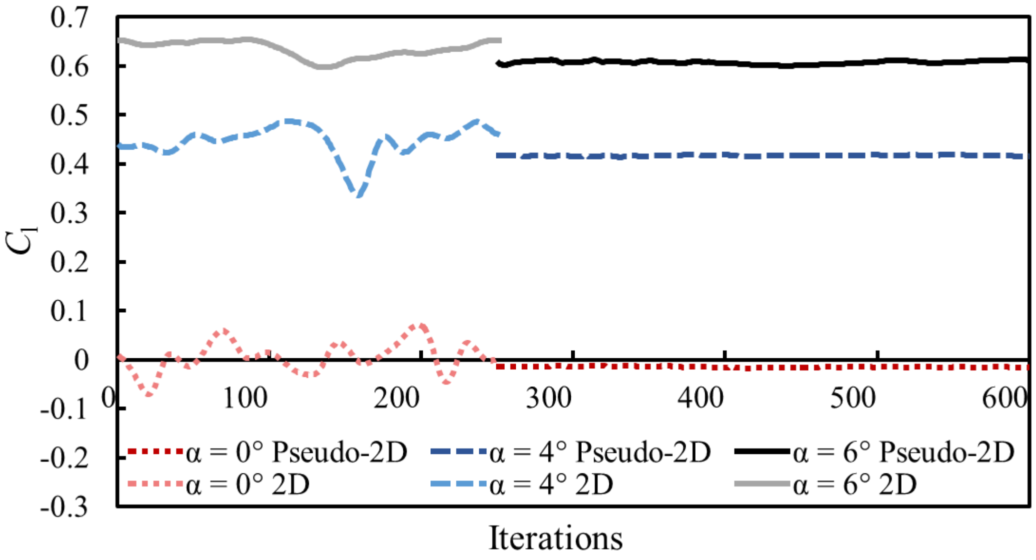

Figure 3.10: C_l values over number of iterations for the 2D and P2D models for α = 0°, 4° and 6° in a steady simulation.

The U_x/U and U_y/U flow-fields for the α range 0, 0.5, 2, 4, 6, 8° for the 2D and P2D models are shown in Figure 3.11 and Figure 3.12, respectively. Except at $\alpha = 8°$, the 2D flow-field has numerous vortex-like structures that cannot be steady, and cannot be time averages. The P2D fields look more likely to be converged on an average. The average vorticity flow-field was used to show the separation and reattachment points as predicted by the 2D and P2D models (Figure 3.13). In numerical results the first separation and reattachment points can be defined by successive zero crossings for the wall shear stress, and these locations are superimposed on the maps of spanwise vorticity in Figure 3.13. The two computations differ from each other, as in Figure 3.11 and Figure 3.12, in the marked separation and reattachment points. The 2D simulation is not steady at any α and the P2D will be unsteady for $\alpha > 4°$. Regardless, the flow-fields in Figures 3.11 to 3.13, if not true averages, are still solutions to the RANS equations even if they are best regarded as snapshots of an underlying unsteady flow-field. This gives an indication to what might be expected when visual flow-field experiments are conducted. Also, even though the flow-fields are mere snapshots, the force values compare within 6% to that of the experimental measurements, which mean even RANS models can give reasonable estimates for wing analysis without the computational cost of unsteady, LES or DNS simulations.

At $\alpha = 0°$, the flow about the NACA0012 has a fairly symmetrical flow pattern and separates on both sides before the trailing-edge. At $\alpha = 0.5°$, the separation point has moved forward on the upper (suction) surface, but has moved aft on the lower (pressure) surface (Figure 3.11 and Figure 3.11, row 2). As the boundary layer moves over the trailing-edge, the near-wake pattern is deflected downwards (Figure 3.11, row 2). Regions of $U_y/U < 0$ are more prominent on the upper surface and U_y/U aft of the trailing-edge is asymmetric, with stronger, positive U_y/U on the lower side (Figure 3.12, row2). The laminar separation before the upper surface trailing-edge assures that streamlines here are also deflected slightly away from the upper surface.

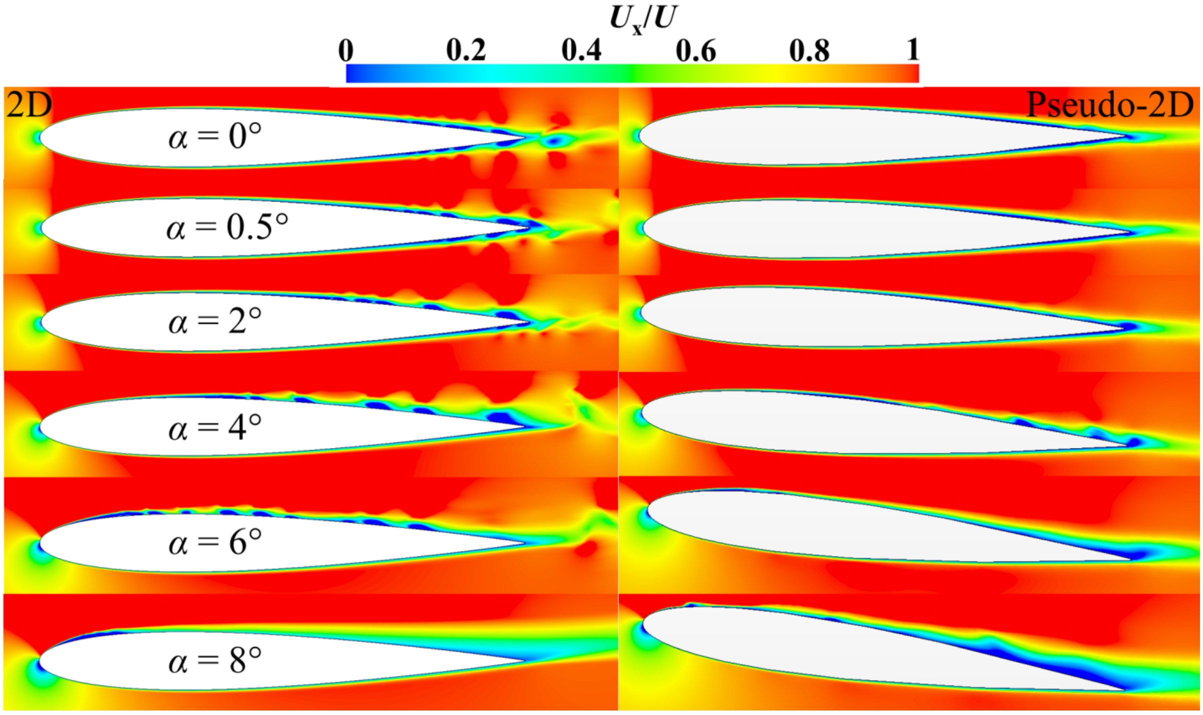

Figure 3.11: Velocity magnitude contours for the 2D and P2D models of a NACA0012 airfoil at $Re_c = 10^5$.

At $\alpha = 2°$ (Figure 3.11, row 3), the streamlines are deflected upwards on the lower surface in the near-wake. Although the separation line has moved further forward (Figure 3.13, row 3) on the upper surface, it still maintains the net flow downwards. The trailing wake shows a small streamwise extension, like an attached recirculation bubble.

At $\alpha = 4°$, the initial point of separation and reattachment (Figure 3.13) moves further upstream and a separation bubble is present on the upper surface (Figure 3.12, row 4), close to where U_y/U has its highest negative value. The flow experiences a higher convex curvature on the upper surface, formed by the combination of the airfoil surface and separation bubble. The changed effective camber leads to a better approximation to the C_l around this α in Figure 3.8a. As the laminar separation bubble moves forward on the upper surface with further increases in α (6° and 8°, Figure 3.11-3.13, rows 5 and 6) the bubble shrinks in streamwise length and the spanwise vorticity becomes more strongly negative at the outer shear layer. This phase is associated with reduced C_l. There is a broad downwash region in U_y/U from the mid-point of the bubble to the airfoil trailing-edge.

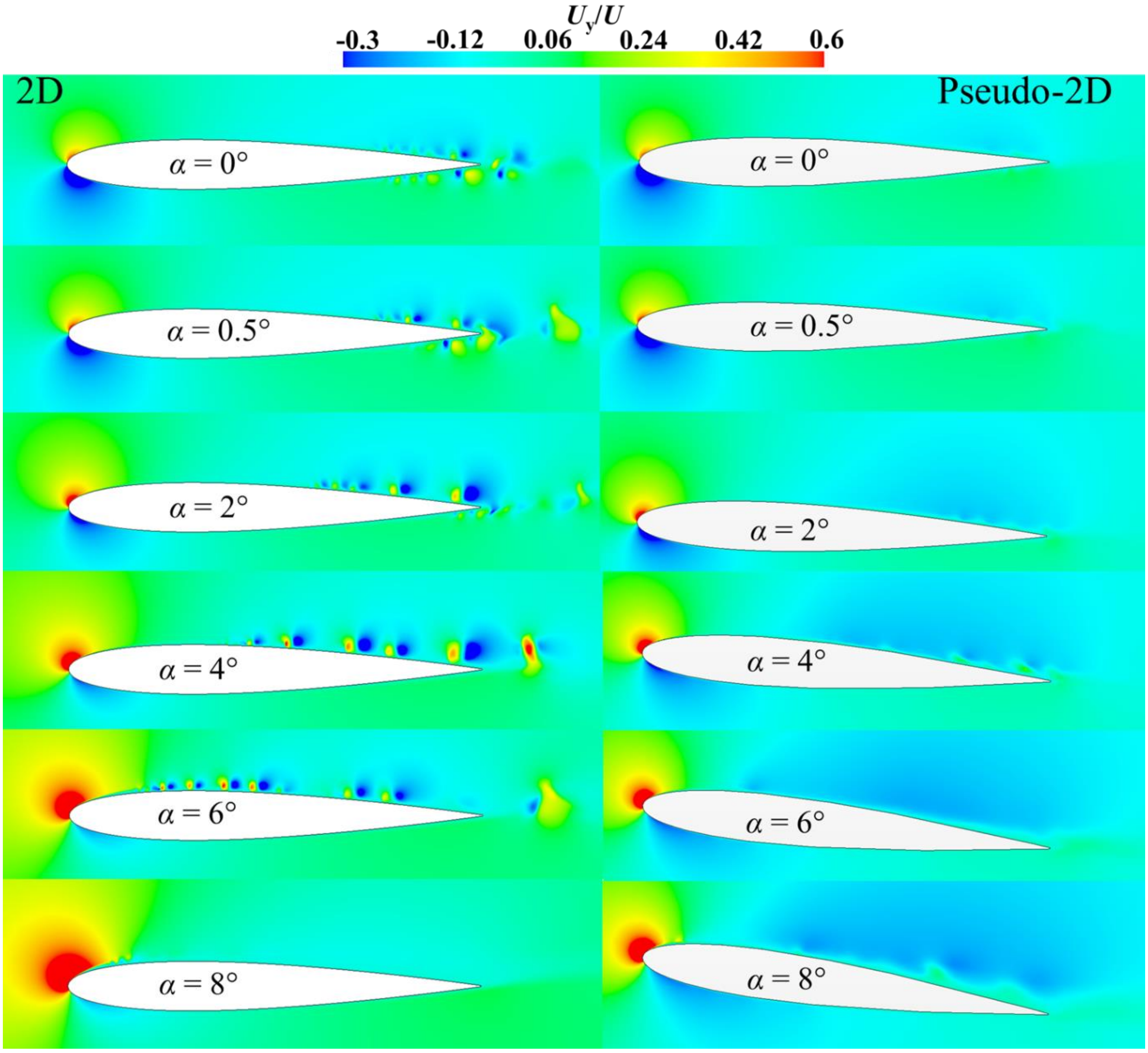

Figure 3.12: U_y/U **contours for the 2D and P2D models of a NACA0012 airfoil at** $Re_c = 10^5$**.**

A broad maximum in L/D is observed at $4° \leq \alpha \leq 8°$ shown in Figure 3.14, for the experimental results. However, the same broad maximum in L/D does not exist for the XFOIL and P2D results which suggest a maximum L/D for $\alpha = 5°$ and $\alpha = 6°$ respectively. This is similar to the maximum L/D in literature of the NACA0012 at higher Re_c. The LSB observed here is associated with improved L/D over this range of α for the experimental results, which is contrary to most literature interpretations based on observations at higher Re_c. As the LSB moves forward on the upper surface with further increases in α (6° and 8°) the LSB shrinks in streamwise extent as for the $Re_c = 5 \times 10^4$ results (Tank *et al.*, 2016).

Bastedo and Mueller (1986), Hsiao *et al*. (1989), Huang *et al*. (1996) and McGhee *et al*. (1988) shows similar observations to Tank *et al*. (2016) that an LSB that extends over a large portion of the chord but moves forward and shortens with increasing α at low Re_c. All support the claim by Lissaman (1983) that bubbles covering a large percentage of the chord can have a significant effect on airfoil performance by altering the outer potential streamlines. It is not always acknowledged, however, that the separation and reattachment of the flow to form an LSB, while associated with lower $C_{l,\alpha}$, is also associated with the highest L/D, or aerodynamic efficiency. The increase in L/D can be deliberately exploited, for example by acoustic forcing (Yang and Spedding, 2013b,c). In the experimental work, L/D has a broad maximum over $4^o \leq \alpha \leq 8^o$, when the LSB reattaches and moves forward on the upper surface.

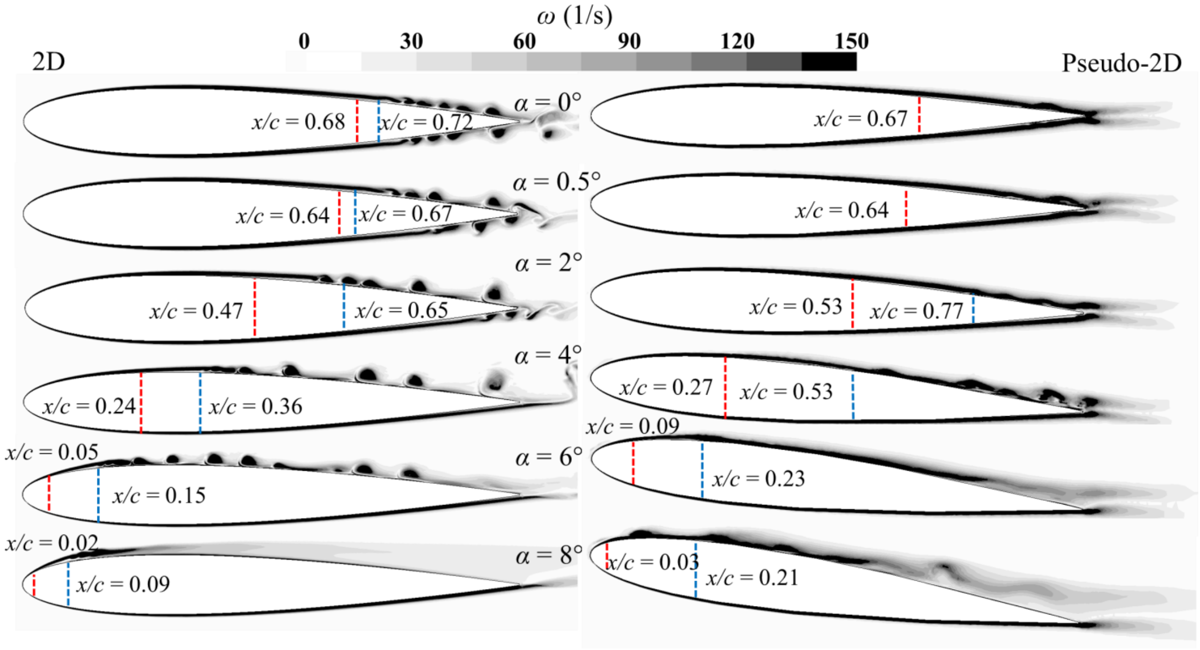

Figure 3.13: Vorticity contours for the 2D and P2D models of a NACA0012 airfoil at $Re_c = 10^5$. The red dashed line indicates the first point of separation and the blue dashed line the first point of reattachment on the upper surface of the airfoil.

The attempt to model the unsteady separation bubbles that exist over a low Re airfoil becomes extremely challenging using RANS. Not only is RANS unable to predict the points of separation and reattachment without the coupling of a transition model, but the steady-state assumption completely disregards the low frequency oscillations of the laminar separation bubbles described by Almutairi *et al*. (2010). In terms of the modeling domain the 2D model is unable to capture the 3D nature of the laminar bubbles, where the P2D model would be a better practice, but the thickness of the domain also has an unquantified influence on the results (Almutairi *et al*., 2010; Jones *et al*., 2008).

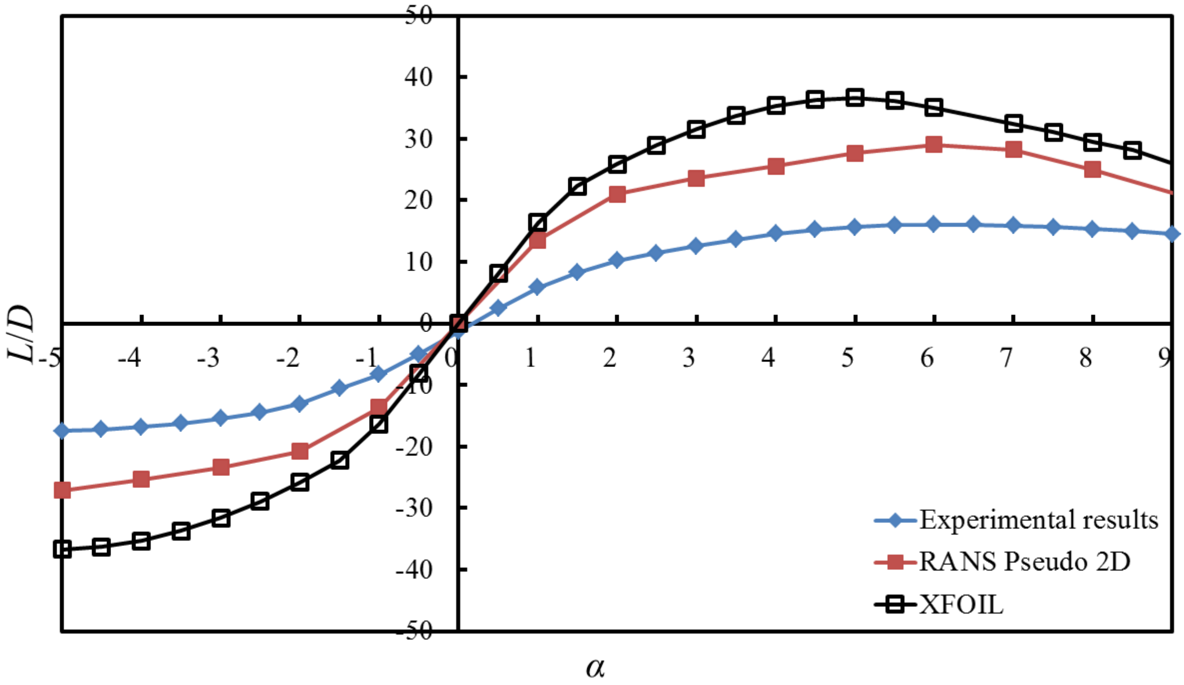

Figure 3.14: L/D curves for a NACA0012 wing modelled at $Re_c = 5 \times 10^4$ compared to results from the experimental measurements.

3.5.2 Three-dimensional results

A NACA0012, rectangular, $AR = 3.7$ wing was modelled at various angles of attack for $Re_c = 10^5$. The results were compared with those from XFLR5 (XFLR5, 2013), which has a linear slope. Figure 3.15a shows C_L as a function of α for all cases with the analytical estimate of $C_L = 2\pi\alpha(AR/(AR+2))$ plotted as reference. There is a similar, non-linear phenomena at a lower α, with a smaller variation around the predicted C_L compared to the airfoil. However, the CFD and experimental results show a different high lift at approximately $\alpha = 3°$ and $\alpha = 2°$ respectively. The laminar separation bubbles now also have a spanwise component, which is unsteady. The experimental results in Kim *et al*. (2011) as well as those performed by Tank *et al*. (2016) show $C_{l,\alpha} < 0$ around $\alpha = 0°$ for the NACA0012 at $Re_c = 5 \times 10^4$. The only numerical result that shows this negative slope is the laminar 2D simulations by Lee *et al*. (2015). The 2D and P2D RANS both show a positive slope around $\alpha = 0°$ at $Re_c = 5 \times 10^4$ (Appendix A) and $Re_c = 10^5$ reported here.

Figure 3.15b shows the polar curves for the wing at various angles of attack. The C_D differs on average by about 10% between the CFD and XFLR5. Results are fairly inconsistent for $-4^o \leq \alpha \leq 4^o$. However, for the more complex WBT to be discussed on Chapter 5, the NACA0012 wing is used at $\alpha = 6^o$, for which there is a difference of less than 5% between the XFLR5 and RANS results for C_L.

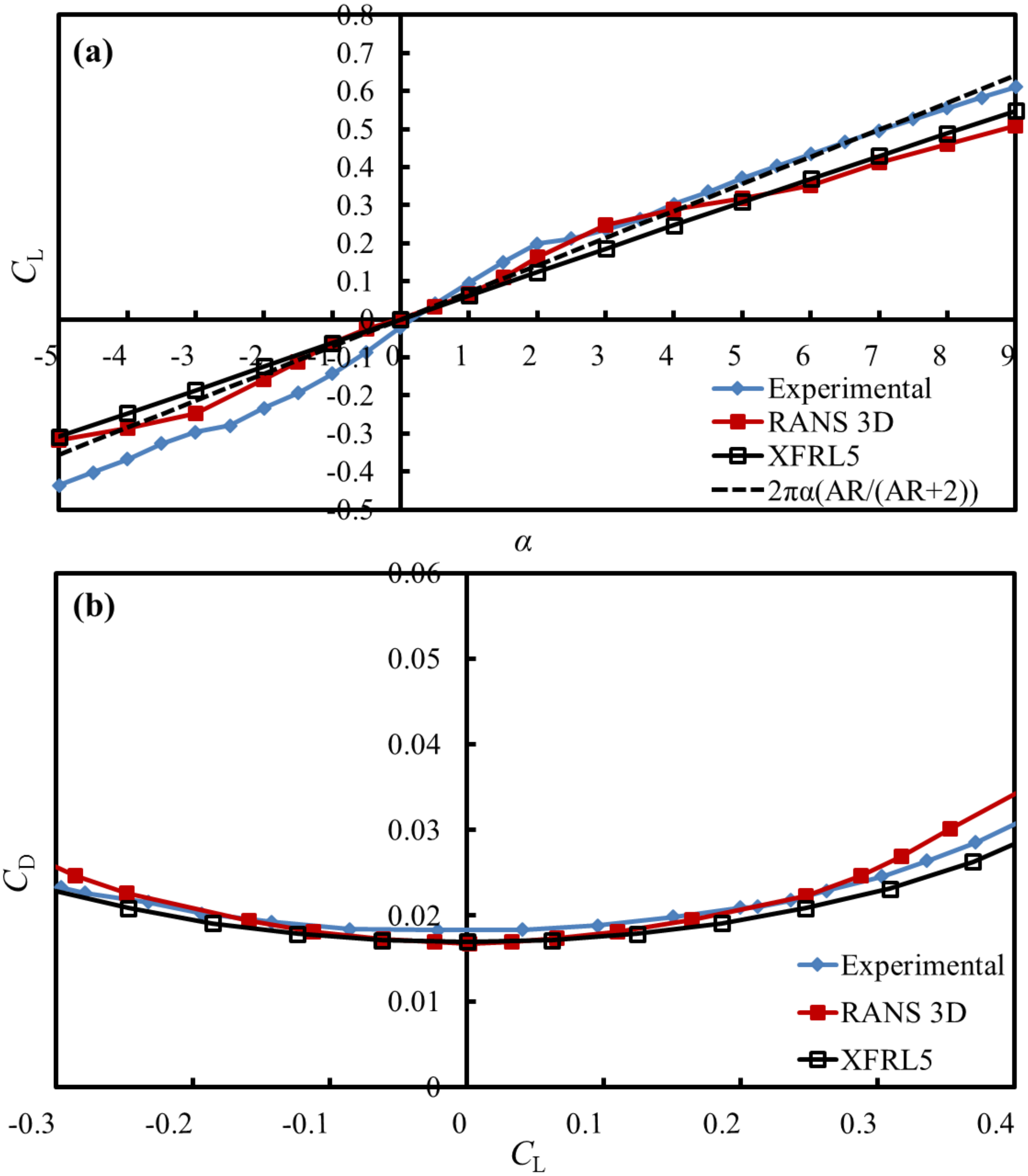

Figure 3.15: (a) C_L and (b) polar curves for a NACA0012 wing modelled at $Re_c = 10^5$ compared to results from XFLR5 and experimental measurements.

3.6 Poor agreement between experimental results and computations

The attempt to provide an accurate set of data with a comparison to RANS is quite challenging, even on a simple NACA0012 wing, since both the computational model and the experimental results are extremely sensitive to multiple sources of environmental or modelling conditions. The point of the simulations is not to make the best possible outcome, but to find the outcomes when readily-available commercial codes were applied to this problem. The critical part is in the viscous boundary layer and the results are affected by modelling the transition, coupled to the SST k-ω turbulence model. XFOIL is, in some respects, a much simpler code. The outer potential flow is inviscid and a viscous boundary layer model with explicit accommodation for separation and transition is coupled with it. Both simulations are therefore quite dependent on the boundary layer modelling.

The wind tunnel experiments only agree well with the P2D RANS in C_l for $4° \leq \alpha \leq 8°$ and for the 3D RANS only for $-2° \leq \alpha \leq 2°$. This range of α is where the flow is dominated by the separation bubble, while small α results are mainly influenced by details of trailing-edge separation. XFOIL has much worse qualitative agreement, compared to the experiment over most αs. Almutairi *et al*. (2010) mentions that the overall agreement between experiment and DNS with varying degrees of sophistication is not much better than with a simpler and faster viscous boundary model, coupled with outer potential flow, such as XFOIL.

All figures in Chapter 4 and 5 showing results from the CFD simulations are based on a steady converged RANS solution. Even though this limits the ability to give specific insight on the exact flow features that could have been solved using unsteady simulations, the exact location and size of these features were not part of the purpose of this work. These highly transitional flows are potentially the most complicated to predict accurately with CFD, since the majority of the turbulence models used in RANS calculations were not meant for this type of flow regimes.

3.7 Summary, conclusions and recommendations

In this chapter, a simple case of the NACA0012 airfoil was used to make a careful comparison between new experiments and computations within this Re_c regime. The diagnostic procedures were intended to help guide the numerical domain set-up for comparisons and predictions in subsequent more complex cases.

The performance of wings at a low Re_c is substantially dictated by the dynamics of the laminar boundary layer as described in Chapter 2.6. The sensitivity to boundary layer separation and reattachment can make accurate and repeatable measurement, even of time-averaged C_l and C_d, difficult, where the similarity between measured $C_l(C_d)$ polars breaks down. A carefully performed wind tunnel test showed an uncertainty of the force measurements of less than 1.5%. Similarly, the CFD set-up and procedure made sure that the global force coefficients obtained from the simulations were as accurate as possible. Although all models predicting C_l had different lift slopes, there was a similarity in the non-linear trends observed for $-2^o \leq \alpha \leq 2^o$, also for the experimental results. The 2D model shows the worst results with no non-linearity present and multiple separation bubbles that cannot be steady, and cannot be time averages. The difficulty in modelling the flow physics at a low Re_c is that the true flow-field was not steady and the model was unable to settle on a single value for C_l as a result of the low-frequency oscillation pattern due to the unsteady nature of the bubble formation. The P2D model stabilises the solution, and fluctuations in amplitude are reduced, but the flow remains unsteady.

The separated shear-layer roll-up and periodic vortex shedding give rise to an oscillating behaviour of the force coefficient values. The attempt to model the unsteady separation bubbles that exist over a low Re_c airfoil becomes extremely challenging using RANS, even with the transition model to predict the onset of turbulent flow. Ideally, these cases should be solved using unsteady RANS, but for average global force estimations, comparisons using the steady RANS simulations are assumed to be sufficient. The criteria for sufficiency was measured by obtaining results within 10% of the experimental data without adding computational cost for unsteady flow solutions or LES solutions.

The NACA0012 has been used as a test case, a canonical example of a smooth airfoil. It has no special design features that make it suitable for use at low Re_c. Since it continues to be used as a test case for the emerging computations of low Re aerodynamics, establishing a reliable set of baseline measurements is a matter of some urgency. The difficulty in doing so is symptomatic of the challenges at low Re_c, for which it remains a sensitive diagnostic and test case. The mechanism proposed for the curious and counter-intuitive result of the negative lift is quite general, and we predict will be shared by any sufficiently smooth, thick, symmetric airfoil in a sufficiently low turbulence environment.

Reasonable agreement of the force prediction compared to XFOIL and XFLR5 results were obtained. The study, however, showed that at $\alpha = 6^{\circ}$, which was used for the WBT in Chapter 5, there was a difference of less than 5% between the XFLR5 and RANS results.

4. LOW-DRAG BODIES MODIFIED TO IMPROVE LIFT

4.1 Introduction

The purpose of this chapter is to investigate the potential of a KE to modify the flow over LDBs, as well as to establish some means of predicting the effectiveness of the LDB-KE combination. A numerical investigation of two LDBs as described in Section 2.3.5, was conducted, after which the geometries were modified by deflecting the aftbody with and without a KE attachment. Forces and flowfields with and without a KE (which are subsequently termed, KE and NKE conditions) at varying δs, were computed to determine the mechanism of the KE/body deflection on both local and global lift and drag, computed from the normal and shear stresses over the whole body assemblage. The experimental body (B-0-NKE/KE) without the wing used in Huyssen *et al*. (2012) and Davis and Spedding (2015) was also modelled to compare the use of the KE to the LDB-KE. The modified slender-body wing theory with an adapted geometric definition (outlined in Section 2.4.5) was used to estimate the effectiveness of the body-tail combination, to confirm guidelines observed from the body-tail interaction.

4.2 Numerical modelling

4.2.1 Geometric model and mesh generation

All three bodies were modelled as 3D axisymmetric bodies inside a 3D computational flow domain, the B-0 as shown in Figure 1.2 and LDBs as shown in Figure 4.1. Three-dimensional (not axisymmetric) grids were necessary to accommodate the later addition of symmetry-breaking KE tails. The simulation of the wind tunnel experiments for the F-57 includes an approximation of the wind tunnel walls, which were originally in octagonal cross-section (Patel and Lee, 1977), but simplified to a square cross-section here (with less than 0.5% influence on the force coefficient results). The λ of the body was 4.75, the height and width of the wind tunnel were $1.25l_F$, and the length of the test section was $6l_F$, as in the experimental investigation (Patel and Lee, 1977).

The Myring LDB with body length, l_M, and $\lambda = 5.56$, was modelled inside a cylindrical domain with a diameter of $4l_M$. The nose of the body was positioned $4l_M$ from the inlet of the grid, and the outlet was $9l_M$ downstream of the tail. The body of the B-0-KE has a $\lambda = 5.33$ (nose length $= 0.33l$ and midsection $0.29l$) and was modelled in the same domain as the 3D NACA0012 wing (Figure 3.2c). Based on the body length of the B-0-KE, the domain was $4.25l$, and the nose was positioned $6l$ from the inlet and $18l$ from the outlet.

The computational grids (Figure 4.2) also consisted of polyhedral cells and were meshed using the Advancing Layer Mesher in Star-CCM+. The growth of the boundary layer along the body and KE starts with a very thin boundary layer over the nose, gradually thickening towards the trailing-edge. Both the LDB-KEs and the B-0-KE had 20 cells across the boundary layer height for accurate drag estimation, while two boundary layer cells were sufficient for the simulated tunnel walls.

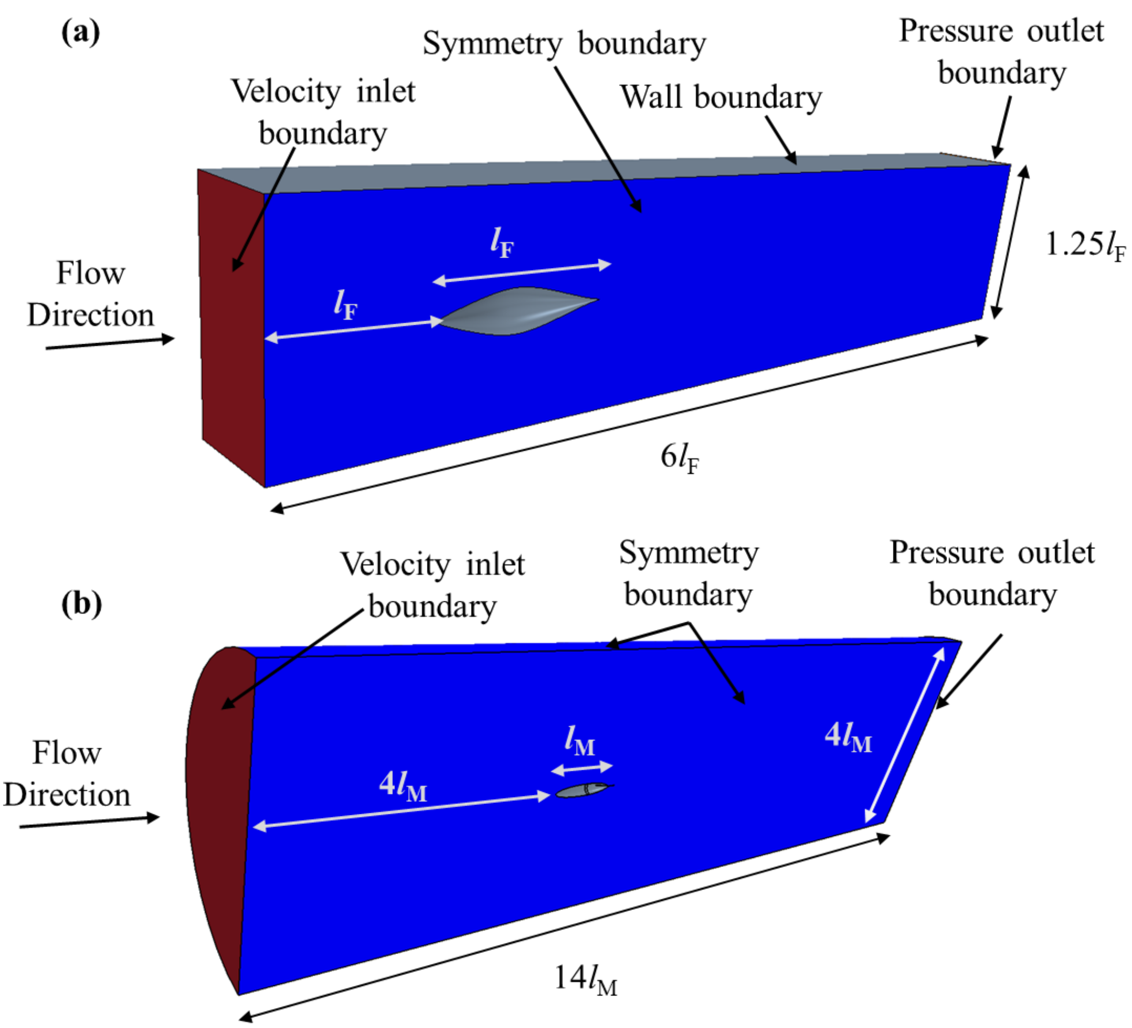

Figure 4.1: Geometric model and the assigned boundary conditions for (a) the F-57 LDB and (b) the Myring LDB.

Three volumetric mesh refinements were used for the two LDB-KE grids and the B-0-KE, refined in the same way as the NACA0012 wing in Section 3.3.4. Additional refinements were applied at the streamwise location on the F-57 LDB, where transition was experimentally forced with a tripwire (Patel and Lee, 1977) (x/l = 0.475), as well as for the nose and tail sections on both bodies.

To ensure mesh independence, the GCI method, as described in Section 3.4.3, was used on the three different mesh sizes of the F-57 LDB. The results are shown in Figure 4.3. The final mesh counts for the F-57 and Myring LDB-NKEs were about 3.6 x 10^6 and 3.3 x 10^6 cells respectively. The B-0-NKE had 3 x 10^6 cells.

The KE tails had the same geometry as described in Huyssen *et al*. (2012) and Davis and Spedding (2015), with the same ratios of tail width to body diameter, and KE length to total body length. The addition of the KE tails increased the body lengths by 10%, but it proved unnecessary to extend the domain length correspondingly. The KE tails increased the cell counts to 4.6 and 3.4 x 10^6 for the F-57 and Myring LDB-KEs respectively and to 3.2 x 10^6 for the B-0-KE.

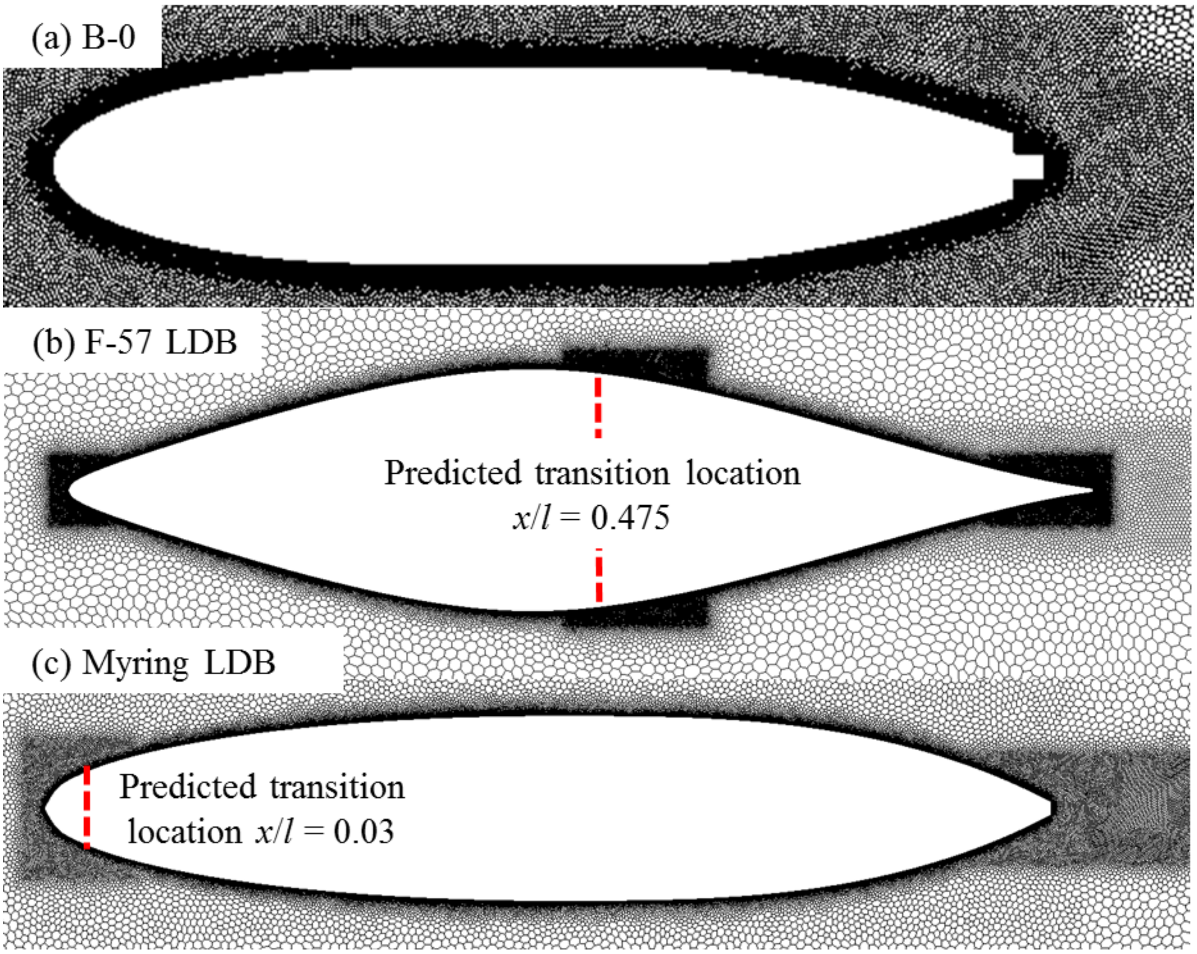

Figure 4.2: Unstructured meshes around (a) the axisymmetric F-57 LDB and (b) Myring's LDB and (c) the B-0. Predicted transition location are indicated on LDBs.

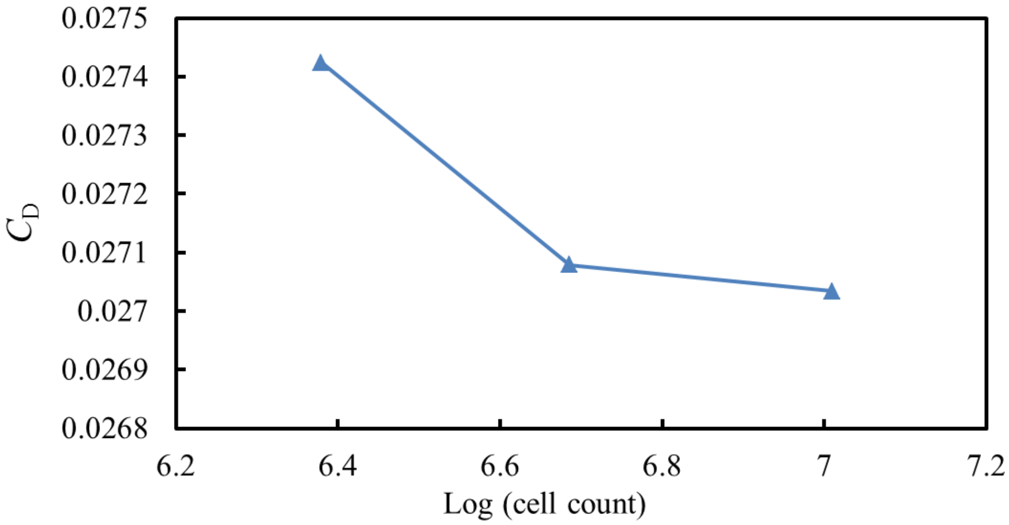

Figure 4.3: C_D as the observed mesh refinement quantity for three mesh sizes on the F-57 LDB.

4.2.2 Boundary conditions, turbulence and transition models

The boundary conditions used for the bodies are indicated in Figure 4.1. The flow was assumed to be steady and incompressible, with a constant velocity inlet condition. Re_l based on body length was 1.2 x 10^6 for the F-57 LDB, 10^7 for the Myring LDB and 4.3 x 10^5 for the B-0-KE. The outlet boundaries were pressure boundaries set at atmospheric conditions. The F-57 LDB's outer surface domains were modeled as no-slip wall boundaries, where the outer boundaries for Myring's LDB had symmetry boundaries. The non-dimensional wall distance criterion, $y^+ < 1$, was satisfied for all cases (the predicted wall boundary thicknesses are less than a wall-bounding computational cell and the boundary layer can therefore be modeled on that cell). The inlet velocity was specified to give the Re_l at which the literature/reference cases were completed. The Star-CCM+ solver settings were the same as for the simulations in Chapter 3.

4.2.3 Comparison with reference bodies

4.2.3.1 F-57 Low-drag body

Figure 4.4a shows the numerically generated pressure coefficients, C_P, over the F-57 in the normalized axial direction, x/l, together with the experimental results of Patel and Lee (1977) at $Re_l = 1.2 \times 10^6$ and the theoretical predictions of Young (1939). Young made use of a modified airfoil method to predict profile drag for smooth bodies of revolution, although he found this method to have some restrictions. At a higher Re_l ($10^7 – 10^8$) and low λ (3.25 – 5.9), where the transition region did not exceed $x/l = 0.05$, the method gives reasonable results compared with experimental cases. However, when both the Re and λ are lower, the assumption of negligible pressure variation in the boundary layer on the aftbody is not correct, since the thickening boundary layer can support substantial pressure variation (Parsons and Goodson, 1972; Patel and Lee, 1977).

There are negligible differences between theory, experiment and simulation (< 7%) up to $x/l = 0.4$. Further aft, close agreement cannot be expected because the experiments were conducted with a tripwire at $x/l = 0.475$ to avoid a separation bubble. The numerical departure in C_P at about $x/l = 0.57$ shows the location of the natural separation bubble without a tripwire. From $x/l = 0.7$ the wind tunnel and simulation results agree well, and depart from the high C_P theoretical line, likely due to finite Re_l effects.

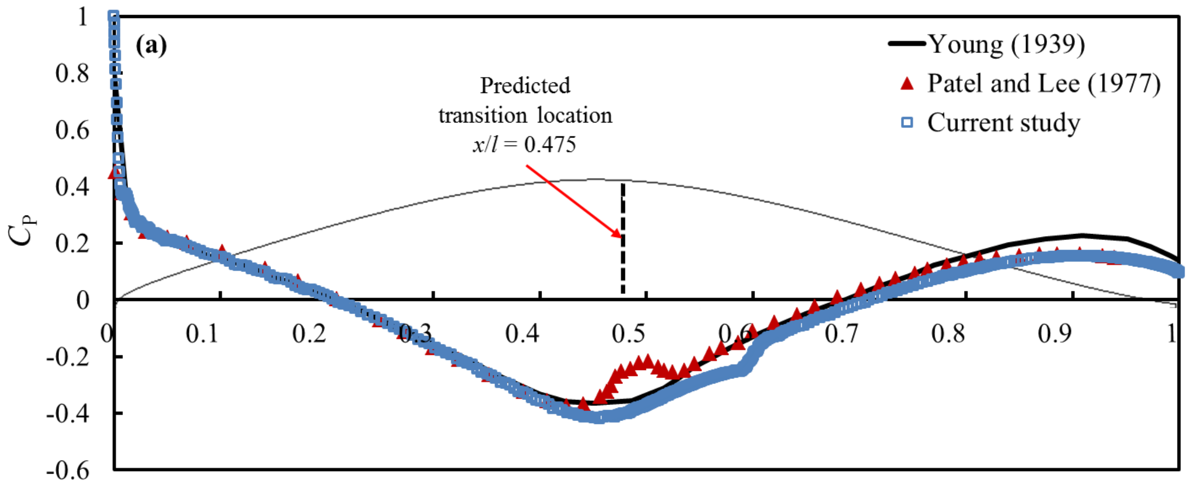

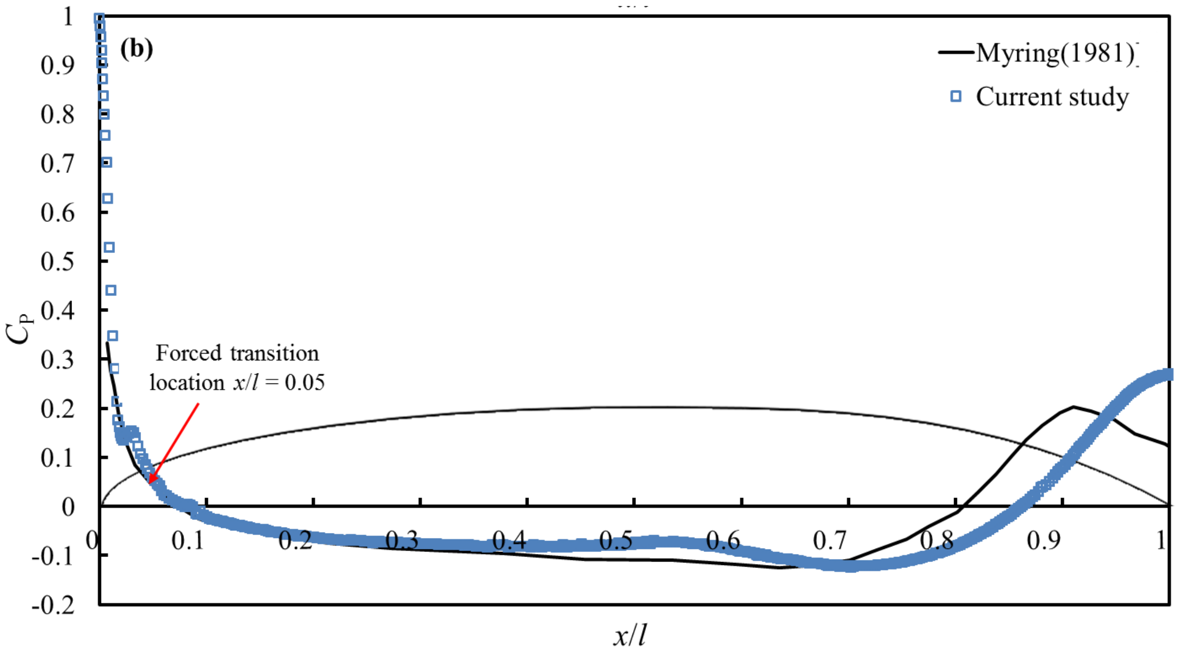

Figure 4.4: Pressure coefficients as a function of body length over (a) F-57 LDB at $Re_l = 1.2 \times 10^6$ and (b) the Myring LDB at $Re_l = 10^7$, comparing the simulations to literature results (Young, 1939; Patel and Lee, 1977; Myring, 1981).

4.2.3.2 Myring's Low-drag body

Figure 4.4b compares the pressure coefficients with the theoretical predictions of Myring (1981) for $Re_l = 10^7$. The overall agreement is reasonable for $x/l < 0.4$. Theory and computation differ downstream of this point, as numerical results show an initial reduction in $-C_P$ before it recovers to a positive tail towards the trailing-edge. Consequently, theory and numerical values have a difference in phase in the undulation in $C_P(x)$. Analogous to the previous F-57 case, Myring (1981) prescribed a transition location at $x/l = 0.05$, where the numerical simulation allows transition to occur naturally at approximately $x/l = 0.48$, which is partially the cause of the difference in phase seen in Figure 4.4b.

4.3 Numerical results for the experimental body-KE

The pressure distributions along the B-0-NKE/KE at varying aftbody deflection angles, δ, are shown in Figure 4.5a. All the cases are similar over the nose and up to $x/l = 0.5$; beyond this point there is a large fluctuation for the pressure distribution from $x/l > 0.6$. This fluctuation is further evaluated in Figure 4.5b with U_x/U contours of off-surface flow over a section of the body ($0.6 < x/l < 1.1$) where various points of separation and reattachments are observed for both NKE and KE. At a lower Re_l, the aftbody design was expected to be more susceptible to flow separation if the body was not specifically optimised for the Re_l regime.

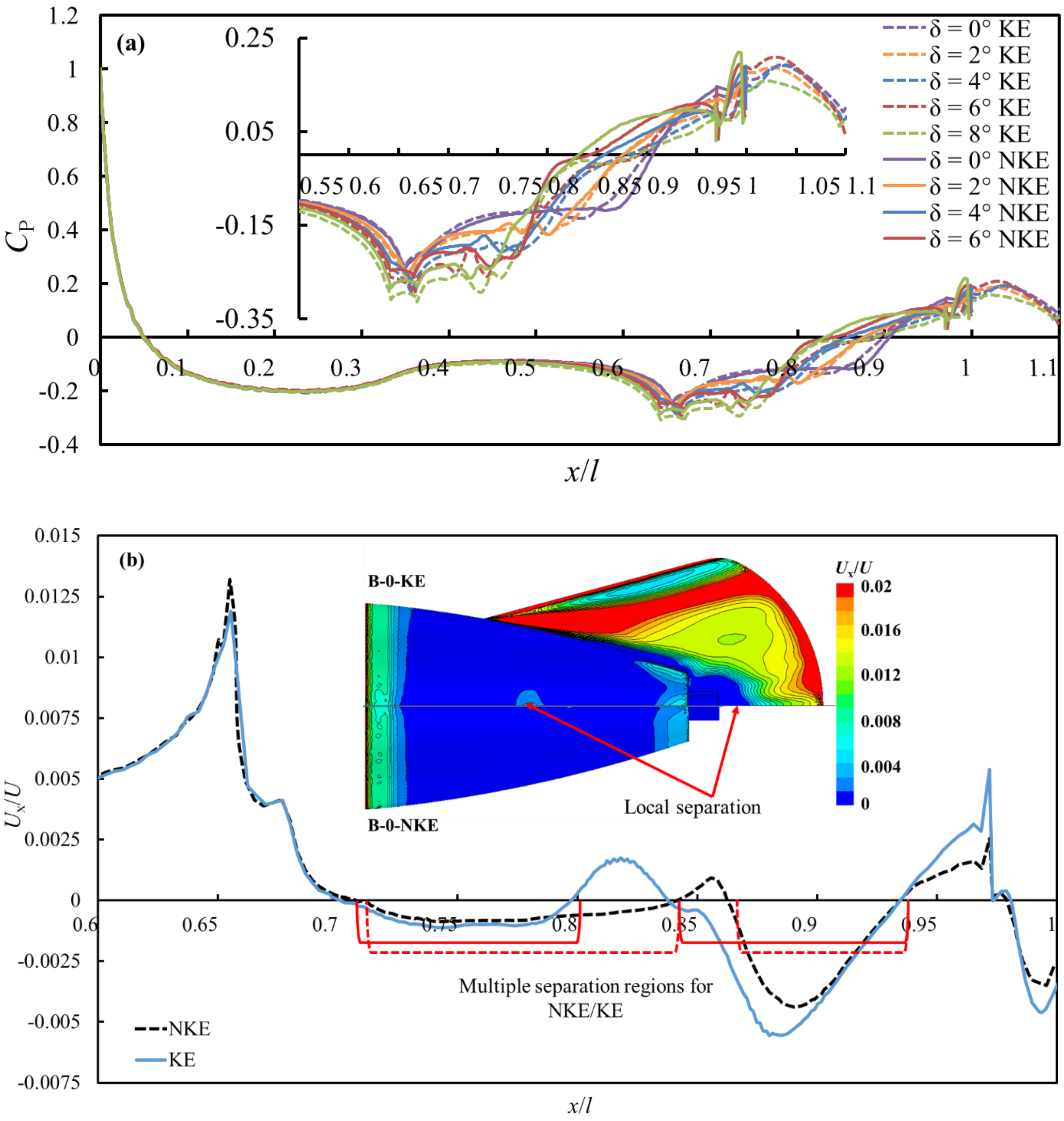

Figure 4.5: (a) C_P of the B-0-NKE/KE at different *δ*s and (b) U_x/U over the section of the body, $0.6 < x/l < 1$ with and without KE at $\delta = 0°$. U_x/U contours show separation patterns as dark blue patches over the aftbody and KE.

Figure 4.6 shows the normalized streamwise wake velocity profile, U_x/U, for $\delta = 4°$ with and without a KE. The downward deflection of the defect profile with KE implies a higher lift, and the colour inset of velocity contours, $||U||$, shows that the displacement is a global field phenomenon.

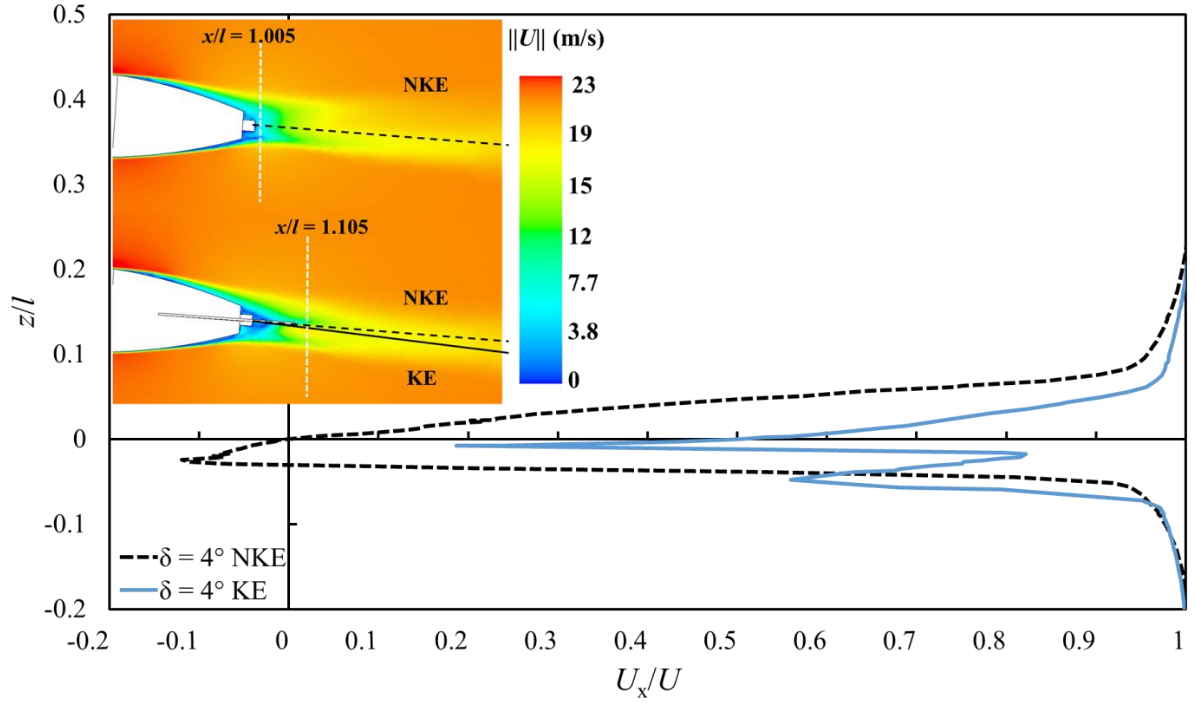

Figure 4.6: Normalized streamwise wake velocity profile at δ = 4º for the B-0-NKE/KE. Profiles are taken at x/l = 1.005 for NKE and x/l = 1.105 for KE (0.5% after either the body or tail ends). Insert shows velocity magnitude contours on the symmetry plane in the wake region.

Figure 4.7a and Figure 4.7b show U_x/U, for δ = 2° and 6°, combined with contours of the relative vertical velocity, U_z/U, on the symmetry plane of the B-0-NKE/KE. Similar to Davis and Spedding (2015), the U_x/U profile has a double-lobe form, as though the upper and lower boundary layers were shed separately into the wake with the KE, which acts like a splitter plate. The lower lobe becomes more pronounced as the δ increases. The boundary layer over the aftbody's top and bottom is split by the KE, which prevents the formation of a proximate mixing zone between these two shear layers.

If the aftbody-KE is not optimised for these low Re_l cases, the benefit of the KE will be lost due to flow separation over the aftbody, which diminishes the function of the KE as it becomes a small movement in an already unstable flow-field. Figure 4.8 shows the additional shed vortices present at x/l = 1.005 for the B-0-NKE/KE at δ = 4º to visualize this disturbed flowfield in which the KE has to function. The red circles show the vortex cores for the B-0- KE and the blue circle for the B-0-NKE. When the KE is added the streamlines from the bottom surface of the body, that curve upward over the aftbody shows a single vortex core just below the body central point. When the KE is added this vortex core is pushed downward by the KE blocking the streamlines from curving upward around the aftbody. The flow over the KE and over the top of the aftbody form additional vortices.

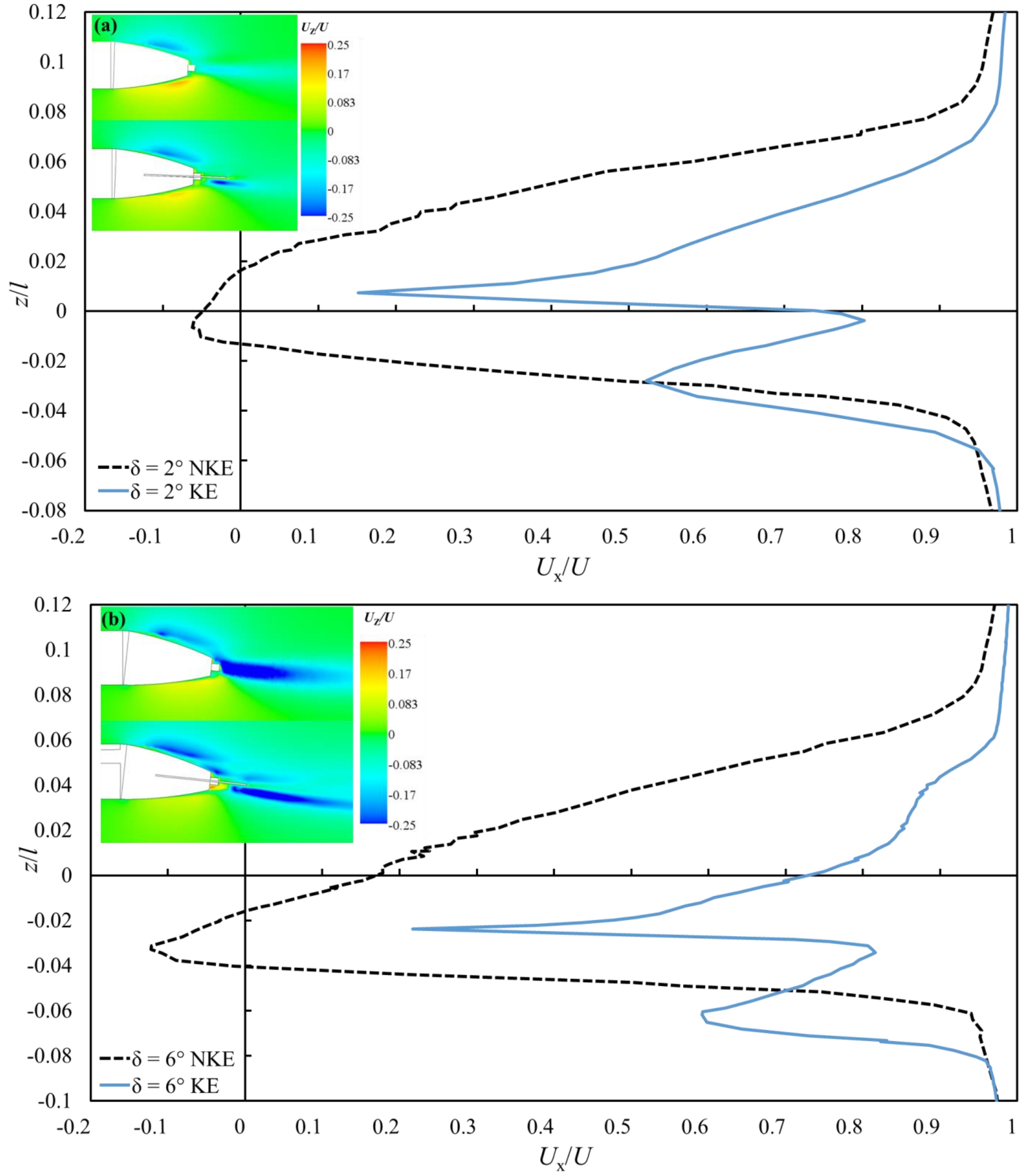

Figure 4.7: Comparison of the normalized streamwise wake velocity profile of (a) δ = 2º and (b) δ = 6º for the B-0-NKE/KE. Inserts show relative vertical velocity contours on the symmetry plane in the wake region.

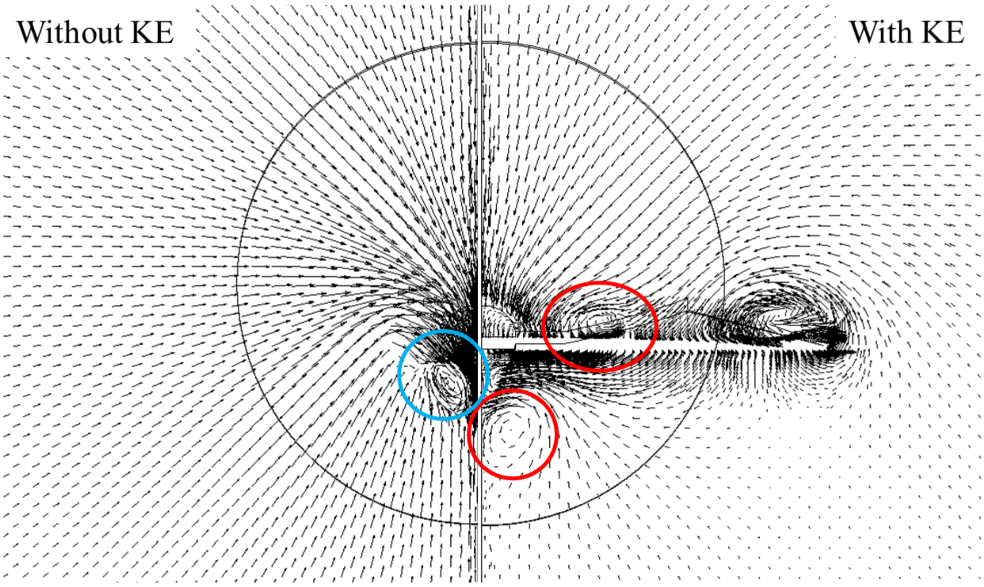

Figure 4.8: The velocity vectors at *x*/*l* = 1.005 for B-0-NKE/KE at δ = 4º with (right) and without (left) KE.

The B-0-KE shows an overall increase in both the NKE and KE cases for $C_{DV,p}$ shown in Figure 4.9a, which was expected from the velocity wake profiles in Figure 4.6 and Figure 4.7. The sharper gradient of the $C_{DV,p}$ in both NKE/KE cases indicates the drag penalty from the separation over the aftbody portion of the B-0-KE.

In Figure 4.9b, when the KE is added, C_L for the body-tail combination increases almost linearly with δ. One can define an average lift slope, $\Delta C_L/\Delta\delta = C_{L,\delta}$ = 4.7/rad. The lift slope, $C_{L,\alpha}$, of a 3D delta wing is $AR\pi/2$, and if the AR for the KE tail is set to be about 1, the expected lift slope is $\pi/2$ = 1.6 /rad. The fact that $C_{L,\delta}$ is approximately 3 times this value indirectly argues for the effect of the tail being non-local, increasing lift on the whole body.

Figure 4.10a and Figure 4.10b show the vertical velocity component U_z/U as a function of the spanwise normalized body radius, y/r, with and without a KE for (a) δ = 0º to 4º and (b) δ = 6º and 8º. At all nonzero δs, the NKE and KE profiles are very different, with a much stronger net downwash for all δs for the KE. A larger downwash peak is observed at the centre of the body for the B-0-NKE compared to the B-0-KE. For the B-0 no specific attention was given to the overall geometry.

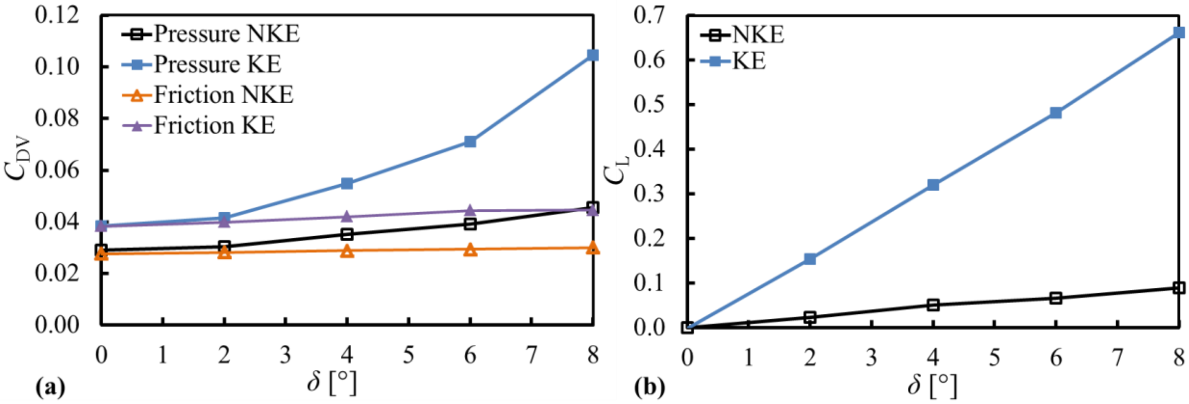

Figure 4.9: (a) $C_{DV,p}$ and $C_{DV,f}$ and (b) C_L for B-0-NKE/KE at different δs.

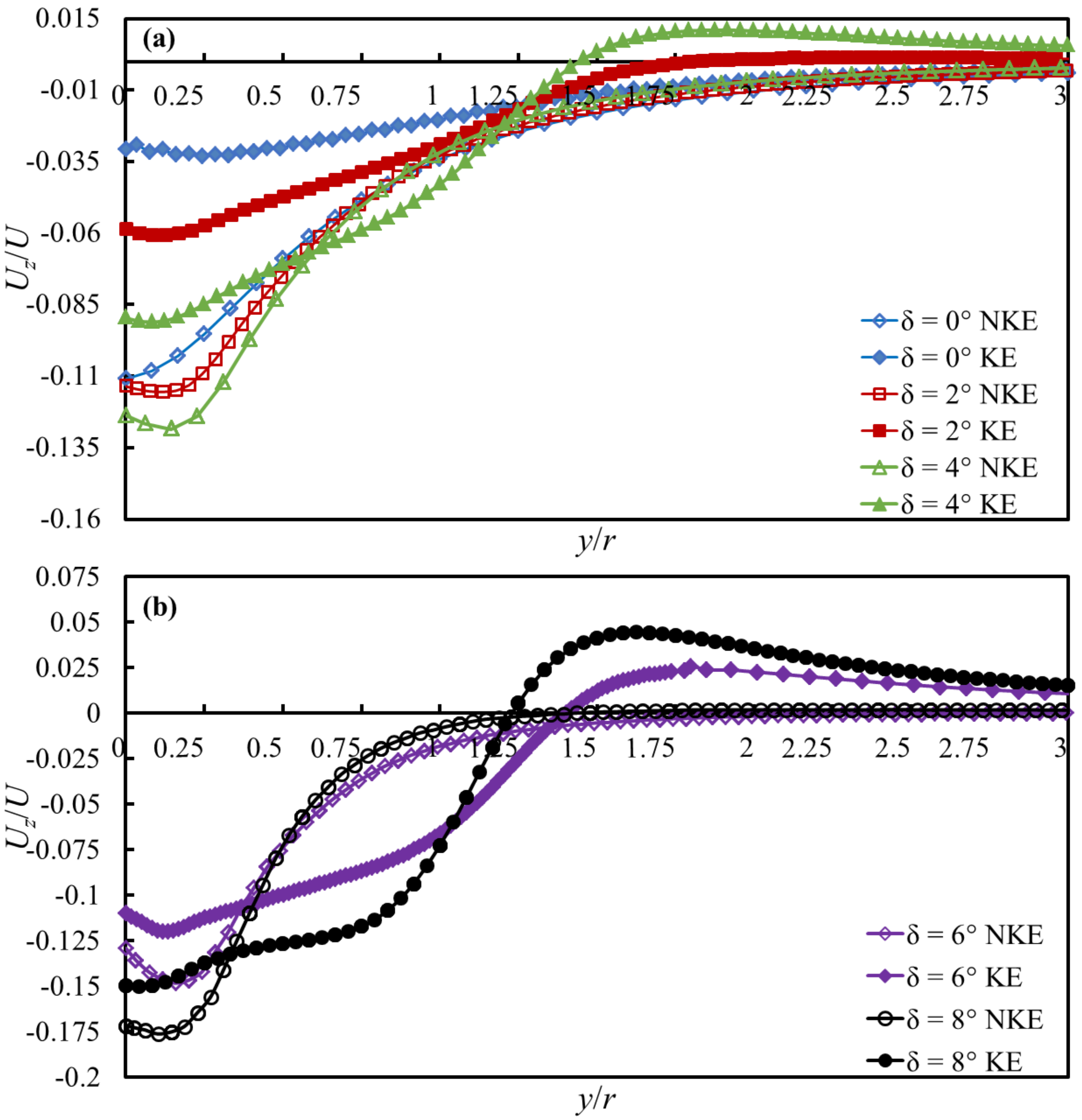

Figure 4.10: Vertical velocity component U_z/U as a function of the spanwise normalized body radius, y/r, at location z/r = 0.7 and x/l = 1.005 without a KE and 1.105 with a KE, for the reference body, (a) δ = 0° to 4° and (b) δ = 6° and 8°.

4.4 The aerodynamic effect of deflected tail plates on low-drag bodies

The pressure distributions along the F-57 LDB for both the NKE/KE conditions at varying aftbody deflection angles, δ, are shown in Figure 4.11a. All the cases are similar over the nose and up to $x/l = 0.57$, after which a separation bubble occurs up to approximately $x/l = 0.6$. This separation bubble is shown in Figure 4.11b with the τ_W over a section of the body ($0.55 < x/l < 0.62$) where a recirculation zone occurs inside a separation bubble for both the KE and NKE. The details of the bubble geometry are sensitive to the numerical stability of the transition model and the prescribed turbulence intensity, but its existence is not unreasonable.

The aftbody deflection point is at $x/l = 0.63$ in Figure 4.11a. Immediately afterwards, $\mathrm{d}P/\mathrm{d}x$ is strongly positive, and C_P changes sign at about $x/l = 0.72$. For NKE, $\mathrm{d}P/\mathrm{d}x$ increases with an increasing δ. The peak amplitude of the positive C_P is much higher for NKE than KE and when

$\delta = 8°$, the KE case has a very shallow plateau (shown by the black solid and dashed lines). The KE starts at $x/l = 0.77$ where it is immediately associated with a reduction in C_P (relative to NKE), and the maximum positive C_P is found further downstream.

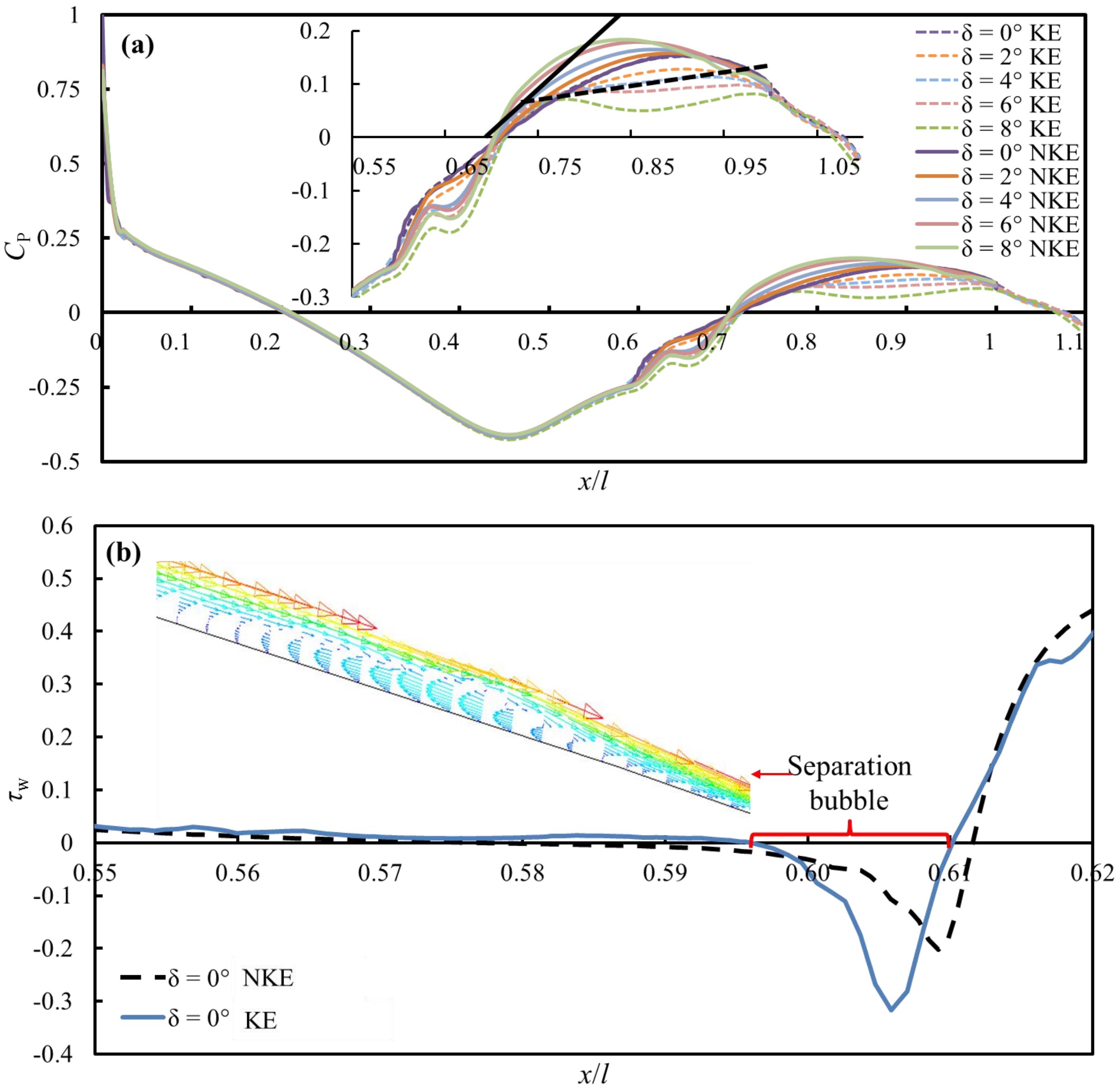

Figure 4.11: (a) Pressure coefficient of the F-57 LDB-NKE/KE at different δs and (b) wall shear stress over the section of the body $0.55 < x/l < 0.62$ with and without the KE at $\delta = 0°$.

Figure 4.12 shows the pressure distribution over the Myring LDB for NKE/KE cases at varying δs. The Myring LDB (at the higher Re) does not have a prominent separation bubble (unlike the F-57 LDB). There is, however, a brief and abrupt pressure drop as the flow accelerates over the aftbody deflection point at $x/l = 0.63$. After this point the KE curves are all lower than the NKE cases for much of $x/l > 0.7$ (as they were for the F-57 in Figure 4.11a). The B-0-KE (Figure 4.5a) has a similar C_P profile compared to the Myring LDB over the nose. However, the fact that the Myring LDB does not have larger negative peaks or variation in C_P over the majority of the body means that it would be an improved body compared to the B-0-KE.

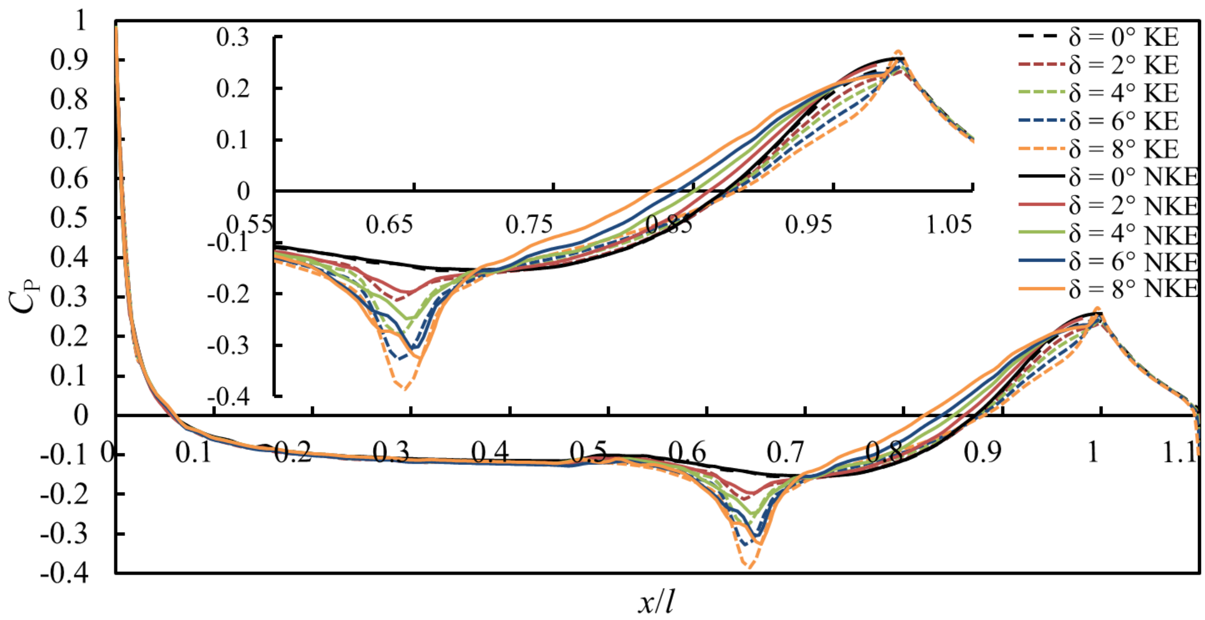

Figure 4.12: Pressure coefficient as a function of dimensionless body length for the Myring LDB-NKE/KE at different *δ*s.

Figure 4.13 shows the normalized streamwise wake velocity profile, U_x/U, for $\delta = 4°$ for (a) F-57 LDB-NKE/KE and (b) Myring LDB-NKE/KE. The Myring LDB-KE has a stronger downward deflection of the wake than the F-57 LDB-KE. Overall the wake deficit for the B-0-NKE/KE is far greater than that of the LDB-NKE/KEs, with the double-lobe profile being more pronounced for the B-0-KE.

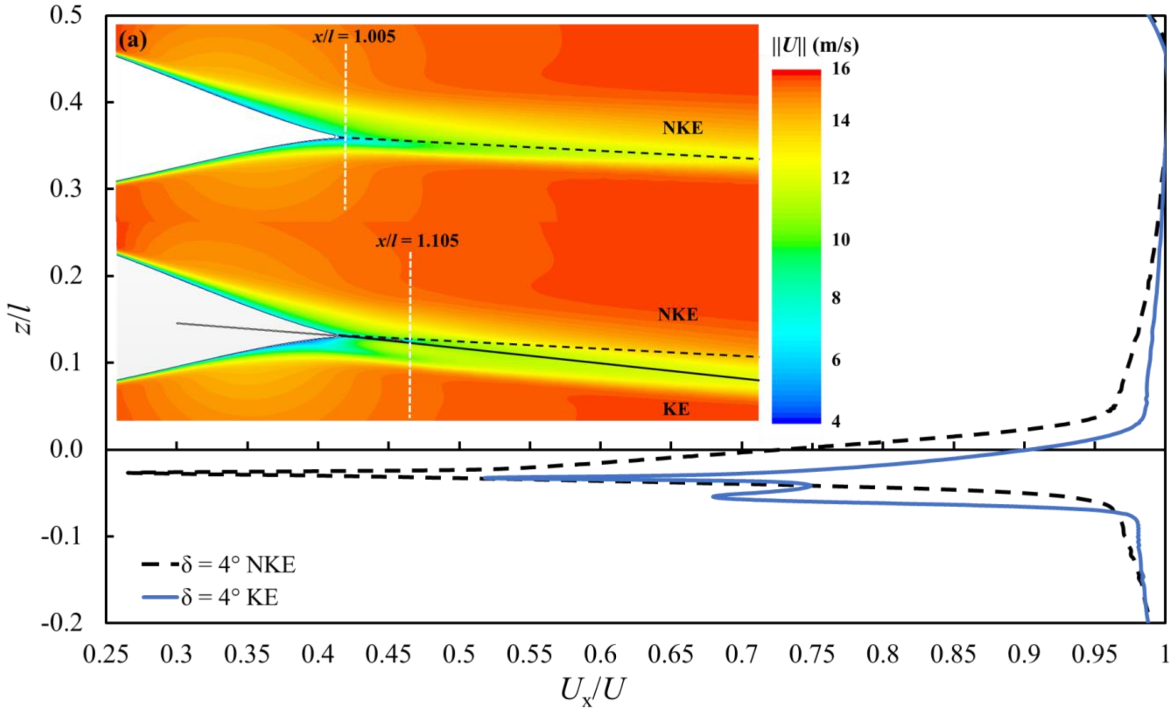

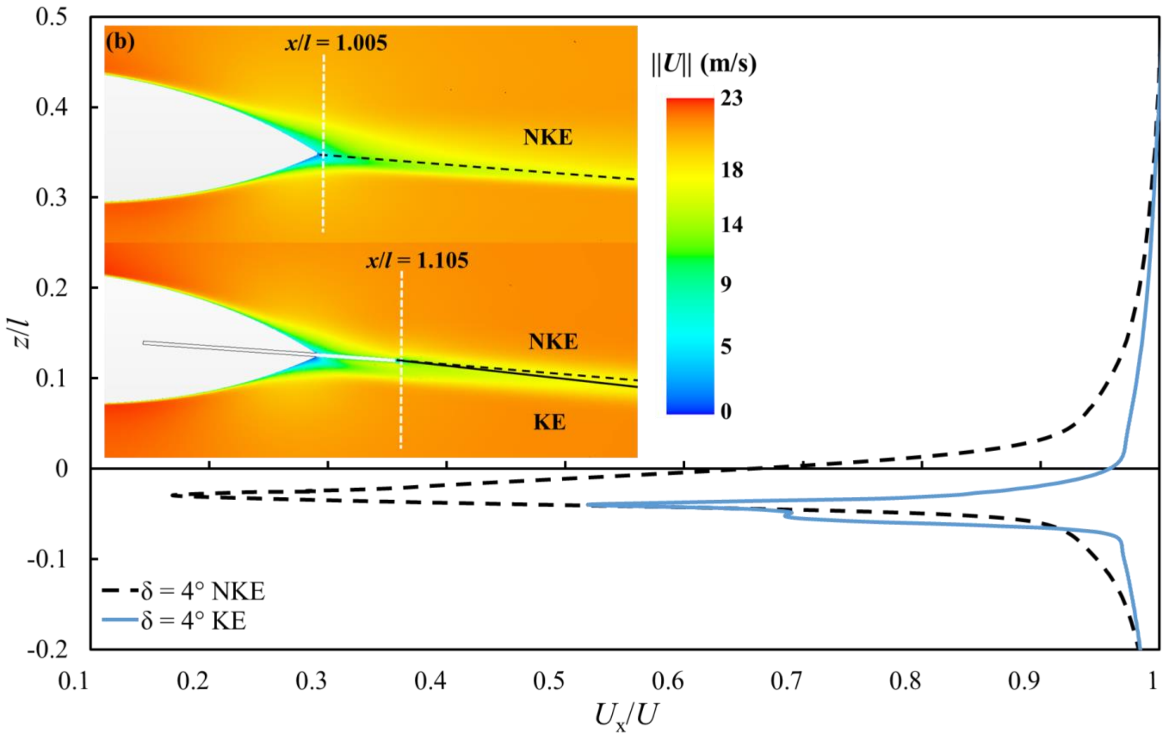

Figure 4.13: Normalized streamwise wake velocity profile at δ = 4º for (a) F-57 LDB-NKE/KE and (b) Myring LDB-NKE/KE. Profiles are taken at x/l = 1.005 for NKE and x/l = 1.105 for KE (0.5% after either the body or the tail ends). Insert shows velocity magnitude contours on the symmetry plane in the wake region.

Figure 4.14a and Figure 4.14b show U_x/U for δ = 2° and 6°, combined with contours of the relative vertical velocity, U_z/U, at the symmetry point of the F-57 LDB with and without a KE. The flow around the F-57 LDB-KE shows a larger vertical deflection over the aftbody than the equivalent NKE. Again, the double-lobe profile is present, but far less pronounced than for the B-0-KE. The B-0-NKE/KE wake velocity profile differences are more significant than for the F-57 LDB-KE. The wake diameter is also markedly thicker than for the F-57 LDB-KE, which would lead to a larger potential lift, but also a larger drag penalty.

In the absence of the KE, the presence of a pressure differential between the upper (low pressure) and lower (high pressure) surface of the body leads to an upward and swirling flow around the aftbody edge as indicated in Figure 4.15. The addition of the KE blocks the upward flow on the body of the LDB and the pressure difference now drives the flow to form a tip vortex on the outer edge of the KE. The blockage of the LDB on-body vortex formation and consequent transverse flow around the KE forms the double-lobe in the velocity profile (Figure 4.14).

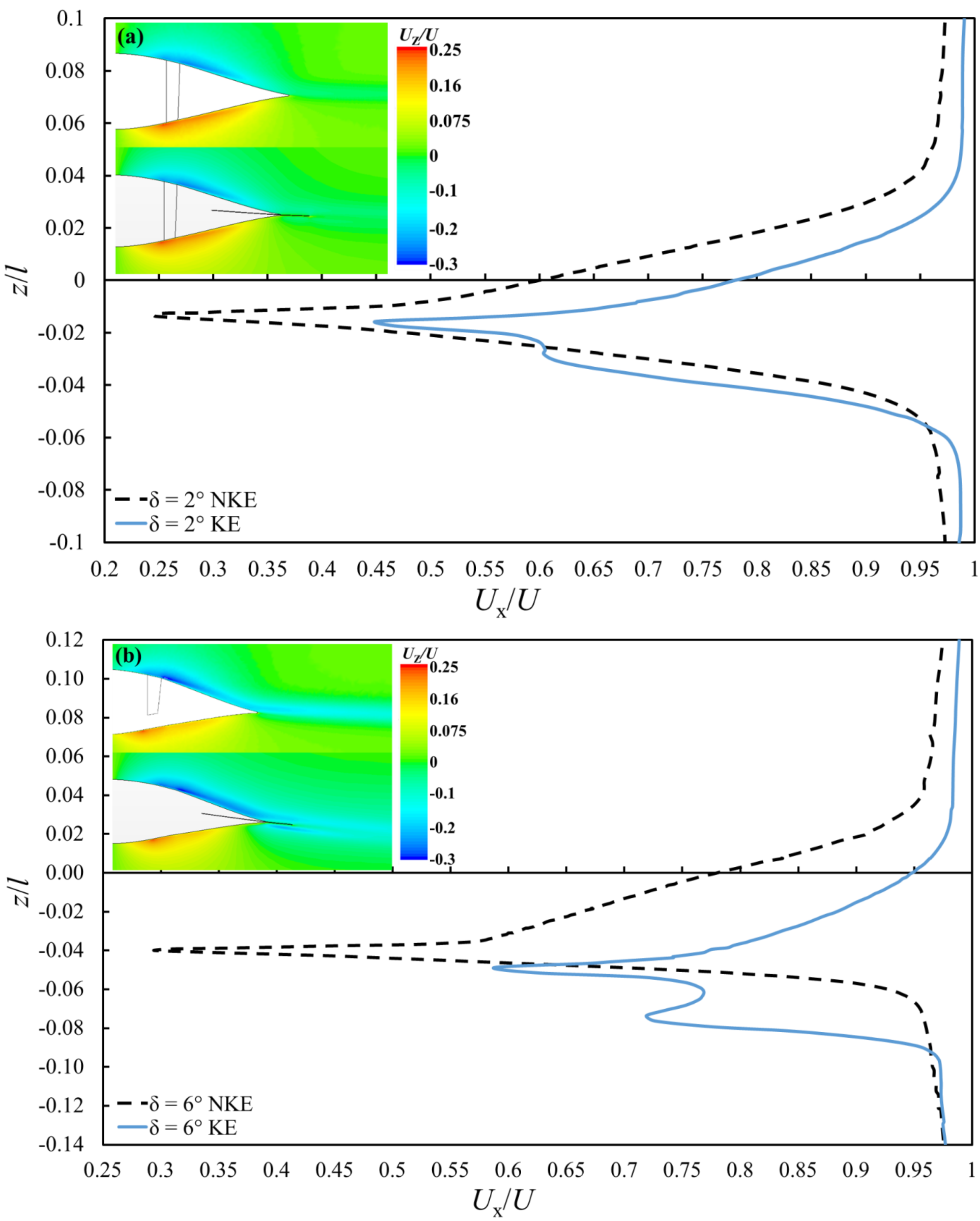

Figure 4.14: Comparison of the normalized streamwise wake velocity profile of (a) δ = 2º and (b) δ = 6º for the F-57 LDB with and without the KE. Inserts show relative vertical velocity contours on the symmetry plane in the wake region.

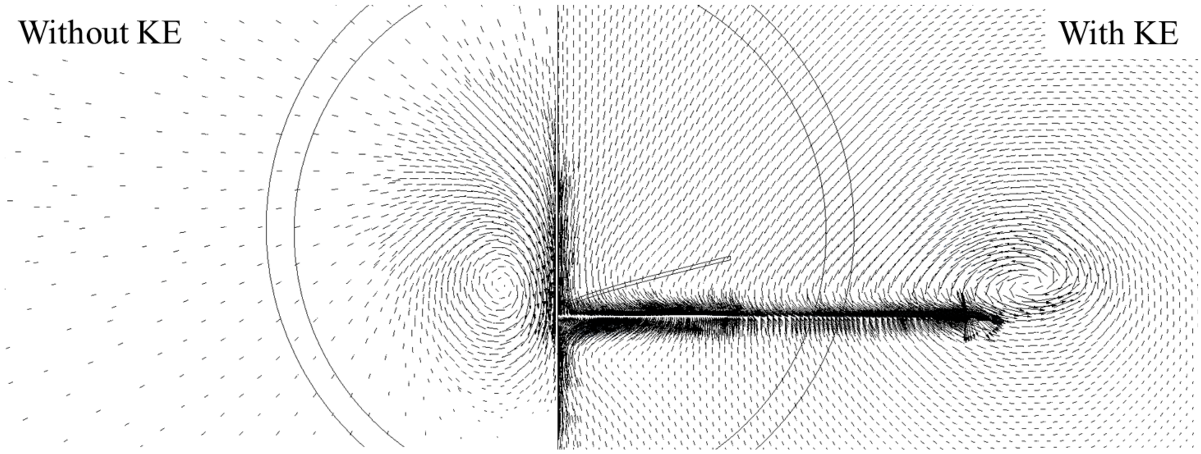

Figure 4.15: The velocity vectors at x/l = 1.005 for F-57 LDB-KE at δ = 4º with (right) and without (left) KE.

Figure 4.16a and Figure 4.16b show that the KE condition is always associated with a greater deflection of the U_x/U profiles, which are nonetheless weaker than the NKE equivalents. Again the addition of the KE leads to a transverse flow over the aftbody to produce the double-lobe velocity profile as with the F-57 LDB. However, the double-lobe is less pronounced for the Myring LDB, a fact that can be traced back to differences in boundary layer development across the aftbody. The Myring LDB was designed with a combination of delay of transition and reduction of adverse pressure over the aftbody, without a large amplitude streamwise variation in pressure (Figure 4.5a and Figure 4.5b). The F-57 LDB was designed only on the condition for delayed transition. The differences in aftbody design criteria lead to differing boundary layer conditions at the LDB-KE interface.

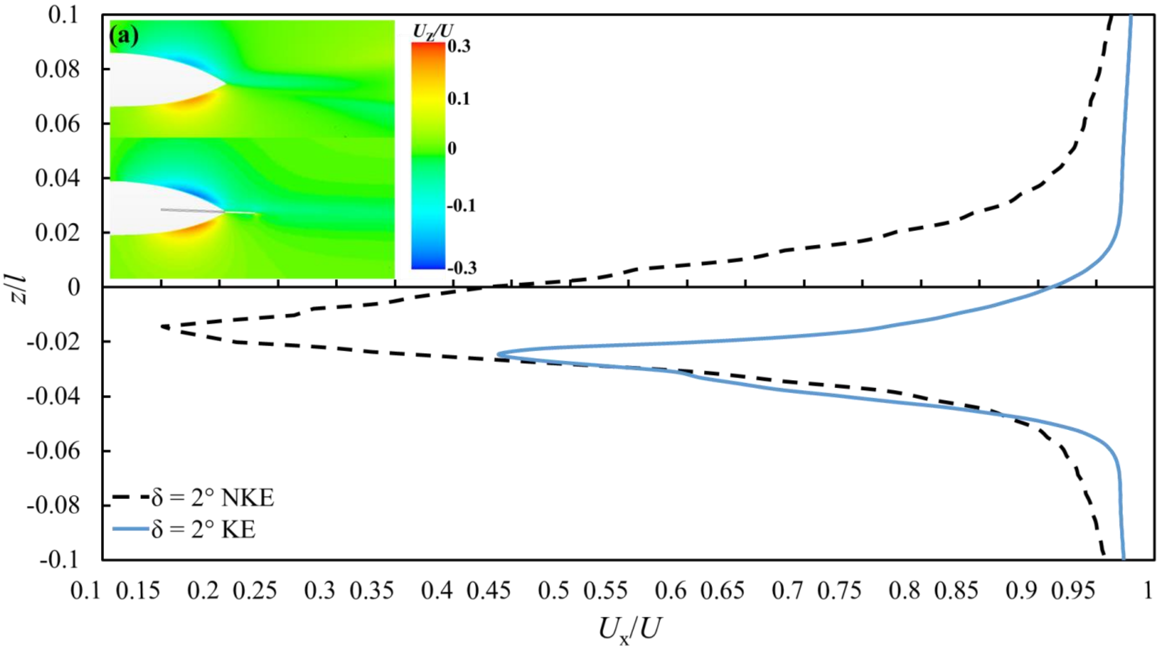

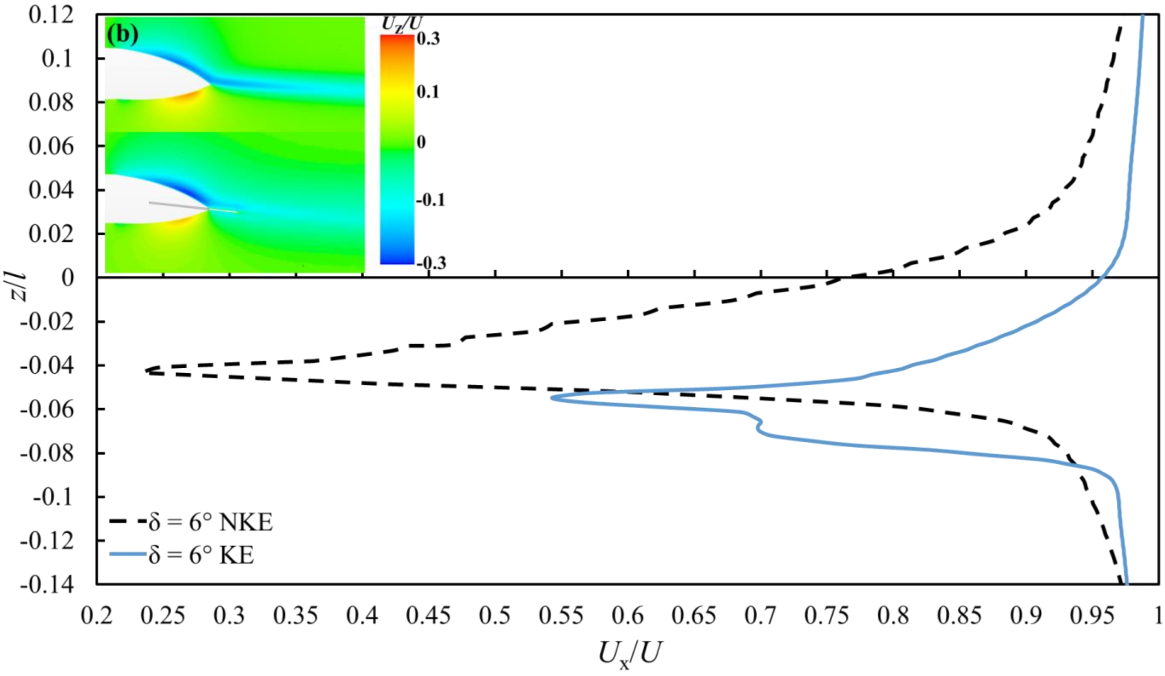

Figure 4.16: Comparison of the normalized streamwise wake velocity profile of (a) δ = 2º and (b) δ = 6º for the Myring LDB with and without the KE. Inserts show relative vertical velocity contours on the symmetry plane in the wake region.

Figure 4.17 shows the profiles of the top and bottom surface boundary layers for the two LDBs with and without the KE, with inserts of velocity vector profiles through the boundary layers over the aftbodies at x/l = 0.99. The boundary layer for the F-57 LDB-KE has a steeper dU/dz than the Myring LDB-KE because of the sharper tapered aftbody geometry and more gradual pressure recovery (Figure 4.5a and Figure 4.5b).

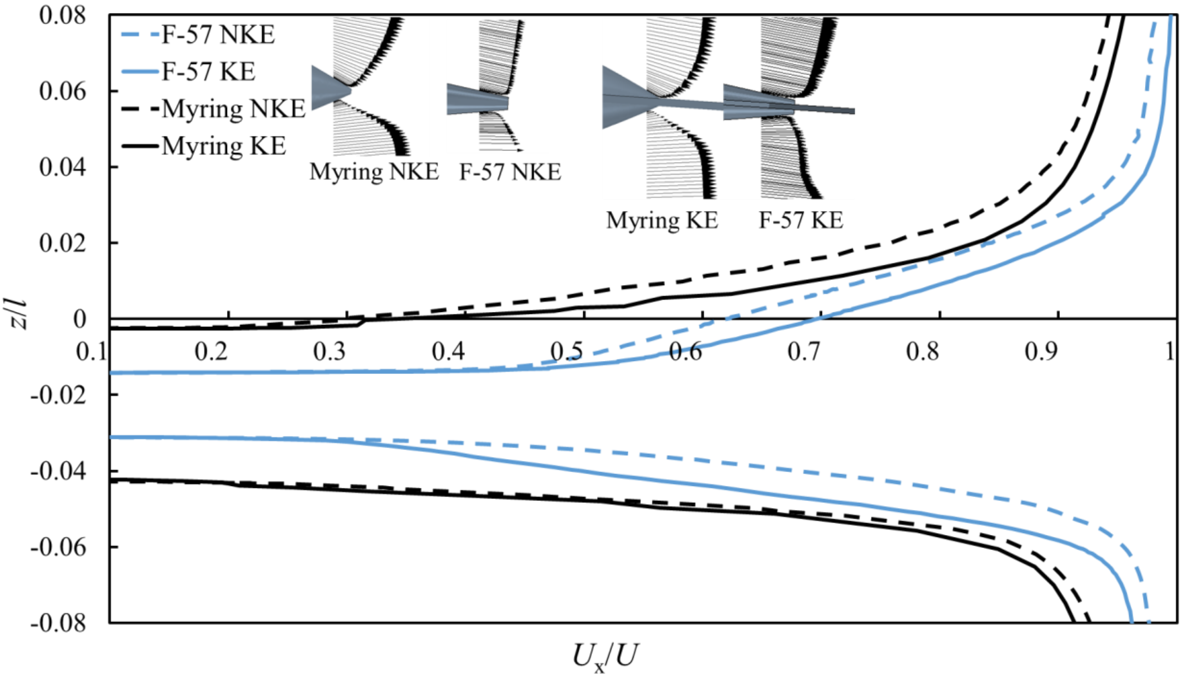

Figure 4.17: Profiles of the top and bottom surface boundary layers for the two LDBs with and without the KE at δ = 4º. Insert shows velocity vectors of the boundary layers over the aftbodies on the symmetry plane at x/l = 0.99.

Figure 4.18 shows that the ΔP for the Myring LDB-KE from $y/r = 0$ to 6 is about twice that of the F-57 LDB-KE under the same conditions. The Myring LDB has a better interaction with the KE owing to the bluffer aftbody geometry and gradual pressure recovery, and the attendant less pronounced double-lobe wake profile (Figure 4.16).

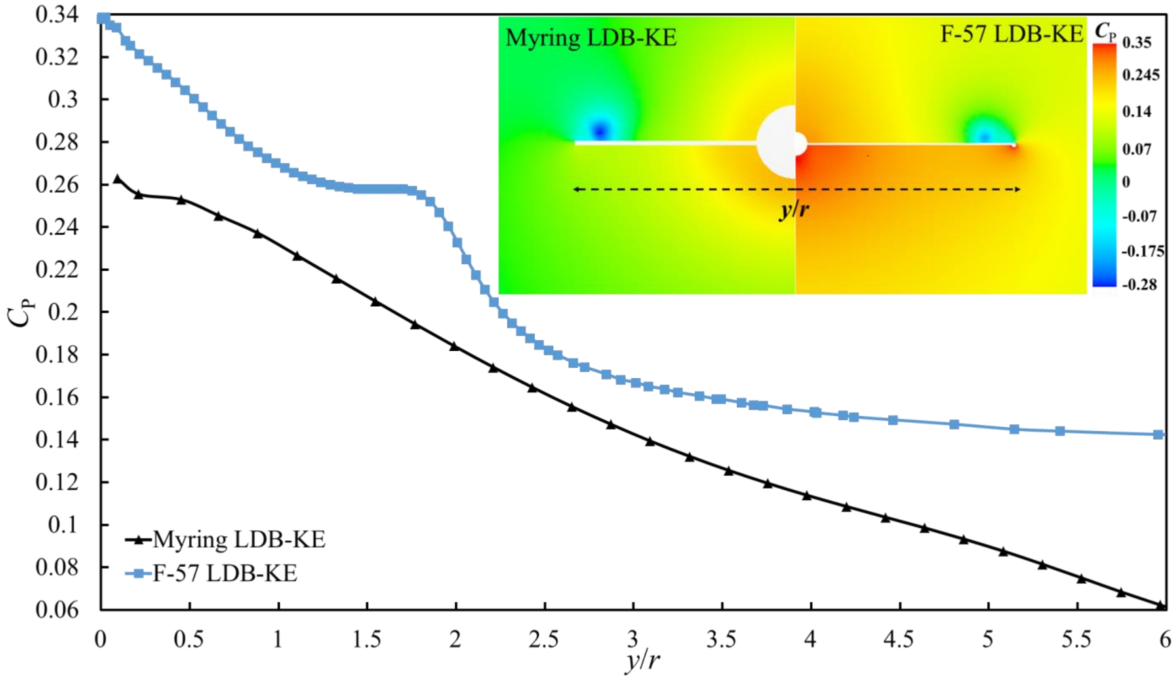

Figure 4.18: C_P at $x/l = 0.96$ for the F-57 and Myring LDB-KE at $\delta = 4°$. Insert shows pressure contours on the cross-stream plane at $x/l = 0.96$.

Figure 4.19a shows that neither the pressure $C_{DV,p}$ nor the friction $C_{DV,f}$ components of C_{DV} for the F-57-NKE vary significantly with δ. However, with KE, $C_{DV,p}$ increases by almost a factor of four from $\delta = 0°$ to $\delta = 8°$. This $C_{DV,p}$ increase is due to the increase in the effective base area when the KE deflects downwards, indicated by the schematic inset of Figure 4.19a. The wake deficits shown in Figures 4.14 and 4.16 also show that as δ increases the defect increases and is deflected downwards more. Although it general it seems like the KE combinations reduce the wake diameter, the three-dimensional wake effects lead to an overall increase in the pressure drag rather than a decrease as the two-dimensional slices in Figures 4.14 and 4.16 would suggest.

In Figure 4.19b, C_L is shown as a function of δ for the F-57 LDB, with and without KE. Without KE, the maximum increase in C_L based on the frontal area is only 3% for the largest $\delta = 8°$. With KE, C_L for the body-tail combination increases almost linearly with δ. The average lift slope for the F-57 LDB-KE is $C_{L,\delta} = 4.3$/rad, which is less than the B-0-KE but still approximately 2.7 times the value of the delta wing alone.

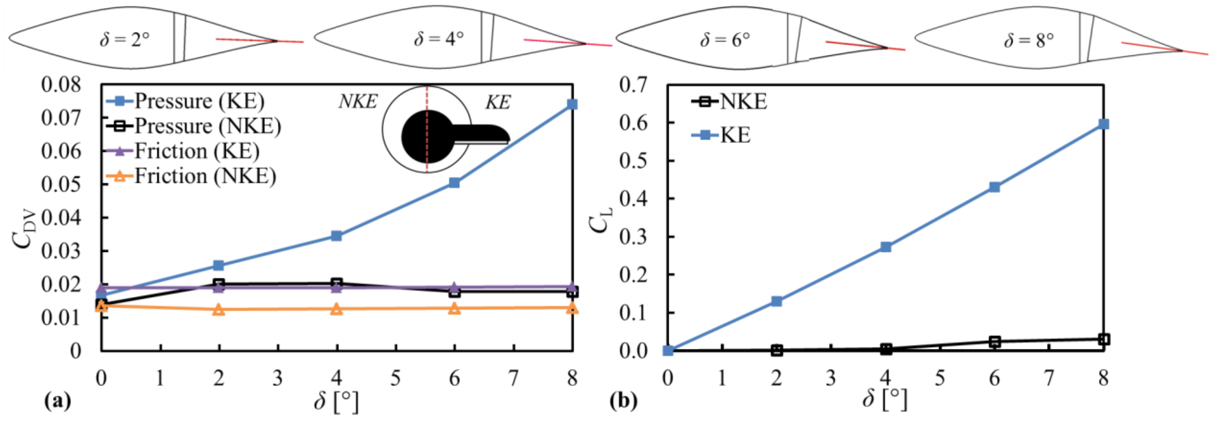

Figure 4.19: (a) Volume-based drag components of pressure and friction and (b) lift coefficients for the F-57 LDB-NKE/KE at different *δ*s. Insert illustrates the effective base area for the NKE and KE.

Figure 4.20a shows $C_{DV,f,p}(\delta)$ for the two NKE/KE configurations. According to Myring (1981), the skin friction drag contributes 90% of the total drag experienced by the unmodified body, Figure 4.20a for the NKE case at $\delta = 0^o$ shows that the $C_{DV,f}$ is approximately 85% of C_{DV}. The Myring LDB and F-57 LDB show similar, and quite large, increases in $C_{DV,f}$ when the KE is added, with little sensitivity to increasing *δ*. The $C_{DV,p}$ for the Myring LDB-KE at $\delta = 0^o$ initially contributes to 33% of the C_{DV} and becomes the leading contribution to C_{DV} after $\delta = 4^o$. By contrast, $C_{DV,p}$ previously shown for the F-57 LDB-KE in Figure 4.19a, initially contributes 45% of the total at $\delta = 0^o$, but then has a sharper increase with *δ*, rising to $C_{DV} = 0.07$ at $\delta = 8^o$, compared with about 0.04 here for the Myring LDB.

The drag penalty from the separation over the aftbody portion of the B-0-KE, is larger than that of the LDB-KEs. The B-0-KE has approximately 58% more $C_{DV,p}$ than the F-57 LDB-KE and 81% more $C_{DV,p}$ than the Myring LDB at $\delta = 0°$.

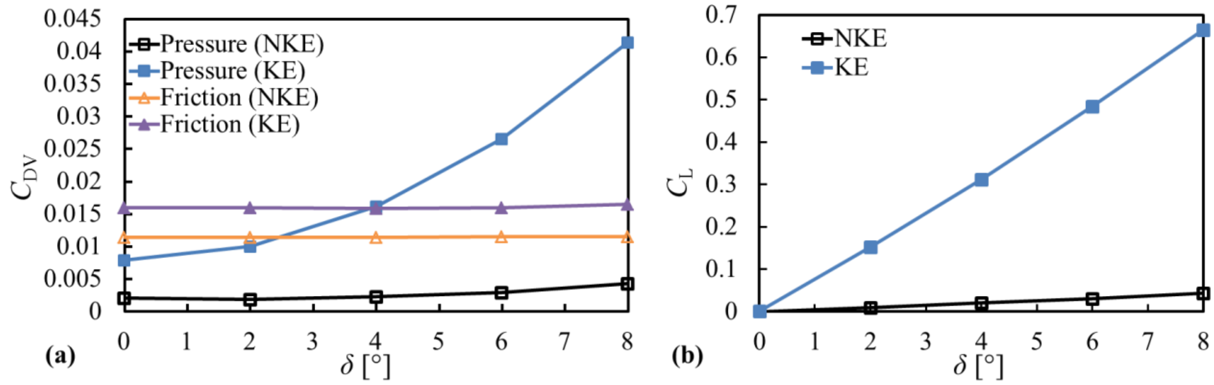

Figure 4.20: (a) $C_{DV,p}$ and $C_{DV,f}$ and (b) C_L for the Myring LDB-NKE/KE at different *δ*s.

The Myring LDB also has a steep increase of C_L with *δ* (Figure 4.20b), with a mean lift slope, $C_{L,\delta} = 4.8$ /rad, which is higher than for the F-57 LDB but close to the 4.7 /rad of the B-0-KE. The mean lift slope of the Myring LDB and the B-0 is very similar, where both have more bluff aftbodies leading to a larger C_L slope, but with the improved geometry of the Myring LDB the C_{DV} reduces by almost 60% compared to the B-0-KE at $\delta = 8°$. The reasons may be traced to the different environments in which the KE is immersed, which come from the differing design emphases.

The different conditions can be seen in the contours of skin friction distribution on the upper and lower KE surfaces for the two bodies (Figure 4.21). If one sets a threshold, C_f, at the expected flat plate boundary layer value for the inlet conditions onto the KE for both, then a central wake can be distinguished from an exterior region that has much higher C_f fluctuation amplitudes, and might be imagined to be exposed to freestream conditions. More of the outboard surface of the F-57 LDB-KE is exposed to freestream conditions than the Myring LDB. If the desired effect of the KE is to modify streamlines that have passed over the body, then the larger wake influence of the Myring body might be preferred. Since the KE is already immersed in a low-speed wake, the smaller increase in C_{DV} may also be both preferred and expected.

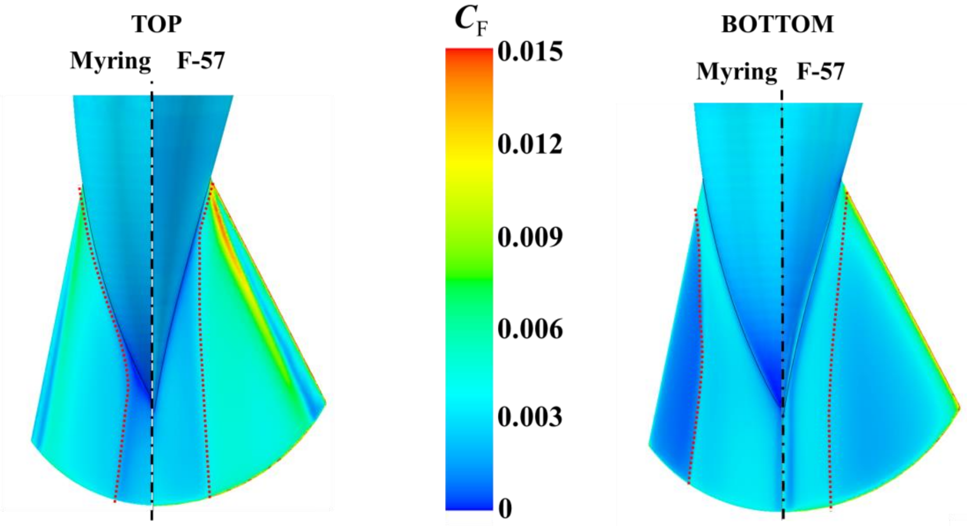

Figure 4.21: Skin friction coefficients on the top and bottom surface of the KE for the F-57 and Myring LDB-KE at $\delta = 4°$. Dashed lines show the wake edge on the body surface.

Figure 4.22 shows U_z/U as a function of y/r for (a, b) F-57 LDB-NKE/KE and (c, d) Myring LDB-NKE/KE at similar location to the B-0-NKE/KE in Figure 4.10. The maximum body diameter is at $y/r = 1$ and the KE ends at approximately $y/r = 1.45$. The downwash profiles at $\delta = 0^o$ (Figure 4.24a) aft of the body are indistinguishable for NKE and KE, as one might expect. As δ increases to 4^o, the KE leaves a much stronger and broader downwash signature.

With further increases in δ (Figure 4.22b,d), although the centreline value of U_z may be similar between KE and NKE, the spanwise region that is influenced is more extensive in the KE condition. The KE case at a high δ is associated with significant upwash for $y/r > 1.1$, and the net integrated downwash increment (and hence lift) might be expected to be smaller, based on this observation alone. One may again be able to infer that the lift is determined to a large extent by the global influence of deflected streamlines over the entire body, and not just localised at the tail.

The B-0-NKE/KE has greater downwash peaks compared to the LDB-NKE/KEs, this is attributed to the greater wake diameter to body diameter ratio of the B-0-NKE/KE (Figure 4.7) and also has the consequence of a larger drag penalty shown in Figure 4.9.

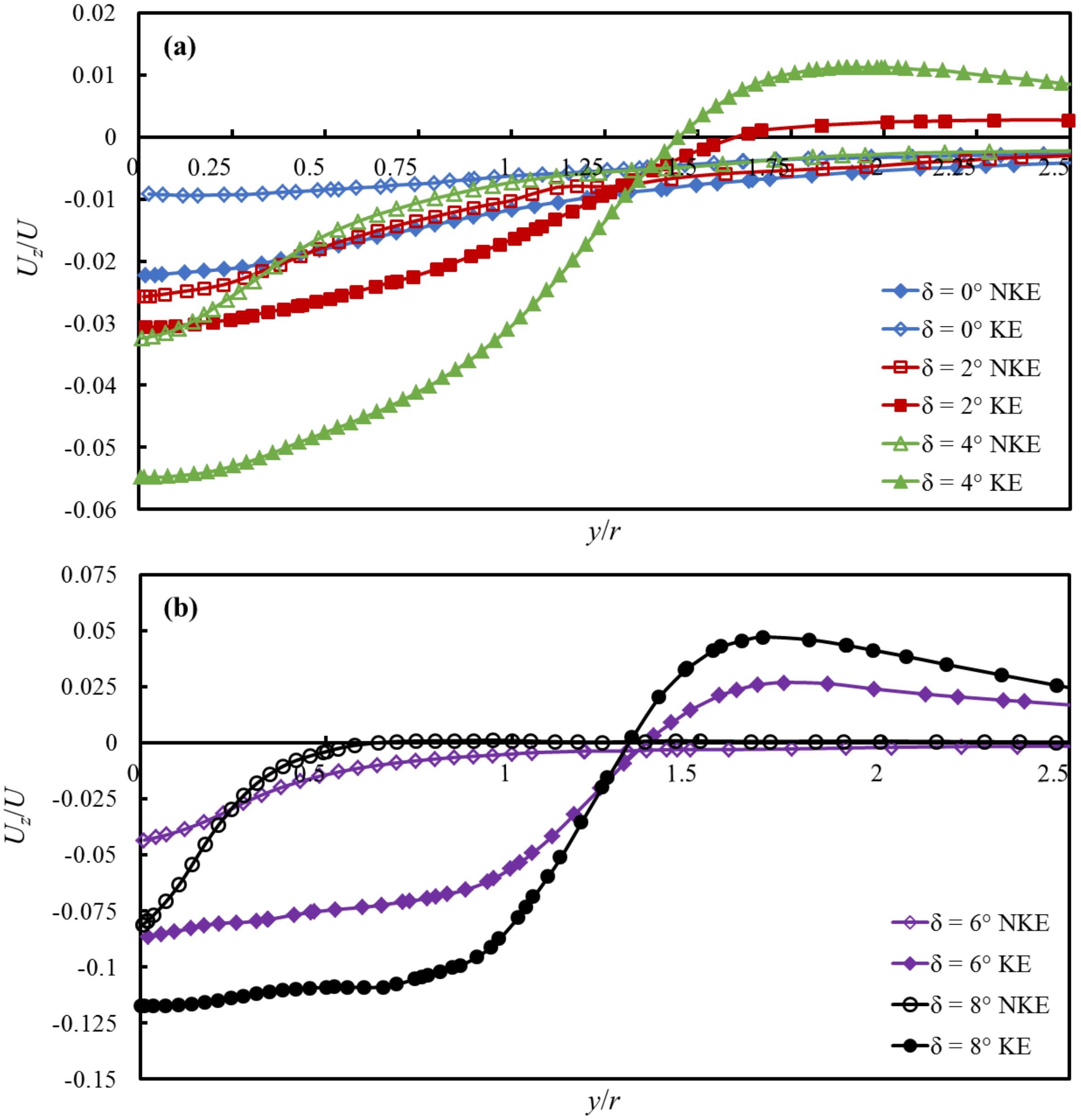
(a)
0.02
0.01
0
-0.01
-0.02
-0.03
-0.04
-0.05
-0.06
0
0.25
0.5
0.75
1
1.25
1.5
1.75
2
2.25
2.5
U_z/U
y/r
δ = 0° NKE
δ = 0° KE
δ = 2° NKE
δ = 2° KE
δ = 4° NKE
δ = 4° KE
(b)
0.075
0.05
0.025
0
-0.025
-0.05
-0.075
-0.1
-0.125
-0.15
0
0.5
1
1.5
2
2.5
U_z/U
y/r
δ = 6° NKE
δ = 6° KE
δ = 8° NKE
δ = 8° KE

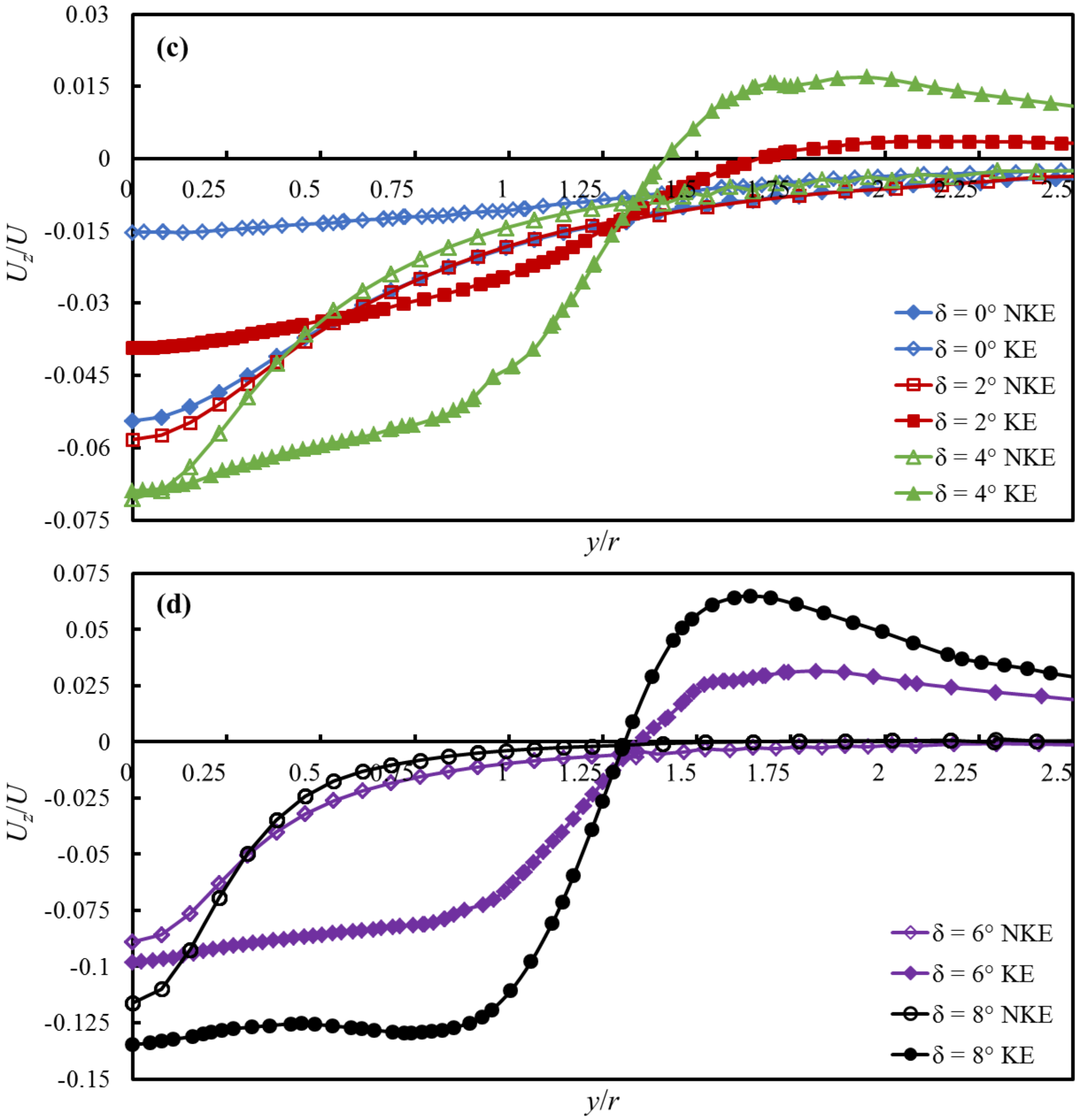

Figure 4.22: Vertical velocity component U_z/U as a function of spanwise normalized body radius, y/r, at location x/l = 1.005 without a KE and 1.105 with a KE, for the F-57 LDB (a) δ = 0° to 4° and (b) δ = 6° and 8° and for the Myring LDB, (c) δ = 0° to 4° and (d) δ = 6° and 8°.

The KE influence for the three bodies are compared for δ = 4° in Figure 4.23. The Myring LDB-KE has much larger positive and negative peaks in U_z compared to the F-57 LDB-KE, which nevertheless leads to it having a larger $C_{L,\delta}$ (compare Figures 4.22a and c). The B-0-KE shows a larger negative peak and slightly lower positive peak, leading to a slightly lower $C_{L,\delta}$ (see Figure 4.10a).

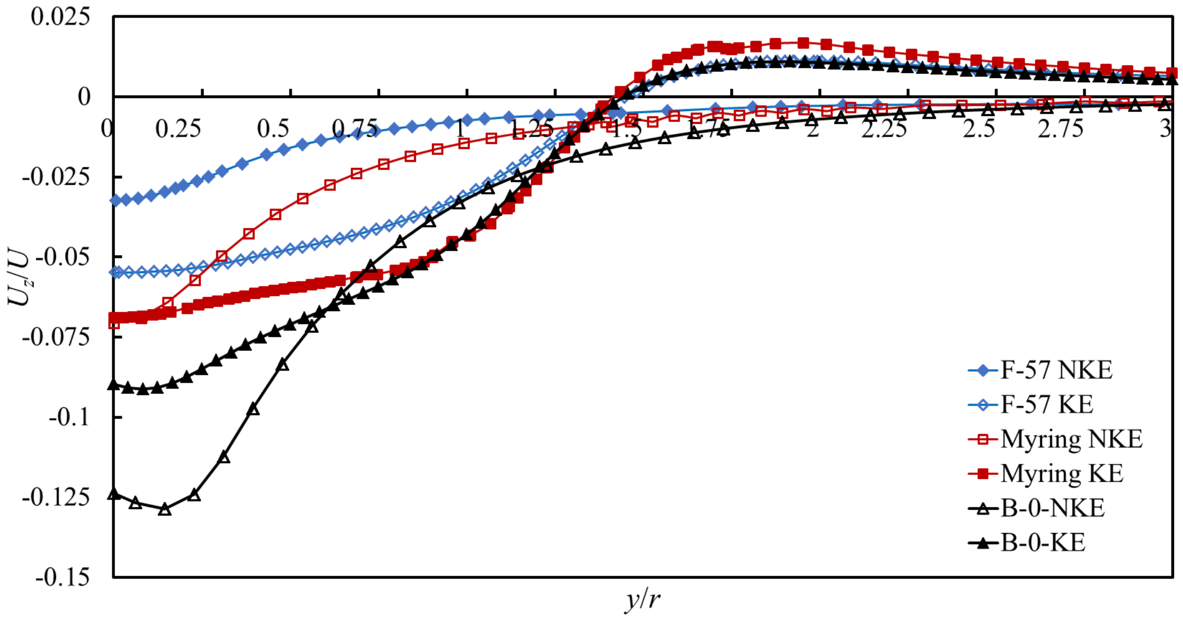

Figure 4.23: Comparison of U_z/U as a function of y/r, for the F-57 LDB, Myring LDB and B-0-NKE/KE at δ = 4°.

Figure 4.24 shows $L/D\,(\delta)$ for both LDBs and the B-0. L/D is about 3 to 4 times higher for the KE than for the NKE for all bodies. If L/D is a performance objective, then it is much better to have a deflector plate than to simply camber the body itself at this Re. At all δ, the Myring LDB has superior L/D, for -either KE or NKE condition.

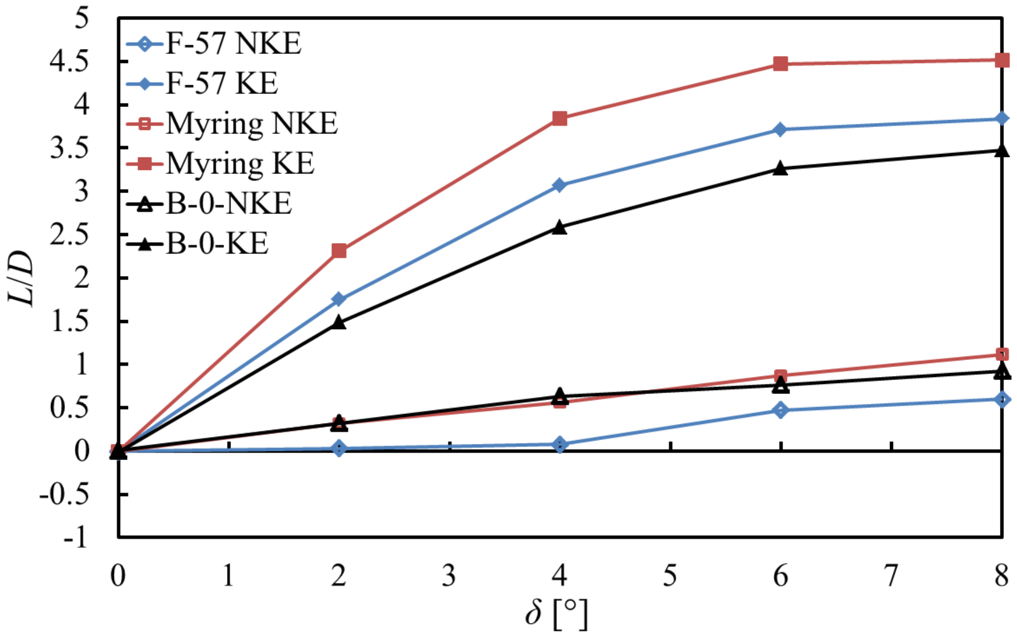

Figure 4.24: The efficiency, L/D for the F-57 and Myring's LDBs and B-0-NKE/KE at different δs.

4.5 Effectiveness of the Kutta edge to provide lift

In order to predict the effectiveness of the KE in combination with a body to provide lift, the SBT was used, as described in Section 2.4.5. Interference factors can be quantified between the body and the KE in order to provide guidelines in terms of the KE geometry.

For all three cases, $A_{\mathrm{KE,mod}} = 0.63A_{\mathrm{KE}}$ and the remaining geometric values are shown in Table 4.1. The r/S_{m} values are all similar as per the definition in Section 2.4.5, where the tail geometries were kept proportionally similar to evaluate the effect of the body-tail combinations.

Table 4.1: Geometric properties for the B-0-KE, F-57 and Myring LDB-KE

	B-0-KE	**F-57 LDB-KE**	**Myring LDB-KE**
r/S_{m}	0.7	0.7	0.7
$r_{\mathrm{mod}}/S_{\mathrm{m,mod}}$	0.73	0.49	0.63
Λ_0	75	52.5	78
AR	1.07	1.84	1.47
AR_{mod}	0.57	1.05	0.88

Figure 4.25 shows CFD results for $(\partial C_L/\partial\delta)_C$ compared to the predicted values for the three different methods, SM, SBT and $\mathrm{SBT_{mod}}$ (slender-body theory using the equivalent geometric definition), as well as an inserted table of the overall results of increasing aftbody-KE deflection angles for the B-0-KE. SM shows the closest match to the CFD results to predict C_L with an average difference of less than 3% for $(\partial C_L/\partial\delta)_C$. The SBT method as well as the $\mathrm{SBT_{mod}}$ over-predicts the $K_{\mathrm{KE(B)}}$. The SBT method over-predicts $K_{\mathrm{B(KE)}}$ expecting more lift carry-over from the KE to the aftbody. The $\mathrm{SBT_{mod}}$ expects slightly less carry-over, but gives a far better estimation.

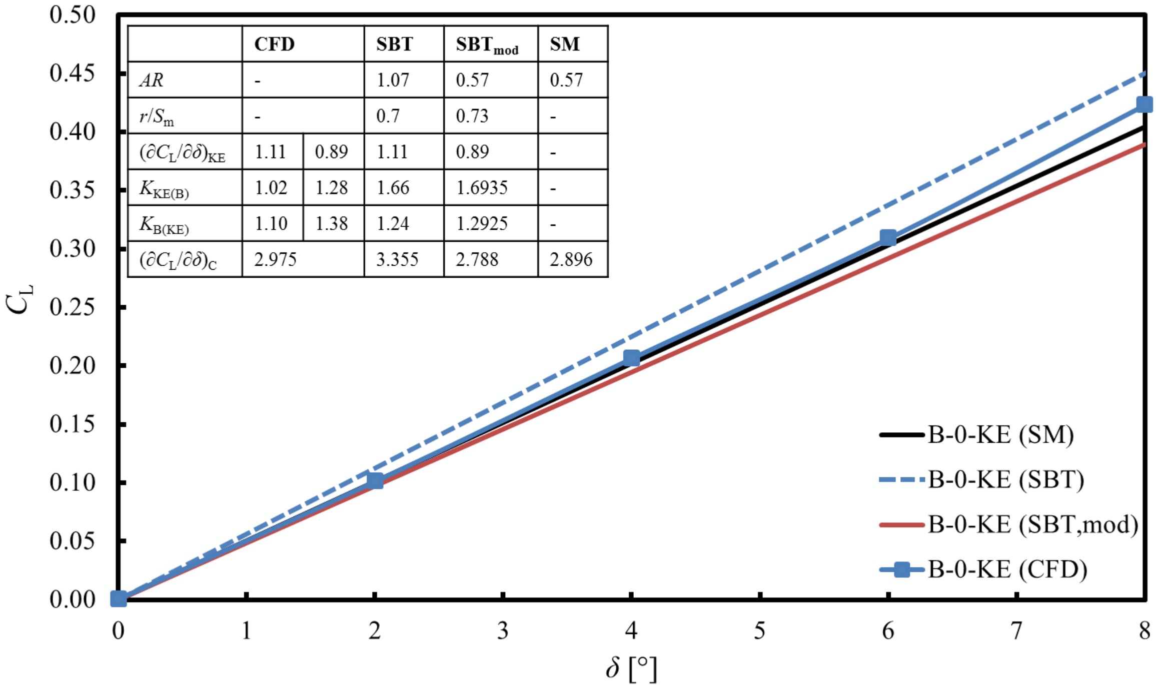

	CFD		**SBT**	**$\mathrm{SBT_{mod}}$**	**SM**
AR	-		1.07	0.57	0.57
r/S_{m}	-		0.7	0.73	-
$(\partial C_L/\partial\delta)_{\mathrm{KE}}$	1.11	0.89	1.11	0.89	-
$K_{\mathrm{KE(B)}}$	1.02	1.28	1.66	1.6935	-
$K_{\mathrm{B(KE)}}$	1.10	1.38	1.24	1.2925	-
$(\partial C_L/\partial\delta)_C$	2.975		3.355	2.788	2.896

Figure 4.25: Estimation of C_L for the B-0-KE combination using the SM, SBT and $\mathrm{SBT_{mod}}$ method in comparison to the predicted CFD results.

Figure 4.26 shows the C_L results for the different approaches with increasing aftbody-KE deflection angles for the F-57 LDB-KE. The F-57 LDB has a sharp nose and tail section, which would mean that the SM method assumption that the nose and front part of the body can be assumed to be a cylindrical body will lead to an inaccurate prediction of the lift over the nose.

Also, the sharp tail section leading into the KE, the values for the body aiding the KE in terms of lift and the lift carried over by the KE onto the body are much less than the theoretical models predict.

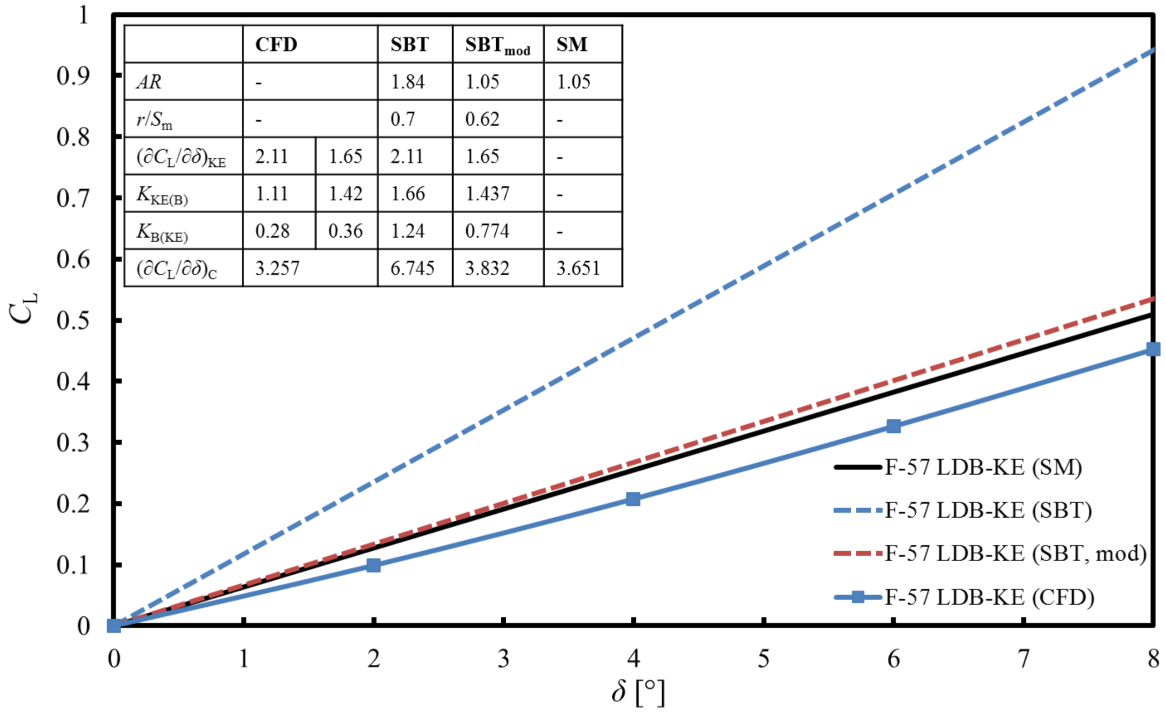

	CFD		**SBT**	**SBT$_{\text{mod}}$**	**SM**
AR	-		1.84	1.05	1.05
r/S_m	-		0.7	0.62	-
$(\partial C_L/\partial \delta)_{KE}$	2.11	1.65	2.11	1.65	-
$K_{KE(B)}$	1.11	1.42	1.66	1.437	-
$K_{B(KE)}$	0.28	0.36	1.24	0.774	-
$(\partial C_L/\partial \delta)_C$	3.257		6.745	3.832	3.651

Figure 4.26: Estimation of C_L for the F-57 LDB-KE combination using the SM, SBT and SBT$_{\text{mod}}$ method in comparison to the predicted CFD results. Table insert shows the values to calculate the $(\partial C_L/\partial \delta)_C$.

The Myring LDB-KE combination has the highest C_L slope for increasing δ, shown in Figure 4.27. Again, SM shows the closest match to the CFD results with an average difference of less than 1.5% for $(\partial C_L/\partial \delta)_C$. Again, the expected upwash predicted by the SBT from the body adding to the lift of the KE is greater than the simulation results. When the geometry is adjusted for SBT$_{\text{mod}}$ there is a much closer estimation for the contribution of lift. In terms of the carry-over lift of the KE onto the aftbody, $K_{B(KE)}$ is under-predicted with both SBT and SBT$_{\text{mod}}$ indicating that the body is providing a larger portion of the lift than expected.

Overall, the SM method seems to be able to predict $(\partial C_L/\partial \delta)_C$ reasonably well with bodies that do not have a large continuous cross-sectional variation like the F-57 LDB. However, as a measure of effectiveness of the body-tail combination, the SBT$_{\text{mod}}$ allows a means to indicate the estimated percentage of lift contributed by the aftbody to the KE, as well as the amount of carry-over lift the body contributes to the KE.

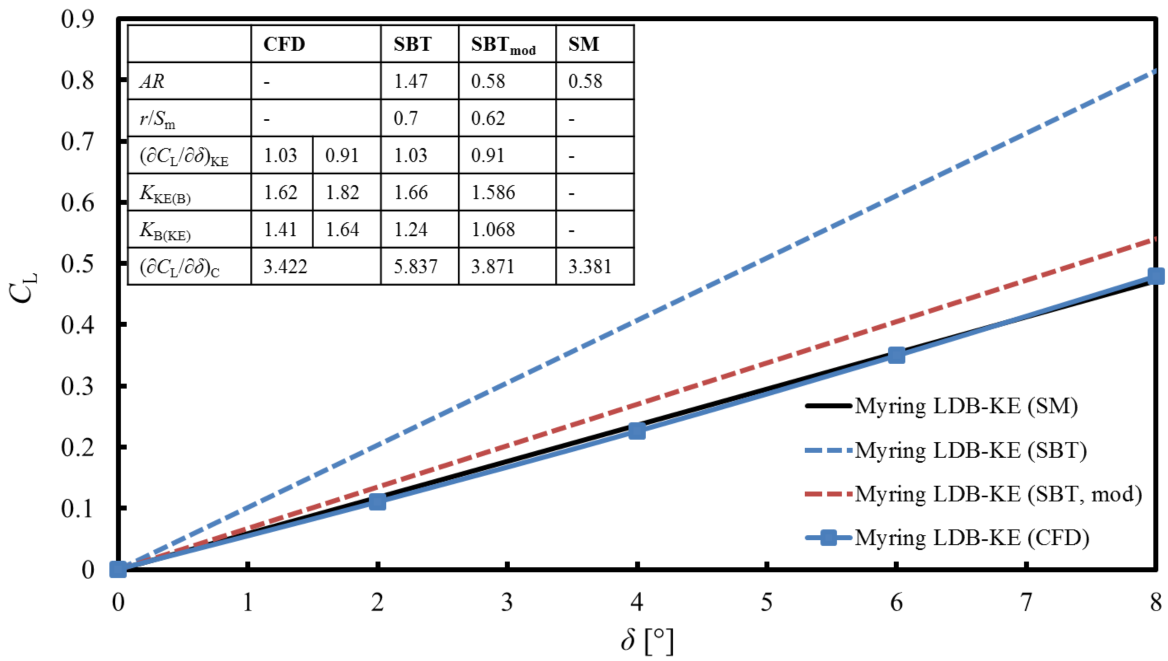

	CFD		SBT	SBT_{mod}	SM
AR	-		1.47	0.58	0.58
r/S_m	-		0.7	0.62	-
$(\partial C_L/\partial \delta)_{KE}$	1.03	0.91	1.03	0.91	-
$K_{KE(B)}$	1.62	1.82	1.66	1.586	-
$K_{B(KE)}$	1.41	1.64	1.24	1.068	-
$(\partial C_L/\partial \delta)_C$	3.422		5.837	3.871	3.381

Figure 4.27: Estimation of C_L for the Myring LDB-KE combination using the SM, SBT and SBT_{mod} method in comparison to the predicted CFD results.

In terms of KE effectiveness, the Myring LDB-KE was found to be the best combination based on $K_{KE(B)}$ and $K_{B(KE)}$ with more than 80% contribution from the body upwash to lift on the KE and more than 60% carry-over lift supported by the aftbody from the KE. The B-0-KE had the worst combination in terms of contribution of the aftbody upwash to the KE, providing less than 30% additional lift, due to the separation over the aftbody as discussed in Section 4.3.3. The F-57 LDB-KE has the worst carry-over lift from the KE, primarily due to the fact that such a small ratio of the body is actually part of the KE due to the sharp aftbody taper.

4.6 Summary, conclusions and recommendations on the function of the KE

RANS simulations were conducted for two LDBs and compared with theoretical and experimental literature, as well as the B-0 used in Huyssen *et al*. (2012) and Davis and Spedding (2015). The comparisons were close enough to encourage the subsequent testing of novel body-tail combinations, where the B-0, F-57 LDB and Myring LDB shapes were combined with a deflected tail plate (termed a Kutta edge, from its design objective to manipulate a trailing Kutta edge condition). The configurations were thus B-0-KE/NKE, F-57 LDB-KE/NKE and Myring LDB-KE/NKE. In all cases, the plate deflection was achieved by deflecting the entire aftbody, so a deflection angle, δ, describes both the plate and aftbody deflection.

Lift can be supported on a body simply by adding camber to the body of revolution. This strategy, combined with a trailing-edge tail/plate yields quite significant performance benefits. In summary, the Myring LDB seems to adhere to the main principles of an ideal body-tail combination. The highest lift contribution was attributed to the fact that the aftbody was designed to be bluff, as well as the fact that the KE stays within the wake of the body fairly well. Overall, there was also a reduction in the drag contribution due to the geometry of the Myring LDB, which had no separation over the aftbody like the other two bodies. Finally, in terms of the effective use of the body-tail combination, the Myring LDB-KE offers the lowest interference factor between the two parts, allowing for a beneficial interaction between the body and the KE.

The flow around all three bodies showed a larger vertical deflection over the aftbody than the equivalent NKE as δ increases. The Myring LDB had the best overall performance when fitted with a KE, explained by the boundary layer development across the aftbody. The Myring LDB was designed for delayed transition and a gradual pressure recovery over the aftbody, whereas the F-57 LDB was only designed for delayed transition and the B-0-KE was merely fitted with a truncated cone as the aftbody.

Simple deflection of the aftbody provided camber and so, predictably, increases lift in all cases, even with no tail. This lift increase was greatly enhanced with the addition of the KE, and the average lift slope of the Myring LDB-KE was higher than for the F-57 LDB-KE and the B-0-KE. In all cases, the lift was significantly greater than that of a delta wing alone, which indicates that the effect of the tail is non-local and increases the lift over the whole body-tail combination.

The B-0-KE and Myring LDB-KE had the largest potential to provide lift (since both aftbodies were quite bluff), with which a larger drag penalty was associated (as the effective base area increases). However, the Myring LDB had approximately 81–60% less C_{DV} as the δ increased, compared to the B-0-KE. The multiple separation and reattachment areas on the B-0-KE aftbody led to a larger drag penalty, as well as lower Re environments in which the KE was immersed, meaning that the flow was more sensitive to the non-optimal aftbody design of the B-0-KE. Although the F-57 LDB-KE had a smaller lift slope, the drag penalty was equally high, again due to separation over the aftbody, but also because the outboard surface KE was more exposed to freestream conditions compared to the Myring LDB-KE.

As a measure of effective use of the KE, the SBT with a modified geometric description gives a fairly reliable means to estimate the percentage of lift contributed by the aftbody to the KE, as well as the amount of carry-over lift the body contributes to the KE. Both the F-57 LDB-KE and the B-0-KE were less effective than the Myring LDB, but for different reasons. The definitions used by the SBT indicated that the B-0-KE was largely ineffective due to the amount of separation over the aftbody, leaving the KE within the viscous wake without the ability to control circulation. The F-57 LDB also tapered too sharply towards the KE, indicating that the body and KE work as separate units with an accumulated penalty.

It appears that the width of the KE, relative to the LDB geometry, influences the overall efficiency of the LDB-KE configuration. Therefore, it is recommended that the aftbody and tail geometry be designed as a continuous unit and not in isolation, on the condition that the KE should be located entirely within the bounds of the viscous wake. This maximises the favourable manipulation of streamlines over the preceding body contours, while minimising the drag penalty of being exposed to the freestream.

5. WING-BODY-TAIL CONFIGURATION

5.1 Introduction

The purpose of the study done in Chapter 3 was to provide confidence in the numerical simulation domain for a basic wing (NACA0012) and body in order to expand to a more complex WBT configuration. Previous investigations were only experimental studies (Huyssen *et al*., 2012; Davis and Spedding, 2015) and initial CFD investigations on the WBT were reported in Smith *et al*. (2016). The specific influence of the wing, body and tail could not be determined by only regarding the global flow-field.

Two LDBs with aftbody deflections and a short KE tail were numerically investigated to determine the nature of the KE and body interactions in Chapter 4 without adding the NACA0012. Therefore, it is the purpose of this chapter to investigate the LDB-KE when fitted with a NACA0012 wing at $\alpha = 6°$. The proposed WBT is modelled in two different ways: with the tail and without. Each configuration is modelled at aftbody deflection angles of 0, 2, 4, 6 and 8°. The three different WBT configurations are modelled at their design Re_c in this chapter based on chord instead of body length, as in Chapter 4. Therefore, the Re_c are 2.7 x 10^5, 2.4 x 10^6 and 10^5 for the three respective bodies: F-57, Myring and the B-0 used in Huyssen *et al*. (2012), Davis and Spedding (2015) and Smith *et al*. (2016; 2017).

The overall purpose of this study was to provide some insight into the differences between the previous experimental and numerical studies and to investigate a potential design space of the initially tested WBT configurations. This exploration of the design space was conducted by using 10 discrete WBT configurations (five δ with and without KE) for the WBT-0 at chord based Reynolds number, $\mathrm{Re}_c = 10^5$ (Huyssen *et al*., 2012; Davis and Spedding, 2015; Smith *et al*., 2016) and two LDBs at their specific design body length based Reynolds number, Re_l (1.2 x 10^6 for F-57 LDB and 10^7 for Myring LDB).

5.2 Numerical modelling

5.2.1 Geometric model, solution domain and mesh generation

The WBT geometries have fineness ratios, l/d = 4.75, 5.56 and 5.33, for the WBT-0, F-57 and Myring profiles, as shown in Figure 5.1. A NACA0012 section, rectangular wing with set angle of attack, $\alpha = 6°$, AR = 6.67 was prescribed with a reduced chord length, 0.98c for a numerically convenient blunt trailing-edge. The wing leading-edge was placed at x/l = 0.4 from the nose and z/r = 0.8 down from the largest vertical extent of the fuselage. Re_c was different in each case, based on the specific design Re_l for the LDBs (Re_c = 2.7 x 10^5, 2.4 x 10^6 for F-57, Myring). Since the LDBs are designed for specific Re_l, changing the Re_c based on the wing was a better option.

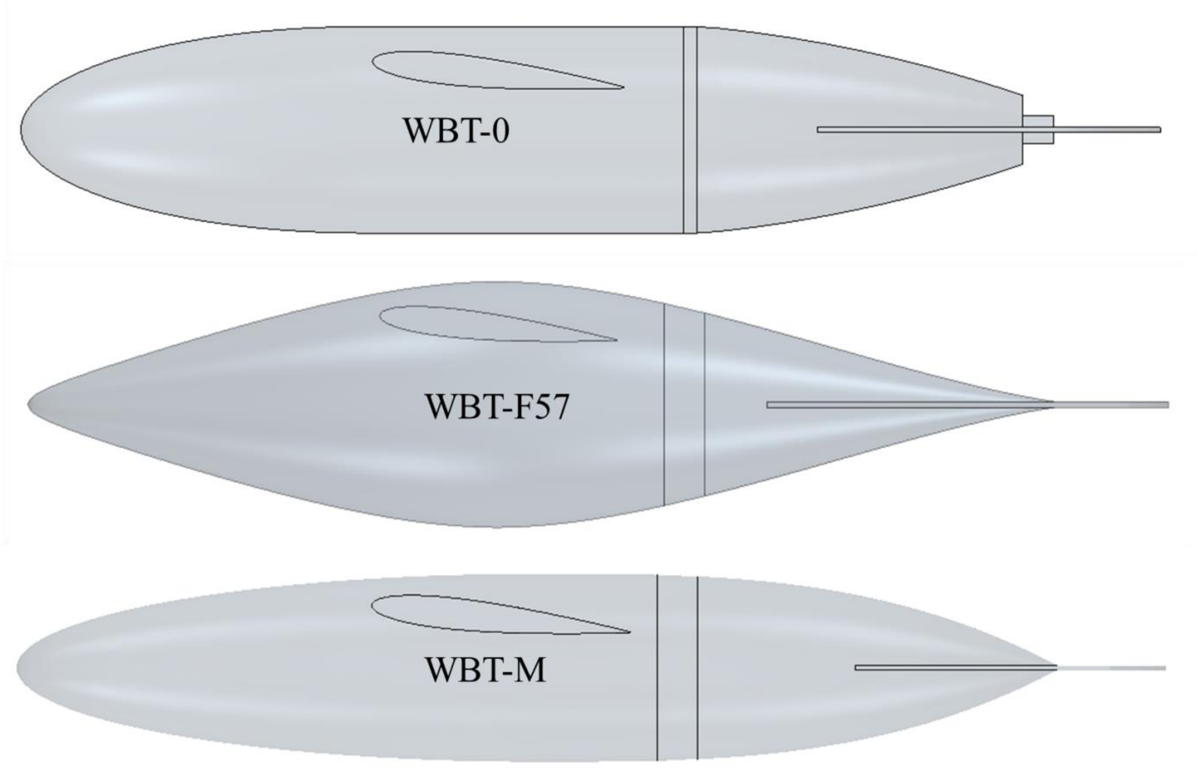

Figure 5.1: The F-57, Myring and WBT-0 geometries.

In the 6 cases for each WBT-NKE/KE combination, the KE was set to have the same geometric ratios of tail width, T_W to body diameter, d and KE length, defined by two ratios l_1/l and l_2/l shown in Figure 5.2. The wings are also placed in the same geometric ratio to the reference WBT (the same horizontal and vertical distance away from the KE).

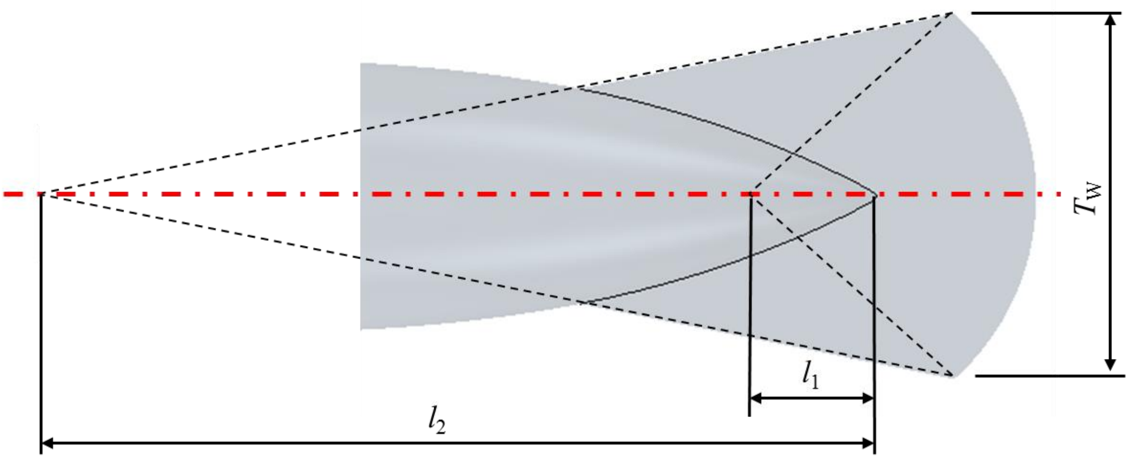

Figure 5.2: KE width and length dimension relationships for all three WBTs.

The WBT-0 was modelled in a simplified cylindrical shape representing the octagonal Dryden wind tunnel test section (Huyssen *et al.*, 2012; Davis and Spedding, 2015) which was a reasonable simplification since, the difference on the lift and drag forces were only 0.25%. Modelling a wall boundary compared to having an open domain increased the force values approximately 2%, due to the blockage effects present when the walls were added. All solution domains were of half models with a symmetry plane. The diameter of the wind tunnel is 4.5*l* (since *b*/2 = 0.8*l* this leaves 1.45*l* as the distance to the wall from the wing tip) and WBT-0 was positioned 6*l* from the inlet and the total domain was 25*l* as shown in Figure 5.3.

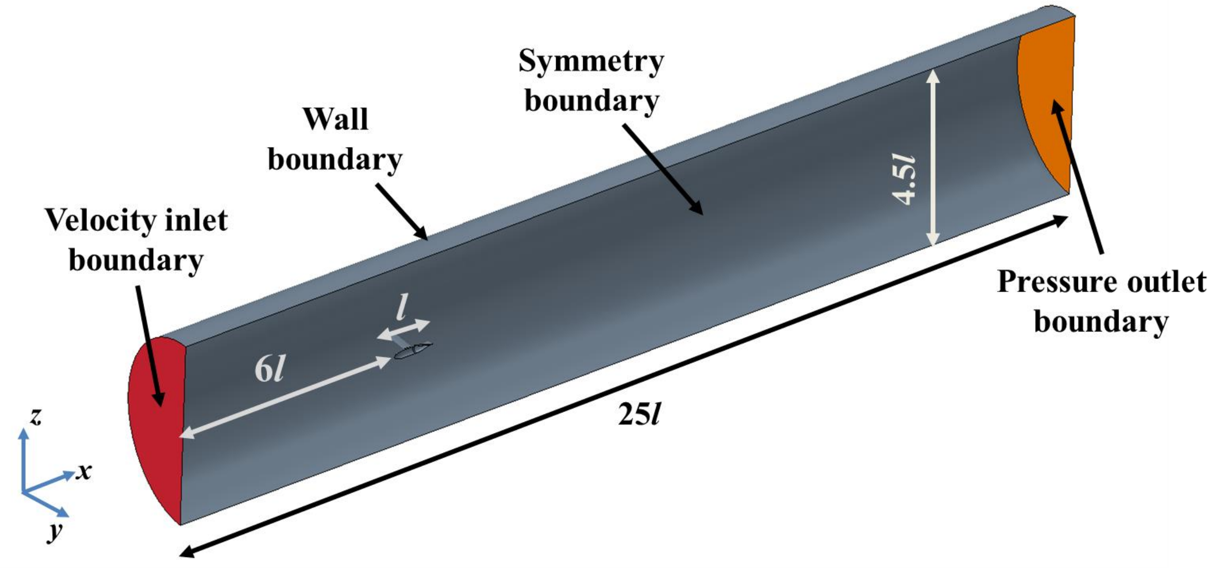

Figure 5.3: Solution domain with coordinate system and boundary conditions for the WBT-0.

All bodies were meshed using the same mesh functions and boundary layer mesh growth rate as Chapter 4. The WBT model had 15 boundary layer cells and two cells on the outer wall boundary were sufficient for force predictions (without the wall cells there is a 2% difference of the force values). The domain refinements were modelled in the same way as described in Chapters 3 and 4. Additional refinements were placed around the wing and downstream of the wing into its wake. Figure 5.4 shows the mesh around the WBT-0 model.

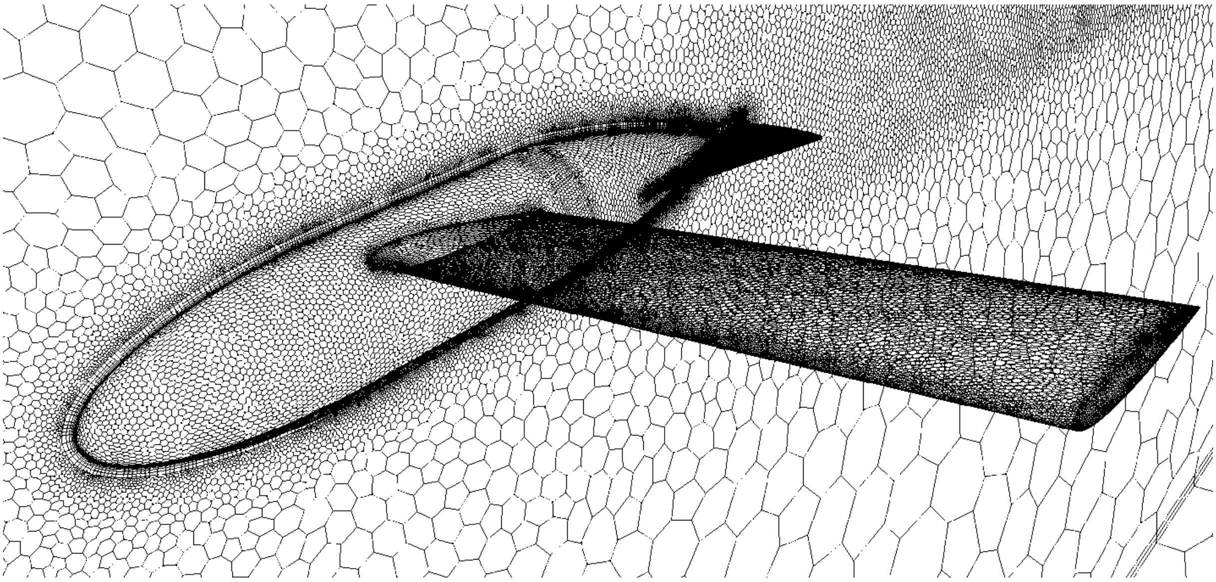

Figure 5.4: Unstructured mesh around the WBT-0-KE model.

The GCI method described in Chapter 3.4.3 was used to ensure that drag estimates were not sensitive to further mesh refinement. All mesh sizes were in the order of 3-5 x 10^6 and the criterion $y^+ < 1$, which is a measure of boundary layer resolution, was satisfied for all cases.

5.2.2 Boundary Conditions, Turbulence and Transition Models

The flow was steady and incompressible, with constant velocity inlet and outlet pressure boundary set at atmospheric (Figure 5.3). The outer domains for the WBT-0 and-F57 were modelled as no-slip wall boundaries, whereas WBT-M had symmetry plane outer domain boundaries. The shear-stress transport (SST) k-ω turbulence model (Menter, 1994) coupled to a γ-Re_θ transition model (Menter *et al.*, 2004) was selected as in Chapters 3 and 4. The transition model is required for $\mathrm{Re}_c < 10^6$ where laminar separation bubbles and transition become important to predict the aerodynamic forces with reasonable accuracy.

5.3 Simulations of the experimental WBT configuration at $Re_c = 10^5$

First the global force values of the experimental model WBT-0 were considered after which the flow mechanisms responsible for the force trends were investigated. Figure 5.5a shows the variation with δ of the pressure and friction drag coefficients components (normalized by wing planform area, A as is the standard for aircraft configurations) for the WBT-0. Friction drag is almost unchanged at all δ, while pressure drag increases noticeably in the KE configuration. The WBT-0 C_D curves shows that a shallow minimum total drag for the KE condition occurs at $\delta = 2°$ for KE and $\delta = 4°$ for NKE.

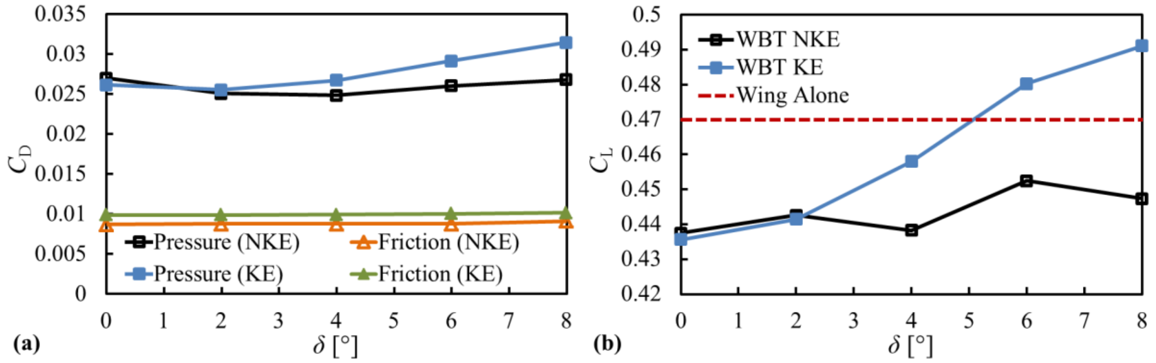

Figure 5.5: The effect of varying δ on C_D (a) and C_L (b) for the WBT-0-NKE/KE.

Figure 5.5b shows that in general, the lift coefficient, C_L for the KE increases with δ, and it does so much faster than the NKE configuration. At $\delta = 0°$, C_L for both WBT-0-NKE/KE are lower than that of the wing alone since part of the wing span, b is situated within the non-lifting fuselage. C_L of the WBT at $\delta = 5°$ is about the same as for the NACA0012 wing alone at $\alpha = 6°$. It is not obvious from the dissimilar scales of Fig 5.5a and b, but the relative change in drag, $dC_D/C_{D,\delta=2°}$ is approximately 0.17 (taken between $\delta = 2°$ and $\delta = 8°$), which is larger than the relative change in lift $dC_L/C_{L,\delta=2°}$ of approximately 0.11.

In Figure 5.6 the normalized streamwise velocity, U_x/U, of the first boundary layer mesh cell, over the top of the body at $\delta = 4°$, shows the regions of recirculation indicated in dark blue on the colour insert (the lower U_x/U value was restricted to zero to show negative velocities as a uniform dark blue section). For both the KE and NKE cases there are large areas of recirculation over the aftbody with separation occurring eventually at x/l = 0.88. Even though there are regions of recirculation over the top of the aftbody, the KE still shows attached flow over the largest part of its area. The pressure drag penalty due to the large sections of recirculation on the aftbody overshadows the gain of lift from the KE. These recirculation regions are common in low Re flow-fields and specifically in bodies of revolution if the aftbody is not designed to avoid separation (Parsons and Goodson, 1972; Smith *et al.*, 1981).

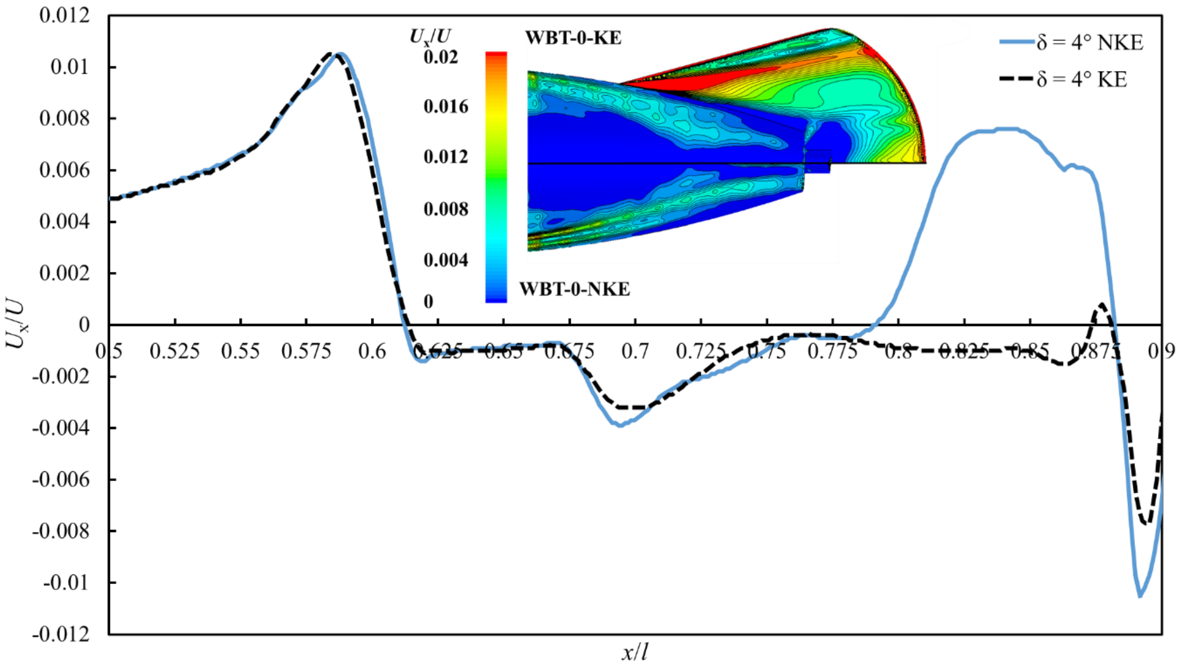

Figure 5.6: U_x/U over the aftbody section (0.5 < x/l < 0.9) of the WBT-0-NKE/KE at δ = 4° on the symmetry plane. Colour insert shows the U_x/U contours over the top of the aftbody for the WBT-0-NKE/KE.

Figure 5.7 shows the wake velocity profile for δ = 4° of the WBT-0-NKE/KE on the symmetry plane. There are three lobes present for the WBT-0-KE in the wake profile. The bottom and top lobes are due to the separation of the upper and lower boundary layers from the aftbody and the middle lobe the boundary layer over the KE. For the WBT-0-NKE there are only two lobes for the bottom and top aftbody boundary layer separation. Both cases have a faster central U_x/U approximately at z/l =0.015 due to the wing-induced wake. The same wake profiles are observed for other δ with Figure 5.8 showing the U_x/U contours for δ = 0°, 4° and 8° on the symmetry plane. At δ = 0° the wake is deflected slightly upward even with the KE. This is due to the downwash of the wing which then meets the upwash from the body and the interaction creates an initial slight upwash in the near-wake.

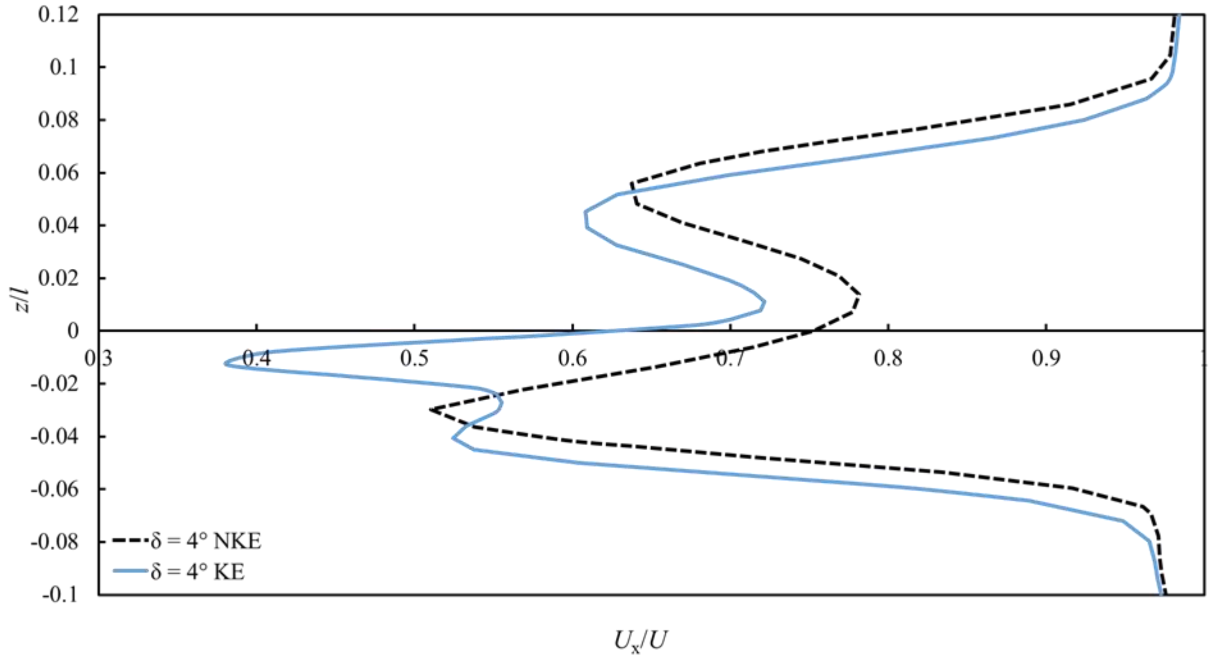

Figure 5.7: U_x/U as the wake profile for the at δ = 4º for the WBT-0-NKE/KE.

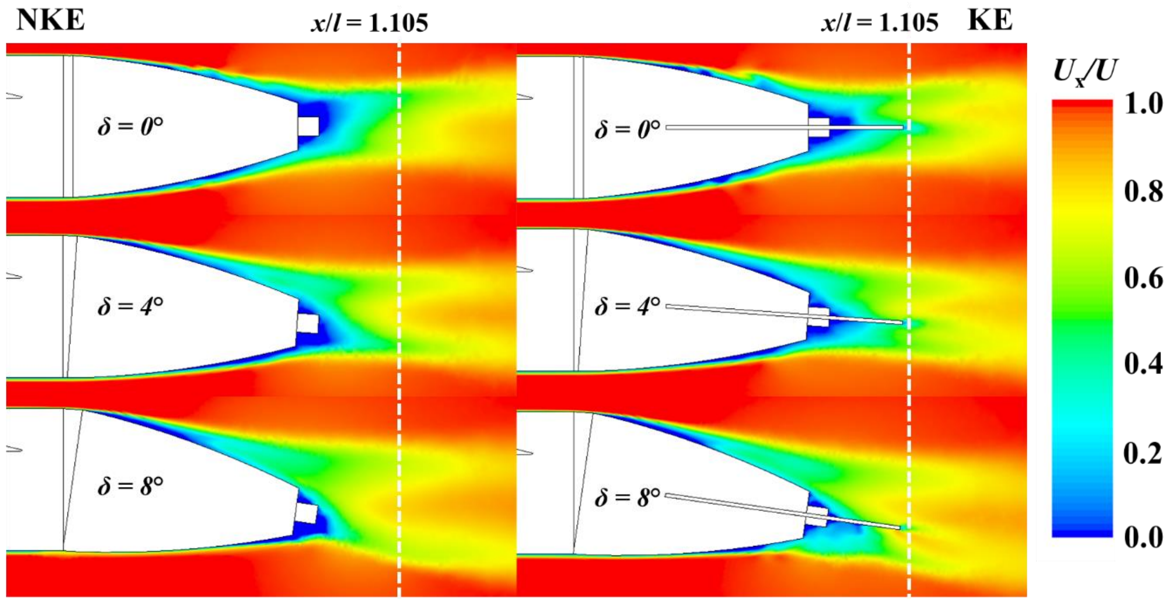

Figure 5.8: U_x/U colour contours on the symmetry plane at δ = 0º, 4º, 8º for the WBT-0-NKE/KE.

Figure 5.9 shows the P_{Total} contours (left) over the aftbody section at different locations for the WBT-0-NKE/KE. To visualize the complexity of the three-dimensional wake structure, vorticity magnitude, ω, iso-surfaces with streamlines are shown in Figure 5.9 (right). The iso-surfaces are created by restricting the vorticity range to show only the viscous wake and each colour is made transparent with an opacity of 0.5. Figure 5.9a and b shows the WBT-0-NKE/KE at $\delta = 0°$ and Figure 5.9c and d at $\delta = 4°$. The P_{Total} contours show lower values at the center of the vortices that are formed along the aftbody and P_{Total} increases outward from these low points to create the curved path of the flow particles shown by the streamline plots. At both δ there is an interaction between the boundary layer forming on the KE as well as the thickening of the boundary layer over the top and bottom of the aftbody which is clear from the vorticity iso-surfaces and streamlines. The wing-induced flow-field modifies the flow over the aftbody-KE and at $\delta = 0°$ the KE lies inside the deflected viscous wake behind the wing which leads to complex interaction and the leading-edge vortices on the top of the KE cannot form properly (compare Fig 5.9b and 5.9d P_{Total} contours). At $\delta = 4°$ the downwash of the wing and thickening of the boundary layer over the aftbody adjusts the effective angle of attack of the flow as it reaches the leading-edges of the KE and the vortex pair is formed on top of the KE. Ideally the KE should be integrated into the aftbody to avoid the interaction with the wing-induced flow-field and the aftbody-KE should be shaped in a way where there is no separation.

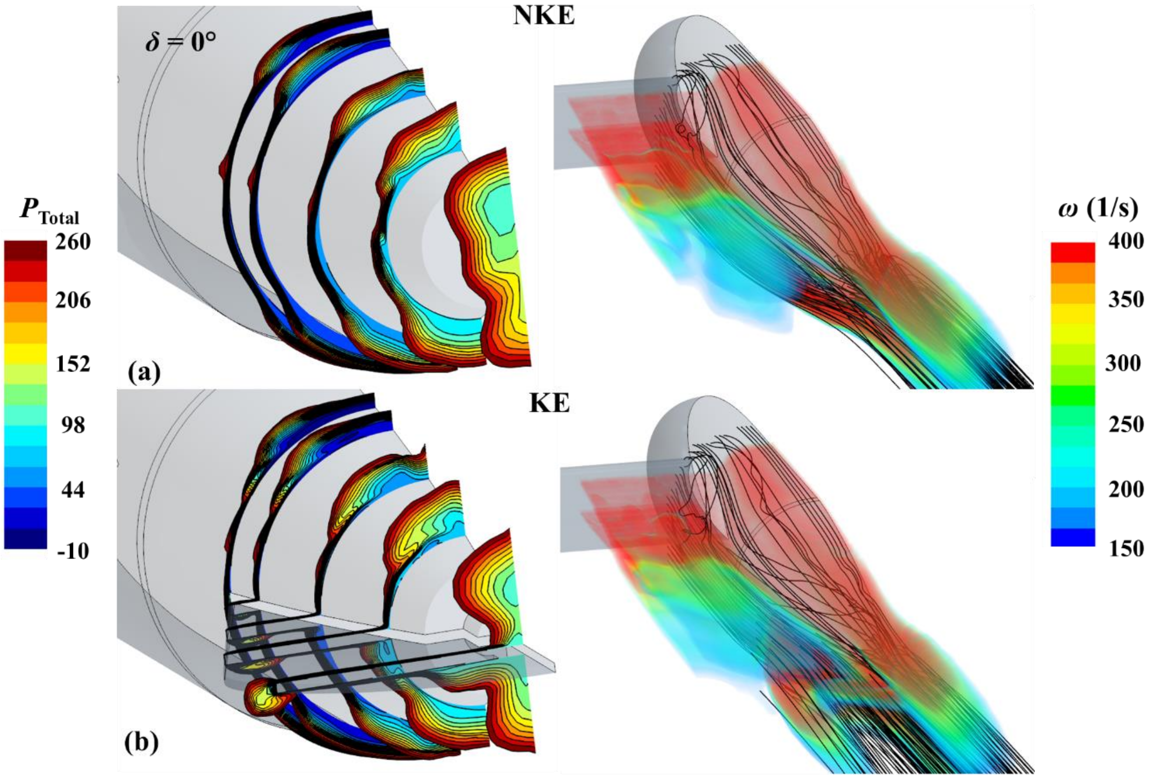

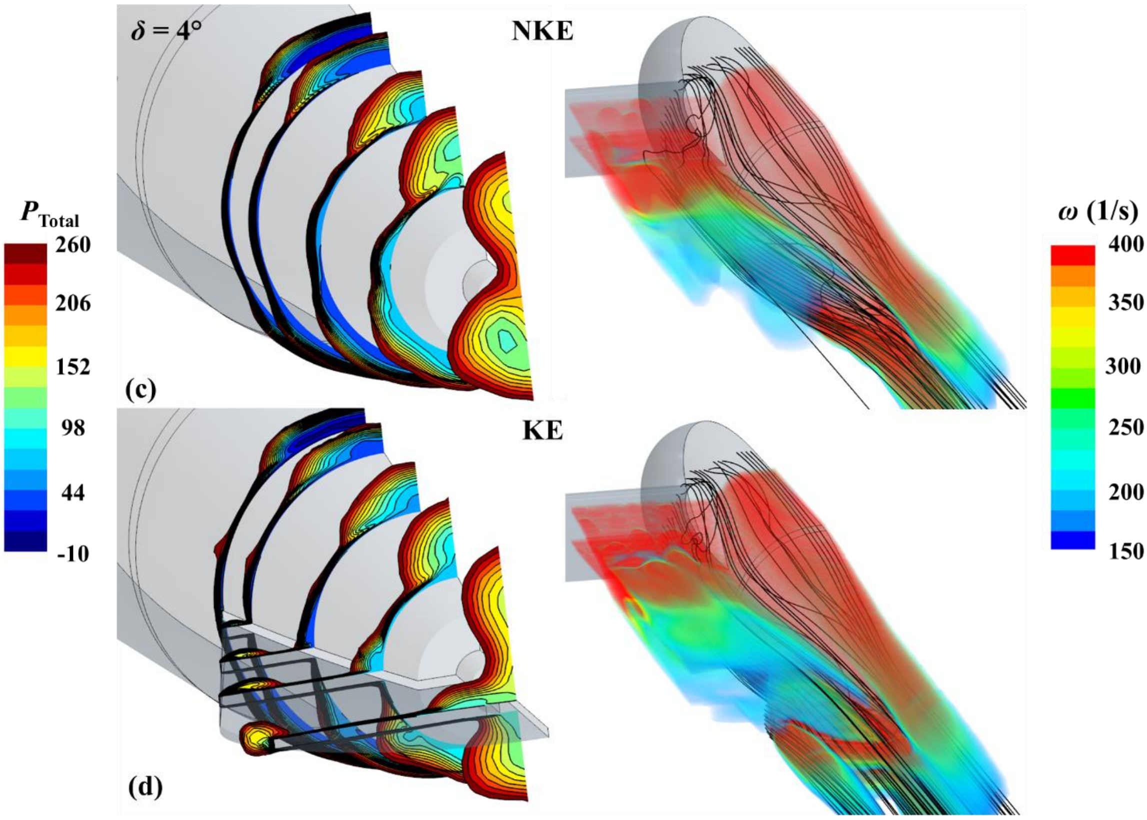

Figure 5.9: P_{Total} contours at different streamwise locations over the aftbody (left) and vorticity iso-surfaces and streamlines (right) for the WBT-0-NKE/KE at (a) and (b) at δ = 0º, and (c) and (d) at δ = 4º.

For comparative purposes Figure 5.10a and b shows the P_{Total} contours over the aftbody of the BT-0-NKE/KE at δ = 0° and 4°, to show the influence the wing has on the downstream wake structure of the aftbody and KE. At δ = 0° the BT-0-NKE/KE both have a symmetrical wake structure which is not the case for the WBT-0-NKE/KE in Figure 5.9a and b. Also at δ = 4° there is a larger leeward P_{Total} for the BT-0-NKE/KE and a more gradual distribution spanwise across the KE than when the wing is added (Figure 5.9d).

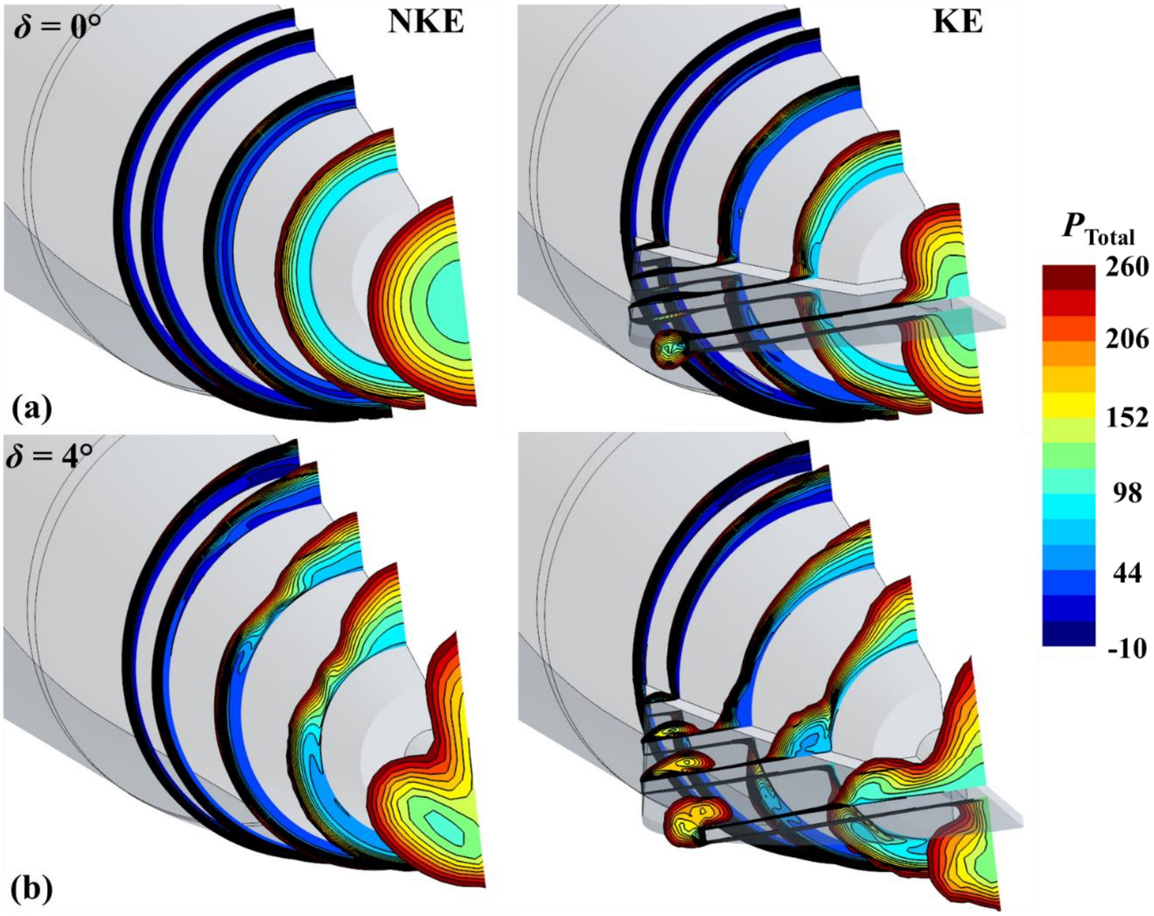

Figure 5.10: P_{Total} contours at the same location as Fig. 9 for BT-0-NKE/KE at (a) $\delta = 4°$ and (b) $\delta = 0°$.

The overall objective of the KE is to restore the circulation over the (previously non-lifting) body so that the downwash distribution is (a) more uniform (lower induced drag) and (b) overall stronger so that the integrated total yields higher lift. The current geometry appears to be achieving some of these goals simply by body deflection alone, with no KE. Figure 5.11 shows the downwash distributions as the normalized cross-stream velocity, U_z/U, along the normalized half span ($2y/b$), behind the WBT-0-NKE/KE at each δ. The profiles were taken at $x/l = 1.105$ and $z/r = -1.5$ and the orange line indicates the position behind a NACA0012 wing alone at $\alpha = 6°$. The wingtip is at $2y/b = 1$ and the KE ends at approximately $2y/b = 0.17$. For all δ there is a large spanwise variation at the center. At $\delta = 0°$, the KE configuration appears worse than the NKE, with a greater downwash defect behind the body. This is due to the upwash from the body-KE and downwash from the wing-induced wake interacting (c.f. Figure 5.8). When $\delta = 2°$, the KE and NKE has very little difference in downwash distribution, but as δ increases the KE seems to offer an improvement. If the objective has been to restore the circulation profile to the wing only case, then the KE can produce the downwash centrally but at the expense of having upwash around the KE tip. Clearly some careful matching would need to be done if a uniform downwash were to be achieved.

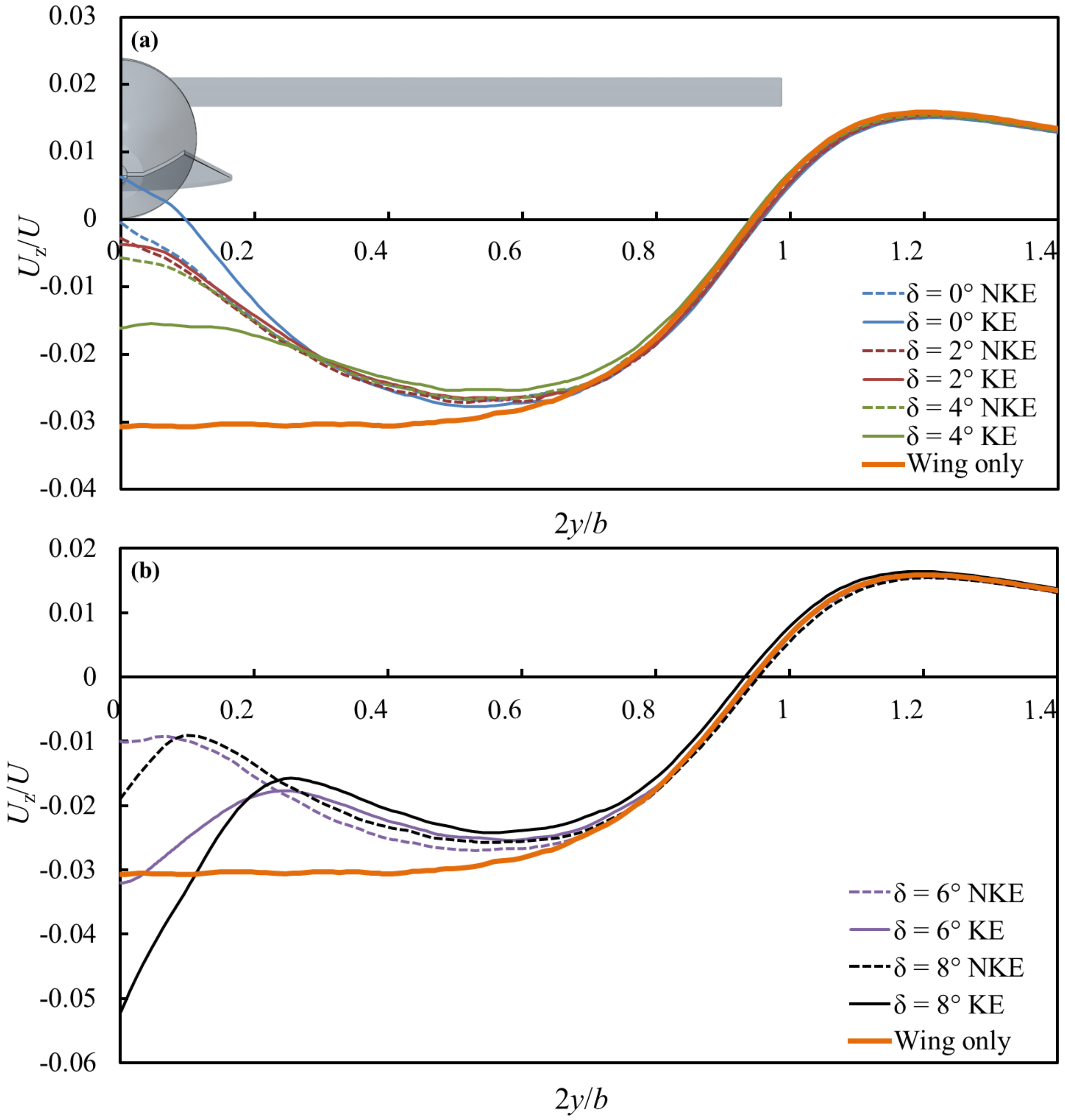

Figure 5.11: Spanwise distribution U_z/U at $z/r = -1.5$ and $x/l = 1.105$ as a function of $2y/b$ for the WBT-0-NKE/KE, (a) $\delta = 0°$ to $4°$ with a schematic of the WBT-0-KE and (b) $\delta = 6°$ to $8°$.

Figure 5.12 shows the U_z/U contour plots for $\delta = 0°$, $4°$ and $8°$ at the same x/l location as the profiles in Figure 5.11. There are multiple traces of upwash and downwash regions from the body and KE and these will have to be reduced to obtain a uniform spanwise downwash as shown by the wing only U_z/U contour in Figure 5.13.

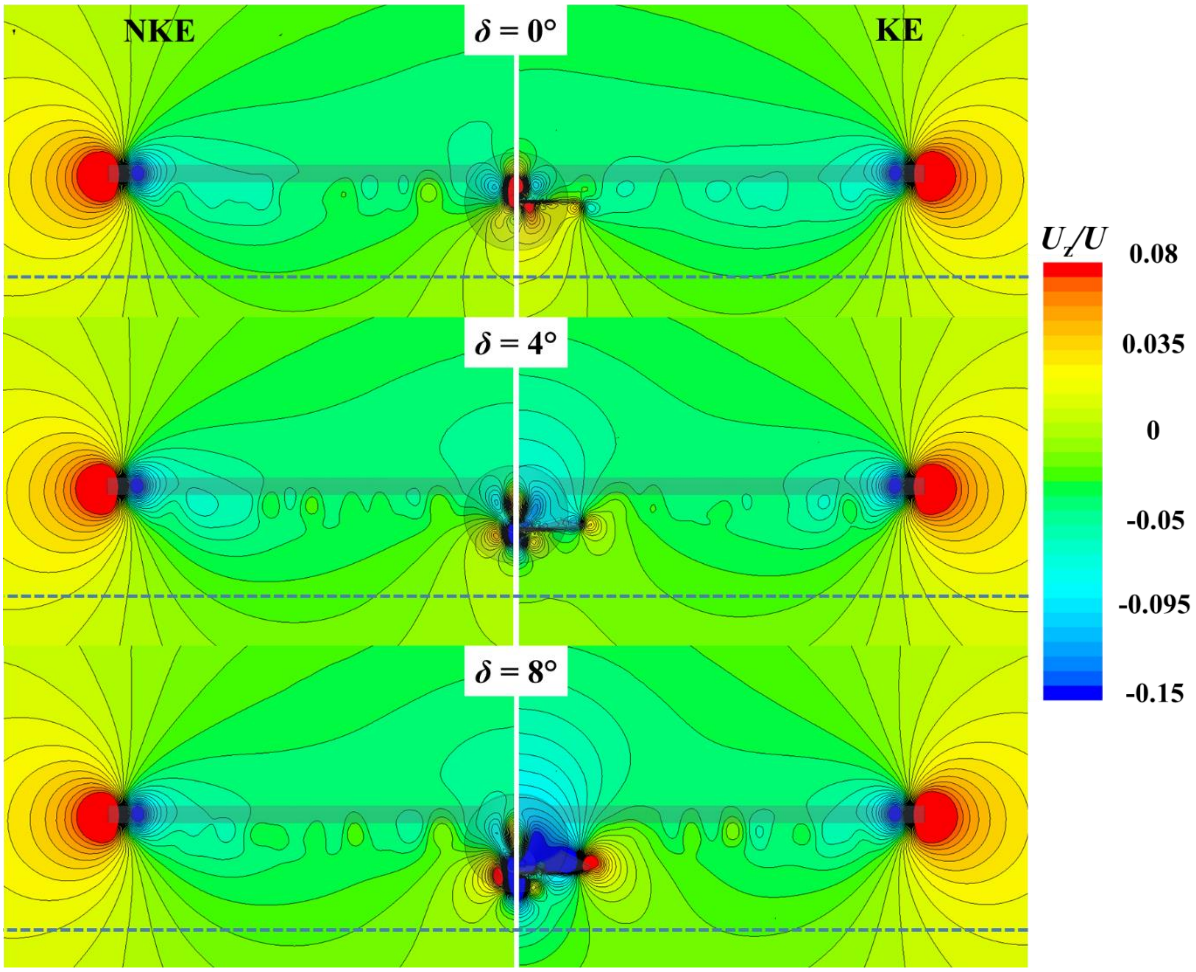

Figure 5.12: U_z/U contours for the WBT-0-NKE/KE at δ = 0°, 4° and 8°. Dashed line indicating the location z/r = -1.5.

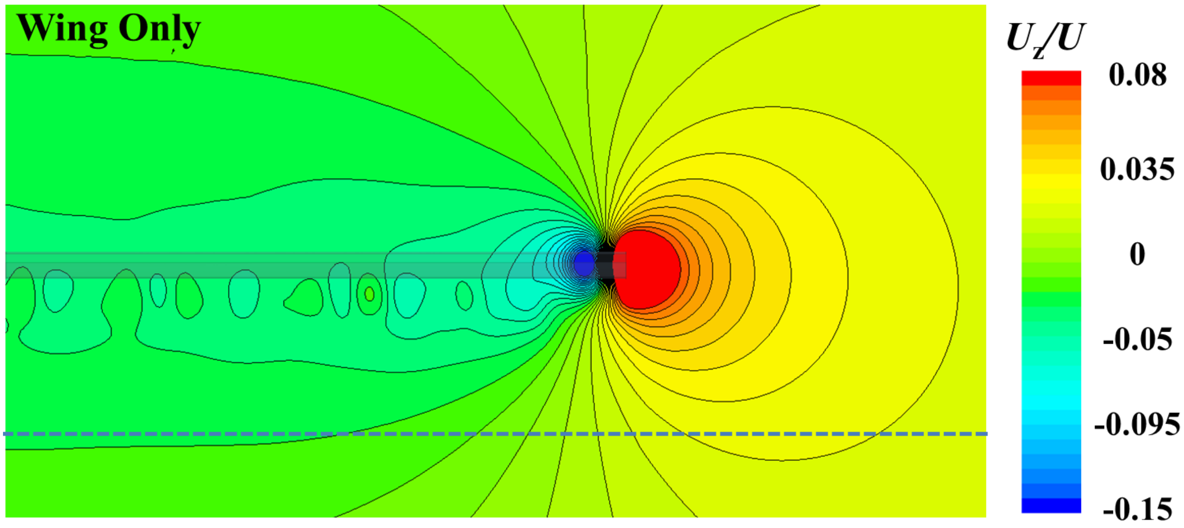

Figure 5.13: U_z/U contours for the NACA0012 wing alone. Dashed line indicating the location z/r = -1.5.

Figure 5.14 shows a systematic breakdown of the lift provided by the body and KE relative to the wing alone $C_L/C_{L,wing}$ of the WBT-0-NKE/KE as well as for the wingless case, BT-0. The WBT-0 body shows a larger increase in $C_L/C_{L,wing}$ than the BT-0 body since the wing that is added contributes to normal forces over the body to increase the overall lift. However the KE has a reduction in the $C_L/C_{L,\text{wing}}$ when the wing is added due to the change of the effective angle of attack the KE experiences from the upstream wing.

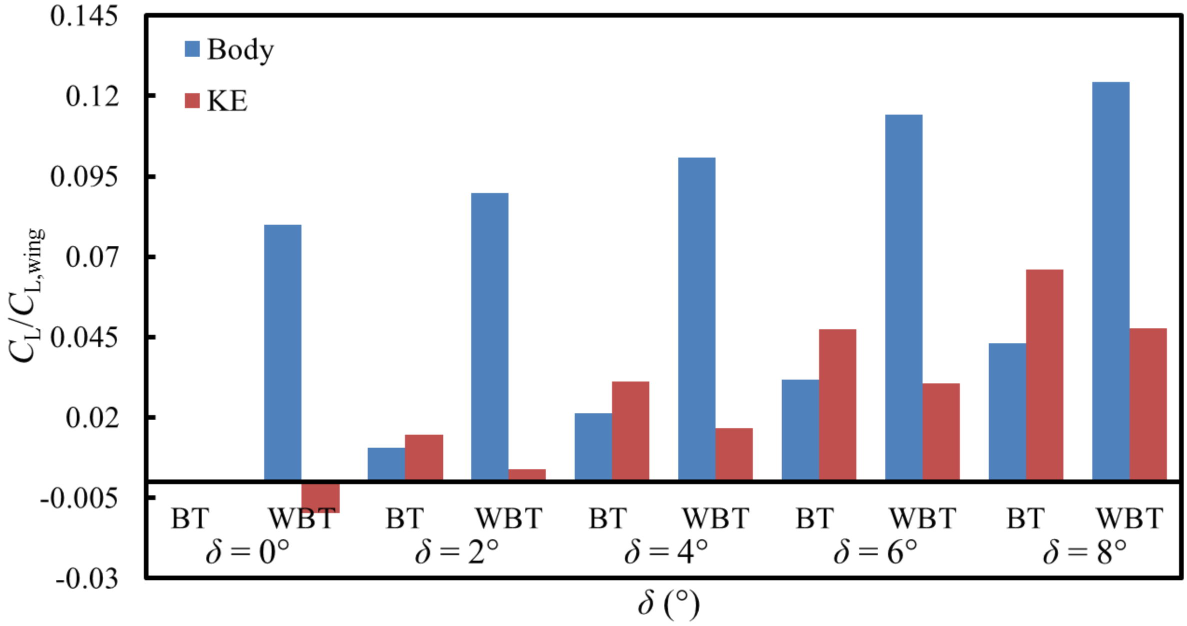

Figure 5.14 $C_L/C_{L,\text{wing}}$ for the WBT-0-KE and BT-0-KE combinations at varying.

Even though the KE does seem to be a step in the right direction to restore the downwash distribution, its effectiveness is influenced by the separation over the aftbody and the wing-induced wake. Separation over the aftbody-KE will lead to a drag penalty that outweighs this potential benefit. As an attempt to investigate the contribution of the aftbody design, the two LDBs considered in Chapter 4 were used in the WBT.

5.4 Numerical investigation of LDBs in the WBT

Figure 5.15a shows the variation of C_D with δ for the WBT-F57 and WBT-M, both in NKE/KE configurations. The C_L values for WBT-F57 and WBT-M both show a linear increase as δ increases similar to the WBT-0 as one might expect. C_L increases much more visibly with KE, and C_L has been restored almost to the wing alone value at $\delta > 3°$ for WBT-F57-KE and at $\delta > 7°$ for WBT-M-KE, as shown in Figure 5.15b. The relative change in drag $dC_D/C_{D,\delta=2°}$ for the WBT-F57-KE it is approximately 0.21 and for WBT-M-KE approximately 0.18, which is larger than their respective $dC_L/C_{L,\delta=2°}$ of approximately 0.12 and 0.09. All three WBTs share a similar trend in $dC_D/C_{D,\delta=2°}$ but the WBT-M-KE has the lowest C_D values overall. C_L increases for all three WBTs with the WBT-F57-KE at a higher rate than the WBT-0 and WBT-M-KE.

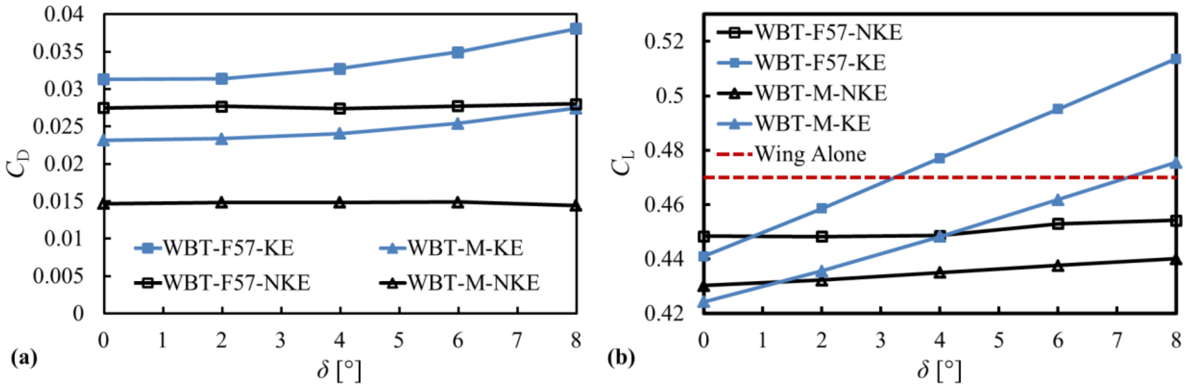

Figure 5.15: (a) Drag coefficient, C_D and (b) lift coefficient C_L varying with δ for the WBT-F57 and WBT-M-NKE/KE.

The reduction in the dC_L/$C_{L,\delta=2^\circ}$ for the WBT-M compared to the WBT-F57-KE is attributed to the aftbody shape, where the WBT-F57 has a sharper taper there is larger surface area of the KE exposed (approximate 26% more) that can provide a lift force than the more bluff Myring aftbody-KE. However Figure 5.15a shows that the benefit in lift when considering the WBT-F57-KE is outweighed by the drag penalty. The F-57 and Myring LDB were originally designed to reduce drag (Parsons and Goodson, 1972) but not with wings attached.

Even without the wing, the Myring LDB-KE outperformed the F-57 LDB-KE in terms of drag and lift components In Chapter 4. Figure 5.16 shows the portions of separation and reattachment over the aftbody of the F-57 WBT where the same flow features are not present for the Myring WBT. The interference from the wing-body connection aggravates the already unstable flow over the aftbody of the F-57 WBT, leading to a larger drag component.

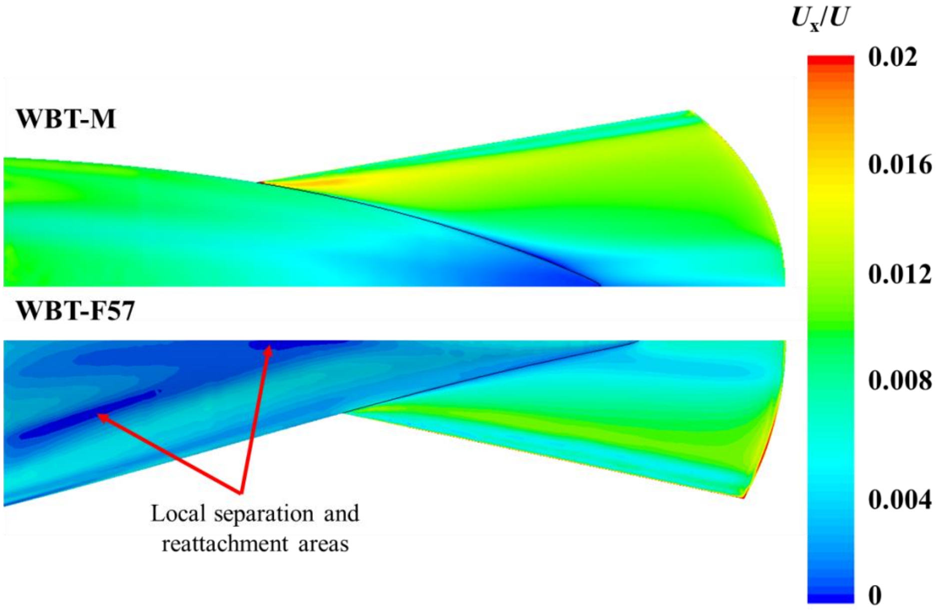

Figure 5.16: Normalized streamwise velocity contours over the aftbodies of the WBT-F57- and WBT-M-KE.

The F-57 LDB design focused on primarily transition delay to reduce drag while the Myring LDB focused on the reduction of separation over the aftbody. Both LDBs have lower drag compared with the WBT-0-KE. Figure 5.17a shows colour contours of U_x/U at δ = 0°, 4° and

8º for the WBT-F57-NKE/KE and Figure 5.17b for WBT-M-NKE/KE. The vertical wake thickness is reduced when the KE is added and the downward deflection of the wake increases with increasing δ in both cases. This was not clear in Figure 5.8 of the WBT-0 and overall all the wake thicknesses of the WBTs with LDBs are smaller, consistent with the observed reduction in drag. The WBT-F57 shows areas of separation (shown by the $U_x/U < 0$) over the aftbody similar to the WBT-0, more so for the NKE than KE, but these separation areas are smaller for the WBT-M-NKE/KE. Also, for all WBTs at $\delta = 0^\circ$ there is an initial upwash deflection of the streamwise wake defect present as the downwash from the wings interact with the upwash from the aftbody.

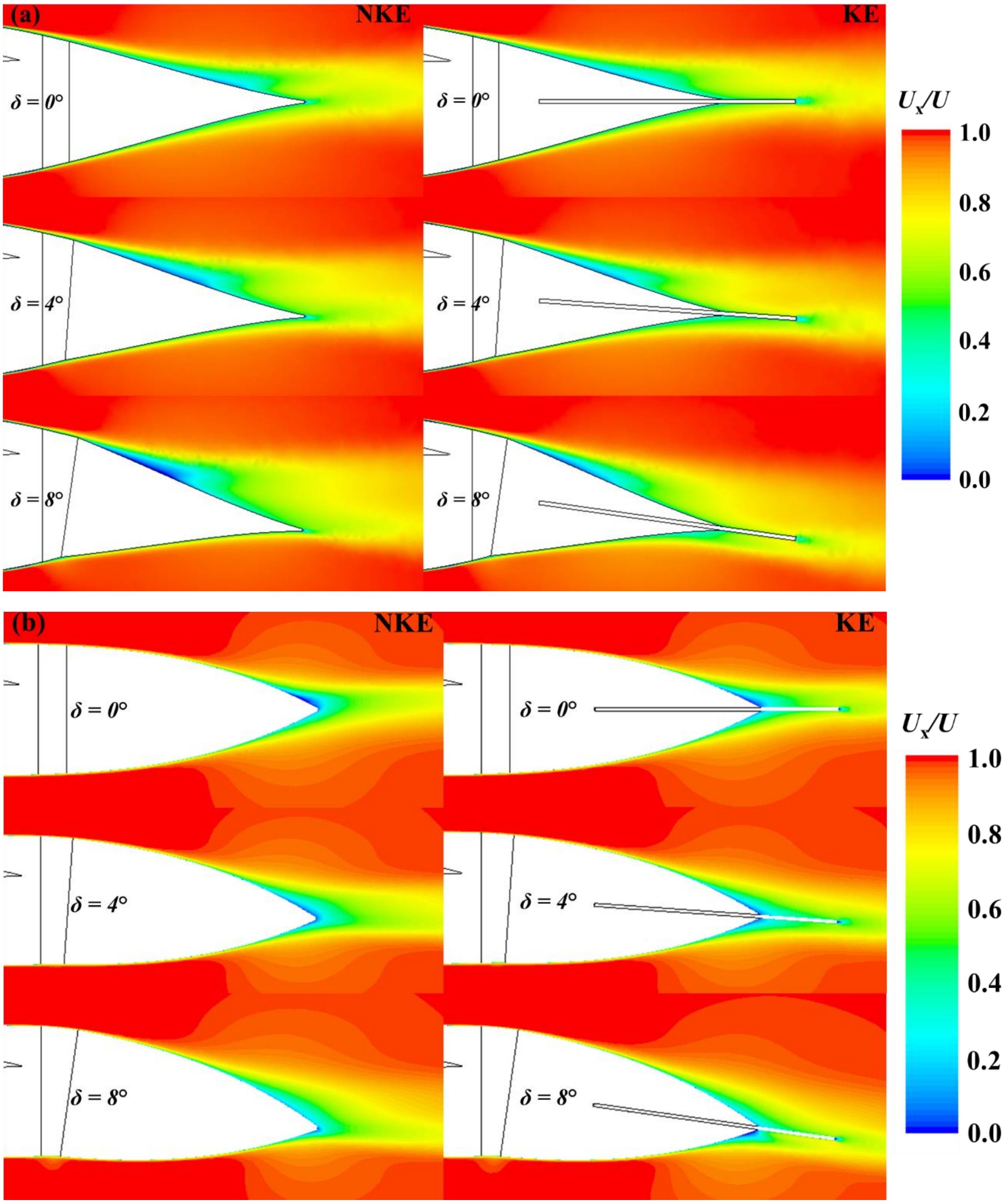

Figure 5.17: U_x/U colour contours for the (a) WBT-F57-NKE/KE and (b) WBT-M-NKE/KE at $\delta = 0^\circ, 4^\circ, 8^\circ$.

Figure 5.18 shows the streamwise velocity profiles, U_x/U, for $\delta = 4°$ of the WBT-F57-NKE/KE with and without the wing. The velocity profiles and contours of $\|U\|$ both show that the wings cause the wake behind the body to thicken, as though separation were occurring further upstream. There is little difference when the KE is present. With no wings, the KE appears to protrude upwards through the thin wake (Figure 5.18b) and with wings, it is always inside a presumed separated wake. It is clear that the wing has a direct and negative influence on the trailing-edge conditions, again emphasizing the importance of careful matching within the WBT when any sort of trailing-edge device is added or the aftbody deflected.

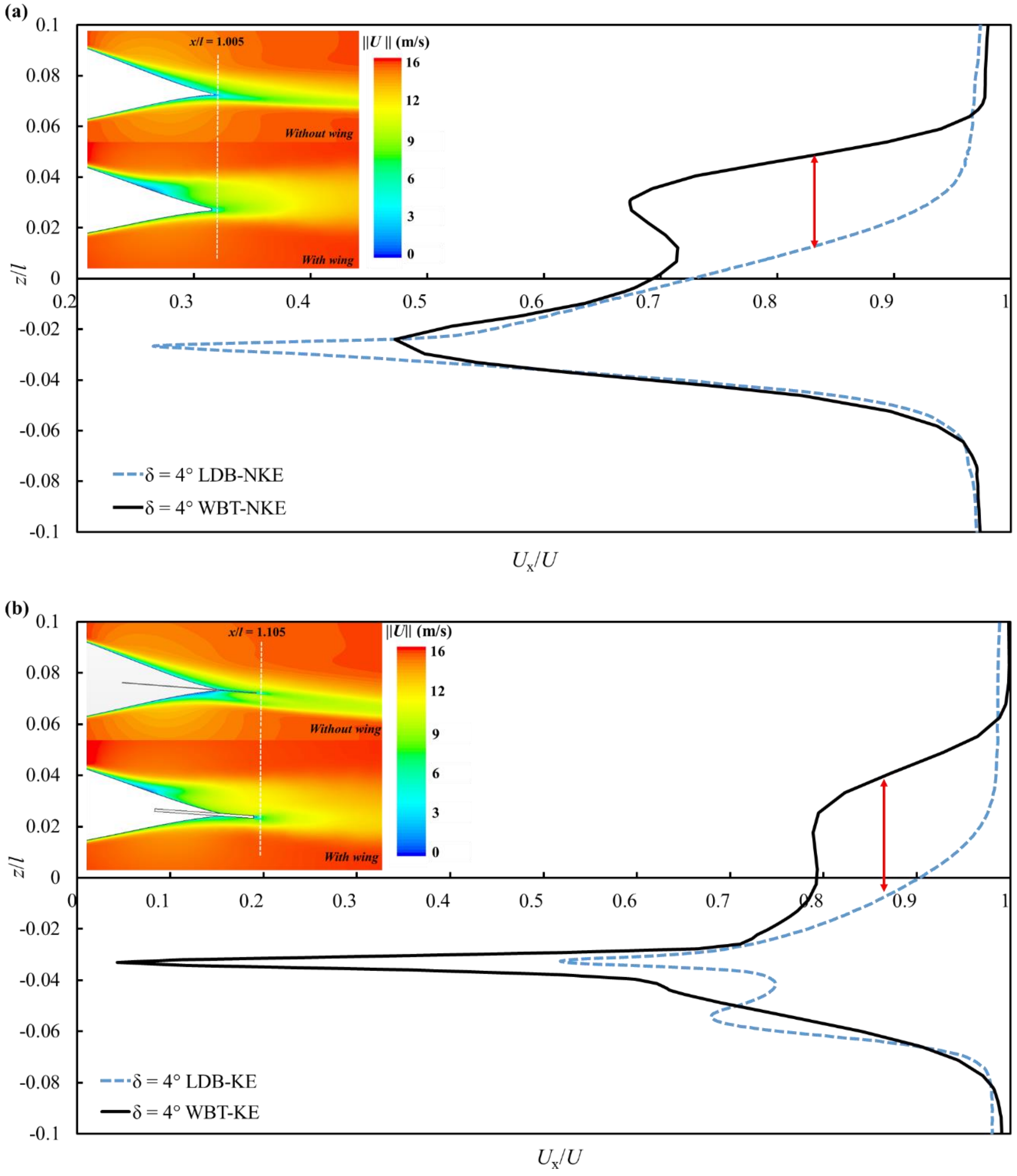

Figure 5.18: U_x/U as the wake profile for the F-57 LDB and WBT (a) without KE and (b) with KE at $\delta = 4^{o}$. Red arrows indicate the difference between the wake profile with and without a wing.

U_x/U, for $\delta = 4°$ of the WBT-M-NKE/KE and WBT-F57-NKE/KE is shown in Figure 5.19. Again the downward deflection of the wake is observed with the addition of the KE and for the WBT-M, a double-lobe profile is not present, in contrast to the WBT-F57. The gradual aftbody taper to the sharp trailing-edge of the WBT-F57, actually leads to premature separation on the aftbody when wings are present. The WBT-M has a smoother wake profile and a smaller wake defect which explains the smaller pressure drag increase compared with the WBT-F57 in Figure 5.15.

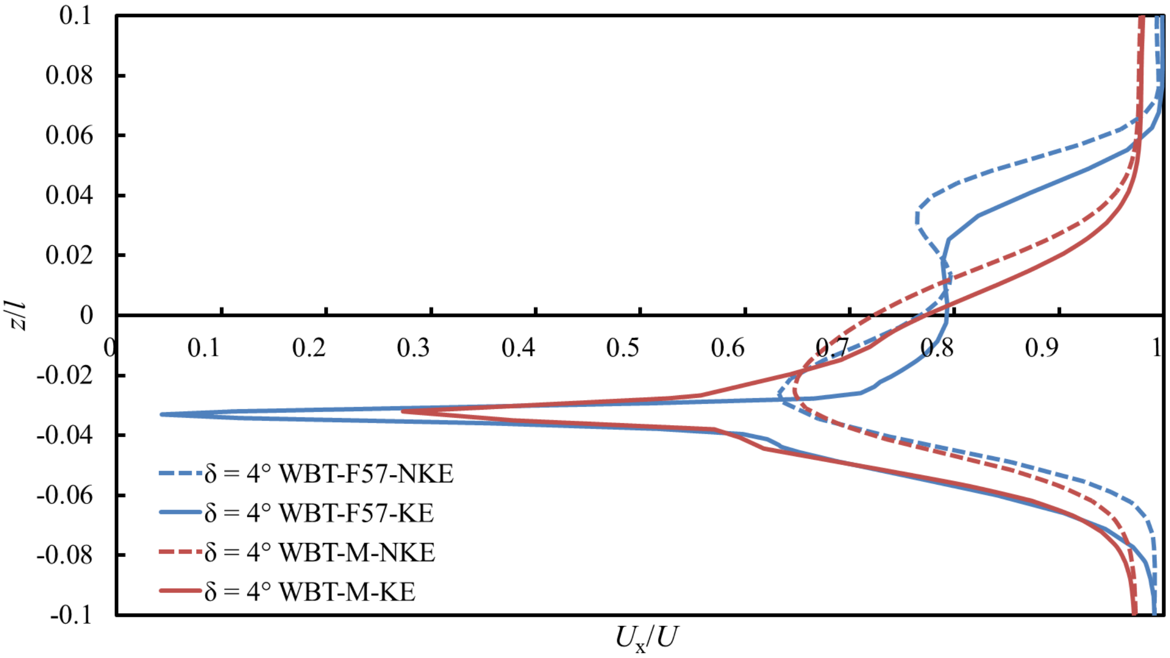

Figure 5.19: U_x/U at $\delta = 4°$ for the WBT-M-NKE/KE compared with the F57 WBT-NKE/KE at $x/l = 1.105$.

Figure 5.20a to d shows the spanwise distribution for the WBT-F57 and WBT-M-NKE/KE at $\delta = 0°$ to 8°. These values were extracted at the same streamwise location as for the WBT-0-NKE/KE. Similar to the WBT-0-NKE/KE in Figure 5.11, the downwash profiles for $\delta = 0°$ and KE show an increased upwash as the KE is immersed in a wing downwash so the local KE incidence angle is negative, generating negative lift (Figure 5.14). The WBT-F57-NKE has very little variation with changes in δ, possibly due to the more rapid termination of the aftbody of the F-57 LDB. For WBT-F57- and -M-KE, at $\delta > 6°$ the central downwash distribution of the wing alone is exceeded and much stronger than the WBT-0-KE, though uniform downwash distribution was never realised. Overall WBT-F57 and -M show similar spanwise distributions with $\delta = 2°$ and 4° seeming most promising.

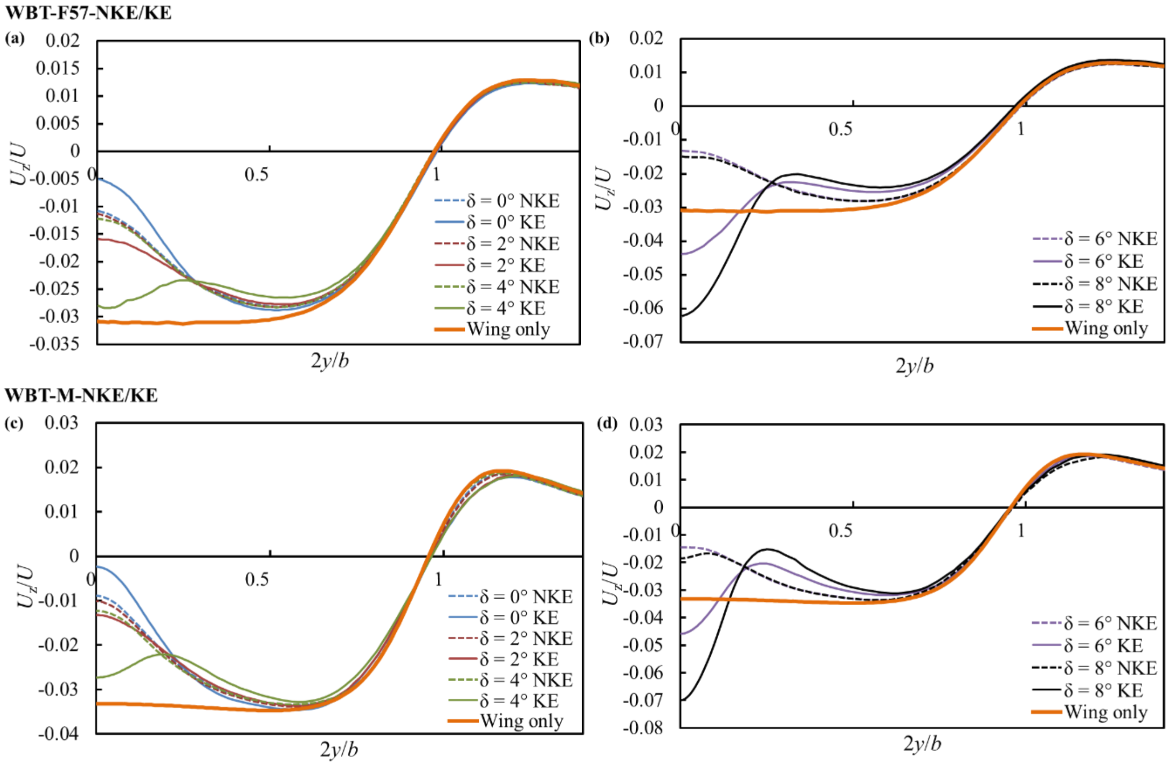

Figure 5.20: U_z/U as a function of 2y/b for the WBT-F57-NKE/KE, (a) δ = 0° to 4° and (b) δ = 6° to 8° and WBT-M-NKE/KE, (c) δ = 0° to 4° with a schematic of the WBT-0-KE and (d) δ = 6° to 8° at the same location as Figure 5.11.

Figure 5.21a and b shows the U_z/U contours for the (a) WBT-F57 and (b) WBT-M-NKE/KE at x/l = 1.105, respectively, with the view direction and location of the contour plot shown at the top of Figure 5.21. There are far less local upwash and downwash regions behind the body and KE of the WBT-F57 and WBT-M-NKE/KE compared to the WBT-0-KE/NKE in Figure 5.12. WBT-M-NKE/KE has a smaller and more central upwash region at δ = 0° (Figure 5.21b) than the WBT-F57-NKE/KE. However, at δ = 4° and 8° the WBT-M-NKE/KE has a larger central downwash region than the WBT-F57-NKE/KE.

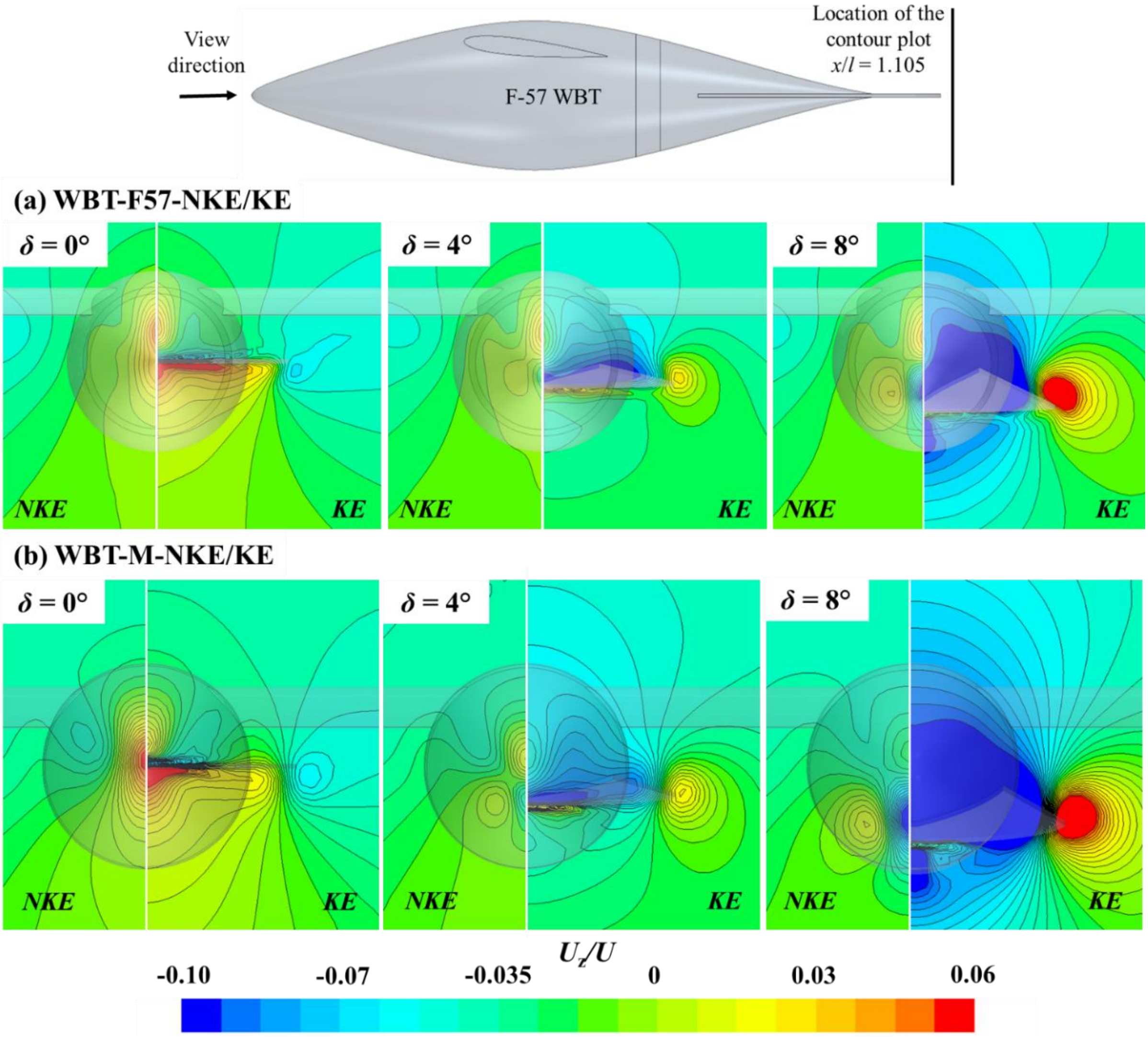

Figure 5.21: U_z/U contours for the (a) WBT-F57-NKE/KE and (b) WBT-M-NKE/KE at δ = 0°, 4° and 8° downstream at x/l = 1.105. The location of the contour plot as well as the view direction is shown at the top.

5.5 Discussion

The WBT-0 aftbody was not designed to provide any pressure recovery or reduce separation over the afbody and as a result the boundary layer separates, leading to a high pressure drag, and thick associated wake. For both the WBT-F57 and WBT-M-NKE/KE, the wakes have lower fluctuation in U_x/U, a reduced wake deficit and lower pressure drag.

In terms of lift provided by the different WBT arrangements Figure 5.22 gives an breakdown of C_L relative to the $C_{L,wing}$ (based on the amount of lift provided by the wing alone) for the body and KE components. All of the WBT-KEs show (c.f. Figures 5.8 and 5.17) an upward deflection of the wake for the $\delta = 0°$ with the largest upward deflection seen at WBT-0 and WBT-F57-KEs. At all increasing δ the WBT-KEs shows an increase in lift on the body, with the WBT-F57-KE body showing a larger contribution compared to the other two WBT-KEs.

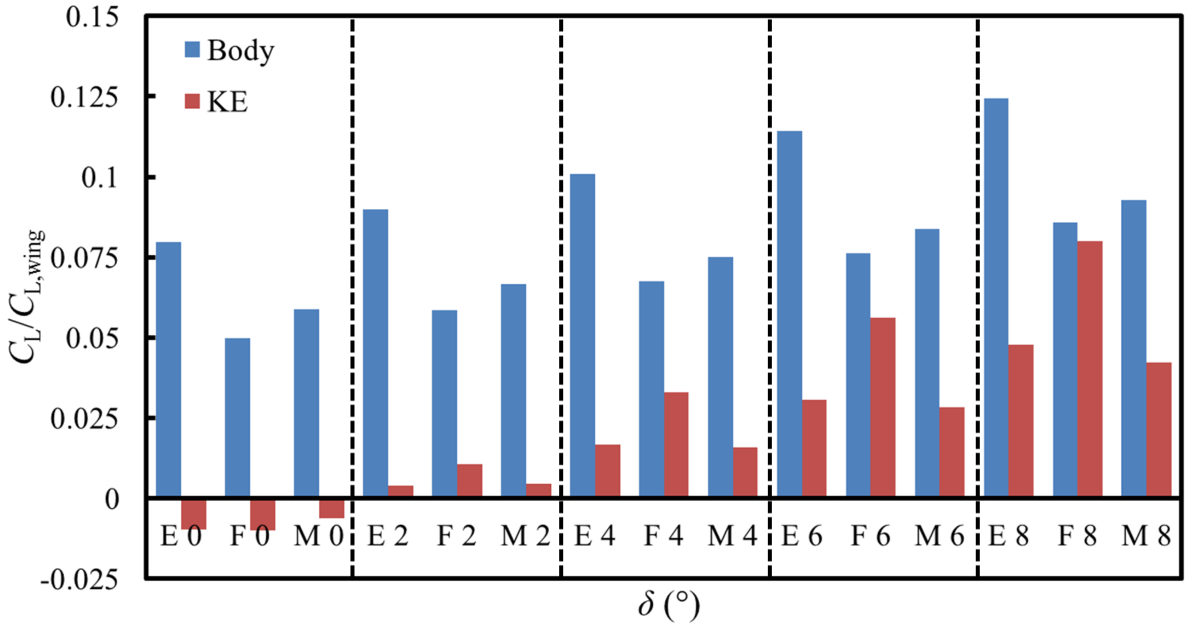

Figure 5.22: $C_L/C_{L,\text{wing}}$ for the three WBT-KEs at varying δ (E refers to WBT-0).

The KE of the two bluff bodies WBT-0 and WBT-M have a smaller lift contribution compared to the KE of WBT-F57 with an overall rate of increase that is smaller as well. This, as suggested before, is due to the sharper taper of the F-57 LDB leaving a larger surface area exposed and also allowing the leading-edge vortices to develop without as much interference from the body vortices, but as a consequence is more sensitive to the wing-induced downwash. The WBT-0 body shows a largest contribution in lift compared to the WBT-F57 body. The large contribution by WBT-0 body is attributed to the strong upper and lower body vortices that developed over the aftbody.

Any given wing-fuselage geometry has a higher *L*/*D* for a simple body deflection (NKE) then with tail (KE) (Figure 5.24). Though the KE adds lift, it does so with a drag cost that is relatively higher. For increment in lift alone, the WBT-F57 seems to be the most feasible option (Figure 5.15), but the drag increment reduces *L*/*D*, so if this is the figure of merit, the WBT-M would be considered the best candidate to further explore.

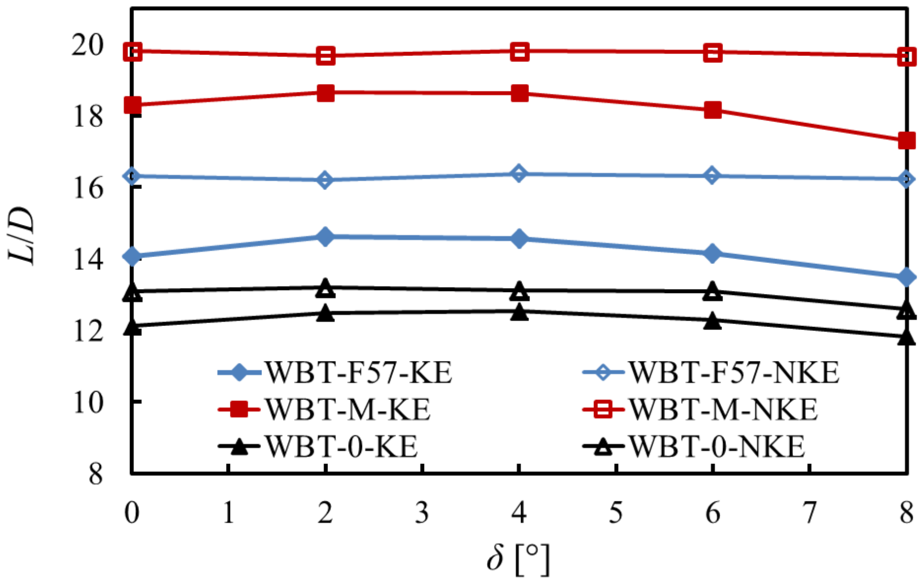

Figure 5.23: The effect of varying δ on L/D for KE and NKE for all three WBT combinations.

5.6 Summary, conclusions and recommendations

As an extension of the RANS simulations LDB-NKE/KEs, a NACA0012 wing was added (at $\alpha = 6°$) to form the proposed WBT with an LDB. The two proposed fuselage design objectives that were tested were to reduce the overall drag by using an LDB and to add a KE to restore the circulation over the (previously non-lifting) body so that the downwash distribution returns to that of a wing alone. The KE provided additional lift to restore the downwash distribution of the WBT and, in principle, should reduce the induced drag. However, this had a pressure drag penalty in the current configuration, primarily from the pressure drag component. The penalty was due to the specific geometry of the aftbody-tail section, where multiple separation and reattachment points were seen in the CFD results.

This work confirms that the KE can influence the WBT wake structure as initially estimated in experiment (Huyssen *et al*., 2012; Davis and Spedding, 2015). The results here suggest that the original Kutta Edge tail concept requires careful matching in the reality of viscous flows over bodies and wings at finite Re_c. In particular, if the KE is wholly or partially immersed in a wake that derives from earlier upstream separation, then the KE cannot operate effectively and the body termination conditions must already be judged to be sub-optimal. If there is an optimal WBT configuration that leads to significant benefits in L/D, then it presumably would have to live in a domain where separation is almost completely avoided. The second modifying consideration is that if an entire system is designed for a certain lifting objective, then the option of providing that weight support through a modified geometry that includes a KE might not be well described by a single number such as L/D. When system benefits of reduced wing length, area and weight are included (and subsequently fed back into the new design set-point for C_L), the interlocked design benefits of each component might be difficult to isolate. The properties of the idealized WBT project with real bodies at finite Re are not easy to predict, and a helpful start might involve selected parameter sweeps that test design sensitivities close to realistic operating conditions.

6. CONCLUSIONS AND PROPOSED FUTURE WORK

6.1 Summary

When an aircraft fuselage is relieved of the requirement of supporting an empennage, it can immediately assume a lower fineness ratio, with lower drag per unit volume and lower structural mass. Moreover, a carefully-shaped aftbody can be constructed, with a terminating trailing-edge, so as to impose the location of the rear stagnation point and generate circulation (and hence lift) over the body itself. Providing some lift by the body has advantages, one of which is that a more uniform spanwise lift distribution could improve the span efficiency. The initially proposed WBT configuration Huyssen *et al*. (2012) had a trailing-edge deflector flap, termed a Kutta Edge (KE), as it fixes the location of the rear stagnation point. The KE was affixed to a body with low fineness ratio ($l/d = 4.75$), which, although much closer to an optimal shape for low drag per unit volume, did not have any particular geometric features to assure low drag of the body itself.

The investigation of the proposed WBT configuration led to the consideration of three external aerodynamic applications, a wing, a low-drag body and the wing-body-tail combination. Although the study focuses on the changes in terms of the body and the KE, the addition of the wing in the final configuration and the low Re_c, at which the previous experimental work was done, led to an investigation of the wing alone. The NACA0012 used in the WBT is modelled at $Re_c = 10^5$ using steady, incompressible RANS in three different domains: 2D, pseudo-2D or P2D (a thin three dimensional slice) and 3D. The RANS results are compared to carefully conducted wind tunnel experiments at both $Re_c = 10^5$ and $Re_c = 5 \times 10^4$.

In a preliminary attempt to bring specifically-designed low-drag bodies (LDB) into the design space, Smith *et al.* (2017) conducted a numerical study to investigate the effect of adding a KE to two LDB's whose properties have been well established in the technical literature (Parsons and Goodson, 1972; Myring, 1981). LDBs are typically shorter and wider than a conventional fuselage, with the nose contours shaped to delay transition and aftbody contours to prevent separation. The combined effect can be a reduction of viscous and pressure drag. Initial experimental tests on KE deflection were always accompanied by aftbody deflection, and the same procedure was adopted in the numerical studies, so tail deflection was achieved through deflection of the entire aftbody.

Finally, a NACA0012 wing was added to the LDBs. The assemblage was expanded to include the KE and compare the drag, lift and span efficiency of the models. Two previous experimental studies (Huyssen *et al.*, 2012; Davis and Spedding, 2015) deal with the characteristics of what we term the WBT-0 configuration, with simply-specified geometry and no special attention to separation control. PIV measurements were made for the WBT-0 at various δ, (Huyssen *et al.*, 2012; Davis and Spedding, 2015) and in Davis and Spedding (2015) were compared with preliminary force balance measurements. Because of the lumped measurement of forces, it was not possible to identify the specific contributions of the various aerodynamic surfaces to the experimental global force coefficient. The overall purpose of this study was to provide some insight into the differences between the previous experimental and numerical studies and to investigate a potential design space of the initially tested WBT configurations. This exploration of the design space was conducted by using 10 discrete WBT configurations (five δ with and without KE) for the WBT-0, WBT-F57 and WBT-M.

6.2 Conclusions

A baseline result between experimental and numerical work provided some insight into sensitivities at these low Re_c. The 2D and P2D modelling domains were compared to XFOIL and with 2D wind tunnel data, with a force measurement uncertainty of less than 1.5%. The 3D model was compared to XFLR5 and 3D wind tunnel data. The P2D model, XFOIL and the experimental data showed a similar non-linearity of the $C_l(\alpha)$ profile at a small α. The wind tunnel experiments only agree well with the P2D RANS in C_l for $4° \leq \alpha \leq 8°$ and for the 3D RANS only for $-2° \leq \alpha \leq 2°$.This range of α was where the flow was dominated by the separation bubble. XFOIL had much worse qualitative agreement, compared to the experiment over most αs.

The strong dependence on the dynamics of the laminar boundary layer when considering a low Re_c influenced the choice of RANS model, the coupling and modelling of the transition, as well as the mesh domain and refinement. Repeatable and accurate measurements, even of time-averaged C_l and C_d are also made difficult by the sensitivity to boundary layer separation and reattachment as similarity between measured $C_l(C_d)$ polars breaks down. The prediction of the separation and reattachment regions and periodic vortex shedding, which gave rise to an oscillating behaviour of the force coefficients, becomes challenging when unsteady RANS is not used. Coupling of the transition model offers an improvement to the steady RANS and would be much less computationally expensive than the unsteady equivalent. Ideally, these cases should be solved using unsteady RANS, but for average global force estimations, comparisons using the steady RANS simulations were assumed to be sufficient. There was a lack of agreement, as expected, at these lower Re_c due to various numerical and experimental sensitivities. However, a diagnostic procedure was established, which guided the numerical domain set-up for the subsequent more complex cases.

Making use of the RANS, coupled to the transition model, the more complex LDBs from literature were modelled and showed reasonable comparison to available experimental results. Simple deflection of the aftbody provides camber and so predictably, increases lift in all cases, even with no tail. This lift increase is greatly enhanced with the addition of the KE, and the average lift slope of the Myring LDB-KE is higher than for F-57 LDB-KE. The lift contribution when the KE is added is far greater than what was expected from a delta-like wing alone, leading to the conclusion that the effect of the tail is non-local and increases the lift over the whole body-tail combination.

It appears that the width of the KE relative to the LDB geometry influences the overall efficiency of the LDB-KE configuration. Though the lift increment was larger when a tail was added (KE condition), the drag would also increase. It was further noted that such measures were quite sensitive to details of separation over the body and tail and that, paradoxically, a preferred arrangement would be to locate the KE entirely within the bounds of the viscous wake. This maximizes the favourable manipulation of streamlines over the preceding body contours while minimizing the drag penalty of being exposed to the freestream.

Overall, the Myring LDB-KE showed the best performance (*L*/*D*) compared to the F-57 LDB- and B-0-KE, not only because of the effective use of the KE to provide lift, but also since its design for delayed transition and preventing aftbody separation had the lowest drag penalty. Important design principles could be derived from the Myring LDB. These included the presence of a bluff aftbody that prevents separation and allows for the KE to remain within the viscous wake.

Finally, the NACA0012 wing was added to the LDBs-KE. The two bluff bodies WBT-0 and WBT-M had a larger portion of the KE embedded into the aftbody and therefore had a lower exposed surface area of the KE compared to the WBT-F57. As a consequence the WBT-F57 had a larger lift contribution but is also more sensitive to aftbody boundary layer and wing-induced wake interferences. If considering the increments in lift alone the WBT-F57 seems to be the most feasible solution however its drag increase reduces the overall *L*/*D* of the configuration. Therefore, if *L*/*D* was considered as the figure of merit for performance, as with the LDB study, the WBT-M would be considered the best candidate to further explore.

Initial speculation in terms of successful implementation of the KE by Huyssen *et al*. (2012) identified that with the fuselage contributing a portion of the lift for a given design objective, the wing size could be reduced. This in turn will lead to an improved transport efficiency as the overall aircraft mass and wetted surface could be reduced. *L*/*D* is an incomplete measure of such total system benefits and these design modifications may offer an overall benefit to the configuration that outweigh drag penalties observed here. However an optimisation study with a fully parameterised body of revolution at a given volume and flight speed could be useful to find a fuselage for low drag, and there are additional potential payoffs from lift provision by means of a blended aftbody-KE, rather than the somewhat piecemeal attachment offered here.

6.3 Recommendations and proposed future work

The exploration of this design space is far from complete. Although some preliminary guidelines in terms of the proposed WBT have been addressed there are multiple avenues along which the current study can continue.

A couple of immediate studies that may proceed from recommendations made in this work are as follows:

- ***Reliable wind tunnel and numerical datasets need to be established for bodies and wings at low Re$_c$.***

  A careful consideration of transition models and the implications of conducting experimental tests at Re$_c$ < 10^5 for LDBs and simple wing sections is necessary. Experiments reported here at Re$_c$ = 10^5 do not have other reported datasets in the literature to compare to, and none agree with existing computations either. The results have been comprehensively established at Re$_c$ = 10^5 and Re$_c$ = 5 x 10^4 for one single airfoil shape, the

NACA0012. The NACA0012 provided, at a Re_c range far below its original design point, a delicate and sensitive laboratory for the study of the viscous-inviscid balance that can have far-reaching effects in global aerodynamics.

Steady SST k-ω turbulence model coupled to the γ-Re_θ transition model were the only models used with variations in the 2D domain set-up. There are various alternatives in terms of the transition model as well as the turbulence models that can be tested. Jones *et al*. (2008), Almutairi *et al*. (2010) and Lee *et al*. (2015) consider a variety of models including 2D Laminar, LES and DNS, but even these results vary quite substantially.

At present, we cannot claim to have agreement on even the integrated aerodynamics of the time-averaged, steady, rigid case. A reasonable criterion for agreement would be when any two studies show overlap of their aerodynamic coefficients within experimental or numerical uncertainty. There is one such data set in Tank *et al*. (2016) and a technically sound baseline would require more to calibrate RANS models to ensure reasonable results in this Re_c without the computational expense of LES and DNS.

- ***The aftbody KE should be an integrated blended optimised design with the full WBT.***

The results here suggest that the original KE concept requires careful matching in the reality of viscous flows over bodies and wings at finite Re_c. If there is an optimal WBT configuration that leads to significant benefits in L/D, then separation would be almost completely be avoided. The LDBs used in this study were not optimised to reduce drag within a WBT configuration. If such a body is parameterised and then optimised in the presence of a wing-induced wake with an option to blend and camber the aftbody into a trailing-edge, different LDBs would surely be produced.

The second design requirement of the body shape should be that the entire WBT configuration meet a certain lifting objective. The camber and trailing-edge of the body will offer an additional lift to the WBT. This would lead to a snowball effect of reduced wing length, area and weight. Therefore a parameter sweeps can test design sensitivities close to realistic operating conditions of the WBT by allowing the body to be modified according to the requirements to avoid separation and contributing to lift, while at the same time the wing is allowed to change planform shape and blend to the body to accommodate the overall system and feed back into the new design set-point for C_L.

As part of this investigation the WBT can be optimised for different Re_c regimes. Parsons and Goodson (1972) and Smith *et al*. (1981) found that there is a unique LDB for each Re_l in laminar flow. It was also shown that if the body was not at its optimum λ there would be additional Re_l sensitivities. Whether this would hold for the WBT and overall Re_l is unclear at present.

- ***Detailed application studies for an airliner and glider.***

This work merely considered the flow physics and potential aerodynamic benefits for the proposed WBT configuration. However, various avenues of flight mechanics, propulsion and practical design would need to be addressed to prove this concept as a feasible candidate to replace the CDC. The guidelines provided here in terms of the LDB and the implementation of the KE can be applied to an airliner fuselage to determine the potential improvements compared to a reference fuselage.

An initial investigation by Kruger (2017) compares the CSR-01 reference aircraft (CeRAS, 2014) (Figure 6.1a) to a Myring LDB (that was suggested as a good starting point from the LDB-KE and WBT studies in Chapter 4 and 5) with the fuselage aftbody as a single continuous aftbody-KE unit (Figure 6.1b).

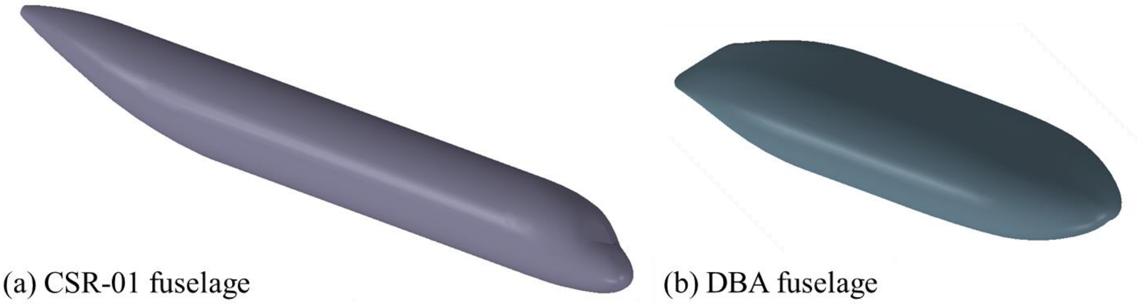
(a) CSR-01 fuselage

(b) DBA fuselage

Figure 6.1: (a) Double-bubble fuselage design and (b) the CSR-01 fuselage.

An initial cabin layout design led to a double-bubble concept to evaluate flight economy, compared to the CSR-01 reference aircraft (CeRAS, 2014) with flight mission requirements listed in Table 6.1. The CSR-01 represents a medium-range single-aisle airliner, two-class layout with 12 business and 138 economy class seats.

Table 6.1: Flight mission requirements for the CSR-01 reference aircraft.

Requirement	**Value**
Design range	5093 km
Maximum payload	20 000 kg
Initial cruise Ma	0.78
Initial cruise altitude	10 000 m

The CSR-01 was used to verify low-order physics-based computer software codes, SUAVE and TASOPT to determine whether these codes could predict known weight and drag values of the CSR-01. The CSR-01 fuselage was then substituted with the double-bubble concept fuselage, and first-order weight and drag estimations were obtained. The purpose of the investigation of Kruger (2017) was to determine whether the LDB will lead to an overall fuselage drag and weight reduction, and predict the potential secondary reduction effects of the configuration. The potential induced drag reduction was also considered based on the original premise by Huyssen *et al*. (2012) that the fuselage trailing-edge can restore the downwash distribution to that of an ideal wing.

It was estimated that the primary reductions (for changing the CSR-01 fuselage to the double-bubble concept fuselage) in weight and drag directly increase the range of the aircraft by 9%, with a potential further improvement up to 33% due to secondary reduction. The double-bubble concept has a potential fuel-burn saving of 20–25% with an overall L/D improvement of 6.5% at a cruise Mach number of 0.78. If the cruise Mach number is reduced, which many other candidate configurations were also considering (D8 configuration (Drela, 2011)), an overall L/D improvement of 20% at a Mach number of about 0.65 can be expected.

Therefore, it seems that even with the immediate drag increase due to the KE, the overall benefits could potentially outweigh this penalty. With further investigation and optimisation of the aftbody-KE, the aerodynamic performance could have an even larger improvement. This is merely the first study with encouraging results. However, a much more rigorous and careful assessment of the system would be required, with detailed CFD analysis rather than low-fidelity model estimates.

Other aspects to explore in terms of the practical application would be a stability analysis of the full WBT and also integrate propulsion systems into the configuration. These can either be conventional propulsion systems, but the optimisation and reshaping of the aftbody can also be explored for benefits when considering boundary layer ingestion propulsion systems as with the D8 in Drela (2011).

REFERENCES

Abbott, I.H. and Von Doenhoff, A.E., 1959. *Theory of wing sections*, Dover ed., McGraw-Hill, New York.

Agenbag, D.S., Theron, N.J. and Huyssen, R.J., 2009. “Pitch handling qualities investigation of the tailles Gull-Wing configuration,” *Journal of Aircraft*, Vol. 46, No. 2, pp. 683–691.

Almutairi, J.H., Jones, L.E. and Sandham, N.D., 2010. “Intermittent bursting of a laminar separation bubble on an airfoil,” *AIAA Journal*, Vol. 48, No. 2, pp. 414–426.

ASME V&V 20, 2009. Standard for verification and validation in computational fluid dynamics and heat transfer. American Society of Mechanical Engineers.

Barlow, J.B., Rae, W.H. and Pope, A., 1999. *Low-speed wind tunnel testing*, 3rd ed., Wiley, New York, NY.

Bastedo, W.G. and Mueller, T.J., 1986. “Spanwise variation of laminar separation bubbles on wings at low Reynolds numbers,” *Journal of Aircraft*, Vol. 23, pp. 687–694.

Bhat, S.S. and Govardhan, R.N., 2013. “Stall flutter of NACA0012 airfoil at low Reynolds numbers,” *Journal of Fluid Structures*, Vol. 41, pp. 166–174.

Boltz, F.W., Kenyon, G.C. and Allen, C.Q., 1960. “Boundary layer transition characteristics of 2 bodies of revolution,” *NASA TN D-309*.

Carmichael, B.H., 1964. “Computer study to establish the lower limit of length-to-diameter rates advisable for low-drag bodies,” SID64-1938, North American Aviation.

Carmichael, B.H., 1966. “Underwater vehicle drag reduction through choice of shape,” *AIAA Paper* 66-657.

Castiglioni, G. and Domaradzki, J.A., 2015. “Numerical modelling of separated flows at moderate Reynolds numbers appropriate for turbine blades and unmanned aero vehicles,” *Ph.D Dissertation*, University of Southern California, Los Angeles, CA.

Catalano, P. and Tognaccini, R., 2010. “Turbulence modelling for low-Reynolds-number flows,” *AIAA Journal*, Vol. 48, No. 8, pp. 1673–1685.

Cebeci, T., 1989. “Application of CFD to reduction of skin-friction drag,” *Progress in Aeronautics and Astronautics*, *Viscous Drag Reduction in Boundary Layers*, Vol. 123, pp. 115–178.

Central Reference Aircraft Data System (CeRAS), 2014, “CSR-01 Reference aircraft data,” Aachen University, http://ceras.ilr.rwth-aachen.de/trac.

Chappell, P.D., 1978. “Analysis of axisymmetric body profile drag data at zero incidence using Myrings method,” *ESDU Memorandum*, No 28.

Chevray, R., 1968. “The turbulent wake of a body of revolution,” *Journal of Basic Engineering*, Vol. 90, No. 2, pp. 275–284.

Coiro, D.P. and Nicolosi, F., 1994. “Design of natural laminar flow fuselages,” *ICAS 94-4.7.4*.

Davis, T.W. and Spedding, G.R., 2015. “Lift and drag measurements of a Gull-Wing configuration aircraft,” *53rd AIAA Aerospace Sciences Meeting*, AIAA 2015-0027. Kissimmee, FL, 5–9 January.

Dodbele, S.S., Van Dam, C.P., Vijgen, P.M.H.W. and Holmes, B.J., 1987. “Shaping of airplane fuselages for minimum drag,” *Journal of Aircraft*, Vol. 24, No. 5, pp. 298–304.

Drela, M., 1989. “XFOIL: An analysis and design system for low Reynolds number airfoils.” In *Low Reynolds Number Aerodynamics*, T.J. Mueller ed., Lecture Notes in Engineering No. 54, Springer-Verlag, Berlin, pp. 1–13.

Drela, M., 2011. “Development of the D8 transport configuration,” *29th AIAA Applied Aerodynamics Conference*, AIAA Paper 2011-3970, Honolulu, Hawaii, 27–30 June.

Drela, M. and Giles, M.B., 1987. “Viscous-inviscid analysis of transonic and low Reynolds number airfoils,” *AIAA Journal*, Vol. 25, No. 10, pp. 1347–1355.

Drela, M. and Youngren, H., 2001. XFOIL 6.9 user primer. Department of Aeronautics and Astronautics, Massachusetts Institute of Technology, Cambridge, MA.

ESDU, 1984. “The influence of body geometry and flow conditions on axisymmetric velocity distributions at subcritical Mach numbers,” *Engineering Sciences Data Item No.78037*.

ESDU, 1995. “Lift-curve slope of wing-body combinations,” *Engineering Sciences Data Item No.91007*.

Fincham, A.M. and Spedding, G.R., 1997. "Low cost, high resolution DPIV for measurement of turbulent fluid flow," *Experiments in Fluids* Vol. 23, No. 6, pp. 449–462.

Freeman, H.B., 1932a. “Measurements of flow in the boundary layer of a 1/40-scale model of the US airship ‘Akron’,” *NACA Report 430*.

Freeman, H.B., 1932b. “Force measurements on a 1/40-scale model of the US airship ‘Akron’,” *NACA Report 432*.

Gertler, M., 1950. “Resistance experiments on a systematic series of streamlined bodies of revolution – for application to the design of high-speed submarines,” *David Taylor Model Basin*, Report No. C-297, Washington DC.

Granville, P.S., 1953. “The calculation of the viscous drag of bodies of revolution,” *David Taylor Molel Basin*, Report No. DTMB-849, Washington DC.

Grundy, T.M., Keefe, G.P. and Lowson, M.V., 2001. “Effect of acoustic disturbances on low Reynolds number aerofoil flow,” *Fixed and flapping wing aerodynamics for micro air vehicle applications*, AIAA, Reston, VA, pp. 91–113.

Guglielmo, J.J. and Selig, M.S., 1996. “Spanwise variations in profile drag for airfoils at low Reynolds numbers,” *Journal of Aircraft,* Vol. 33, pp. 699–707.

Hammache, M., Browand, F.K. and Blackwelder, R.F., 2002. “Whole-field velocity measurements around an axisymmetric body with a Stratford–Smith pressure recovery,” *Journal of Fluid Mechanics*, Vol. 461, pp. 1–24.

Hess, J.L. and James, R.M., 1976. “On the problem of shaping an axisymmetric body to obtain low drag at high Re,” *Journal of Ship Research*, Vol. 20, No. 1, pp. 51–60.

Hoerner, S.F. 1965. *Fluid dynamic drag*. Hoerner Fluid Dynamics, Bakersfield.

Hoerner, S.F. 1985. *Fluid dynamic lift*. Hoerner Fluid Dynamics, Bakersfield.

Hsiao, F.B., Liu, C.F. and Zen, T., 1989. “Aerodynamic performance and flow structure studies of a low Reynolds number airfoil,” *AIAA Journal*, Vol. 27, pp. 129–137.

Huang, R.F. and Lee, H.W., 1999. “Effects of freestream turbulence on wing-surface flow and aerodynamic performance,” *Journal of Aircraft,* Vol. 36, pp. 965–972.

Huang, R.F., Shy, W.W., Lin, S.W. and Hsiao, F.B., 1996. “Influence of surface flow on aerodynamic loads of a cantilever wing,” *AIAA Journal*, Vol. 34, pp. 527–532.

Huyssen, R.J., Mathews, E.H., Liebenberg, L. and Spedding, G.R., 2012. “Wing-body circulation control by means of a fuselage trailing-edge,” *Journal of Aircraft*, Vol. 49, pp. 1279–1289.

Huyssen, R.J., Spedding, G.R., Mathews, E.H. and Liebenberg, L., 2016. “On the wing density and the inflation factor of aircraft,” *The Aeronautical Journal*, Vol. 120, No. 1224, pp. 291–312.

Jones, L.E, Sandberg, R.D. and Sandham, N.D., 2008. “Direct numerical simulations of forced and unforced separation bubbles on an airfoil of incidence,” *Journal of Fluid Mechanics*, Vol. 602, pp. 175–207.

Jones, R.T., 1980. *Wing theory*, Princeton University Press, Princeton, NJ.

Kim, D.H., Chang, J.W. and Chung, J., 2011. “Low-Reynolds-number effects on aerodynamic characteristics of a NACA0012 Airfoil,” *Journal of Aircraft*, Vol. 48, pp. 1212–1215.

Krauss, E.S., 1968. “Effect of shapes of conventional fuselages and of streamlined bodies on drag at subsonic speeds,” *Zeitscrift fur Flugwissenschaft und Weltraumforschung*, Vol. 16, pp. 429–438.

Kruger, M. 2017. “Implementing a low fineness ratio fuselage in an airliner,” Masters Dissertation, University of Pretoria, Pretoria.

Kuntawala, N.B., 2011. “Aerodynamic shape optimization of a blended-wing-body aircraft configuration,” Ph.D Dissertation, University of Toronto, Toronto.

Laitone, E.V., 1996. “Aerodynamic lift at Reynolds numbers below 7 x 104,” *AIAA Journal*, Vol. 34, pp. 1941–1942.

Lamar, J.E., 1974. “Extension of leading-edge-suction analogy to wings with separated flow around the side edges at subsonic speeds,” NASA-TR-R-428, Langley Research Center, Hampton, VA.

Langtry, R.B., 2006. “A Correlation-based transition model using local variables for unstructured parallelized CFD codes,” Ph.D Dissertation, Stuttgart University, Stuttgart.

Langtry, R.B., Menter, F.R., Likki, S.R., Suzen, Y.B., Huang, P.G. and Völker, S., 2006. “A correlation-based transition model using local variables – Part II: test cases and industrial applications,” *Journal of Turbomachinery*, Vol. 128, No. 3, pp. 423–434.

Lee, D., Nonomura, T., Oyama, A. and Fujii, K., 2015. “Comparison of numerical methods evaluating airfoil aerodynamic characteristics at low Reynolds number,” *Journal of Aircraft*, Vol. 52, No. 1, pp. 296–306.

Lee, T. and Su, Y.Y., 2012. “Low Reynolds number airfoil aerodynamic loads determination via line integral of velocity obtained with particle image velocimetry,” *Experiments in Fluids*, Vol. 53, pp. 1177–1190.

Li, Y., Nahon, M. and Sharf, I., 2011. “Airship dynamics modelling: a literature review,” *Progress in Aerospace Science*, Vol. 47, pp. 217–239.

Liebeck, R.H., 2004. “Design of the blended wing body subsonic transport,” *Journal of Aircraft*, Vol. 41, No. 1, pp. 10–25.

Liebeck, R.H., Page, M.A. and Rawdon, B.K., 1998. “Blended-wing-body subsonic commercial transport,” *Proceedings of the 36th Aerospace Science Meeting and Exhibit*, AIAA 98-0438, Reno, Nevada, 12–15 January 1998.

Lissaman, P.B.S., 1983. “Low Reynolds number airfoils,” *Annual Review of Fluid Mechanics*, Vol. 15, pp. 223–239.

Lutz, T. and Wagner, S., 1998. “Drag reduction and shape optimization of airship,” *Journal of Aircraft*, Vol. 35, No. 3, pp. 345–351.

Malan, P. and Suluksna, K., 2009. “Calibrating the γ-Re_θ transition model for commercial CFD,” *47th AIAA Aerospace Sciences Meeting*, AIAA 2009-1142. Orlando, FL, 5–8 January 2009.

Markatos, N.C., 1984. “The computation of thick axisymmetric boundary layers and wakes around bodies of revolution,” *Proceedings of the Institution of Mechanical Engineers, Part C: Journal of Mechanical Engineering Science*, Vol. 198, Iss. 1, pp. 51–62.

Marchman, J.F., 1987. “Aerodynamic testing at low Reynolds numbers,” *Journal of Aircraft*, Vol. 24, pp. 107–114.

McCroskey, W.J., 1987. "A critical assessment of wind tunnel results for the NACA0012 airfoil," NASA Technical Memorandum 100019.

McGhee, R.J., Jones, G.S. and Jouty, R., 1988. "Performance characteristics from wind-tunnel tests of a low-Reynolds-number airfoil," *AIAA 26th Aerospace Sciences Meeting*, Reno, NV, Jan 1988.

Meier, H.U. and Kreplin, H.P., 1981. "Experimental investigation of boundary layer transition and separation on a body of revolution," *Zeitscrift fur Flugwissenschaft und Weltraumforschung*, Vol. 4, pp. 65–71.

Menter, F.R., 1992a. "Improved two-equation k-ω turbulence model for aerodynamic flows," NASA Technical Memorandum TM-103975, NASA Ames, CA.

Menter, F.R., 1992b. "Performance of popular turbulence models for attached and separated adverse pressure gradient flows," *AIAA Journal*, Vol. 30, No. 8, pp. 2066–2072.

Menter, F.R., 1994. "Two-equation Eddy-viscosity turbulence models for engineering applications," *AIAA Journal*, Vol. 32, No. 8, pp. 1598–1605.

Menter, F.R., Langtry, R.B., Likki, S.R., Suzen, Y.B., Huang, P.G. and Volker, S., 2006. "A correlation-based transition model using local variables – Part 1: model formulation," *Journal and Turbomachinery*. Vol. 128, No. 3, pp. 413–422.

Morikawa, G., 1952. "Supersonic wing-body-tail interference," *Journal of Aeronautical Science*, Vol. 19, No. 5, pp. 333–340.

Mueller, T.J., 1999. "Aerodynamic measurements at low Reynolds numbers for fixed wing micro-air vehicles," RTO AVT/VKI Special Course on Development and Operation of UAVs for Military and Civil Applications, VKI, Belgium, 13–17 September 1999.

Mueller, T.J. and Batill, S.M., 1982. "Experimental Studies of Separation on a Two-Dimensional Airfoil at Low Reynolds Numbers," *AIAA* Journal, Vol. 20, pp. 457–463.

Multhopp, H. 1942. *Aerodynamics of the fuselage*. NACA.

Munk, M.M., 1923. "The minimum induced drag of aerofoils," NACA TR-121.

Myring, D.F., 1972. "The profile drag of bodies of revolution in subsonic axisymmetric flow," Royal Aircraft Est. TR72234.

Myring, D.F., 1981. "A theoretical study of the effects of body shape and Mach number on the drag bodies of revolution in subcritical axisymmetric flow," Royal Aircraft Est. TR8100.

Nielsen, J.N., 1988. *Missile aerodynamics*. NASA Ames Research Center.

Ol, M.V., McAuliffe, B.R., Hanff, E.S., Scholz, U. and Kahler, C., 2005. "Comparison of laminar separation bubble measurements on a low Reynolds number airfoil in three facilities," *135th AIAA Fluid Dynamics Conference*, AIAA Paper 2005-5149, June 2005.

Ohtake, T., Nakae, Y. and Motohashi, T., 2007. “Nonlinearity of the aerodynamic characteristics of NACA0012 aerofoil at low Reynolds numbers,” *Journal of the Japan Society for Aeronautical and Space Sciences*, Vol. 55, pp. 439–445.

Parsons, J.S. and Goodson, R.E., 1972. “Optimum shaping of axisymmetric bodies for minimum drag in incompressible flow,” Ph.D Dissertation, Purdue University, Lafayette.

Patel, V.C. and Chen, H.C., 1986. “Flow over tail and in wake of axisymmetric bodies: review of the state of the art,” *Journal of Ship Research,* Vol. 30, No. 3, pp. 201–214.

Patel, V.C. and Lee, Y.T., 1977. “Thick axisymmetric turbulent boundary layer and near wake of a low-drag body of revolution,” Iowa Institute of Hydraulic Research, IIHR Report 210, University of Iowa, Iowa City, IA.

Patel, V.C., Nakayama, A. and Damian, R., 1974. “Measurements in the thick axisymmetric turbulent boundary layer near the tail of a body of revolution,” *Journal of Fluid Mechanics*, Vol. 63, No. 2, pp. 345–367.

Pelletier, A. and Mueller, T.J., 2001. “Effect of endplates on two-dimensional airfoil testing at low Reynolds number,” *Journal of Aircraft*, Vol. 38, No. 6, pp. 1056–1059.

Pinebrook, W.E. and Dalton, C., 1983. “Drag minimization on a body of revolution through evolution,” *Computer Methods in Applied Mechanics and Engineering*, Vol. 39, pp. 179–197.

Pitts, W.C., Nielsen, J.N. and Kaattari, G.E., 1957. “Lift and center of pressure of wing-body-tail combinations at subsonic, transonic and supersonic speeds,” NACA-TR-1307, Ames Aeronautical Lab, Moffett Field, CA.

Polhamus, E.C. 1971. “Prediction of vortex-lift characteristics by a leading-edge suction analogy,” *Journal of Aircraft*, Vol. 8, No. 4, pp. 193–199.

Portsdam, M.A., Page, M.A. and Liebeck, R.H., 1997, “Blended wing body analysis and design,” AIAA Paper 97-2317, *15th Applied Aerodynamics Conference*, Atlanta, GA.

Prandtl, L., 1932. “Uber tragflugel kleinsten induzierten widerstandes,” *Zeitschrift fur Flugtecknik und Motorluftschiffahrt*, Vol. 28, No. XII,.

Qin, N., Vavalle, A. and Le Moigne, A., 2005. “Spanwise lift distribution for blended wing body aircraft,” *Journal of Aircraft*, Vol. 42, pp. 356–365.

Radespiel, R., Windte, J. and Scholz, U., 2007. “Numerical and experimental flow analysis of moving airfoils with laminar separation bubbles,” *AIAA Journal*, Vol. 45, No. 6, pp. 1346–1356.

Reneaux, J. 2004. Overview on drag reduction technologies for civil transport aircraft. *Tiré à part-office national d'études et de recherches aerospatiales*.

Rumsey, C.L. and Spalart, P.R., 2009. “Turbulence model behaviour in low Reynolds number regions of aerodynamic flow-fields,” *AIAA Journal*, Vol. 47, No. 4, pp. 982–993.

Roache, R.J., 1997. “Quantification of uncertainty in computational fluid dynamics,” *Annual Review of Fluid Mechanics*, Vol. 29, pp. 123–160.

Selig, M.S., Guglielmo, J.J., Broeren, A.P. and Giguere, P., 1995. *Summary of low-speed airfoil data*, Vol. 1, SoarTech Publications, Virginia Beach, VA.

Smith, A.M.O., Stokes, R.T. and Lee, R.S., 1981. “Optimum tail shapes for bodies of revolution,” *Journal of Hydronautics*, Vol. 15, No. 1–4, pp. 67–73.

Smith, L., Spedding, G.R. and Meyer, J.P., 2016. “Numerical and laboratory experiments on a new wing-body-tail configuration,” *54th AIAA Aerospace Sciences Meeting*, AIAA 2016-0800, San Diego, CA, 4–8 January.

Smith, L., Craig, K.J., Meyer, J.P. and Spedding, G.R., 2017. “Modifying low-drag bodies to generate lift: a computational study,” *Journal of Aircraft*, Vol. 54, No. 3, pp. 1150–1161.

Spedding, G.R. and Rignot, E.J., 1993. “Performance analysis and application of grid interpolation techniques for fluid flows,” *Experiments in Fluids*, Vol. 15, pp. 417–430.

Star-CCM+, CD-Adapco, 2013. User’s guide, Version 8.06, Melville, NY.

Stoney Jr, W.E., 1961. “Collection of zero-lift drag data on bodies of revolution from free-flight investigations,” *NASA-TR-R-100*.

Tank, J., Smith, L. and Spedding, G.R., 2017. “On the possibility (or lack thereof) of agreement between experiment and computation of flows at moderate Reynolds number,” *Interface Focus*, Vol. 7, Iss. 1, pp. 1–15.

Torenbeek, E., 1982. Synthesis of subsonic airplane design, Delft University Press, Kluwer Academic Publishers.

Tsuchiya, T., Numata, D., Suwa, T. and Keisuke, A., 2013. “Influence of turbulence intensity on aerodynamic characteristics of an NACA0012 at low Reynolds numbers,” *51st AIAA Aerospace Sciences Meeting*, 2013-0065, Grapevine, TE, January 2013.

Weinig, F., 1947. “Lift and drag of wings with small span,” *NACA-TM-1151*.

White, F.M., 2009. *Viscous fluid flow*. 6th ed., McGraw-Hill, Singapore.

Wickens, R.H., 1990. “Aerodynamic design of low drag fuselages,” *Canadian Aeronautics and Space Journal*, Vol. 36, No. 4, pp.189–201.

Windte, J., Scholz, U. and Radespiel, R., 2006. “Validation of RANS simulation of laminar separation bubbles on airfoils,” *Aerospace and Science and Technology*, Vol. 10, No. 6, pp. 484–494.

XFLR5, 2013. Analysis of foils and wings operating at low Reynolds numbers, Guidelines v6.02.

Yang, S.L. and Spedding, G.R., 2013a. “Spanwise variation in circulation and drag of wings at moderate Reynolds number,” *Journal of Aircraft*, Vol. 50, No. 3, pp. 791–797.

Yang, S.L. and Spedding, G.R., 2013b. “Separation control by external acoustic excitation on a finite wing at low Reynolds numbers,” *AIAA Journal*, Vol. 51, pp. 1506–1515.

Yang, S.L. and Spedding, G.R., 2013c. “Passive separation control by acoustic resonance,” *Experiments in Fluids*, Vol 54, pp. 1603.

Yang, S.L. and Spedding, G.R., 2014. “Local acoustic forcing of a wing at low Reynolds numbers,” *AIAA Journal*, Vol. 52, pp. 2867-2876.

Yonemoto, K., Takato, K., Ochi, H. and Fujie, S., 2008. “Kutta condition violation in two-dimensional NACA0012 airfoil at low Reynolds numbers,” *26th AIAA Applied Aerodynamics Conference*, AIAA, Paper 2008-6399, Honolulu, Hawaii, August 2008.

Young, A.D., 1939. “The calculation of the total and skin friction drags on bodies of revolution at zero Incidence,” Reports and Memoranda 1874, Air Ministry.

Yuan, W., Khalid, M., Windte, J., Scholz, U. and Radespiel, R., 2005. “An investigation of low Reynolds number flows past airfoils,” *23rd AIAA Applied Aerodynamics Conference*, AIAA, Paper 2005-4607, Toronto, Canada, June 2005.

Zabat, M., Farascaroli, S., Browand, F.K., Nestlerode, M. and Baez, J., 1994. “Drag measurements on a platoon of vehicles,” *California Partners for Advanced Transit and Highways Institute of Transportation Studies*, University of California, Berkeley, CA, UCB-ITS-PRR-93-27, pp. 18–31.

Zedan, M.F., Seif, A.A. and Al-Moufadi, S., 1994. “Drag reduction of airplane fuselages through shaping by the inverse method,” *Journal of Aircraft*, Vol. 31, No. 2, pp. 279–287.

APPENDIX A: NACA0012 AT RE = 5 x 10^4

A.1 Introduction

Experimental datasets were taken at $Re_c = 5 \times 10^4$ and $Re_c = 10^5$. Only the results for $Re_c = 10^5$ was shown and discussed in the main report since all consecutive CFD were done at this Re_c. However, there are more experimental and numerical datasets on the NACA0012 at $Re_c = 5 \times 10^4$ and so the same procedure was followed and reported on in this Appendix.

A.2 Wind tunnel experiments

The wind tunnel experiments were conducted in the same wind tunnel as describe in Chapter 3.2. For the $Re_c = 5 \times 10^4$ case the NACA0012 wing has a chord, c = 7.5 cm and span, b = 48 cm (AR = 6.4). In addition to the force measurements, particle image velocimetry (PIV) readings were also recorded. Figure A.1 shows a 3D illustration of this arrangement.

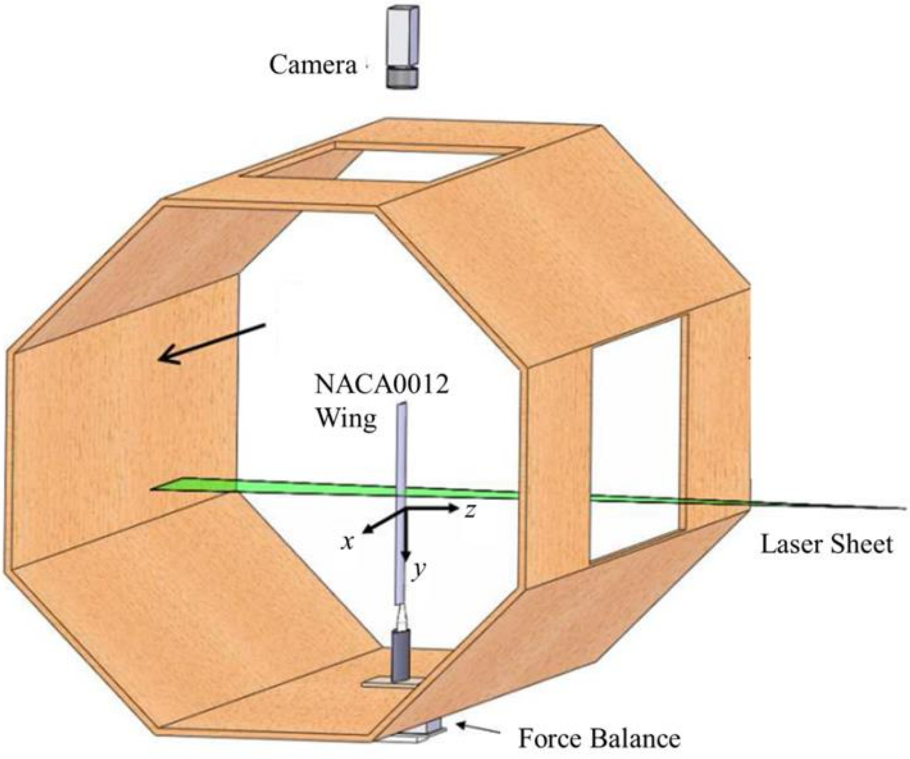

Figure A.1: Dryden wind tunnel set-up for the PIV and force balance system and the NACA0012 wing model (Adapted from Yang and Spedding, 2013).

A.2.1 Particle image velocimetry

PIV images are used to obtain qualitative flow visualization of velocity fields and profiles and spanwise vorticity. The flow in the wind tunnel is seeded with a Pea Soup "Rocket" glycerin-based smoke typically generating particles that are 0.2 – 0.3µm in size. These specific particles are large enough to take up several pixels in diameter to increase the accuracy of the PIV displacement calculation and small enough to accelerate in the flow (Fincham and Spedding, 1997).

The particles in the flow are illuminated by a Quantel EverGreen (class IV laser) double-pulsed Nd:YAG laser. The laser sheet of 6.35mm thickness is oriented in the *zx*-plane across the tunnel, illuminating a single chordwise span position and can be moved streamwise and spanwise for different locations.

An Image Pro X 2M (CCD) with KAI-2001 image sensor with 1600x1200 pixels (14-bit) and a Nikon 70 - 210mm f/4-5.6 NIKKOR AF lens is placed above the wind tunnel at a perpendicular position to the laser sheet to acquire images. The camera could transverse in a streamwise direction while maintaining a constant distance from the laser sheet.

Because the model was symmetric, the suction and pressure sides were illuminated by rotating the model in positive and negative α. To increase spatial resolution, the flow-field on each side of the airfoil was split into two, slightly overlapping sub-regions that were imaged in separate experiments. 200 image pairs were captured for each sub-region at a sample rate of 9.6 Hz, and the time delay between images in an image pair (δt = 8 μs – 30 μs) was carefully tuned to maximize the dynamic range of observable displacements while minimizing peak locking errors.

The images were processed with LaVision’s DaVis software to produce velocity field estimates in the streamwise and vertical directions, on a uniform grid using a multi-pass algorithm, with initial 64 x 64 pixel interrogation windows reducing to 16 x 16 pixels by the final pass. A 50% overlap gave a final spatial resolution of 8 pixels, which is 0.27 mm, or 0.0036c.

All 200 instantaneous velocity fields were averaged to produce one time-averaged velocity field for each sub-region. A built in Matlab thin-plate smoothing spline with a single smoothing parameter, similar to the spline used in Spedding and Rignot (1993), was applied to the averaged results in order to remove random noise. The average change in either velocity component in a sub-region due to smoothing was always less than 0.4% of the maximum value of that component in the sub-region. All four averaged and smoothed sub-region velocity fields were finally stitched together to form one complete velocity field, on both sides of the airfoil, for each α (Tank *et al*., 2016). All PIV flow-fields are shown near the mid-span section through the AR = 6.4 wing and therefore should not be affected by the wing tip vortices and could be assumed to be 2D.

A.3 Results

A.3.1 Force comparisons

Figure A.2a,b shows C_l and C_d for the 2D and P2D RANS simulations and the wind tunnel experiment from Tank *et al*. (2016). In Figure A.2a both the wind tunnel measurements and XFOIL the lift slope, dC_l/dα, or $C_{l,\alpha}$, is negative about $\alpha = 0°$ with C_l reaching a local minimum value at $\alpha = 0.5°$ for the experimental results and at $\alpha = 1°$ for XFOIL. Both lines then increases with a slope significantly below the theoretical thin airfoil result ($C_{l,\alpha} = 2\pi$) up to $\alpha = 2°$ for the experiment where it then follows the theoretical line up to $\alpha = 4°$ and then follows a smaller slope. The wind tunnel experiments only agree well with the RANS in C_l for $4° < \alpha < 8°$, which is α where the flow is dominated by the LSB itself, where at small α they are mainly influenced by details of trailing-edge separation.

The P2D RANS results never follow along the theoretical thin airfoil line and have a smaller $C_{l,\alpha}$. The 2D RANS simulated results show very little agreement with the experimental results and follows the theoretical curve for $C_l(\alpha)$ more closely than the experiment. Here, the lack of agreement on the RANS performance is largely determined by 2D approximation of the boundary layer and transition model coefficients which could be calibrated to reliable wind tunnel or LES values which currently do not exist. There is another problem with a RANS-type calculation in that the true flow-field is not steady, even at small α. A RANS estimate will converge to some solution, but that state is not necessarily a good measure of a time-average. Similar to the results at $\mathrm{Re}_c = 10^5$ in Chapter 3, in the P2D RANS case the 3D flow-field can stabilize the solution, even though the flow remains unsteady. The complicated structure of the RANS solution in 3D is seen in Figure A.3, where the skin friction coefficient, C_f is used as a means to indicate the locations of transition on the airfoil at $\alpha = 4°$. The variations show streamwise streaks in the LSB footprint and irregular wavy structures just upstream of the trailing-edge.

The lift-drag polar (Figure 2.Ab) has a characteristic loop with $C_l = 0$ at three different C_d points for both the experimental and XFOIL results. These multiple $C_l = 0$ crossings are not usual in any circumstance of low Reynolds numbers and their existence is unclear at this stage. dC_l/dC_d is quite steep, up to $C_l = 0.4$ for the RANS P2D results as well as the experimental results. They also follow a different trend line to the XFOIL and 2D RANS results that both have minimum C_d values, XFOIL at $C_l = 0.55$ and 2D RANS at $C_l = 0.35$.

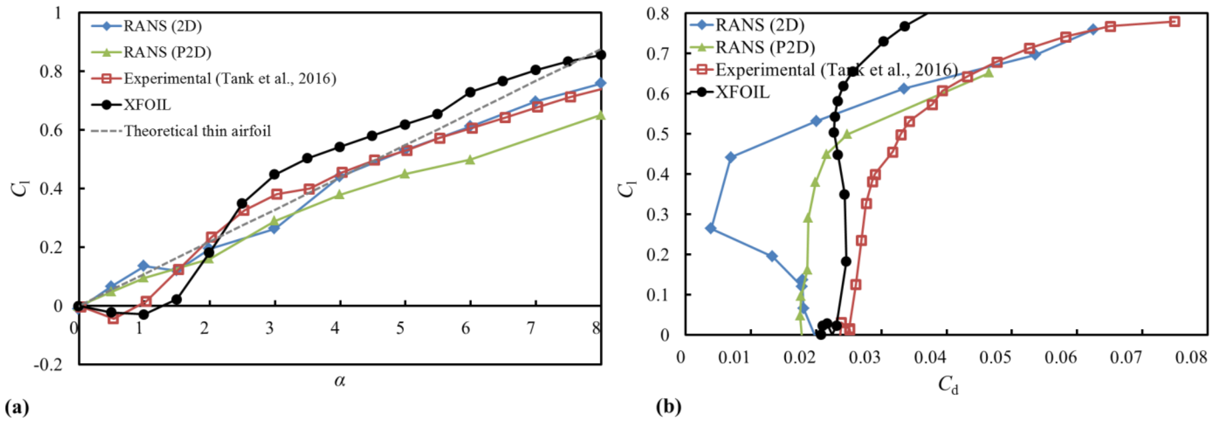

(a) (b)

Figure A.2: (a) Lift coefficients and (b) polar curves for a NACA0012 wing modelled at $\mathrm{Re}_c = 5 \times 10^4$ compared to results from the experiment, CFD and XFOIL.

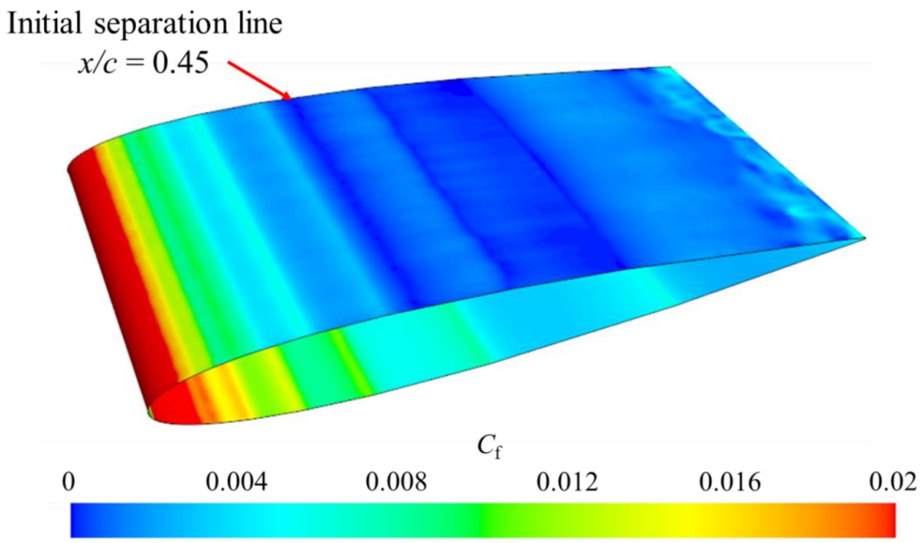

Figure A.3: Skin friction contour plot on the P2D and 3D NACA0012 models for α = 4º in a steady simulation.

Figure A.4 compares the more complete available experimental data at moderate $\mathrm{Re_c}$ as well as computational results from literature with the current results. Tank *et al*. (2016) include uncertainty bands, which Kim *et al*. (2011) do not show. In Figure A.4a a strict interpretation of the line plots is that for $0° < \alpha < 3°$ the experimental data do not compare well. There is also a large disagreement between the SST *k-ω* 2D and P2D RANS simulations and the 2D Laminar and 2D Baldwin-Lomax RANS simulation by Lee *et al*. (2015).

C_d of both experiments are significantly different, probably because of the difference in turbulence levels, which increase C_d at these $\mathrm{Re_c}$. In general, the specific reasons for the disagreements are not clear.

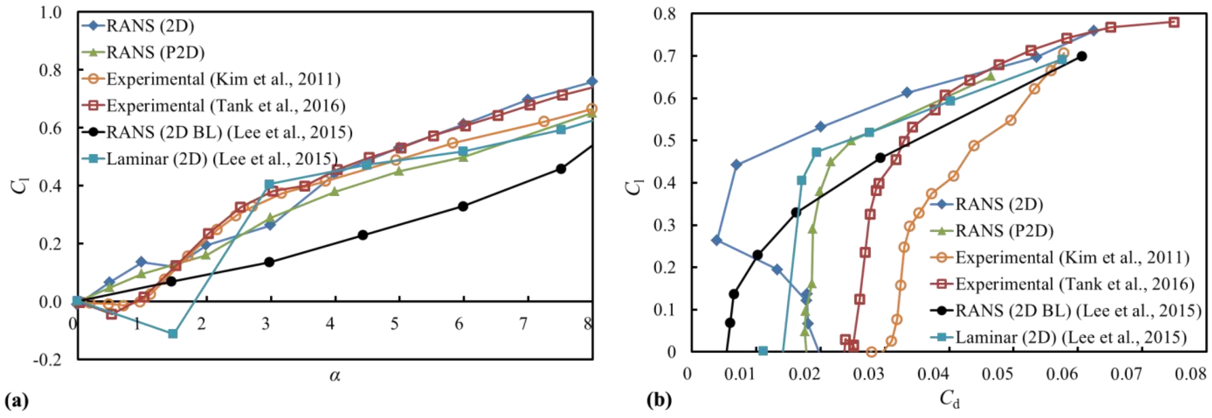

Figure A.4: (a) Lift coefficients and (b) polar curves for a NACA0012 wing modelled at $\mathrm{Re_c} = 5 \times 10^4$ compared to results from the experiment, literature sources and CFD.

The experimental observations from Figure A.2 are not peculiar to the 2D case (as simulated with endplates), but are just as evident for the finite wing, *AR* = 6.4 geometry shown in the equivalent Figures A.5. C_L is measurably and repeatedly negative for small positive α; the three, almost-linear slopes all differ from an expected value,

$$C_{L,\alpha} = C_{l,\alpha}\left(\frac{AR}{AR+2}\right), \tag{A.1}$$

where the 2D value, $C_{l,\alpha} = 2\pi$ is decreased as AR decreases (we ignore the correction for span efficiency, which is close to 1), though it remains a good average value over all α. For $3° < \alpha < 6°$, C_L significantly exceeds the theoretical value. In comparison to the RANS simulations a similar trend is observed and for $-3° < \alpha < 3°$ after which the RANS simulations have a smaller slope than the experiments.

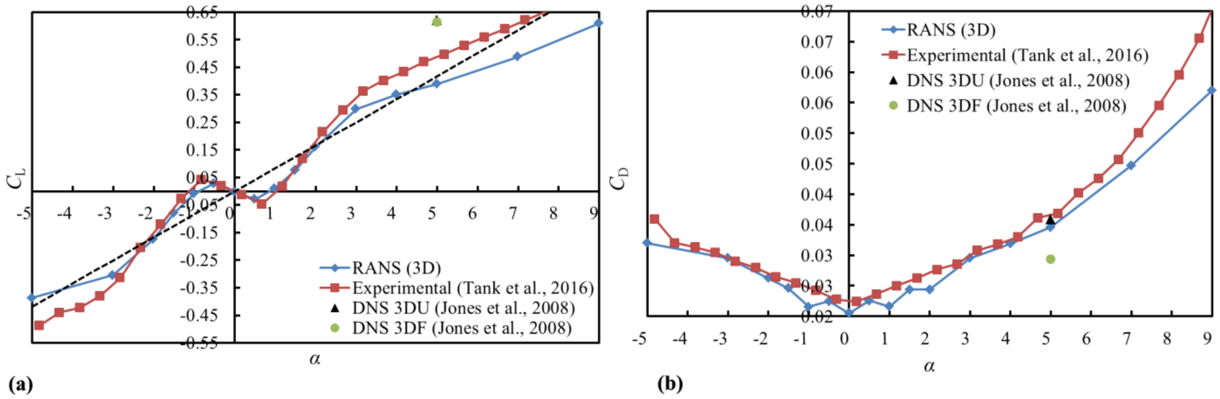

Figure A.5: (a) C_L and (b) C_D curves for a NACA0012 wing modelled at $Re_c = 5 \times 10^4$ compared to results from the experimental measurements and Jones et al. (2008).

The DNS computations of Jones *et al*. (2008) were one of the main motivations for making the NACA0012 comparison. A strict interpretation of Figure A.5a is that no simulation has results that are the same as experiment. In Figure A.5b for C_D, there is very little agreement between RANS and the experiment. The simulations persistently predict C_D lower than experiment, and perhaps one might expect this direction of bias when the experiment has low, but not zero turbulence. However, C_D in the 3D unforced case of Jones *et al*. (2008) is equal to the wind tunnel result. This is the single clear point of agreement.

A.3.2 Flow-field comparisons

PIV-derived, CFD 2D and P2D time-averaged streamwise velocity field, U_x/U for the α range {0, 0.5, 2, 4, 6, 8}° in Figure A.6 explain the force balance observations. As for the Re = 10^5 results, all three cases at $\alpha = 0°$ and $\alpha = 0.5°$ have the same forward movement of the separation point on the upper surface and aft movement of the lower (pressure) surface.

The PIV contour plots show that at this α, the lowest U_x/U of the airfoil is below the trailing-edge and a slightly favourable pressure gradient allows the streamlines to follow the curvature into an upward direction. The net acceleration is upwards, as the lower streamlines have higher curvature, and the net lift is negative. At the same time, the laminar separation before the upper surface trailing-edge assures that streamlines here are also deflected slightly away from the airfoil surface. Although the 2D CFD results also show deflection away from the airfoil surface, the steady RANS does not specifically solve the oscillating nature of the flow-field that an unsteady RANS or LES could, but rather gives an estimate of the expected flow-field. This explains the difference in the 2D, P2D and force measured results from Figure A.4.

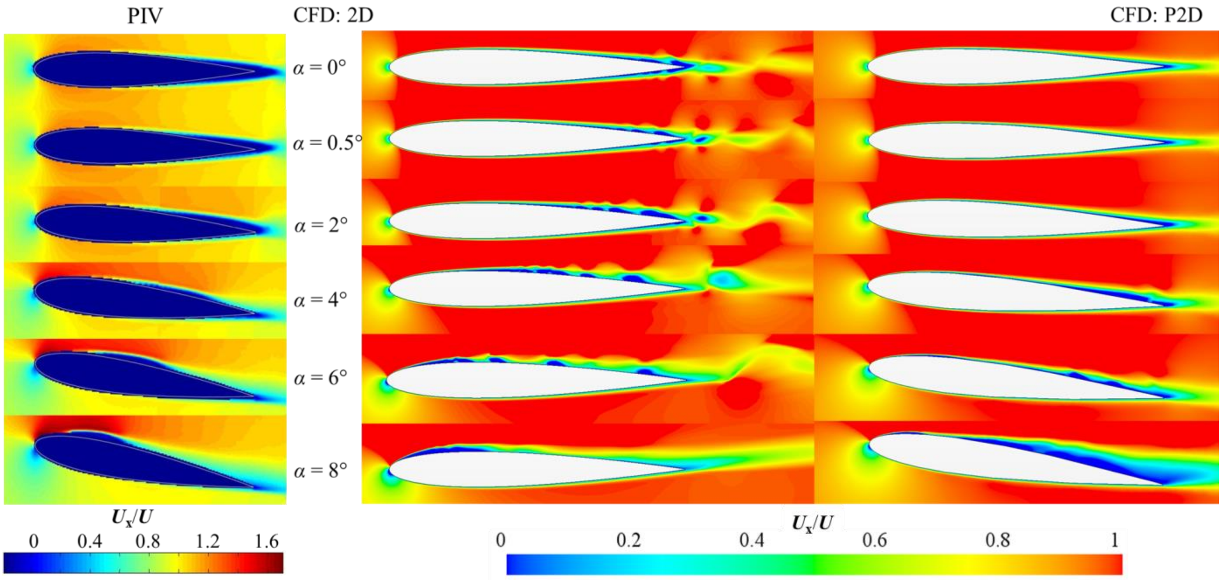

Figure A.6: Averaged streamwise velocity flowfields for 2D and P2D models at α = 0º, 0.5º, 2º, 4º, 6º and 8º.

At α = 2°, for all three cases the streamlines are not deflected strongly upwards on the lower surface, and though the separation line has moved further forward on the upper surface, the net flow has returned downwards. The 2D CFD shows an unrealistic amount and spread of recirculation bubbles, and although it agrees with the PIV that such bubbles should exist towards the trailing-edge, the PIV shows what appears to be a single large bubble. The flow is highly unsteady here, and explanations on time-averaged fields need careful interpretation in both PIV and CFD results.

At α = 4°, all fields show signatures of a separation bubble that reattaches on the upper surface. The flow acts as if the airfoil had a higher convex curvature on the upper surface, formed by the combination of airfoil surface and separation bubble. The changed effective camber accounts for the better than expected C_l around this α (Figure A.2a), with the drag cost comparatively small (Figure A.2b). This α-range marks the beginning of the broad maximum in L/D (Figure A.7) for the experimental results. However, the same broad maximum in L/D does not exist for the RANS results which suggest a maximum L/D for $5° < \alpha < 6°$ which is similar to literature of the NACA0012 at higher Re_c.

If the separation bubble can be termed a Laminar Separation Bubble (LSB) in the classical sense, then the LSB is associated with improved L/D over this range of α for the experimental results, which is contrary to most literature interpretations based on observations at higher Re_c. As the LSB moves forward on the upper surface with further increases in α (6° and 8°) the LSB shrinks in streamwise extent (Tank *et al.*, 2016). This is somewhat similar for the 2D RANS case, but there are still more recirculation bubbles rather than the single bubble suggested by the PIV.

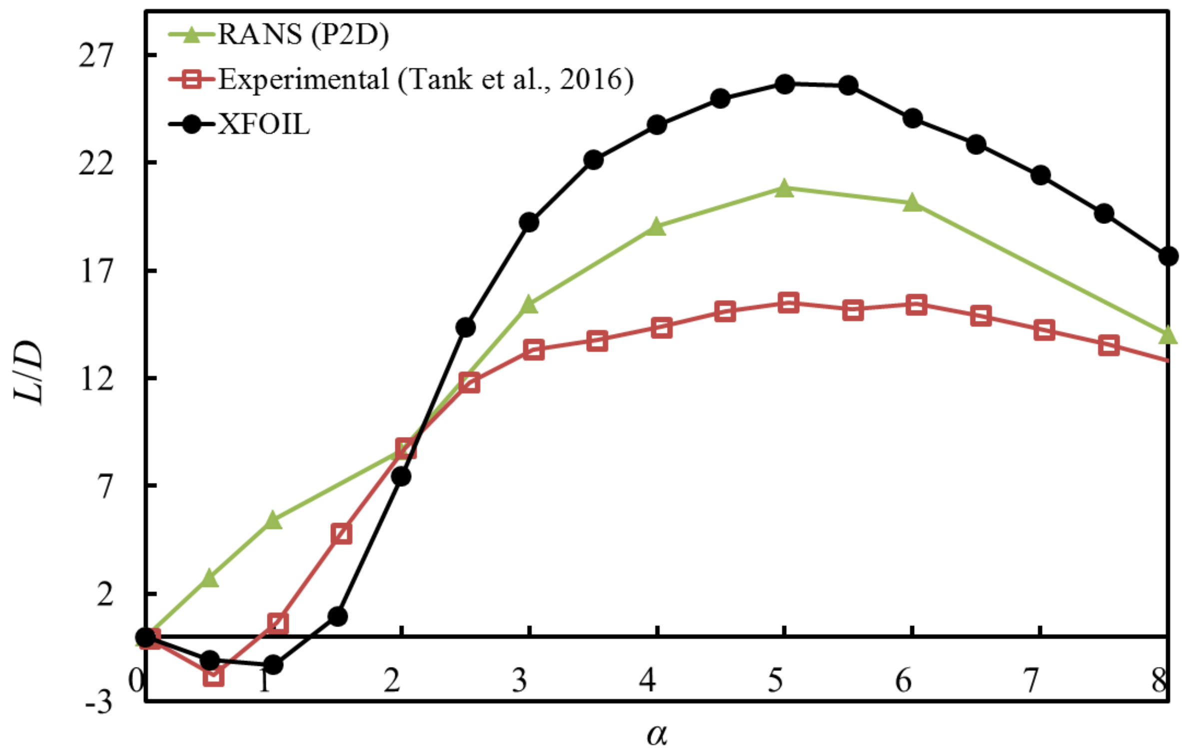

Figure A.7: L/D curves for a NACA0012 wing modelled at Re$_c$ = 5 x 10^4 compared to results from the experimental measurements.

Qualitatively, the U_x/U flow-fields for the CFD show the LSB signature as reduced in size, or absent in comparison to the PIV or rather than one multiple recirculation regions. In this respect, though much care has been taken in experiment to not over-smooth the data during spline interpolation, recall that all PIV data are spatial averages over the smallest correlation box, which is 16 pixels, or two grid points (0.54 mm) in size. This compares with an estimated LSB height (normal to the surface) of between 7 and 11 grid points for $\alpha = 4 - 11^{o}$, so is small but may smear out the apparent height by a factor of 2/7 at worst (Tank *et al.*, 2016).

In numerical results the first separation and reattachment points can be defined by successive zero crossings for the wall shear stress, and these locations are superimposed on the maps of spanwise vorticity in Figure A.8. The two computations differ, as in Figure A.6, but the marked separation and reattachment points in P2D are not as different from experiment as a simple inspection would suggest. The 2D simulation cannot be steady, at any α, and the P2D will be unsteady. Regardless, the fields in Figures A.6 and A.8, if not true averages, are still solutions to the RANS equations but are best regarded as snapshots of an underlying unsteady flow-field.

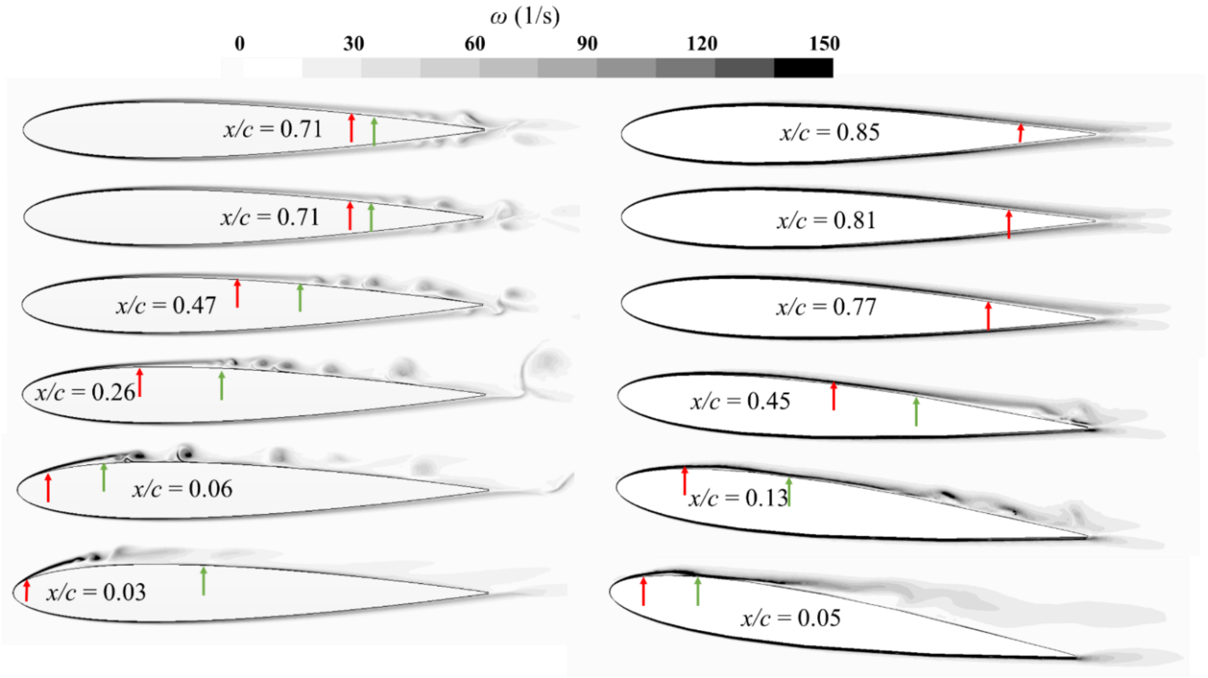

Figure A.8: Averaged spanwise vorticity for 2D and P2D models at α = 0°, 0.5°, 2°, 4°, 6° and 8°. The initial separation point is indicated by the red arrow and the initial reattachment point by the green arrow.

A.4 Discussion

A.4.1 Negative lift slope

The experimental result is quite surprising and opposite of any existing theoretical treatment. The correct explanation involves Re_c, the airfoil thickness and curvature, and the natural laminar separation point at small α. At small positive α, the flow around the lower airfoil surface is accelerated upwards because the separation point moves back, since the lowest part of the airfoil is below the trailing-edge. The corresponding separation point on the upper surface of the airfoil moves forward on the upper surface, decreasing the downward-induced velocities there at the same time.

In a vigorous check of existing literature, it was found that the negative lift had been seen before, but in isolated instances and with no general explanation. Most particularly Mueller and Batill (1982) showed a similar shaped $C_l(\alpha)$ curve (their Fig. 5), with initial negative C_l for $0 \leq \alpha \leq 3^\circ$, and high $C_{l,\alpha}$ thereafter. This peculiar result has stood alone in the literature – some product of the airfoil shape and low to moderate Re_c. Here, we propose that the robust appearance of this same result for the common NACA0012 shape implies that in careful experiments, most smooth, symmetric airfoils with sufficient thickness ($t/c \geq 10\%$) will show negative $C_{l,\alpha}$ at some Re_c, depending also on the surface finish and the ambient turbulence levels. The other relevant literature studies do not contradict this contention, though examples are isolated. Tsuchiya *et al*. (2013) measured $C_l(\alpha)$ for a NACA0012 at $\mathrm{Re}_c = 4.7 \times 10^4$, and reported nonlinear $C_l(\alpha)$ curves but no negative lift. The resolution in α was only 1° and $T = 0.5\%$. Negative C_l at $\alpha = 1^\circ$ for $\mathrm{Re}_c = 2.5 \times 10^4$ ($T = 1\%$) can be seen in their data but is not discussed. In 2D Navier-Stokes calculations, Yonemoto *et al*. (2008) investigated the negative lift observed in experiments by Othake *et al*. (2007), and proposed that a reversed flow at the trailing-edge upper surface could accelerate the corresponding boundary layer on the lower surface. Unique challenges with 2D computations have been noted in section A.3.1.

A.5 Conclusions

We conclude that the experiments reported here do not agree in a meaningful way with any others reported in the literature, and that none agree with existing computations either. The result have been comprehensively established at one single Reynolds number for one single airfoil shape.

Serendipitously, the venerable NACA0012 provides, at a low Re_c far below its original design point, a delicate and sensitive laboratory for the study of the viscous-inviscid balance that can have far-reaching effects in global aerodynamics. At present, we cannot claim to have agreement on even the integrated aerodynamics of the time-averaged, steady, rigid case. A reasonable criterion for agreement would be when any two studies show overlap of their aerodynamic coefficients within experimental or numerical uncertainty. There is one such data point in this paper, and a technically sound baseline would require more.